

(NASA-CR-176764) STATISTICAL PREDICTION OF  
DYNAMIC DISTORTION OF INLET FLOW USING  
MINIMUM DYNAMIC MEASUREMENT. AN APPLICATION  
TO THE MELICK STATISTICAL METHOD AND INLET  
FLOW (Kansas Univ. Center for Research,

N86-24933

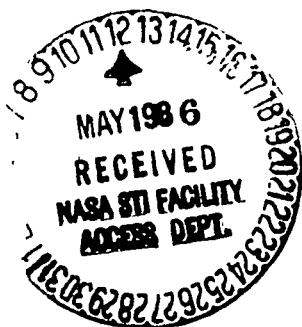
Unclas  
G3/34 42987

STATISTICAL PREDICTION OF DYNAMIC  
DISTORTION OF INLET FLOW USING MINIMUM  
DYNAMIC MEASUREMENT -- AN APPLICATION  
TO THE MELICK STATISTICAL METHOD

AND

INLET FLOW DYNAMIC DISTORTION  
PREDICTION -- WITHOUT RMS MEASUREMENTS

# CRINC



**THE UNIVERSITY OF KANSAS CENTER FOR RESEARCH, INC.**

2291 Irving Hill Drive-Campus West

Lawrence, Kansas 66045



THE UNIVERSITY OF KANSAS CENTER FOR RESEARCH, INC.

2291 Irving Hill Drive—Campus West  
Lawrence, Kansas 66045-2969

Telephone (913) 864-3441

**STATISTICAL PREDICTION OF DYNAMIC  
DISTORTION OF INLET FLOW USING MINIMUM  
DYNAMIC MEASUREMENT -- AN APPLICATION  
TO THE MELICK STATISTICAL METHOD**

**AND**

**INLET FLOW DYNAMIC DISTORTION  
PREDICTION -- WITHOUT RMS MEASUREMENTS**

**NASA Grant No. NAG 3-11  
FINAL REPORT  
Volume I**

**William G. Schweikhard  
Principal Investigator**

**and**

**Yen-Sen Chen  
Graduate Research Assistant**

**April 1986**

**PART I**

**STATISTICAL PREDICTION OF DYNAMIC  
DISTORTION OF INLET FLOW USING MINIMUM  
DYNAMIC MEASUREMENT — AN APPLICATION  
TO THE MELICK STATISTICAL METHOD**

## SUMMARY

A simplified explanation to the Melick method of inlet flow dynamic distortion prediction by statistical means has been included. A hypothetical vortex model is used as the basis of the mathematical formulations. The main variables of this model are identified by matching the theoretical total pressure rms ratio with the measured total pressure rms ratio. Data comparisons using HiMAT inlet test data set indicate satisfactory prediction of the dynamic peak distortion for cases with boundary layer control device --- vortex generators.

A method of the dynamic probe selection, an essential part of this research, has been developed. Validity of the probe selection criteria has been demonstrated by comparing the reduced-probe predictions with the 40-probe predictions. Results indicate that the number of dynamic probes can be reduced to as few as 2 and still retain good accuracy.

## TABLE OF CONTENTS

SYMBOLS . . . . .	ii
INTRODUCTION . . . . .	1
THE MELICK METHOD . . . . .	6
Vortex Model . . . . .	6
Matching Model to a Particular Test Case . . . . .	11
Determination of Mean Vortex Size . . . . .	13
Determination of Vortex Flux. . . . .	15
Determination of $K$ and $\sigma_K$ . . . . .	16
Contribution of Errors in $n$ and $m$ to Final Result . . . . .	17
Effect of Engine Response Characteristics . . . . .	19
Special Treatment for Some Distortion Factors . . . . .	20
Melick Mapping Methods . . . . .	21
DATA COMPARISONS . . . . .	22
METHOD OF PROBE SELECTION . . . . .	27
Development of Probe Selection Criteria . . . . .	27
Accuracy of the Criteria . . . . .	30
CONCLUSIONS . . . . .	35
REFERENCES . . . . .	37
APPENDIX . . . . .	39
TABLES . . . . .	50
FIGURES . . . . .	54

## SYMBOLS

APD	amplitude probability density
a	radius of vortex core (radius at the point where maximum velocity occurs)
$\bar{a}$	mean vortex core size
b	radial weighting factor, see table I
$D_j$	diameter of ring j, see table I
erf(x)	the error function of x, $\text{erf}(x) = \frac{2}{\sqrt{\pi}} \int_0^x e^{-\xi^2} d\xi$
f	frequency, Hz
$f'$	intermediate frequency used to match theoretical and analytical PSD functions
$f_c$	characteristic engine response frequency
$G_{\Delta p_t}/q_2$	real part of the power spectral density function of the total pressure fluctuations
H	function describing filter characteristics
IDC	circumferential distortion factor, (see table I)
IDR	radial distortion factor, (see table I)
K	generic distortion factor
$K_{A2}, K_\theta, K_{RAD}$	combined, circumferential & radial distortion factors respectively, (see table I)
$K_{D2}$	distortion factor, (see table I)
$K_{inst}$	generic instantaneous value of K
$K_{max}$	generic maximum value of K used in the beta distribution function
$K_{max-inst}$	most probable maximum value of $K_{inst}$
$K_{ss}$	generic steady-state value of K
$\bar{K}$	mean value of $K_{inst}$

$\Delta K$	difference between $\bar{K}$ and $K_{SS}$ , $\Delta K = \bar{K} - K_{SS}$
$k$	normalizing factor in beta probability density function
$m$	exponent in beta probability density function
$N$	total vortex flux, number per second
$n$	exponent in beta probability density function
OD	outer duct diameter, (see table I)
$P$	probability density function
PSD	power spectral density
$P_1$	cumulative probability
$P_2$	probability density function for peak distortion factor
$p$	static pressure
$p_t$	total pressure
$\Delta p_t$	total pressure fluctuation relative to the mean
$q$	dynamic pressure, $(q = \frac{1}{2} \rho v^2)$
$R_{\Delta p_t / q_2}$	autocorrelation function of the total pressure fluctuations
$R_T$	compressor tip or duct radius
$R_V$	$\sqrt{Y_V^2 + Z_V^2}$ , shortest distance from probe to vortex
$r$	radius from vortex centerline
rms	root mean square
$r_p$	radius from vortex center line to probe
$T$	period of time over which the maximum instantaneous is to be determined
$t$	time
$U_2$	mean duct velocity
$u$	x component of velocity induced by the vortex

$u_x$	X component of velocity induced by the vortex at the probe
$v$	y component of velocity induced by the vortex
$v_\theta$	tangential component of velocity induced by the vortex
$w$	z component of velocity induced by the vortex
$X, Y, Z$	fixed coordinate system at the compressor face, (figure 9)
$X_p, Y_p, Z_p$	coordinates of a compressor face pressure probe
$X_v, Y_v, Z_v$	location of the $x'y'z'$ coordinate system relative to the $X, Y, Z$ system, (figure 9)
$x, y, z$	local coordinate system of the vortex, (figure 9)
$x', y', z'$	coordinate system parallel to the $X, Y, Z$ system but with the same origin as the $x, y, z$ system, (figure 9)
$\beta$	vortex orientation angle between the y-axis and the $x'-y'$ plane, (figure 9)
$\Gamma(n)$	denotes the gamma function of $n$ , $\Gamma(n) = \int_0^\infty e^{-x} x^{n-1} dx, \quad \Gamma(n+1) = n\Gamma(n),$ (figure 3)
$\gamma$	angle between the $x'$ and $x$ axes, with the $x$ axis in the $x'-y'$ plane, (figure 9)
$\theta$	circumferential coordinate at the compressor face
$\mu_n$	$n$ th central moment (taken about the mean) of a statistical distribution
$\xi$	dummy variable
$\rho$	fluid density
$\sigma$	standard deviation or rms of a time-dependent function
$\tau$	time delay in the definition of the autocorrelation function



## Subscripts

a	vortex core size
cir	circumferential
i	index of rake of pressure probes
inst	instantaneous value
j	index of ring of pressure probes
K	distortion factor
max	maximum value
min	minimum value
2	mean flow at the compressor face station
$\Delta p_t$	total pressure fluctuations
rad	radial
ss	steady-state condition
v	vortex or tangential velocity
$\infty$	evaluated for all frequencies

## Superscripts

( )	mean value
( ^ )	variable is a function of a number of random variables

## INTRODUCTION

It has long been appreciated that steady-state inlet flow nonuniformities (flow distortion) may have a significant effect on the stability of a gas turbine engine and may further induce engine stall (surge). Traditionally, steady-state nonuniformities are measured at the inlet/engine interface (compressor face) by using 40 or more steady-state total pressure probes. These measurements are combined in such a way as to produce a single distortion factor according to different definitions (some common ones are listed in Table 1). These distortion factors are then correlated with the surge level.

It was not until recently that attention has been paid to the effect of dynamic distortion which reveals the time-variant characteristics of the distortion pattern measured at the compressor face. This dynamic effect may cause engine surge while the steady-state distortion is substantially below the surge level. Therefore, determination of the dynamic effect of inlet flow becomes more important if high performance inlets are to be attained.

Air flow convecting through the inlet duct is always unsteady due to flow disturbances generated internal and external to the inlet. These disturbances include externally generated turbulence. External turbulence is caused by atmospheric turbulence, the flow field of the aircraft

upstream of the inlet and by external shock waves when in supersonic flight. Internally generated disturbances are caused by non-uniformities due to change in the contours of the inlet duct and by shock boundary layer interactions. Experimentally, this flow unsteadiness is measured at the compressor face in terms of total pressure fluctuations by the use of 40 (commonly used) or more high response total pressure probes (dynamic probes). These unsteady total pressure data are analyzed deterministically in terms of time-variant distortion factor throughout the data recording period. The maximum peak distortion factor value of the dynamic distortion factor is then screened and used as a design reference. This method of data analysis is quite tedious and expensive. There is a real need to develop methods to predict both the peak dynamic distortion factor and the corresponding compressor face total pressure pattern. These are important for inlet design and data analysis, however, they are dependent upon the statistical characteristics of the unsteady total pressure data. It is for this reason that statistical treatments which utilize the randomness of the total pressure data have been employed to predict the peak dynamic distortion factor from limited test data (e.g., root mean square, rms, level of total pressure fluctuations). Improved efficiency and reduction in cost have been achieved by this approach. Success of the statistical approach is made possible due to the fact that probability density distributions of the time-variant distortion factor

and the time-variant total pressure data are nearly Gaussian (normal distribution) around their mean values (ref. 4). This is true for most of the test cases which do not involve inlet flow of strong interaction. Figure 1 shows the physical and statistical characteristics of a typical inlet test data. A time history of the total pressure fluctuations shown in Figure 1(b) is measured by the dynamic probe shown in Figure 1(a). Probability distribution of the total pressure data is shown to be normal as illustrated in Figure 1(b). The time-variant distortion factor resulting from the combined effect of all 40 probes is illustrated in Figure 1(c) which also shows a normal distribution of the probability density of the distortion factor.

Three major statistical approaches have been developed to predict the peak distortion factor and distortion pattern. The first one, due to Jacocks, uses Gumbel's extreme value theorem to extrapolate the peak distortion value within a specified time period from the first short time segment of deterministic information (ref. 1). The second approach, due to Motycka, et al., utilizes a random number generator for simulating the total pressure fluctuations at each probe. The simulated values are based on the measured total pressure rms level and the steady-state value. Time-variant distortion factors are calculated by using the generated total pressure data, from which the peak dynamic distortion factor is determined (ref. 2). The third approach, developed by Melick,

et al., assumes that dynamic effect of the inlet flow is totally attributed to the pressure disturbances caused by a sequence of convecting vortices with random variables. The peak distortion factor is determined from this physical model and its statistical properties. The main variables of the vortex flow model are identified by matching analytical and measured total pressure rms levels (ref. 3).

Although all the three methods produce satisfactory results, the Melick method is least costly in terms of instrumentation and analysis effort. It can be used online while the test is in progress (ref. 5). This makes the Melick method a very attractive tool for early analysis in the inlet design process.

Also, to minimize costs of dynamic instrumentation and overall inlet development, it is desired to predict the dynamic distortion in the early stages of inlet development using a minimum number of dynamic probes. Each high response total pressure probe is very expensive. This can be achieved, in principle, by using the Melick method as mentioned in ref. 3 and ref. 5. Melick's method has the potential to achieve this goal since its peak distortion is predicted by the average value of total pressure rms levels. Ideally, a single probe would be sufficient to provide the same rms level.

Acceptance of the Melick method has been slow due to a lack of understanding by the inlet test and development

engineers. Thus, the first objective of the present study is to explain and clarify Melick's Technique. The second objective is the development of criteria of dynamic probe selection (location) based on the steady-state pressure map.

A brief review and discussion of the Melick method is presented in the first section followed by a series of data comparisons using HiMAT inlet test data set (ref. 6). Finally, the last section contains the development of the criteria for selecting the location of the dynamic probes. The results of numerical experiments to validate the probe selection criteria are shown.

## THE MELICK METHOD

### Vortex Model

Physically, total pressure fluctuations of inlet flow measured at the compressor face can be interpreted as time-variant velocity variations on the compressor face. This time-variant velocity variation can again be expressed in terms of time-variant vorticity variation. Therefore, it is envisioned that the total pressure fluctuations are caused by a sequence of time-variant vortices passing through the compressor face at a rate of  $N$  vortices per second. Each vortex would then create total pressure variations at the compressor face and generate certain instantaneous (time-variant) distortion factors,  $K_{inst}$ , at that instant of time as illustrated in Figure 2. Figure 2(b) shows that the time-variant total pressure, measured by a probe, due to a convecting vortex which has a velocity profile as shown in Figure 2(a).

It is assumed that the instantaneous distortion factor,  $K_{inst}$ , caused by a single vortex is treated as a single discrete event. Thus, there are  $NT$  discrete events during the data recording period  $T$ . Each vortex has an arbitrary location, orientation, and strength. It is further assumed that these discrete events are random and independent drawings from a probability density distribution described by a Beta distribution function (ref. 7). The reason for choosing the Beta distribution is because it is the only distribution function

that has one bounded positive variable and the ability to modify the probability distribution by varying two simple parameters. Figure 3 shows the general characteristics of the Beta distribution function including the effects of the parameters,  $m_x$  and  $n_x$ , on the shape of the distribution. The variable of the distribution,  $x$ , is shown to be bounded within the interval of 0. and 1. The shapes of the distribution are skewed to the left in Figure 3 when  $n_x$  is greater than  $m_x$ . An opposite skew would result if  $n_x$  is less than  $m_x$ . When  $n_x$  and  $m_x$  are identical, a Gaussian (normal) distribution can be obtained.

Using the Beta distribution, the probability density function of the instantaneous distortion factor,  $K_{inst}$ , is given as:

$$P = P \left( \frac{K_{inst}}{K_{max}} \right) = K_K \left( \frac{K_{inst}}{K_{max}} \right)^{m_K} \left( 1 - \frac{K_{inst}}{K_{max}} \right)^{n_K} \quad (1)$$

where  $K_{inst}$  is rescaled (normalized) by its upper bound,  $K_{max}$ , and  $K_K$  is a function of  $m_K$  and  $n_K$  through the gamma function as shown in Figure 3. Equation (1) involves three unknowns,  $K_{max}$ ,  $m_K$  and  $n_K$ , which require three equations for solutions. These three equations can be obtained by using statistical moments analysis for  $P$  (i.e., the first moment, the second moment and the fourth moment, ref. 8). The first and second moments of  $P$  are related to the mean,  $\bar{K}$ , and variance,  $\sigma_K^2$ , of the instantaneous distortion factor,  $K_{inst}$ , respectively. The fourth moment (Kurtosis) of  $P$  is



assumed to be zero since the distribution of  $P$  has been shown (ref. 4) to be nearly Gaussian (normal distribution) for most experimental data. The parameters,  $\bar{K}$  and  $\sigma_K$ , can be obtained from an analytical expression of  $K_{inst}$  and its statistical moments. These can be derived from the vortex flow model with the main variables,  $\bar{a}$  (mean vortex size) and  $N$  (vortex flux) being identified by matching analytical and measured total pressure rms levels. This will be discussed in detail later. Assume, for the moment, that  $\bar{K}$  and  $\sigma_K$  are already obtained and the distribution of  $P$  is known. Figure 4 shows some illustrations of the distributions of  $P$  with various values of  $\bar{K}$  and  $\sigma_K$ . Note that the variable of  $P$ ,  $K_{inst}$ , has been normalized by  $\bar{K}$  and  $\sigma_K$ . That is,

$$P = P\left(\frac{K_{inst}-\bar{K}}{\sigma_K}\right) \quad (1a)$$

Equation (1a) is the essence of the Melick method, from which the peak distortion (i.e. near the right end of Figure 4) can be extrapolated by using the statistical characteristics of the peak values. Unknowns of this model must be related to the inlet flow conditions in order to rescale the analytical model close to the experimental measurements.

It is of primary importance that the peak value of  $K_{inst}$  among the NT events be determined from the distribution of  $P$ . Before this peak value can be found, conditions

for the occurrence of the peak value must be determined. The peak value implies the largest value of  $K_{inst}$  among the whole population of NT events. In other words, it is the only single event that can exceed a certain distortion level. This corresponds essentially to the situation in which the deterministic peak distortion factor is found. Therefore, the probability of one single event that exceeds a certain distortion level needs to be defined. This can be described by a cumulative probability of P above a certain distortion level. Equation (2) defines this cumulative probability of P as  $P_1$ . Results are illustrated in Figure 5 for various values of  $\bar{K}$  and  $\sigma_K$ . Note again that  $K_{inst}$  has been normalized by  $\bar{K}$  and  $\sigma_K$ .

$$\begin{aligned}
 P_1 &= P_1 \left( \frac{K_{inst} - \bar{K}}{\sigma_K} \right) = \left( \text{Prob. of } \frac{K_{inst} - \bar{K}}{\sigma_K} > \frac{K - \bar{K}}{\sigma_K} \right) \\
 &= \int_{\frac{K - \bar{K}}{\sigma_K}}^{\frac{K_{max} - \bar{K}}{\sigma_K}} p \left( \frac{K_{inst} - \bar{K}}{\sigma_K} \right) d \left( \frac{K_{inst} - \bar{K}}{\sigma_K} \right) \quad (2)
 \end{aligned}$$

Since it is required that only one event, caused by one vortex, can create a peak distortion above a certain level, the whole population is therefore required to have only one event with probability  $P_1$  and (NT-1) events with probability  $(1-P_1)$ . This is like the Bernoulli test. The overall probability for the condition of only one peak distortion above a certain level is therefore described by the

Bernoulli (binomial) distribution function given by equation (3) (ref. 7) and is illustrated in Figure 6.

$$P_2 = \binom{NT}{1} P_1(1-P_1)^{NT-1} = NT P_1 (1-P_1)^{NT-1} \quad (3)$$

From equation (3), the objective peak distortion corresponds to the condition when  $P_2$  is maximum for a fixed  $NT$ , (i.e., the most probable condition for the peak dynamic distortion to occur). This condition is found to be  $P_1 = 1/NT$  when  $P_2$  reaches its maximum. This is obtained by letting the first derivative of  $P_2$  (equation 3), with respect to  $P_1$ , equal zero. This can be seen clearly when Figure 4 and Figure 6 are combined with the aid of Figure 5 to produce Figure 7. For example, when  $NT=10$  and  $K/\sigma_K=4$ , Figure 6 shows that at maximum  $P_2$ ,  $P_1 = 0.1$  approximately. Using this value of  $P_1$  in Figure 5, the corresponding value of  $(K_{inst} - \bar{K})/\sigma_K$  can be obtained and shown in Figure 7. In this way, the distribution curves of Figure 6 can be transformed into Figure 7 through the aid of Figure 5. In Figure 7,  $P$  describes the general population of  $K_{inst}$ , and  $P_2$  describes the probability of the peaks of  $K_{inst}$ . The peak dynamic distortion factor is therefore chosen to be the most probable value of  $K_{inst}$  among the population of their peaks,  $P_2$ , for given values of  $NT$ ,  $\bar{K}$  and  $\sigma_K$  as shown in Figure 7. Results of Figure 7 are generalized and expressed in terms of  $\bar{K}$ ,  $\sigma_K$  and  $NT$  and are illustrated in Figure 8. From Figure 8, the most probable maximum value (peak value) of distortion

factors can be obtained easily for given values of  $\bar{K}$ ,  $\sigma_K$  and NT.

In Melick's original formulation, confidence levels of the predicted peak distortion factors were not determined. However, with the help of Figure 7, confidence levels can be determined easily from the distribution of  $P_2$ . Note that the variance of  $P_2$  decreases as NT increases. In most practical applications, NT and  $\bar{K}/\sigma_K$  are large ( $\sim 10^5$  and  $\sim 10$  respectively) such that they fall within the shaded band of Figure 8.

#### Matching Model to a Particular Test Case

Up to this point, prediction of the peak distortion factor for a particular case has been accomplished for given values of the mean and rms values of the instantaneous distortion factor,  $\bar{K}$  and  $\sigma_K$ , and the number of vortices, NT, within data recording period T. It remains to be shown how  $\bar{K}$ ,  $\sigma_K$  and N (vortex flux) can be obtained. From the test data, total pressure rms values are measured at the compressor face. Therefore, it is intended to derive an analytical expression for the total pressure fluctuations based on the hypothetical vortex flow model. The main variables of the vortex flow model, (mean vortex size ( $\bar{a}$ ) and vortex flux (N)), are then identified by matching the analytical and measured total pressure rms levels. In addition, relations between the analytical total pressure fluctuations

and the statistical properties of distortion factor, the mean value ( $\bar{K}$ ) and rms value ( $\sigma_K$ ), are established so that  $\bar{K}$  and  $\sigma_K$  can be determined.

Development of the vortex flow model originates from Melick's hypothesis that the cause of the total pressure fluctuations is totally attributed to the convecting vortices at the rate of  $N$  vortices per second. For simplicity, a one-dimensional incompressible steady vortex flow solution is used for the basis of mathematical development. The basic equation for the velocity profile as a function of distance from the center of the vortex is given by equation (4). (See Figure 2 for definition of terms)

$$\frac{V_\theta}{V_{\theta_{\max}}} = \frac{r}{a} e^{-\frac{1}{2} \left[ \left( \frac{r}{a} \right)^2 - 1 \right]} \quad (4)$$

where  $a$  is designated as vortex size at a radius  $r=a$  such that  $V_\theta = V_{\theta_{\max}}$ .  $V_{\theta_{\max}}$  represents the strength of the vortex which is the maximum swirling velocity around the axis of the vortex. This basic model does not describe the real flow situation but it is desirable to keep the selected model as simple as possible so that the final expressions will not involve too many variables and therefore become overly complex. Since test data are eventually used to identify the main variables, simple expressions do not lose too much in accuracy.

An expression of total pressure fluctuations can be

derived from the 1-D vortex model by the use of incompressible Bernoulli's equation and the spatial relationship between the vortex and the dynamic probe as shown in Figure 9. The final expression of the total pressure fluctuation caused by a single arbitrary vortex on an arbitrary compressor face probe is given by equation (5). (The development of this equation is shown in the Appendix.)

$$\frac{\Delta p_t}{q_2} = \frac{2U_x}{U_2} = f(U_2, V_{\theta_{\max}}, a, Y_v, Z_v, Y_p, Z_p, \gamma, \beta, t) \quad (5)$$

where

$$U_x = V_{\theta_{\max}} \left[ -\frac{Y_p - Y_v}{a} \sin \gamma + \frac{Z_p - Z_v}{a} \cos \gamma \cos \beta \right] e^{-\frac{1}{2} \left[ \left( \frac{r_p}{a} \right)^2 - 1 \right]}$$

and  $r_p$  represents the time-variant distance between the probe and the axis of the vortex.

The subscripts  $p$  and  $v$  refer to the positions of the probe and the vortex respectively. The other variables are shown in Figure 9 and are described in the symbol section. From this expression (equation (5)) and experimental values of total pressure rms levels, three separate branches of development are undertaken to determine the mean vortex size ( $\bar{a}$ ), the vortex flux  $N$ ,  $\bar{K}$  and the standard deviation of the distortion factor,  $\sigma_K$ .

#### Determination of Mean Vortex Size

First, the total pressure rms expression is derived from equation (5) through autocorrelation function and power spectral density (PSD) function transformations (ref. 9) as

shown in detail in the Appendix. In order to do these developments, probability density functions for the variables shown in equation (5) need to be defined to account for the effect of fluctuating data. The Beta distribution function is used for the main variables,  $a$  and  $V_{\theta \max}$ , and a uniform (constant) distribution is used for those spatial variables describing location and orientations of the vortex ( $r_p$ ,  $\gamma$  and  $\beta$ ). The final expression of the analytical total pressure rms relation is given by equation (6).

$$\frac{\sigma^2 \Delta p_t / q_2, f'}{\sigma^2 \Delta p_t / q_2} = \frac{(\text{filtered rms level})^2}{(\text{unfiltered rms level})^2} = \text{erf}\left(7.98 \frac{f' \bar{a}}{U_2}\right) \quad (6)$$

Equation (6) states that the square of the ratio of filtered to unfiltered total pressure rms levels can be expressed by an error function of  $(f' \bar{a})/U_2$  where  $f'$  is the applied filter cut-off frequency and  $U_2$  is the mean flow velocity at the compressor face. Using this equation, the mean vortex size  $\bar{a}$  can be found for given values of  $f'$ ,  $U_2$  and the ratio of filtered and unfiltered rms levels measured by each dynamic probe. It is preferred to choose a certain value of  $f'$  so that the ratio of the rms level of equation (6) is about 0.5. This is because equation (6) corresponds to a one-point curve-fit. An rms ratio of 0.5 assures the best fit over the high and low frequency spectra of the PSD function.

Equation (6) is a numerical approximation derived from equation (5) by assuming that all of the vortices have the

same size, which is the mean value,  $\bar{a}$ , of the distribution. Validity of this assumption is examined by comparing the exact vortex size distribution given by the Beta function and the simplified solutions of the autocorrelation function in terms of percent error as function of  $m_2$  and  $n_2$  (the parameters of Beta distribution function for vortex size  $a$ ). This is shown in Figure 10 along with the range in which the experimental data fall.

#### Determination of Vortex Flux

To determine the vortex flux,  $N$ , a statistical moments analysis (the second and the fourth moments) is applied to the amplitude probability density (APD) function of the total pressure fluctuations shown in equation (5). Since the APD function, for most experimental data, is shown to be nearly Gaussian (ref. 4), both the first moment (mean) of APD function and the 4th moment (Kurtosis) of APD function are assumed to be zero. Using the 2nd and 4th moments of APD function, one simple expression for  $N$  is approximated numerically by further assuming that  $\overline{V_{\theta \max}^4} / (\overline{V_{\theta \max}^2})^2 \approx 1$ . Equation (7) shows the result of this development (see Eqn. 17 Appx. A).

$$N = 0.254 \frac{U_2/R_T}{(\bar{a}/R_T)^2} \cdot \frac{(\overline{V_{\theta \max}^4})}{(\overline{V_{\theta \max}^2})^2} \approx 0.254 \frac{U_2/R_T}{(\bar{a}/R_T)^2} \quad (7)$$

where  $R_T$  denotes the radius of the inlet duct at the compressor face station. The validity of the simplified assumption is also examined and illustrated in Figure 11,



along with the range in which typical experimental data falls. The implications of the discrepancies between theoretical and experimental results will be discussed later.

### Determination of $\bar{K}$ and $\sigma_K$

Using statistical moments analysis, the mean value and the rms value of the instantaneous distortion factor,  $\bar{K}$  and  $\sigma_K$ , can be expressed analytically by using the expression of the total pressure fluctuations (equation (5)). From this,  $\bar{K}$  and  $\sigma_K$  can be obtained for given values of the mean vortex size  $\bar{a}$ , steady-state distortion factor  $K_{SS}$ , and the total pressure rms level.

This is done by substituting equation (5) into the appropriate distortion factor equation of Table 1 and then substituting these into expressions of the first and second statistical moments of the instantaneous distortion factor ( $K_{inst}$ ) as shown in the Appendix. Results of the expressions of  $\bar{K}$  and  $\sigma_K$  are solved numerically in terms of  $\bar{a}$ ,  $K_{SS}$  and total pressure rms level as shown in Figure 12(a) through (f) for several distortion factors of Table 1. These figures show that  $\bar{K}$  and  $\sigma_K$  depend on the value of  $\bar{a}$ ,  $K_{SS}$  and the measured total pressure rms level  $\sigma_{\Delta p_t}/q_2$ . For given values of  $\bar{a}$  (found from equation (6)),  $K_{SS}$  and rms level,  $\bar{K}$  and  $\sigma_K$  can be obtained directly from 12(a) through (f). Using these in equation (7), the value of  $N$  is

calculated and the peak distortion factor can then be obtained from Figure 8.

Details of the above development are shown in the Appendix.

#### Contribution of Errors in $n$ and $m$ to the Final Results

Two major simplifying assumptions in the Melick method has been examined and shown in Figures 10 & 11. One of the assumptions is that the vortex size concentrates on its mean size,  $\bar{a}$ . The other one is that  $\overline{V_{e\max}^4}/(\overline{V_{e\max}^2})^2$  equals to one.

There is no way that these assumptions can be justified by direct comparison with the test data. However, for engineering application purposes, it is possible to judge the validity of these assumptions approximately by using the mean values of the Beta distribution function of the main variables, mean vortex size ( $\bar{a}$ ) and mean vortex strength ( $\overline{V_{e\max}}$ ). Since the mean value of the Beta distribution function is a function of its parameters ( $m$  and  $n$ ) only, values of the parameters can be resolved from the mean values predicted in Melick's program by the test data. These parameters then can be used in Figure 10 and Figure 11 to judge the validity of the two major assumptions. Equations to do this are (8a) and (8b) which give the relationship between the mean values of the two main variables and the parameters of their Beta distribution function.

$$\bar{a}/R_T = \frac{m_a + 1}{m_a + n_a + 2} \quad (8a)$$

$$\overline{V_{e\max}}/U_2 = \frac{m_v + 1}{m_v + n_v + 2} \quad (8b)$$

For values of  $\bar{a}/R_T$  and  $\bar{V}_{\theta \max}/U_2$  calculated in Melick's program, relationships of their parameters ( $m_a$  vs.  $n_a$  and  $m_v$  vs.  $n_v$ ) can be obtained from equations (3a) and (3b). For example, from test data, the calculated values of  $\bar{a}/R_T$  is ranging from .12 to .18 and the calculated values of  $\bar{V}_{\theta \max}/U_2$  is ranging from .06 to .10, errors due to the two major assumptions of the Melick method can be approximated as shown by the shaded area in Figure 10 and Figure 11. Results show that  $\bar{a}/R_T$  is over-estimated by about 15 percent and  $N$  is under-estimated by about 500 percent. The 500 percent error is due to the fact that  $\bar{V}_{\theta \max}^2/(\bar{V}_{\theta \max}^2)^2$  is assumed to be 1.0 instead of 5.0 as indicated by test data. The error in  $\bar{a}/R_T$  is acceptable for engineering applications but the error in  $N$  is alarming at the first glance. However, the prediction of the peak distortion factor is not sensitive to the value of  $N$ . This can be seen clearly in Figure 8 which has a very small slope indicating that large changes in  $N$  and  $T$  can occur without seriously affecting the value of  $K_{\max\text{-inst}}$ . Also, the value of  $\phi_K$  is always an order of magnitude less than  $\bar{K}$  which further reduces the effect on  $K_{\max\text{-inst}}$ . For most of the test data, the value of  $NT$  is between  $10^4$  and  $10^5$ . A 500 percent error in  $N$  can cause only about 2 percent error in the prediction of the peak distortion factor. This 2 percent error is then negligible. This is why the prediction of the peak distortion factor by the Melick method is good even with such gross error in  $N$ .

## Effect of Engine Response Characteristics

Depending on its size and inertia, an engine can only respond to distortions below a certain frequency. Since the engine compressor does not respond to turbulence above this frequency level, pressure measurements should be filtered so that high frequency distortions beyond the engine's response capability do not produce meaningless results. That is, high frequency components are of no concern because the engine can't respond to them, even if they produce distortions in excess of that required to cause a surge. This filtering effect can be accomplished by using a third-order Butterworth filter, which is commonly used to simulate the characteristics of present gas turbine engines (ref. 10). The general filtering process is shown schematically in Figure 13 which shows an input time-dependent function  $Y(t)$ , as passed through a filter  $H(f)$ , produces an output signal  $Y'(t)$  with lower magnitude. By properly selecting the filter characteristics, this filtering process eliminates the pressure or distortion factor fluctuations at frequencies beyond the response characteristics of the engine. Filtering has the effect of reducing the total pressure rms level. The lower the cut-off frequency the lower the rms level. This is seen in Figure 14 which shows the ratio of the filtered and unfiltered rms as a function of the normalized cut-off frequency,  $f_c \bar{a}/U_2$ . From Figure 14, the ratio of filtered to unfiltered rms level can be found for the given value of  $f_c \bar{a}/U_2$  to account for the

engine response characteristics.

### Special Treatment for Some Distortion Factors

Some distortion factors, such as  $K_{A2}$  and  $\Delta PRS$ , are a combination of other indices and must be generated within the Melick program. It is assumed that these indices are independent statistically. Prediction of the peak distortion values of these indices is done by finding the peak distortion values of the individual components independently and then combined into the indices. This approach is based on the assumption that the individual components reach their peak values at the same time which may not be the case in the real situation for two statistically independent indices. This assumption assures the prediction of the objective peak distortion factors will always be conservative.

To illustrate this,  $K_{A2}$  is defined as:

$$K_{A2} = K_{\theta} + bK_{RAD} \quad (9)$$

where the  $b$  factor is a constant. This means  $K_{\theta}$  and  $K_{RAD}$  are independent in equation (9). The peak value of  $K_{A2}$ , therefore, corresponds to the peak values of  $K_{\theta}$  and  $K_{RAD}$  simultaneously. The peak distortion values of  $K_{\theta}$  and  $K_{RAD}$  are determined independently in Melick's program and then combined to obtain the peak value of  $K_{A2}$  by using equation (9).

## Melick Mapping Methods

A very simple method for determining the compressor face peak distortion map is included in the Melick program. It assumes that the linear vortex of size  $\bar{a}$  is oriented along the mean shear line (a straight line) between the steady-state high and low pressure regions. The direction of rotation of this vortex tends to enhance both the low and high pressure regions so that the distortion level can be magnified. The peak distortion map is then obtained by adjusting the strength of the mean vortex until the predicted peak value of the distortion factor is reached.

In reality, the core of the distortion-influence vortex may not be a straight line. This is why the Melick mapping method is not too accurate in predicting dynamic peak distortion patterns. Other methods of adding the vortex effects need to be investigated to improve the prediction.

The Melick method so developed provides a simple and low cost way of predicting the peak dynamic distortion. The validity of the method is illustrated in the next section.

## DATA COMPARISONS

In this section, the accuracy of the Melick method in predicting peak dynamic distortion factor and pattern will be demonstrated by direct comparison with the HiMAT inlet test results. In ref. 6, an experimental investigation of a subscale HiMAT model with forebody, canard and inlet is described. These tests were conducted by NASA in the NASA Lewis 8' x 6' supersonic wind tunnel (ref. 6). The HiMAT model has an under-fuselage inlet with a high-divergence S-shape duct. At the compressor face, there were 40 steady-state total pressure probes and 40 high response total pressure dynamic probes installed on the compressor face station as illustrated in Figure 1. Steady-state total pressure, dynamic fluctuating total pressure and filtered and unfiltered rms total pressure levels were recorded from the compressor face instrumentation during the test. In the present investigation, data obtained in these tests were analyzed by two different methods to determine, by direct comparison, the validity of the results predicted by the Melick technique.

First, the fluctuating total pressure data were digitized and screened, on distortion factor  $\Delta PRS$ , through the Dynamic Data Editing and Computing (DYNADEC) System of Marous and Sedlock (ref. 10), from which the measured peak dynamic distortion factors and patterns were obtained deterministically. Results obtained from this system are

designated as measured results. Second, the filtered and unfiltered total pressure rms levels were used in Melick's statistical method for predicting the peak dynamic distortion factors and patterns for the same length of data run and are designated as predicted results. Steady-state distortion factors and patterns are also included in both measured and predicted outputs.

Because of the high curvature and divergence angle of the inlet duct, boundary layer separation is observed. Fluctuating total pressure data from the tests shows a downward spiking characteristics for most of the test cases with a clean inlet duct (i.e., without vortex generators). This is believed to be caused by intermittent boundary layer separation and reattachment (ref. 6). The spiking phenomenon of the total pressure data, as illustrated in Figure 15, shows random downward spikes bounded approximately by the free stream total pressure at the high end and the local static pressure at the low end (ref. 6). Because of the spiking phenomenon, those cases without vortex generators resulted in more than one peak distortion pattern as shown in the DYNADEC results. A typical example is shown in Figure 16 (a).

In order to prevent the inlet performance from being jeopardized by potential stall due to the spiking phenomenon, a set of vortex generators was installed annularly on the wall of the inlet duct down stream of the cowl in order to trip the boundary layer and prevent flow separation (ref. 6).



Spiking data was not present for most of the test cases with vortex generators, indicating good control of the boundary layer.

In the DYNADEC system, peak dynamic distortion of the HiMAT data set were screened on the distortion factor  $\Delta PRS$  which is a function of IDC and IDR as given by the following equation.

$$\Delta PRS = K_c (IDC) b + K_r (IDR) \quad (10)$$

$K_c$  is the circumferential sensitivity factor,  $K_r$  represents the radial sensitivity factor and  $b$  factor is a function of IDR at the tip of the compressor blade ( $IDR_{tip}$ ). This  $\Delta PRS$  is not predicted in Melick's program. In order to make comparisons possible between measured and predicted peak distortion,  $\Delta PRS$  needed to be computed from the predicted IDC and IDR. It was found the maximum value of  $\Delta PRS$  occurs at the instant when IDC is very close to its maximum and IDR is near its minimum value. This is due to the characteristics of the  $b$  factor, however, the Melick program does not predict minimum instantaneous distortion factor. A study was therefore taken to determine the minimum IDR following Melick's approach. The concept of the prediction of the minimum IDR is similar to that of finding the maximum IDR. This is illustrated in Figure 17 which shows that the maximum value and the minimum value of the predicted instantaneous distortion factors are symmetric to the mean of the whole population,  $\bar{K}$ . Results were then used for computing the peak value

of  $\Delta PRS$ . However, note that the Melick program does not have the capability to predict peak distortion pattern based on PRS. Therefore, the predicted distortion pattern are still based on the maximum IDC.

The range of the test conditions in the data base are listed in Table 2. Data comparisons were made by comparing distortion factors and patterns. The first part was the comparison of distortion factors. The steady-state values obtained from both systems are identical for every case as would be expected. Comparisons of the measured and predicted peak dynamic distortion factors,  $\Delta PRS$ , for cases with and without vortex generators are illustrated in Figure 18(a) and 18(b) respectively. Figure 18(a) shows satisfactory agreement between measured and predicted results. Most of the predicted data shown in Figure 18(a) are about 20 percent above the measured results, which are on the conservative side of the data prediction. This is desirable for an inlet design purpose. On the other hand, large discrepancies are revealed in those cases without vortex generators, which is shown in Figure 18(b). This is because the Melick method can not adequately deal with inlet flow when intermittent separation induced spiking occurs. An improved method is needed to handle the effect of flow separation. An attempt was made to use data measured by those probes that were located in the low pressure region (i.e., where high turbulent fluctuations in terms of rms level was observed) to make the

predictions of the no-vortex-generators cases close to the measured ones, however, no consistent result was obtained.

The second part of the data comparison was concentrated on the distortion patterns. Again, the steady-state distortion patterns from both sources were exactly the same. For cases without vortex generators, peak distortion patterns were not comparable when the spiking phenomenon was observed. A typical example is shown in Figure 16. Comparisons of the measured and the predicted peak distortion patterns for some representative cases with vortex generators (without spiking) are shown in Figure 19(a) through 19(n). Although the predicted peak distortion patterns are based on maximum IDC, instead of  $\Delta PRS$ , good agreement of most of the comparisons are shown. This may be due to the fact that IDC is the dominant term in  $\Delta PRS$ .

In some cases, Figure 19(a), 19(d), 19(j), and 19(m) for instance, discrepancies between measured and predicted patterns are the most apparent. It may be possible to improve the pattern prediction by changing the axis of the main influence vortex from a straight line to a more realistic contour line as discussed previously. More effort is required to improve the prediction.

## METHOD OF PROBE SELECTION

### Development of Probe Selection Criteria

In principle the Melick method requires only one dynamic total pressure rms measurement providing it is located at a point that represents an average rms level for the whole compressor face (i.e., 40-probe average). If the number of probes required to provide this average rms level can be minimized, the cost of test instrumentation and perhaps the flow blockage of the inlet can be reduced greatly.

If it is assumed that dynamic effects of the inlet flow are somehow related to the steady-state total pressure pattern, a basic rationale of dynamic probe selection can be established based on the steady-state pattern. This basic assumption provides a foundation for this investigation.

Since the peak dynamic distortion factor from the Melick method is based on the average values of total pressure rms level and mean vortex size,  $\bar{a}$ , at the compressor face, an examination of the total pressure rms levels at the compressor face should reveal any similarity between the steady-state and dynamic characteristics of the inlet. The relationship between the steady-state total pressure and the rms levels are examined by plotting radial variations of both values as shown in Figure 20(a) through 20(f). It has been found that the rms levels have an inverse relationship to the steady-state values. That is, when the steady-state total pressures

are high, the dynamic content of the flow is low and vice versa. It is further noted that when the rms value crosses the average value ( $rms/rms_{40} = 1$ ) the steady-state total pressure also crosses the mean value ( $P_t/P_{t40} = 1$ ). This observation suggests the possibility of establishing a criterion for selecting apriori the location of dynamic probes that will be close to the mean rms level of the duct. Nevertheless, the rms levels do not represent the entire dynamic effect because another variable, mean vortex size  $a$ , also has an important effect on dynamic behavior.

Two approaches were taken to establish probe selection criteria. The first approach was done by searching for combinations of dynamic-probe subsets which produce average values of rms level and mean vortex size equivalent to the 40-probe average values. This approach was found to be too complex because of the difficulty in handling two variables in conjunction with a multiplicity of combinations of the dynamic probes. A second approach was employed by examining local contributions of dynamic effect to the peak dynamic distortion factor directly. In order to do this, the Melick program was modified so that the peak distortion factor could be predicted by using dynamic data measured by each individual probe. Results were then compared with the peak distortion factor predicted by all 40 probes (40-probe value). Radial variations of these local contributions to peak distortion factor IDC are also plotted on Figure 20. Similarities

between the trend of the rms levels and the distortion factor variations are remarkable as seen in Figure 20. The single-probe distortion factor variations can be interpreted as variations of overall dynamic effect (including the effect of rms level and mean vortex size  $\bar{\alpha}$ ) over the compressor face.

Only IDC was used throughout the development since IDC is the dominant term in computing  $\Delta PRS$  which is the basis for comparison with the DYNADEC results. Results of the present investigation are also applicable to other distortion factors since the influence of the dynamic component to every distortion factor is the same in the Melick method.

In order to find the key probes, the line of perfect agreement between the single-probe value (of peak distortion factor) and the 40-probe value were plotted on the steady-state pressure map which is the basis of dynamic probe selection. Figure 21(a) through 21(l) show this comparison for a number of operating conditions. Note that only the steady-state average pressure contour and the dynamic average line were plotted in Figure 21. This was done for most of the HiMAT test cases with and without vortex generators and covered the whole range of the test Mach number, angles of attack and sideslip. The results show that the lines of perfect agreement (dynamic average lines) coincide fairly well with the steady-state average total pressure lines except in regions of high and low pressure. In other words, the average turbulence line, i.e., the line of perfect

agreement, is in general in the vicinity of the average steady-state total pressure region. This implies that dynamic probes selected close to the steady-state average line would give the prediction of a peak distortion factor very close to that of the 40-probe prediction. It would be preferred that the predicted value always be on the conservative side, i.e., slightly higher than the 40-probe value. This occurs for dynamic probes located on or outboard (toward the low pressure region) of the steady-state average line. On the other hand, agreement between steady-state and dynamic average lines do not hold consistently for regions of particular high and low pressure on the steady-state pressure map. This can be examined in Figure 19, Figure 20 and Figure 21. Using the results of the above analysis, general criteria for the selection of the dynamic probe locations can be drawn.

#### General Criteria:

- (1) The dynamic total pressure probes that are on or just outside (larger radius) of the steady-state average total pressure line should be selected.
- (2) Probes selected should avoid very high and low steady-state pressure regions.

#### Accuracy of the Criteria

The accuracy of the above criteria has been tested by using the HiMAT test data and satisfactory results were

obtained for engineering application purposes. One example of dynamic probe selection is shown in Figure 22 for test point 1948 ( $M=0.9$ ,  $\alpha=7^\circ$  and  $\beta=0^\circ$ ). The steady-state average pressure contour is shown in Figure 20(c) and the associated selected dynamic probes are also illustrated according to the general criteria of dynamic probe selection. The selected circumferential 8 probes are: nos. 1, 7, 12, 20, 24, 30, 32 and 37. The peak distortion factor (IDC) predicted by these 8 probes is 0.0470 which is +4.78% higher than that predicted by 40 probes. When only four probes out of the selected 8 probes are used (i.e., nos. 1, 12, 24, and 32) the predicted peak IDC is +1.12% higher than the 40-probe value. If the number is further reduced to 2 probes (nos. 12 and 32), the predicted peak IDC is +5.10% higher than the 40-probe value. Following the same procedure, results of some typical cases with vortex generators are tabulated in Table 3. Results show that the accuracy for using eight probes circumferentially located near the mean steady-state pressure is within 5 percent, whereas selecting the wrong probe could cause errors of  $\pm 20$  percent as illustrated by the single-probe worst cases. Table 3 also presents satisfactory results for using 2 and 4 probes. The results in Table 3 also fall in the histograms of Figure 23. Figure 23 shows a histogram of all of the probe selection data analyzed with and without vortex generators. With vortex generators, which are representative of conventional low divergence ducts with moderate



bends, the results are generally conservative compared to the 40-probe result. This is especially true of the 2-probe results. However, without vortex generators (a typical high divergence duct with bends or obstructions) the results are still conservative but the 2-probe result is the least conservative.

Pragmatically, the locations of the dynamic probes are preferred to be fixed during the test so that a sequence of test runs can be conducted without stopping to relocate instrumentation on the model. Steady-state total pressure contours can be obtained from prior developmental test data, an analytical prediction or the intuition of an experienced inlet/propulsion engineer. In some cases it may be possible to run some initial tests and then install the dynamic instrumentation later in the wind tunnel test sequence. Once the general shapes of the steady-state pressure maps are obtained, fixed locations of the dynamic probes can then be determined by applying the general criteria.

The above method of utilizing fixed dynamic probes has been examined by using the HiMAT data set (with-vortex-generators cases). Two fixed probe locations were determined from the general shapes of the steady-state average pressure contours shown in Figure 21. Probes no. 12 and 32 are the most promising candidates because they avoid the extreme high and low pressure regions and they usually lie on the low pressure side of the generalized steady-state average

pressure contour. Note that these lie on the opposite side of the approximate line of symmetry connecting the regions of high and low pressures. Generally, this cross-line-of-symmetry combination performs surprisingly well since these two probes usually satisfy the general criteria (1) and (2), especially that of avoiding high and low pressure regions. Results of the fixed 2-probe cases are also included in Table 3 and Figure 23 and are comparable with the other results.

In order to make sure that the general criteria are also valid for other inlet test data, numerical experiments of the general criteria were conducted by using 3 data sets of Melick's test cases for an internal compression supersonic inlet. Results and test conditions of this study are listed in Table 4. Although Melick's test cases do not provide all the 40-probe data (only 14 dynamic probes were used), results of the selected 3 or 4 probes show satisfactory agreement indicating that the criteria are also good for other types of inlets. However, other sources of data should be examined before this criteria can be fully validated.

The general criteria provides a way for selecting correct locations of the dynamic total pressure probes by simply looking at the steady-state total pressure map. Probe reduction becomes possible without significant loss in accuracy. The number of probes can be reduced to as few as 2 instead of

40. Thus, a great deal of savings in instrumentation and analysis costs can be achieved.

## CONCLUSIONS

A simplified description of the Melick method in predicting peak dynamic distortion at the compressor face of a gas turbine engine has been accomplished. The main variables of the assumed inlet flow vortex model have been identified by matching analytical and measured total pressure rms levels. Statistical properties of the instantaneous distortion factor are then related to the main variables, from which the most probable peak value of the instantaneous distortion factor can be extrapolated. The accuracy of the Melick method has been demonstrated by using a HiMAT inlet test data set and comparing it to the measured results of DYNADEC.

The criteria for dynamic probe selection have been established through a sequence of comparisons between a steady-state total pressure map and turbulence behavior at the compressor face. Instead of using 40 dynamic probes, 2 probes will suffice in the early stages of inlet testing with errors of approximately 5 percent compared to the 40-probe results.

The Melick method cannot properly deal with turbulence caused by severe intermittent flow separation and does not predict better peak distortion patterns than Motycka's method does. However, the pattern prediction can be improved with suitable modifications in the computer program.

Another analytical flow model and/or modified statistics are required to handle the effect of intermittent flow separation. On the other hand, other methods of constructing the peak distortion pattern from the effect of mean vortex flow field may be proposed for better prediction of the peak dynamic distortion map.

A logical extension of the current work would be to predict the rms dynamic total pressure fluctuations directly from the steady-state pressure maps so that dynamic total pressure measurements would not be needed. This would allow the Melick technique to be used as a design tool to predict the dynamic distortion before the first developmental tests were run.

## REFERENCES

1. Jacocks, J. L., et al.: STATISTICAL PREDICTION OF MAXIMUM TIME VARIANT INLET DISTORTION LEVELS. Arnold Engineering Development Center, (NTIS) AD/A-004-104, January 1975.
2. Motycka, D. L.: DETERMINATION OF MAXIMUM EXPECTED INSTANTANEOUS DISTORTION PATTERNS FROM STATISTICAL PROPERTIES OF INLET PRESSURE DATA. AIAA Paper 76-705, July 1976, 6 pp.
3. Melick, H. C., Jr., Ybarra, A. H. and Beneze, D. P.: ESTIMATING MAXIMUM INSTANTANEOUS DISTORTION FROM INLET TOTAL PRESSURE RMS MEASUREMENTS. AIAA Paper 78-970, July 1978, 15 pp.
4. Stevens, C. H., Oliphant, R. C. and Spong, E. D.: EVALUATION OF A STATISTICAL METHOD FOR DETERMINING PEAK INLET FLOW DISTORTION USING F-15 AND F-18 DATA. AIAA Paper 80-1109, July 1980, 11 pp.
5. Sanders, M. E.: AN EVALUATION OF STATISTICAL METHODS FOR THE PREDICTION OF MAXIMUM TIME-VARIANT INLET TOTAL PRESSURE DISTORTION. AIAA Paper 80-1110, July 1980, 11 pp.
6. Neumann, H. E., Povinelli, L. A. and Coltrin, R. E.: AN ANALYTICAL AND EXPERIMENTAL STUDY OF A SHORT S-SHAPED SUBSONIC DIFFUSER OF A SUPERSONIC INLET. AIAA Paper 80-0386, January 1980, 12 pp.
7. Milks, Samuel S.: Mathematical Statistics. John Wiley & Sons, Inc., 1963.
8. Marous, J. J. and Sedlock, D.: DYNAMIC DATA EDITING AND COMPUTING SYSTEM (DYNADEC). Proceedings of the Air Force System Command Science and Engineering Symposium, AFSC-TR-003. Vol. 1, October 1973.
9. Bendat, J.S. and Piersol, A. G.: MEASUREMENT AND ANALYSIS OF RANDOM DATA. John Wiley & Sons, Inc., 1968.
10. Marous, J. J. and Sedlock, D.: AN ANALOG EDITING SYSTEM FOR INLET DYNAMIC FLOW DISTORTION, DYNADEC--PAST, PRESENT AND FUTURE. AIAA Paper 80-1108, July 1980, 10 pp.
11. Discus, J. H.: FORTRAN PROGRAM TO GENERATE ENGINE INLET FLOW CONTOUR MAPS AND DISTORTION PARAMETER. NASA TM X-2967, 1974.

12. Melick, H. C., Jr.: ANALYSIS OF INLET FLOW DISTORTION AND TURBULENCE EFFECTS ON COMPRESSOR STABILITY. NASA CR-114577, 1973.

## APPENDIX

### Vortex Flow Model

As described in the main text the total pressure fluctuations of inlet flow is attributed to the existence of random vortices convecting down the inlet duct. For simplicity, the total pressure fluctuations caused by a one-dimensional vortex flow is considered. Then the effect of many random one-dimensional vortices will be considered by integrating over all possible values of the variables.

The tangential velocity of one-dimensional, steady, incompressible vortex is given as:

$$V_{\theta} = V_{\theta_{\max}} (r/a) e^{-1/2 [(r/a)^2 - 1]} \quad (1)$$

where  $V_{\theta}$  is the tangential velocity at radius  $r$  and  $V_{\theta_{\max}}$  represents the maximum  $V_{\theta}$  at radius  $a$ . The size and the strength of the vortex are defined to be " $a$ " and  $V_{\theta_{\max}}$ .

In reality, the effect of vortex decay due to viscous dissipation results in decreased strength and increased size. However, in the present analysis the vortex size and strength are assumed to be constant because the time required for the vortex to travel through the inlet duct is very short and the vortex decay rate is rather small.

The total pressure fluctuations caused by the vortex can be superimposed on the steady-state total pressure component to form the time-variant actual total pressure as



indicated by the following equation.

$$P_T = P_t + \Delta P_t \quad (2)$$

where, by the incompressible Bernoulli's equation,

$$P_T = P_s + \frac{1}{2} \rho (U_2 + U_x)^2 \quad (3a)$$

$$P_t = P_s + \frac{1}{2} \rho U_2^2 \quad (3b)$$

where  $P_T$  represents the time-variant actual total pressure,  $P_t$  is the steady-state total pressure,  $p_t$  is the total pressure fluctuations,  $P_s$  is the local static pressure,  $U_2$  is the mean stream velocity at the compressor face station and  $U_x$  is the perturbed velocity caused by the vortex.

By substituting (3a) and (3b) into (2) and dividing through by the mean dynamic pressure  $q_2 = \frac{1}{2} \rho U_2^2$ . An expression for the total pressure fluctuations is obtained:

$$\frac{\Delta P_t}{\frac{1}{2} \rho U_2^2} = \frac{\Delta P_t}{q_2} = \frac{2U_x}{U_2} + \left(\frac{U_x}{U_2}\right)^2 \quad (4)$$

Since  $U_x$  is assumed to be much less than  $U_2$ , the second term on the right hand side of (4) can be neglected.

$$\frac{\Delta P_t}{q_2} \approx \frac{2U_x}{U_2} \quad (5)$$

Before equation (5) can be used for further development, an expression of  $U_x$  needs to be derived. This can be done easily by relating  $U_x$  to  $V_\theta$  of the one-dimensional vortex through the geometric relationship between the vortex and the pressure probe location. This is illustrated in Figure 9.

For simplicity, all vortices are considered to be effective only when they are crossing the measuring plane and the pressure probe is located at the center of the duct. After a prolonged mathematical development involving geometric transformations, the following expression for  $U_x$  is obtained.

$$U_x = V_{\theta_{\max}} \left[ -\frac{Y_p - Y_v}{a} \sin \gamma + \frac{Z_p - Z_v}{a} \cos \gamma \cos \beta \right] e^{-\frac{1}{2} [(r_p/a)^2 - 1]} \quad (6a)$$

where

$$\left(\frac{r_p}{a}\right)^2 = \left(\frac{U_2 t}{a}\right)^2 + \left(\frac{Y_v - Y_p}{a}\right)^2 + \left(\frac{Z_v - Z_p}{a}\right)^2 - \left[ -\frac{U_2 T}{a} \cos \gamma \cos \beta - \frac{r_p}{a} \cos \gamma \cos \beta - \frac{Z_p}{a} \sin \gamma \right]^2 \quad (6b)$$

$(Y_p, Z_p)$  represents the probe location

$(Y_v, Z_v)$  is a point on vortex axis which has the shortest distance to the probe

$$-\pi/2 \leq \gamma \leq \pi/2$$

$$-\pi \leq \beta \leq \pi$$

With equations (6a) and (6b), equation (5) can be written in function form:

$$\frac{\Delta P_t}{q_2} \doteq \frac{2U_x}{U_2} = f(U_2, V_{\theta_{\max}}, a, Y_v, Z_v, Y_p, Z_p, \gamma, \beta, t) \quad (7)$$

Next, the vortex model will be used to develop an expression for the power spectral density (PSD) function so that test data can be compared. To do this an autocorrelation function will be formulated by the use of equation (7). Finally, randomness of the variables will be taken into

account in the formulation by employing the probability density functions for the variables from the physical consideration of the vortex size, the vortex strength, the vortex orientation and the vortex location, etc.

The autocorrelation function of the total pressure fluctuations due to a single vortex is defined as:

$$R_{\Delta P_t/q_2}(\tau, a, V_{\theta_{\max}}, R_v, \gamma, \beta) = \hat{R}(\tau) = \int_{-\infty}^{\infty} \frac{\Delta \hat{P}_t(t)}{q_2} \frac{\Delta \hat{P}_t(t+\tau)}{q_2} dt \quad (8)$$

where  $\hat{R}$  and  $\Delta \hat{P}_t$  represent the functions that involve the random variables  $(a, V_{\theta_{\max}}, R_v, \gamma, \beta)$  and  $R_v^2 = (Y_v - Y_p)^2 + (Z_v - Z_p)^2$ .

After the probability density function for the variables are used in equation (8) and assuming that there are  $N$  vortices per second of vortex flux traveling down the inlet duct, a complete autocorrelation function of the total pressure fluctuations can be obtained as shown in equation (9).

$$R_{\Delta P_t/q_2}(\tau) = \iiint \iiint \hat{R}_{\Delta P_t/q_2}(\tau) NP(a)P(V_{\theta_{\max}})P(R_v)P(\gamma)P(\beta) da dV_{\theta_{\max}} dR_v d\gamma d\beta \quad (9)$$

all possible values

where  $P(a)$ ,  $P(V_{\theta_{\max}})$ ,  $P(R_v)$ ,  $P(\gamma)$  and  $P(\beta)$  represent the probability density functions for the vortex size  $a$ , the vortex strength  $V_{\theta_{\max}}$ , the vortex location  $R_v$  and the vortex

orientation  $\gamma$  &  $\beta$  respectively. Here, it is assumed that all the variables are independent.

The probability density functions for  $R_v$ ,  $\gamma$  and  $\beta$  are assumed to be distributed uniformly (i.e. constant). Beta distribution function is employed to describe both  $a$  and  $v_{\theta\max}$ . The beta distribution function is given as:

$$P(\xi) = K_{\xi}(\xi)^m(1-\xi)^n, \quad \text{for } 0 \leq \xi \leq 1 \quad (10) \\ \text{and } m, n \geq 0$$

With these assumptions, equation (9) can be normalized and solved numerically in one of two ways. The first is a complete numerical integration which shows that the results depend on the parameters  $m_a$  and  $n_a$ . The second is by assuming a delta function for  $P(a)$  instead of using the beta distribution function. The latter results in a single curve which is independent of  $m_a$  and  $n_a$ , and is dependent only on the mean size of the vortices,  $\bar{a}$ . For simplicity, the results of the second integration will be used for further development in the analysis.

With this numerical solution of the autocorrelation function, a PSD function can be obtained easily through a Fourier transformation. Since only the real part of the transformation is comparable to test data, the real part of the PSD function is shown in the following equation.

$$G_{\Delta P_t/q_2}(f) = 4 \int_0^{\infty} R_{\Delta P_t/q_2}(\tau) \cos(2\pi f\tau) d\tau \quad (11)$$

Equation (11) can be normalized and solved numerically. The numerical results are approximated by an exponential function and the final expression is given by:

$$\frac{G_{\Delta P_t/q_2}}{\sigma_{\Delta P_t/q_2}^2} = 9.0(\bar{a}/U_2)e^{-63.6(f\bar{a}/U_2)^2} \quad (12)$$

Equation (12) is then integrated over part of the frequency spectrum. The left hand side of equation (12) becomes a ratio of the filtered and unfiltered mean square value of the total pressure fluctuations. The integration of the right hand side of equation (12) results in an error function which is described by equations (13a) and (13b).

$$\int_0^{f'} \frac{G_{\Delta P_t/q_2}}{\sigma_{\Delta P_t/q_2}^2} df = 9.0 \int_0^{f'} \frac{\bar{a}}{U_2} e^{-63.6(f\bar{a}/U_2)^2} df \quad (13a)$$

or,

$$\frac{\sigma_{\Delta P_t/q_2}^2 f'}{\sigma_{\Delta P_t/q_2}^2} = \text{erf}\left(7.98 \frac{f'\bar{a}}{U_2}\right) \quad (13b)$$

Equation (13b) is the key equation for finding the main variable  $\bar{a}$ . The ratio on the left is measured in the inlet test for a selected filter cut-off frequency  $f'$ . The mean flow velocity at the compressor face,  $U_2$ , is also measured in the test.  $\bar{a}$  can be solved by using equation (13b) with

the measured data at each probe. This is done on a probe by probe basis and then an average value is taken.

### APD Function Analysis for Finding the Vortex Flux $N$

Having found  $\bar{a}$ , the vortex flux  $N$  remains to be identified. To find solution for  $N$ , statistical moments of the amplitude probability density (APD) function are employed. Since experience with test data indicates that the amplitude distribution of the total pressure fluctuations is nearly Gaussian, its kurtosis (the 4th moment) is assumed to be zero. It will be shown that the second and the fourth moment of the APD function can be used for solving  $N$  and  $\bar{V}_{\theta_{\max}}$ .

First, the  $n$ th moment of the APD function is defined as:

$$\mu_n = N \int \int \int \int \int \int \int \left[ \frac{\Delta \hat{P}_t(t)}{q_2} \right]^n P(a) P(V_{\theta_{\max}}) P(R_v) P(\gamma) P(\beta) dt da dV_{\theta_{\max}} dR_v d\gamma d\beta \quad (14)$$

all possible values

Relations between  $\mu_n$  and the statistical properties of inlet fluctuating pressure data can be described by equations (15).

$$\text{mean} = \mu_1 = 0 \quad (15a)$$

$$\text{mean square} = \mu_2 = \sigma^2 \quad (15b)$$

$$\text{skewness} = \mu_3/(\mu_2)^{1.5} \quad (15c)$$

$$\text{kurtosis} = \mu_4/\mu_2^2 - 3.0 \quad (15d)$$

Equation (14) is solved numerically and normalized for the second and the fourth moment of the APD function,  $\mu_2$  &  $\mu_4$ . Results are approximated as follows.

$$\frac{\mu_2}{(NR_T/U_2)(\overline{v_{\theta_{\max}}}/U_2)^2} = 1.20\sqrt{\pi}(\bar{a}/R_T)^2 \quad (16a)$$

$$\frac{\mu_4}{(NR_T/U_2)(\overline{v_{\theta_{\max}}}/U_2)^4} = 2.75\sqrt{\frac{\pi}{2}}(\bar{a}/R_T)^2 \quad (16b)$$

Using equations (16a), (16b) and assuming that the kurtosis is zero, the following expression is obtained.

$$N = 0.254 \frac{U_2/R_T}{(\bar{a}/R_T)^2} \frac{\overline{v_{\theta_{\max}}^4}}{(\overline{v_{\theta_{\max}}^2})^2} \quad (17)$$

The last term of the above equation is assumed to be 1.0, which is accurate to within 20 percent when  $m_v > 4 + .4n_v$ . Therefore, equation (17) becomes:

$$N = 0.254 \frac{U_2/R_T}{(\bar{a}/R_T)^2} \quad (18)$$

Equation (18) is the solution for vortex flux  $N$  since  $\bar{a}$  is already solved in equation (13b) and  $U_2$  and  $R_T$  are known values.  $\bar{V}_{\theta_{\max}}$  is then obtained by an algebraic solution of equation (16a).

### Distortion Factor Determination

Up to this point, the main variables of this vortex flow model have been identified using the key equations and the experimental data. The next part of the development is to establish relationship between these variables and the dynamic distortion factor of the inlet. The main variables of the vortex model ( $\bar{a}$  and  $N$ ) are useful for predicting the statistical properties (mean and standard deviation) of the distortion factor. From this the extreme (peak) value of the dynamic distortion can be determined by extrapolation.

### Relation Between Total Pressure Fluctuations and the Distortion Factors

Typical distortion factors for the inlet flow are defined in table I. These may be used to describe the variation of pressures at any instant of time. The time-variant total pressures can be characterized in terms of the vortex flow model variables,  $\bar{a}$  and  $N$ , described previously.



Following the same analysis as for the APD function, the mean and the standard deviation of the instantaneous distortion factors,  $\bar{K}$  and  $\sigma_K$ , are found to be functions of  $\bar{a}$ , the steady-state distortion factor ( $K_{ss}$ ) and the total pressure rms level. These parameters are already known at this point so that  $\bar{K}$  and  $\sigma_K$  can be obtained explicitly. See Figures 12(a) through (f) for illustrations.

After  $\bar{K}$  and  $\sigma_K$  are obtained, probability distribution function for the population of the instantaneous distortion factors is defined from which the most-probable peak distortion factor can be picked. The peak value is found to be a function of  $\bar{K}$ ,  $\sigma_K$ ,  $N$  and the data record length  $T$ , which are again known values from the previous analysis.

Now, relations between the total pressure contour measured at the compressor face and the distortion factors are linked by the definitions listed in table I. Since the total pressure and the distortion factors are time-variant, it is more appropriate to use the instantaneous notation. Instantaneous distortion factor with the random variables involved is denoted as  $\hat{K}_{inst}$  which is a function of the instantaneous pressure contour by the definitions of table I as indicated in equation (19).

$$\hat{K}_{inst} = f(\hat{p}_{inst}) = f(p_{ss} + \Delta p_t) = f(t, \bar{a}, V_{\theta_{max}}, R_v, \gamma, \beta) \quad (19)$$

$\Delta p_t$  in equation (19) is obtained from equation (7) and the steady-state total pressure data,  $p_{ss}$ , are assumed for several typical distortion patterns. Statistical moment analysis for  $\hat{K}_{inst}$  is taken so as to relate the mean value  $\bar{K}$  and the standard deviation  $\sigma_K$  to the main variable  $\bar{a}$ . The  $n$ th moment of  $\hat{K}_{inst}$  is defined in equation (20).

$$\overline{K^n} = N \int \int \int \int \int \int \int \left( \hat{K}_{inst}(t) \right)^n P(a) P(V_{\theta_{max}}) P(R_V) P(\gamma) P(\beta) dt da dV_{\theta_{max}} dR_V d\gamma d\beta \quad (20)$$

all possible values

The probability density functions used in the analysis remain the same as those used in the APD function moments analysis. Only the first two moments of equation (20) are needed for finding  $\bar{K}$  and  $\sigma_K$  through the aid of the following relations.

$$\Delta K = \bar{K} - K_{ss} \quad (21a)$$

$$\sigma_K = (\overline{K^2} - \bar{K}^2)^{\frac{1}{2}} \quad (21b)$$

The results of this analysis are solved and approximated numerically, and are shown in Figures 12(a) through (f) for different distortion factors listed in table I. It is shown that  $\sigma_K$  and  $\Delta K$  are functions of  $\bar{a}$  and  $K_{ss}$ . For some of the distortion factors, the results are functions of  $\bar{a}$  only. After  $\bar{a}$  and  $K_{ss}$  are fed into these figures,  $\sigma_K$  and  $\Delta K$  can be determined. Then  $\bar{K}$  is calculated from equation (21a) for the given value of  $K_{ss}$ .

Factor	Equation	Supplemental equations	Definitions	Ref.
IDC <sub>max</sub>	$IDC_{max} = \max \left[ \frac{1}{2} (IDC_1 + IDC_2), \frac{1}{2} (IDC_4 + IDC_5) \right]$	$IDC_j = \frac{(\bar{p}_t)_j - (p_{t,min})_j}{\bar{p}_t}$	$(\bar{p}_t)_j$ = average total pressure for ring j $(p_{t,min})_j$ = minimum total pressure reading in ring j	11
IDR <sub>max</sub>	$IDR_{max} = \max (IDR_1, IDR_5)$	$IDR_j = \frac{\bar{p}_t - (\bar{p}_t)_j}{\bar{p}_t}$	$\bar{p}_t$ = average total pressure at engine face	
K <sub>D2</sub>	$K_{D2} = \frac{\sum_{j=1}^{NR} \bar{\theta}_j (\Delta p_t / p_t) (OD/D_j)}{\sum_{j=1}^{NR} (OD/D_j)}$	$\frac{\Delta p_t}{p_t} = \frac{(\bar{p}_t)_j - (p_{t,min})_j}{(\bar{p}_t)_j} \times 100$	$(\bar{p}_t)_j, (p_{t,min})_j$ = see above $\bar{\theta}_j$ = circumferential extent of largest continuous total pressure depression below $(\bar{p}_t)_j$ , degrees $D_j$ = diameter of ring j; NR = number of ring OD = outer duct diameter	8
K <sub>0</sub>	$K_0 = \frac{\sum_{j=1}^{NR} (A_1)_j (1/D_j)}{(\bar{q}/\bar{p}_t) \sum_{j=1}^{NR} (1/D_j)}$	$(A_1)_j = (a_1^2 + b_1^2)_j$ $(a_1)_j = \frac{1}{M} \left[ \sum_{i=1}^M \frac{p_{t1}}{\bar{p}_t} \cos(\theta_1) \right]_j$ $(b_1)_j = \frac{1}{M} \left[ \sum_{i=1}^M \frac{p_{t1}}{\bar{p}_t} \sin(\theta_1) \right]_j$ $\frac{\Delta p_{t1}}{\bar{p}_t} = \frac{(p_{t1})_j - (p_{t,base})_j}{\bar{p}_t}$	$\bar{p}_t, (\bar{p}_t)_j, D_j$ = see above $\bar{q}$ = average dynamic pressure at engine face M = number of rakes $(p_{t1})_j$ = individual total pressure; rake 1 $\theta$ = angular position of $p_{t1}$ $(p_{t,base})_j$ = base radial profile for ring j; set = 1 for all j b = radial distortion weighting factor=1.0	8
K <sub>RAD</sub>	$K_{RAD} = \sum_{j=1}^{NR} \left  \frac{\Delta p_{t1}}{\bar{p}_t} \right  \frac{\bar{p}_t}{\bar{q}} \frac{1}{D_j}$			
K <sub>A2</sub>	$K_{A2} = K_0 + bK_{RAD}$			12
$\frac{\Delta SPR}{Dist}$	$\frac{\Delta SPR}{Dist} = \frac{\Delta SPR}{[(\bar{p}_t - p_{t,min})/\bar{p}_t]} = f(k)$		$\bar{p}_t$ = see above $p_{t,min}$ = minimum total pressure at engine face	
$\Delta PRS$	$\Delta PRS = k_c (IDC)b + k_r (IDR)$		k = compressor reduced frequency $k_c$ = circumferential distortion sensitivity factor $k_r$ = radial distortion sensitivity factor b = circumferential distortion weighting factor	6

Table 1. Definition of distortion factors

Table 2. Range of test conditions and data bases of HiMat inlet testing model

Mach no.	0.4 ~ 1.36
Angles of attack, $\alpha$	-10 deg ~ +25 deg
Angles of sideslip, $\beta$	0 deg ~ -10 deg
rms filter frequency, $f'$	1000 hz
Engine cut-off frequency, $f_c$	500 hz
Data recording time, T	30 sec
Vortex generators	with and without

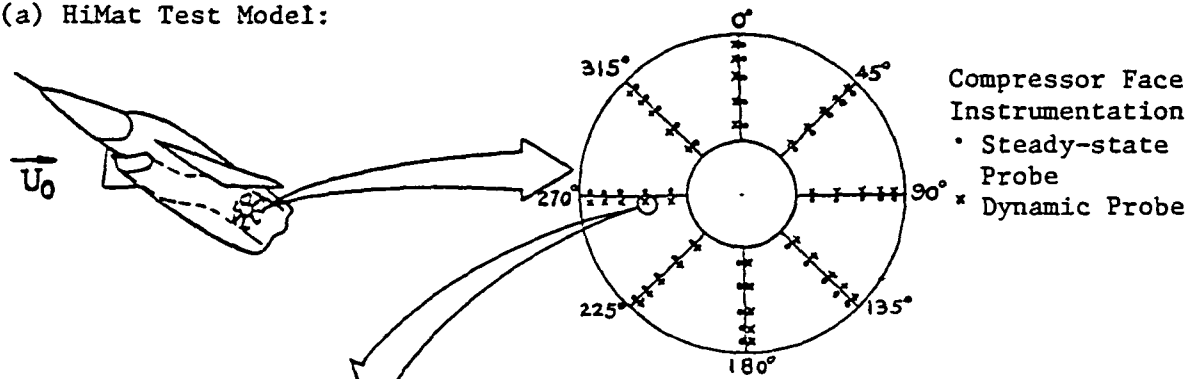
Data Point No.	Test Conditions			40- probe Result (IDC)	worst single probe %error	8 probes		4 probes		2 probes		Fixed 2 probes	
	M	$\alpha$	$\beta$			Probe No.	IDC %error	Probe No.	IDC %error	Probe No.	IDC %error	Probe No.	IDC %error
2436	.6	-5	0	.0451	+15	1, 7, 12, 19, 25, 30, 32, 38	-0.22	1, 12, 25, 32	-1.61	12, 32	+2.94	12, 32	+2.94
2437	.6	0	-5	.0465	+50	2, 7, 12, 19, 25, 29, 32, 37	+2.25	2, 12, 25, 32	-5.27	12, 32	+1.35	12, 32	+1.35
2433	.6	15	0	.0392	+23	2, 7, 12, 19, 25, 29, 32, 37	+3.06	2, 12, 25, 32	+3.51	12, 32	+5.04	12, 32	+5.04
1968	.9	-10	-5	.0520	+28	2, 7, 12, 20, 24, 30, 32, 37	+5.36	2, 12, 24, 32	+1.59	20, 30	+2.69	12, 32	+10.17
1948	.9	7	0	.0449	+15	2, 7, 12, 20, 24, 30, 32, 37	+4.78	2, 12, 24, 32	+1.12	12, 32	+5.10	12, 32	+5.10
1972	.9	10	-10	.0823	+24	2, 7, 12, 19, 24, 30, 33, 39	+1.58	2, 12, 24, 33	-0.91	12, 33	+0.31	12, 32	+8.61
1956	.9	20	0	.0561	+11	2, 7, 12, 20, 23, 30, 32, 37	+4.40	2, 12, 23, 32	+2.76	12, 32	+2.01	12, 32	+2.01
1960	.9	20	-5	.0503	+20	2, 7, 12, 18, 23, 30, 32, 37	+3.77	2, 12, 23, 32	+2.34	12, 32	+2.39	12, 32	+2.39
2361	1.36	-4	-4	.0894	+7	3, 10, 12, 20, 25, 30, 33, 35	+0.51	3, 12, 25, 35	+0.79	12, 35	+8.71	12, 32	+1.01
2358	1.36	4	0	.0369	+23	1, 7, 12, 19, 25, 29, 32, 37	+2.05	1, 12, 25, 32	-0.84	12, 32	+4.65	12, 32	+4.65
2360	1.36	15	0	.0354	+25	2, 7, 12, 19, 25, 29, 32, 37	+3.77	2, 12, 25, 32	+0.84	12, 32	+5.07	12, 32	+5.07
2362	1.36	15	-4	.0360	+27	2, 7, 12, 19, 25, 29, 32, 37	+2.57	2, 12, 25, 32	-0.80	12, 32	+3.63	12, 32	+3.63

Table 3. Numerical experiments of the general criteria of dynamic probe selection for some typical HiMat test cases with vortex generators

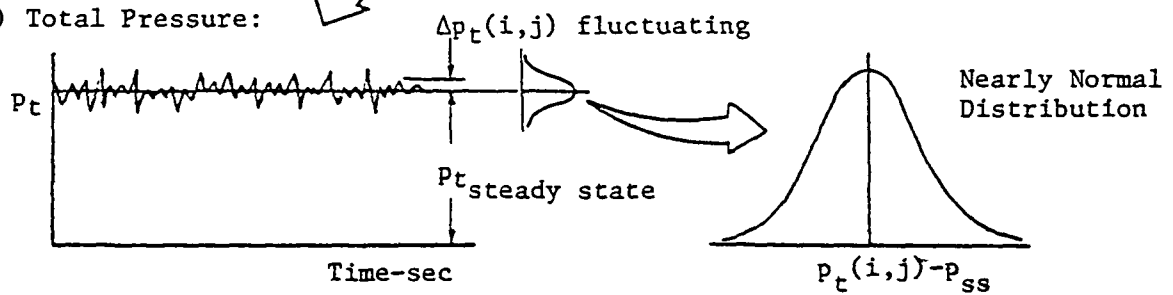
Table 4. Numerical experiments of the general criteria of dynamic probe selection for three Melick's test cases of an supersonic internal compression inlet

Case no.	Test condition			Totally 14 dynamic probes		Available selected probes	
	M	$\alpha$	$\beta$	peak $K_{A2}$	worst single probe (%)	probe no.	Error based on 14-probe value(%)
1	2.5	5	0	1.1638	+35.81 -15.65	18,21,22, 38	-2.56
2	1.6	5	1	1.1636	+16.58 -19.13	4, 17,21, 38	-2.97
3	2.5	5	0	0.7438	+25.67 -14.91	4, 20,24	+4.94

(a) HiMat Test Model:



(b) Total Pressure:



(c) Distortion Factor (resulting from a combination of all probes):

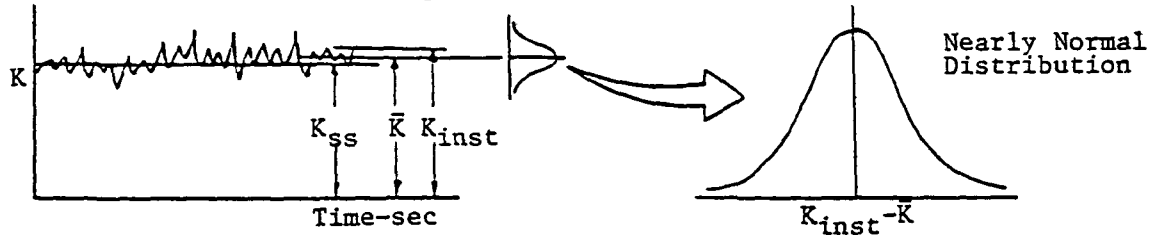
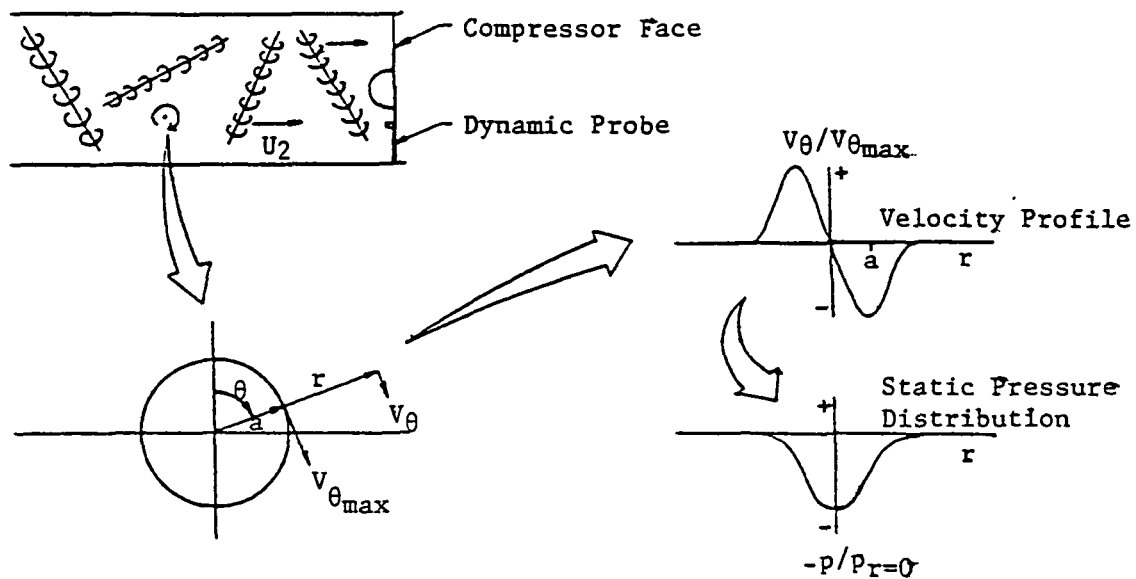


Figure 1. Illustration of a typical inlet test model and the physical and statistical total pressure data and distortion factor

(a)



(b)

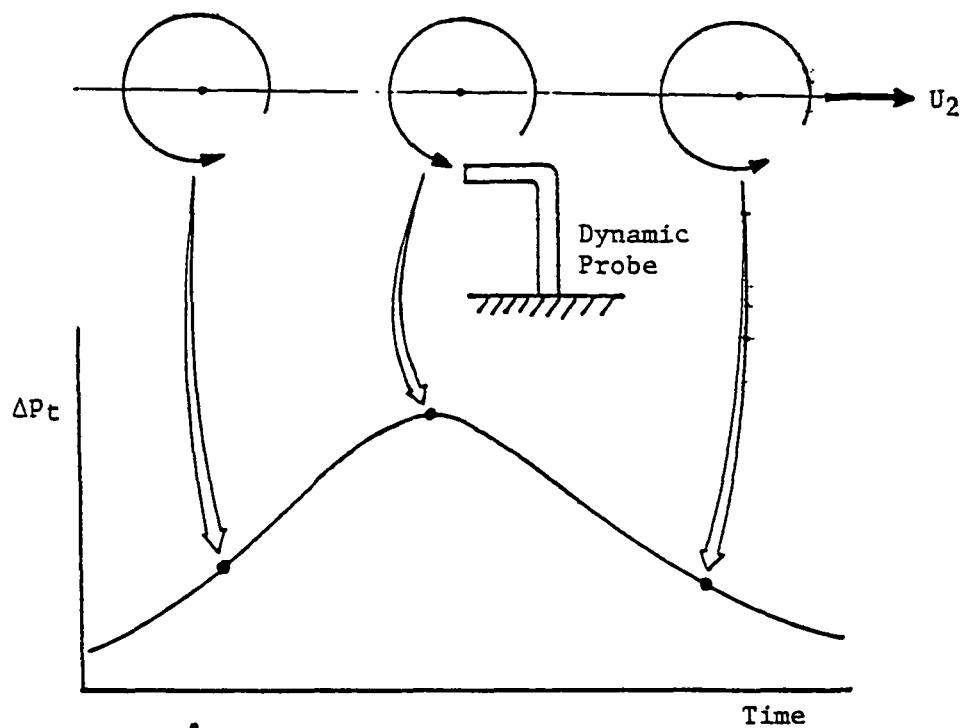


Figure 2. Inlet vortex flow model and perturbation of velocity and static pressure and the time variant total pressure fluctuation caused by a single l-D vortex



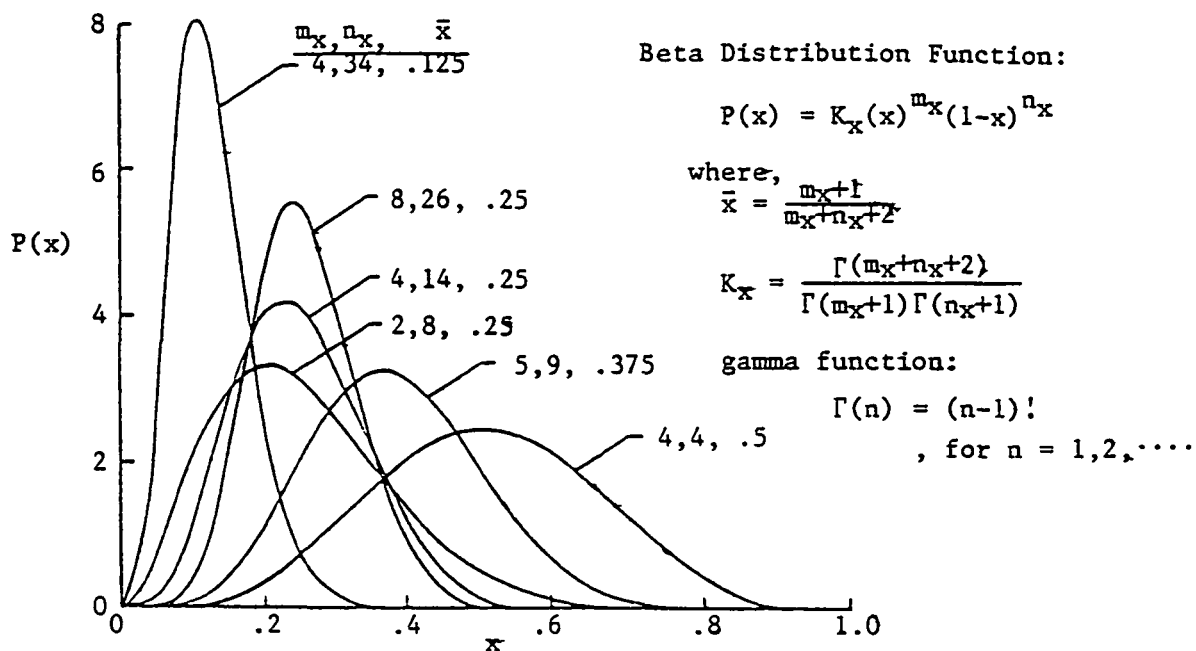


Figure 3. Illustration of the characteristics of Beta distribution function

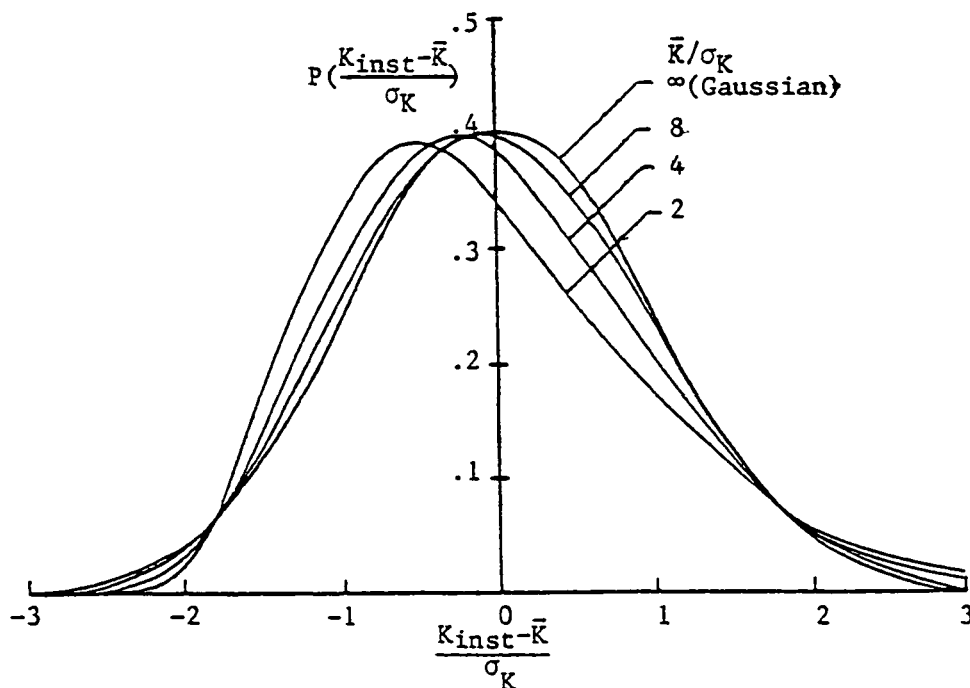


Figure 4. Probability density function of the instantaneous distortion factor,  $K_{inst}$ . Note that the results have been normalized by  $\bar{K}$  and  $\sigma_K$

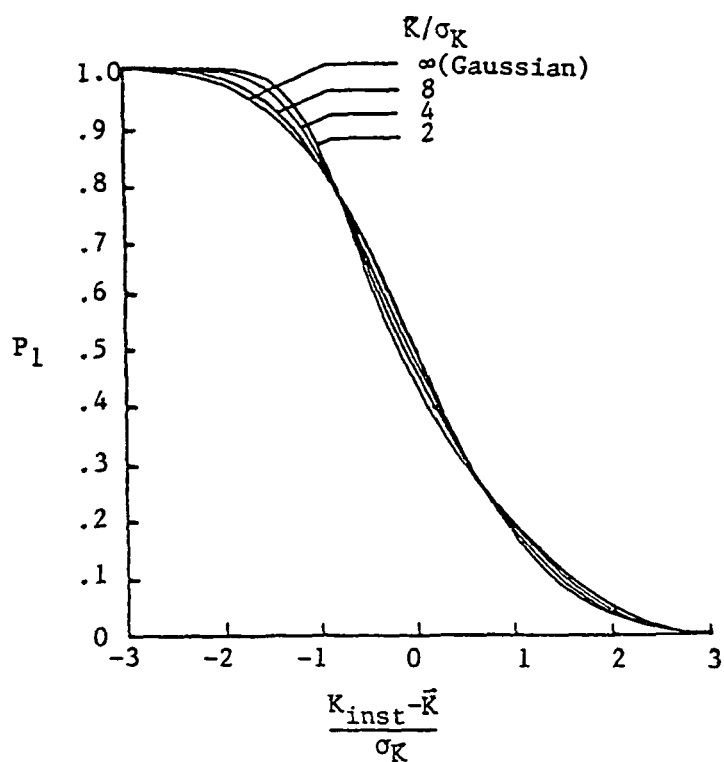


Figure 5. Probability distribution of the cumulative probability function of  $P$

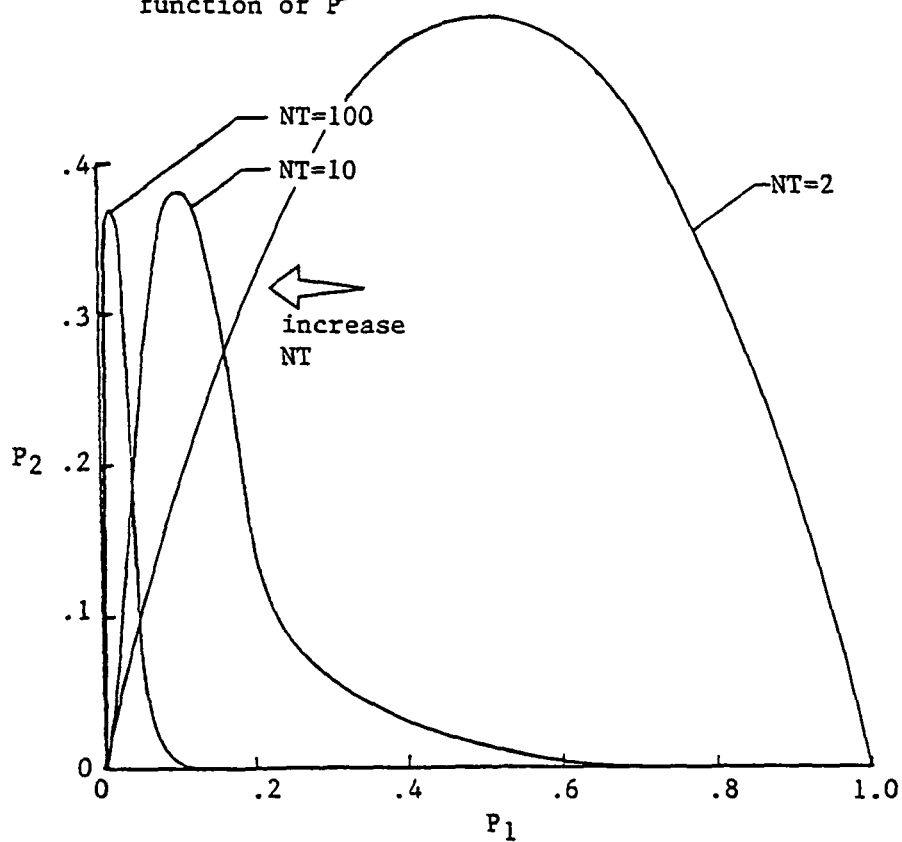


Figure 6. Probability distribution of the peak distortion condition

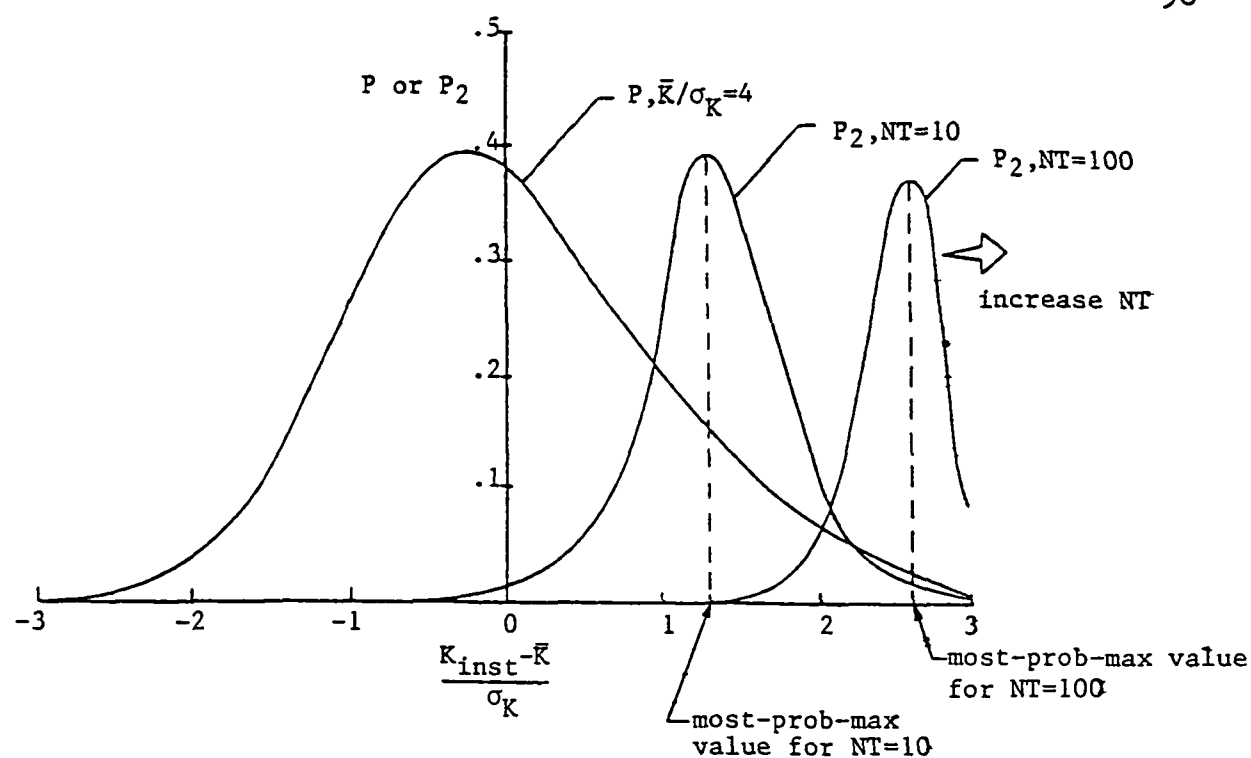


Figure 7. Probability density function of  $K_{inst}$  and the peak distortion value,  $P$  and  $P_2$  respectively

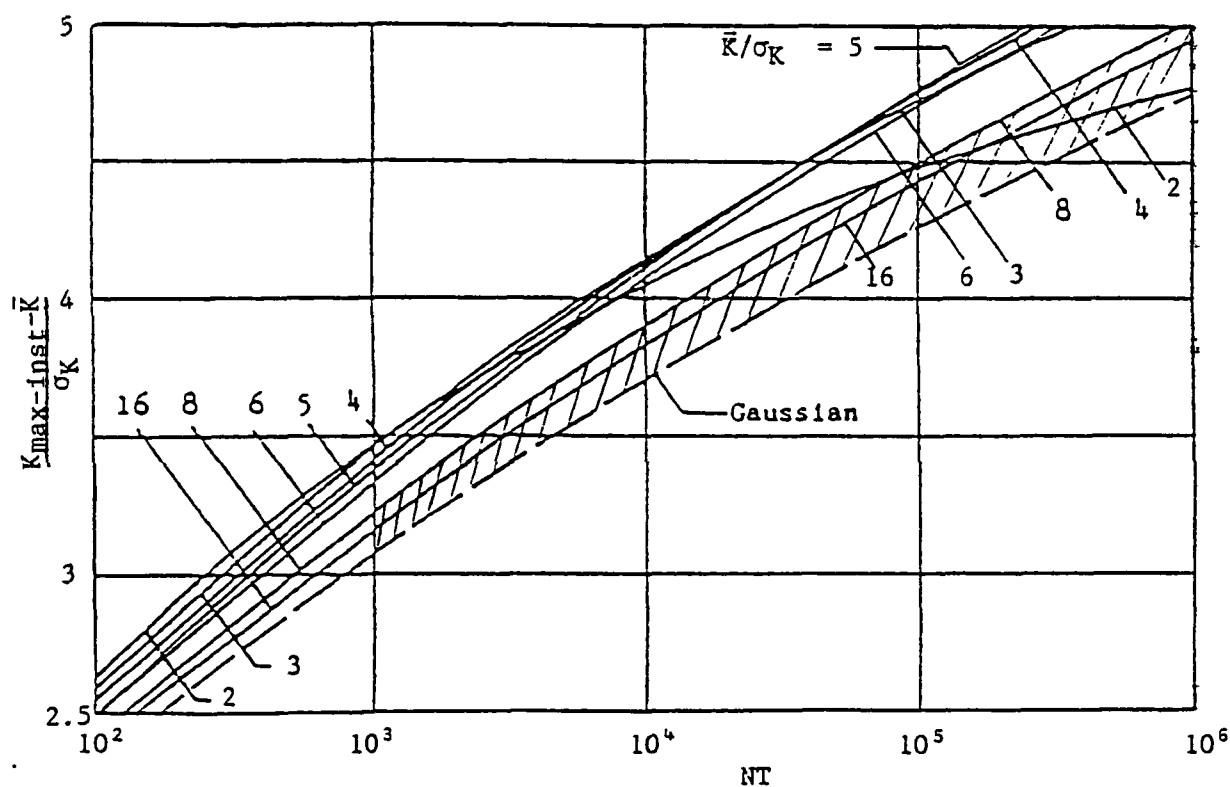


Figure 8. Most probable maximum(peak) instantaneous distortion factor as a function of  $NT$ ,  $\bar{K}$  and  $\sigma_K$

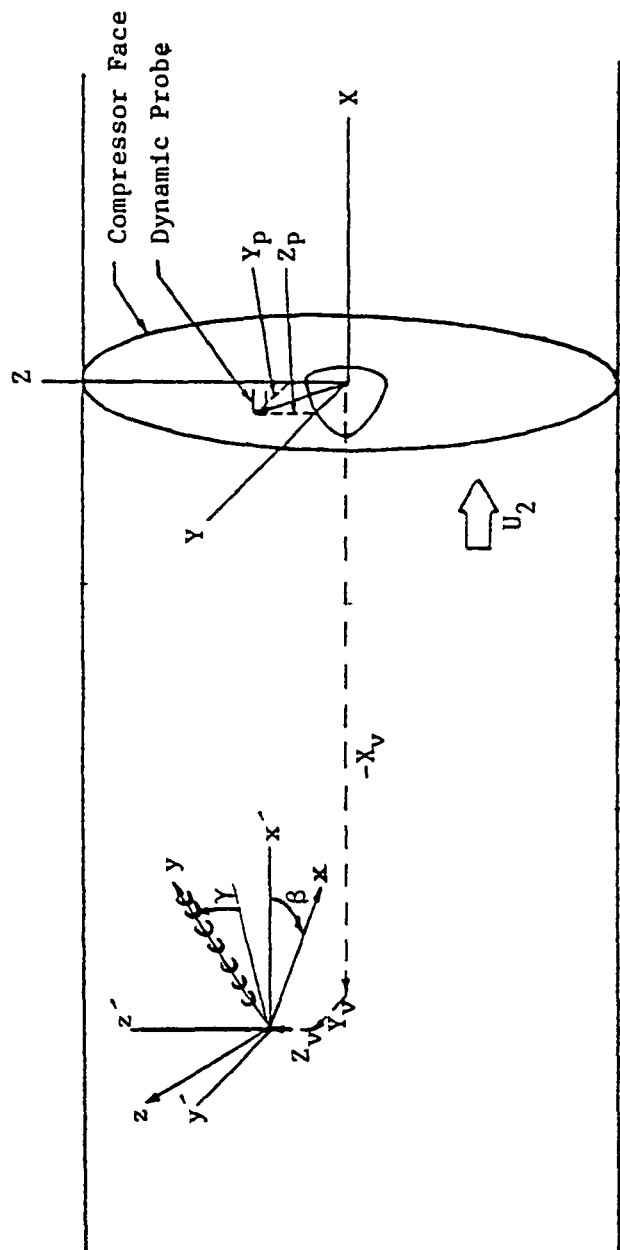


Figure 9. Spatial relationship between the vortex and the total pressure probe

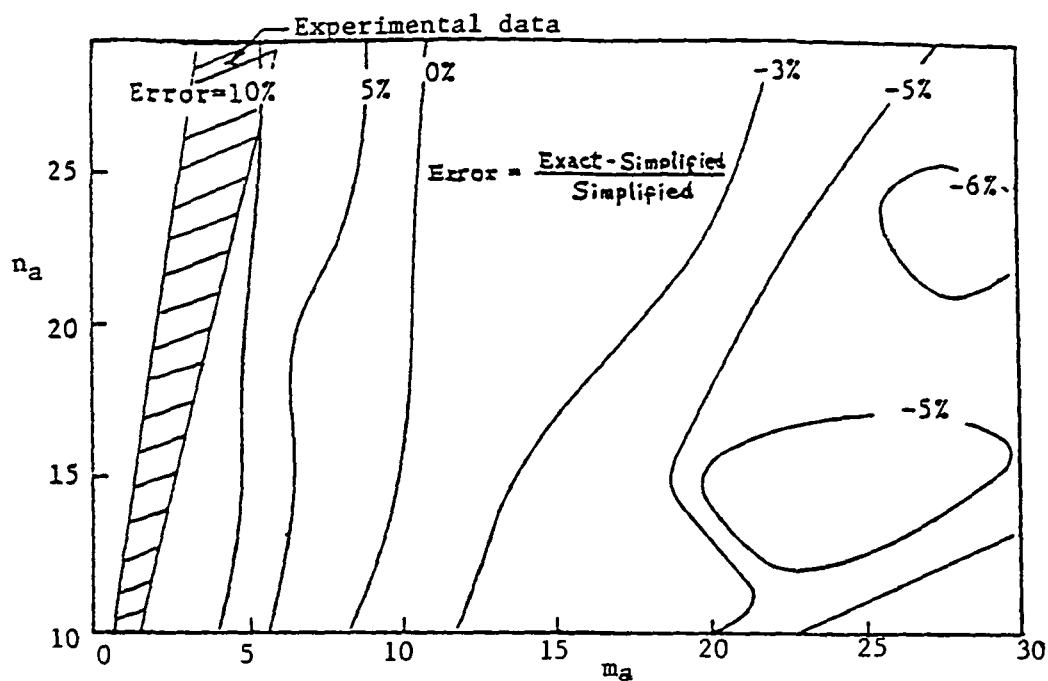


Figure 10. Error of the mean vortex size assumption as a function of  $m_a$  and  $n_a$

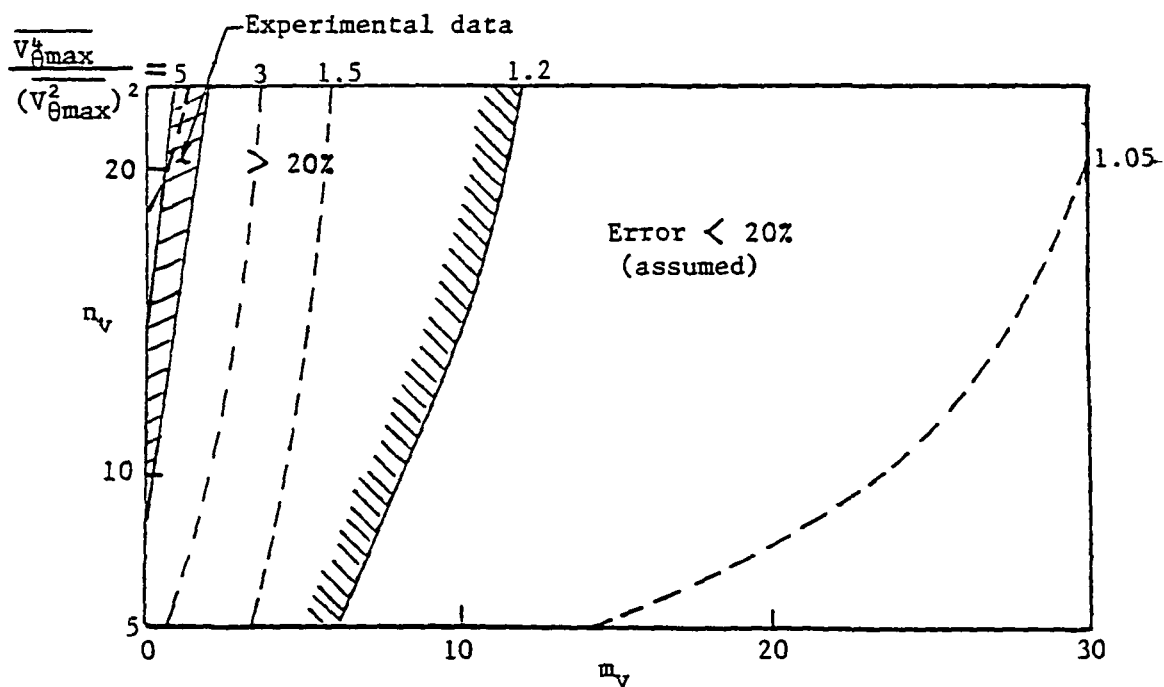


Figure 11. Error in vortex flux,  $N$  (assuming  $\frac{v_{\theta \max}^4}{(v_{\theta \max}^2)^2} = 1$ ), as a function of  $m_v$  and  $n_v$

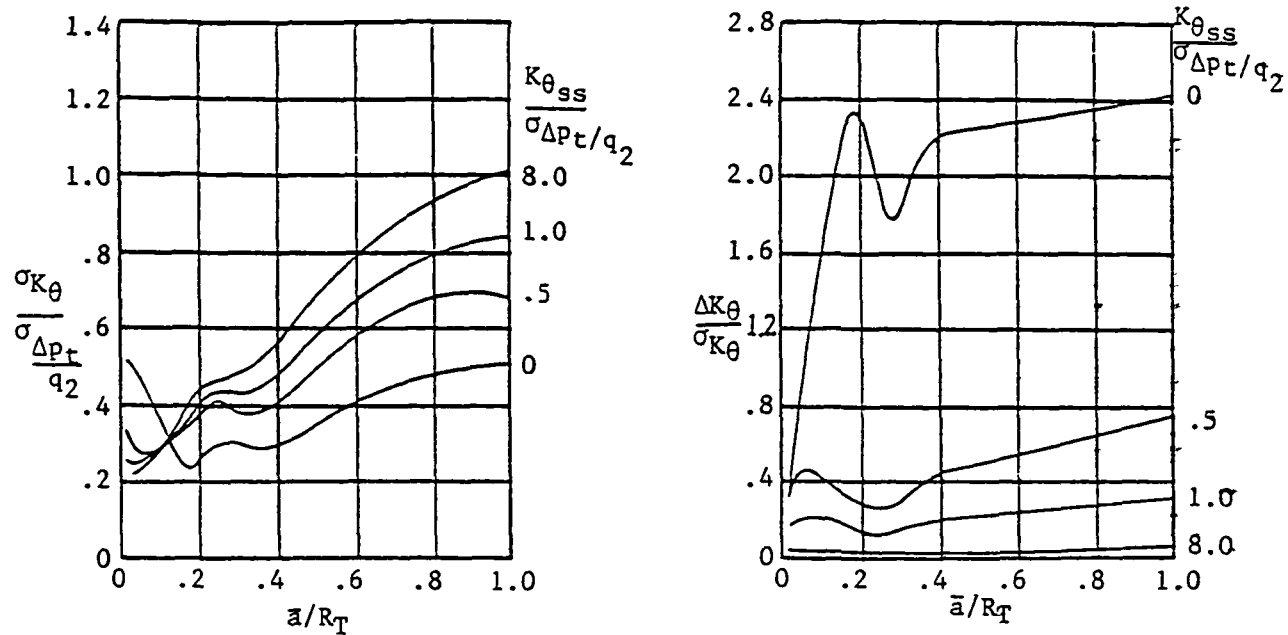
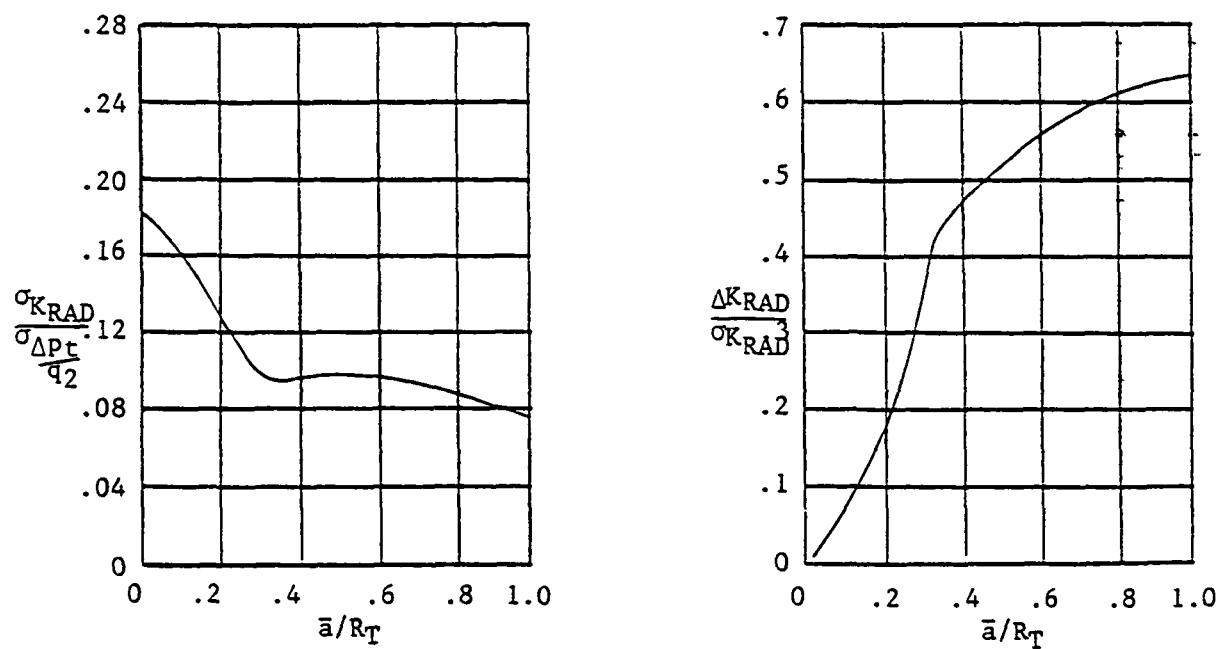
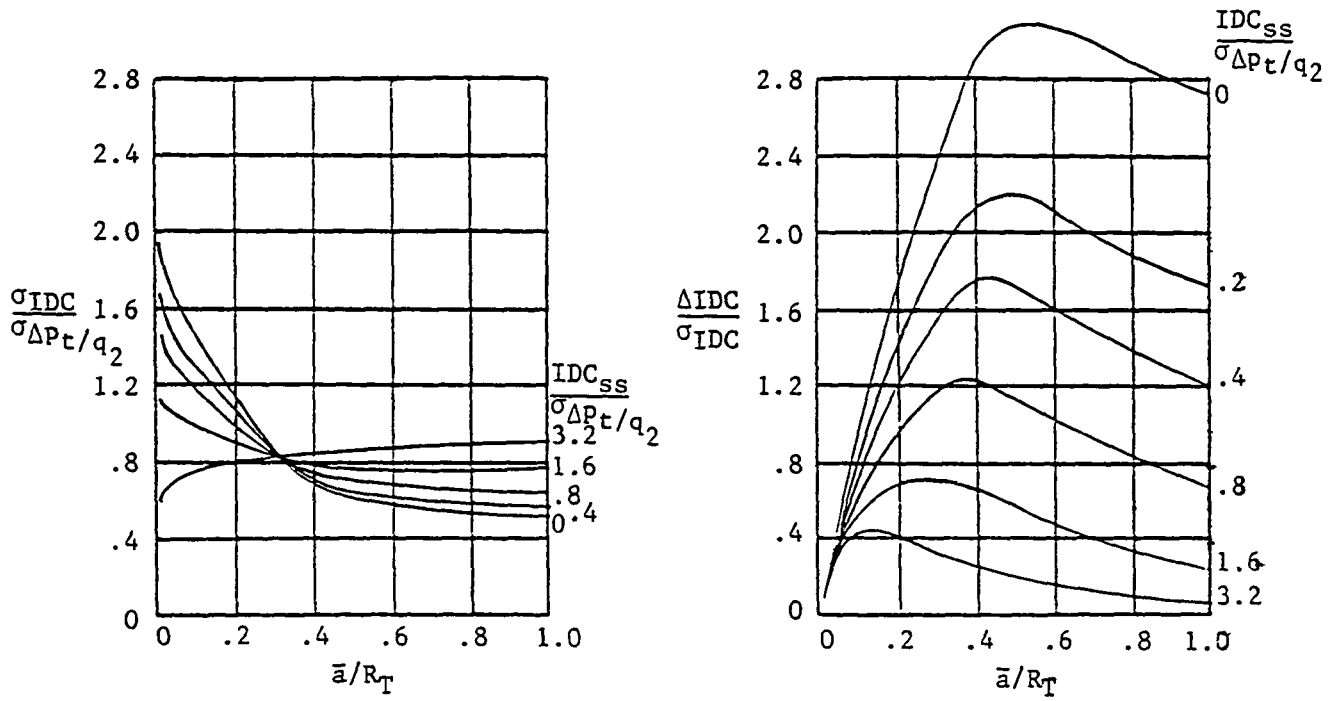
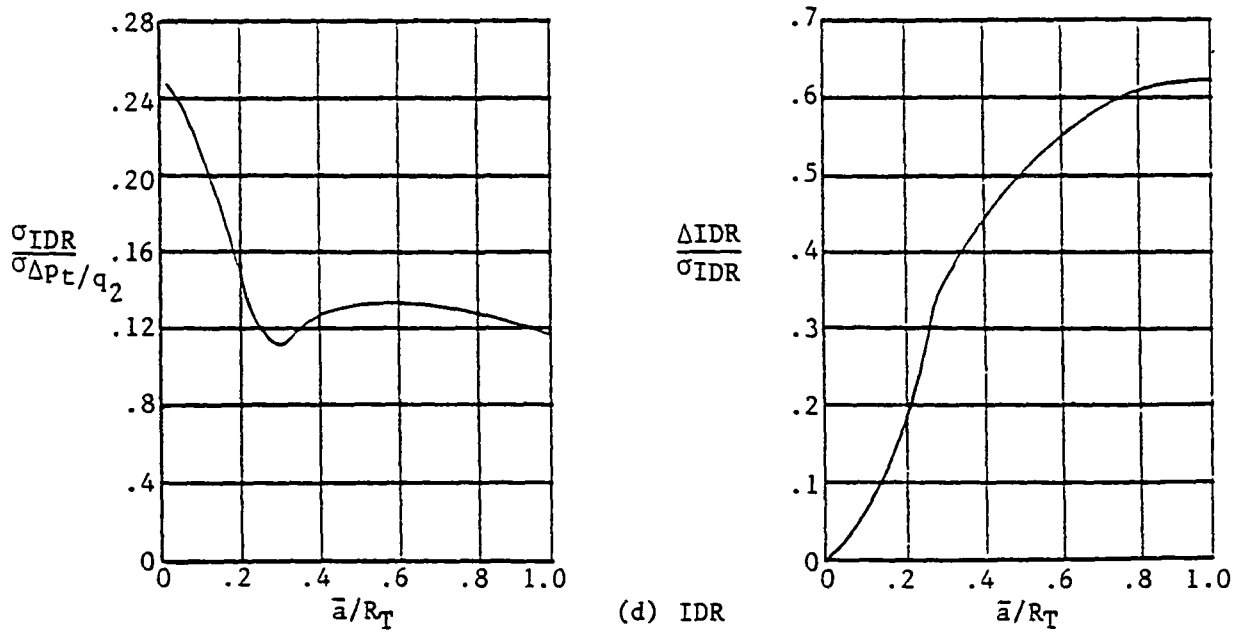
(a)  $K_\theta$ (b)  $K_{RAD}$ 

Figure 12. Distortion factor rms level and mean instantaneous value



(c) IDC



(d) IDR

Figure 12. Continued

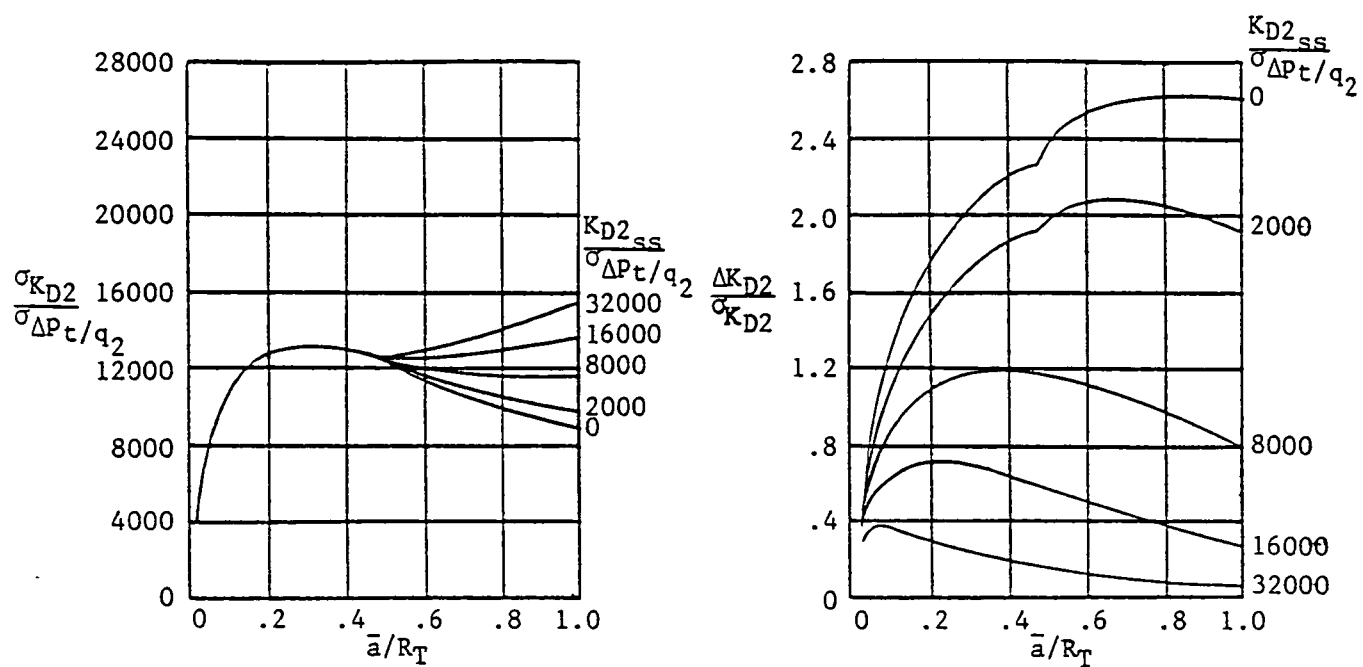
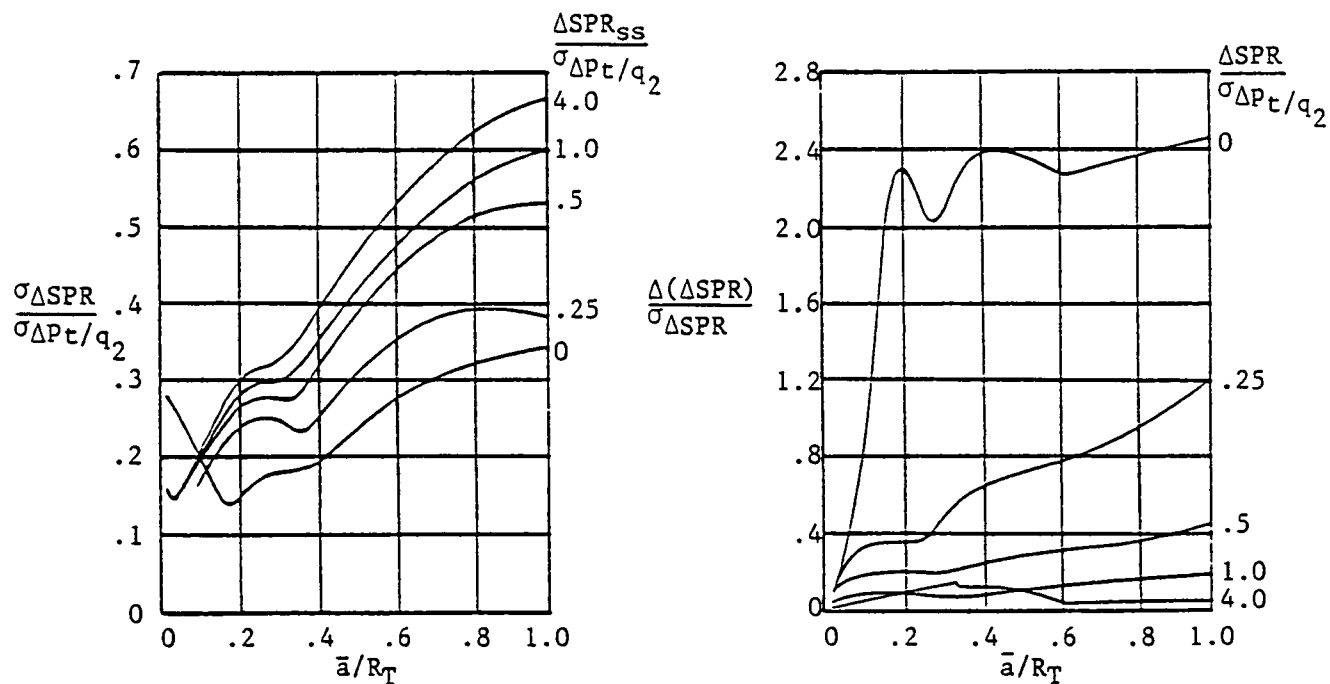
(e)  $K_{D2}$ (f)  $\Delta SPR$ 

Figure 12. concluded



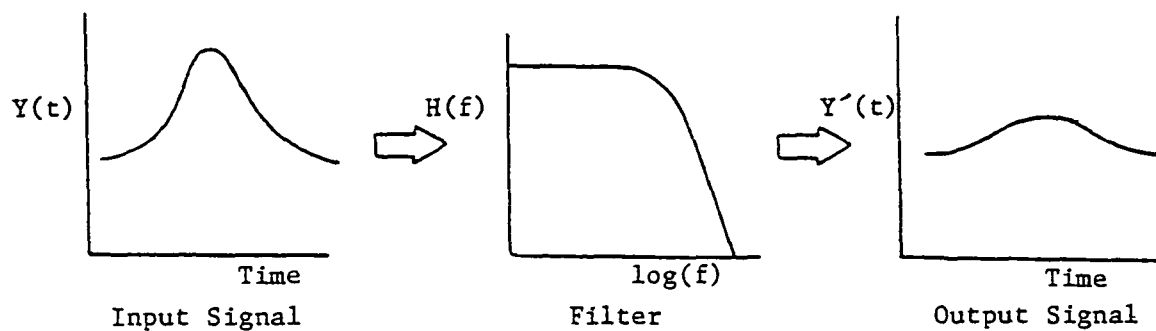


Figure 13. Illustration of the filtering effect for engine response characteristics

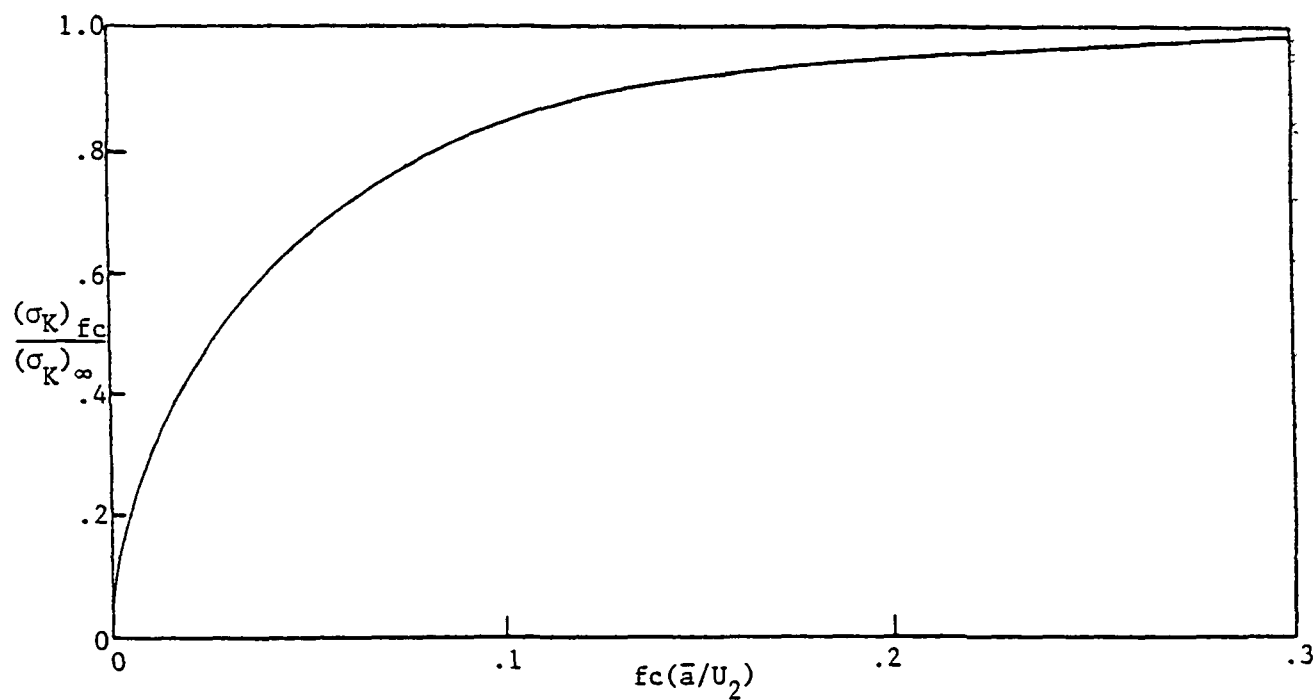


Figure 14. Effect of filter cut-off frequency on distortion factor rms level

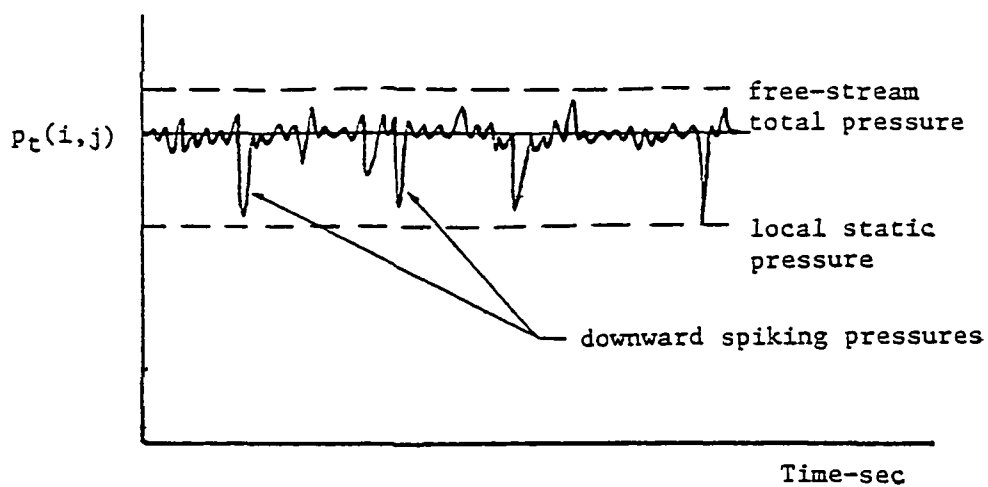
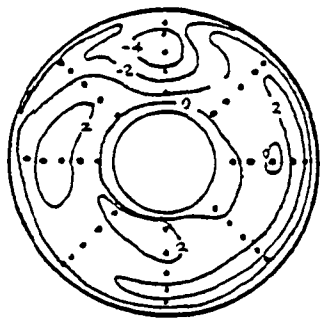
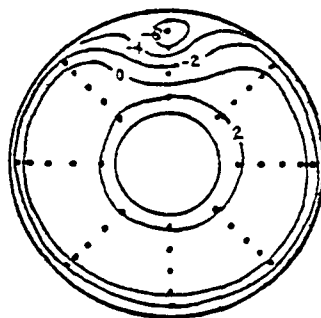


Figure 15. schemetical illustration of total pressure spiking phenomenon

(a) Measured distortion pattern(DYNADEC)

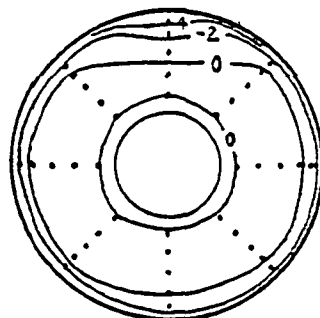


measured peak no. 1



measured peak no. 2

(b) Predicted distortion pattern(Melick's)



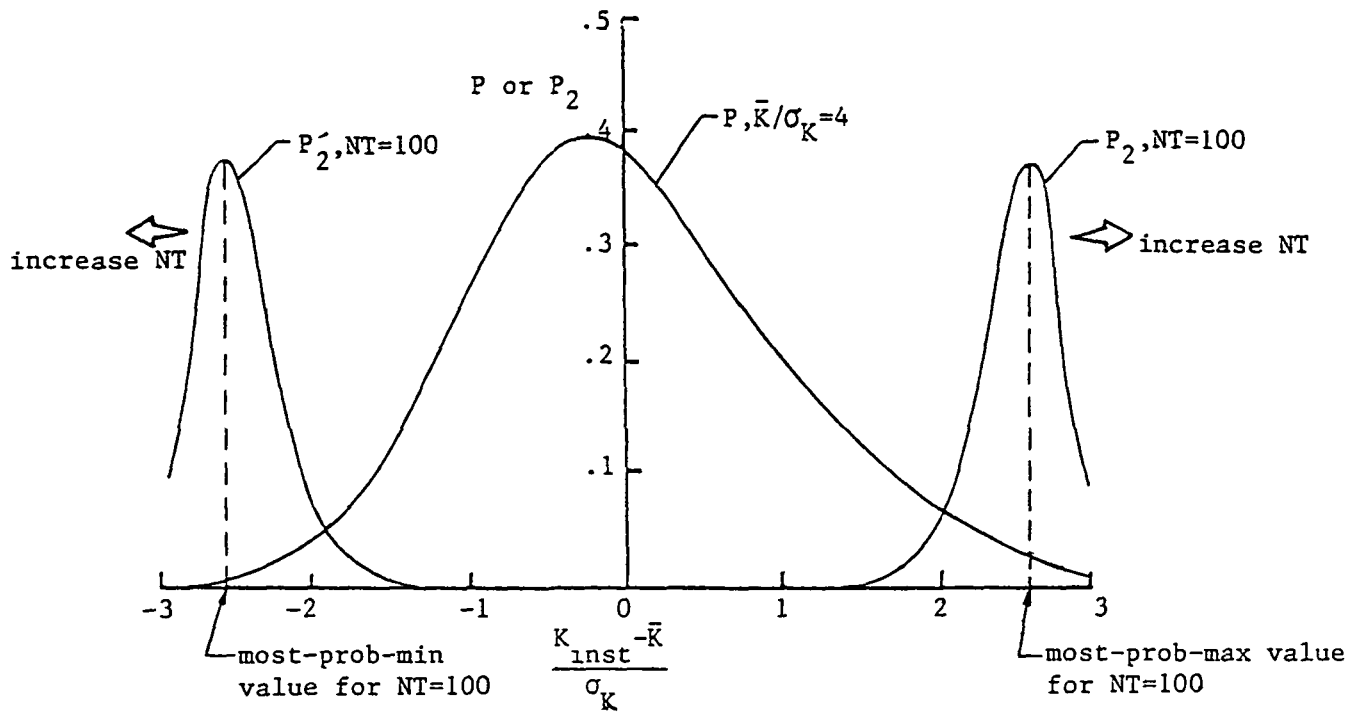
Data Pt.: 1574

Mach No.: 0.9

Angle of Attack: 15 deg

Sideslip Angle: 0 deg

Figure 16. Typical measured and predicted distortion pattern for data with spiking phenomenon



Note:  $P_2$  represents the probability density function for the minimum peak condition

Figure 17. Illustration of the method of finding the minimum peak distortion value

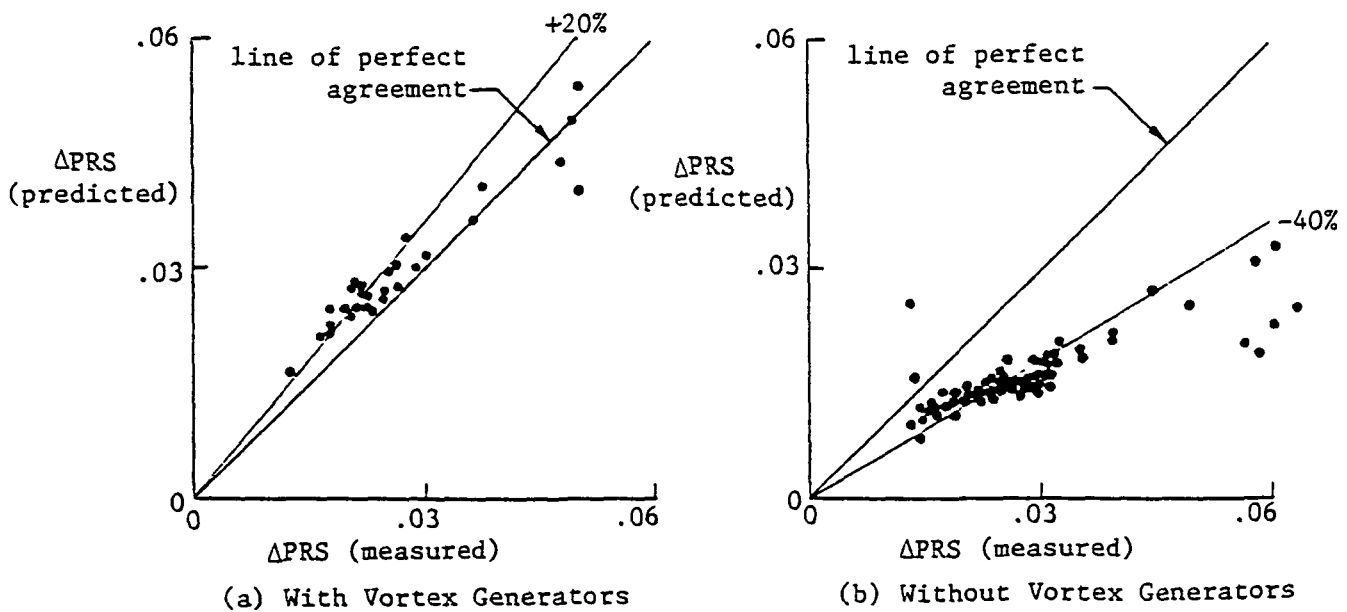
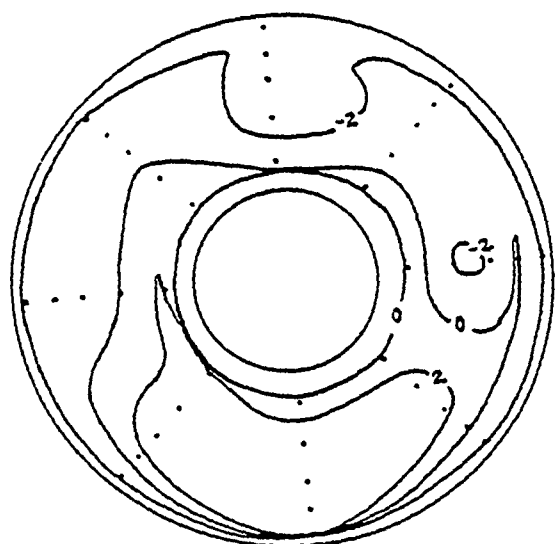
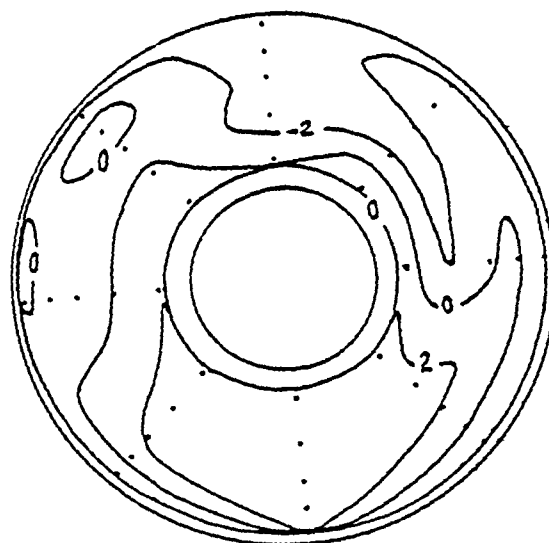
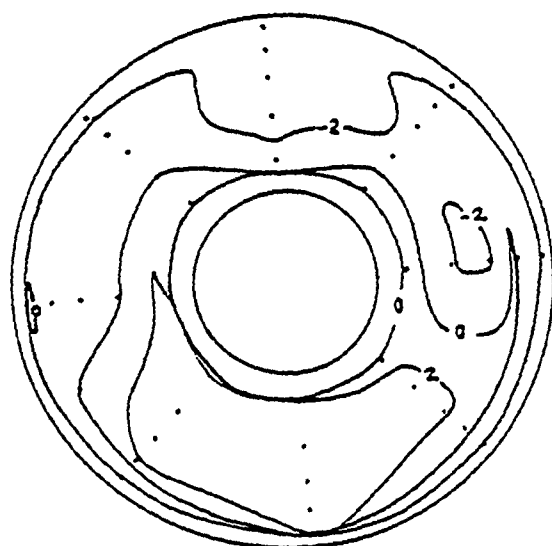


Figure 18. Comparisons of predicted and measured peak distortion value,  $\Delta PRS$



Steady-state

Measured (DYNADEC)  
PeakPredicted (Melick)  
Peak

(a)

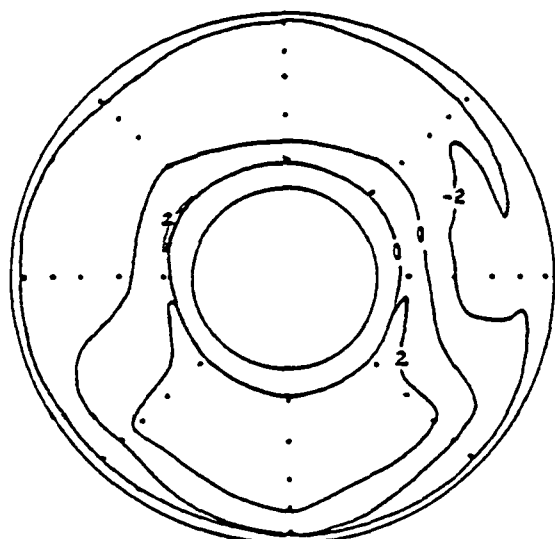
Data Point: 2436

Mach no. = 0.6

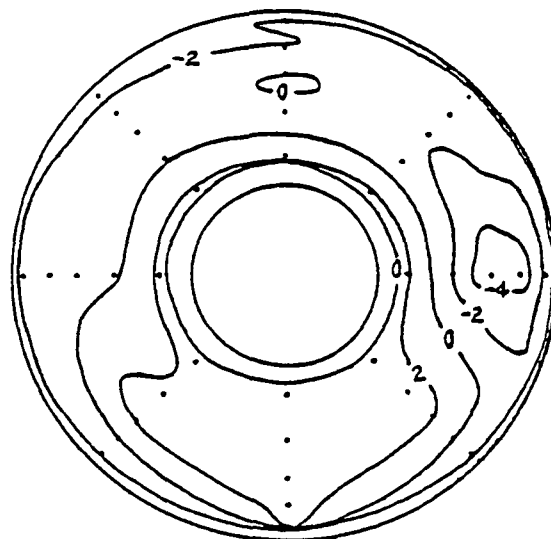
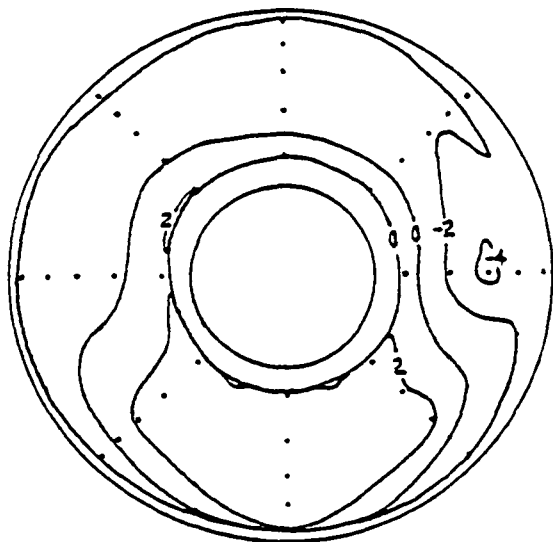
Angle of Attack = -5 deg

Sideslip Angle = 0 deg

Figure 19. Comparisons of measured and predicted peak distortion maps



Steady-state

Measured (DYNADEC)  
PeakPredicted (Melick)  
Peak

Data Point: 2437

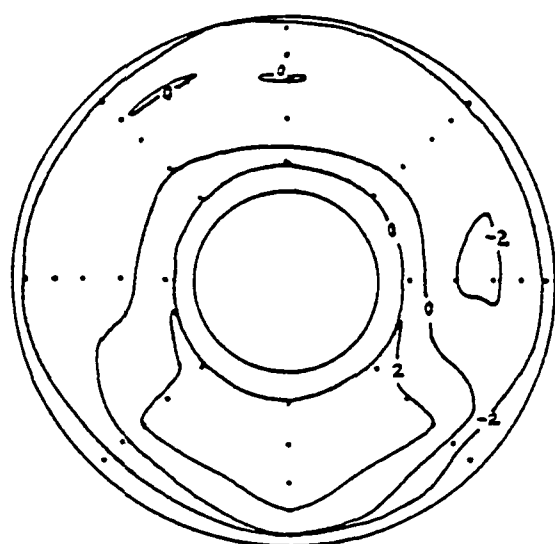
Mach no. = 0.6

Angle of Attack = 0 deg

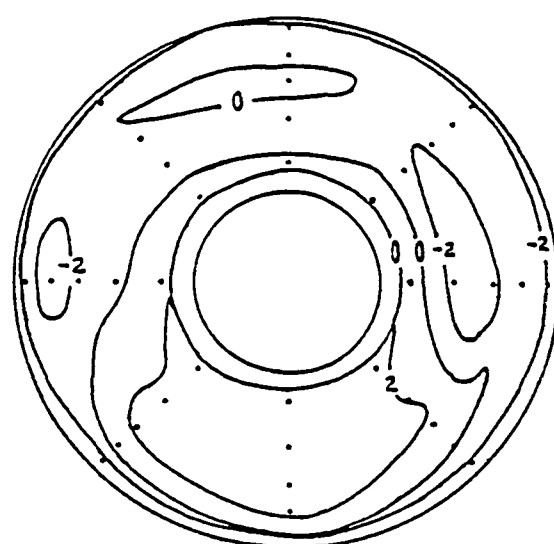
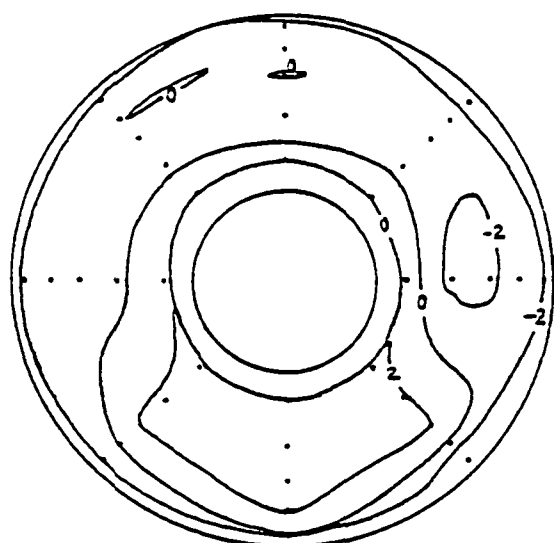
Sideslip Angle = -5 deg

(b)

Figure 19. Continued



Steady-state

Measured (DYNADEC)  
PeakPredicted (Melick)  
Peak

Data Point: 2433

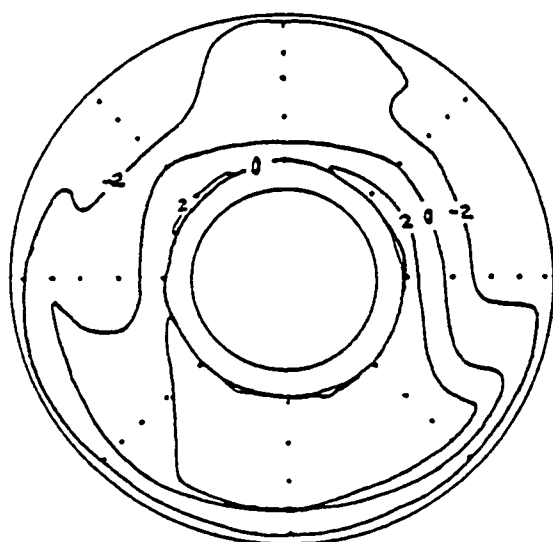
Mach no. = 0.6

Angle of Attack = 15 deg

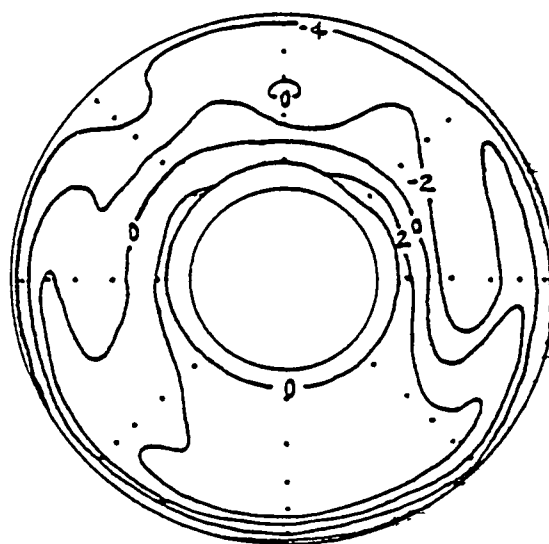
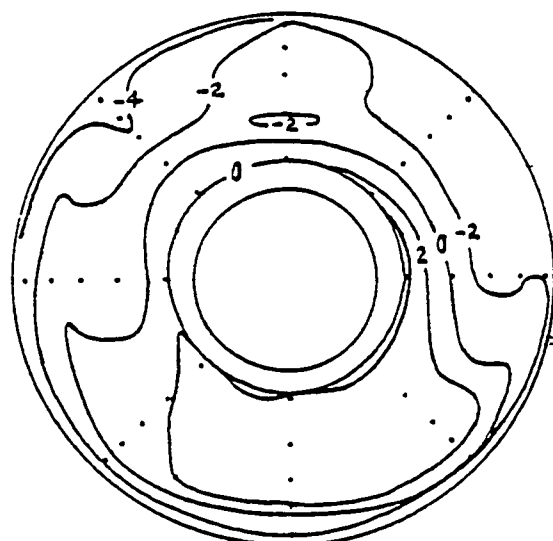
Sideslip Angle = 0 deg

(c)

Figure 19. Continued



Steady-state

Measured (DYNADEC)  
PeakPredicted (Melick)  
Peak

Data Point: 1968

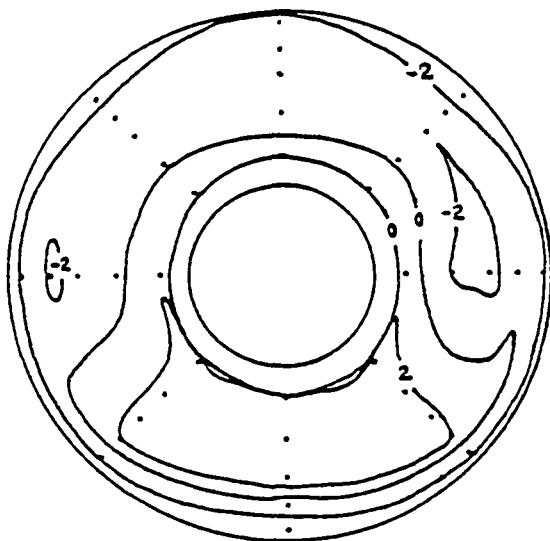
Mach no. = 0.9

Angle of Attack = -10 deg

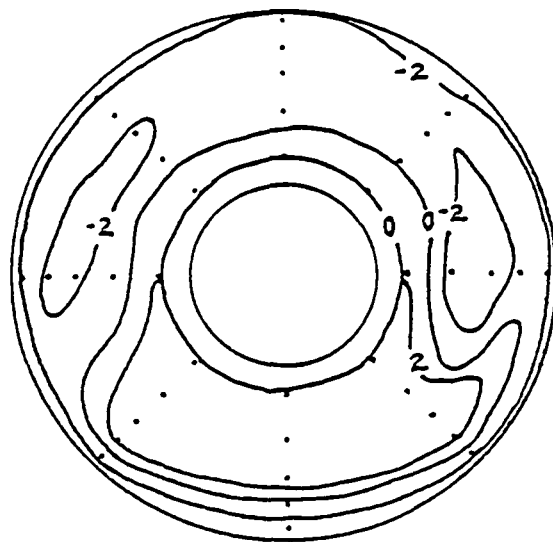
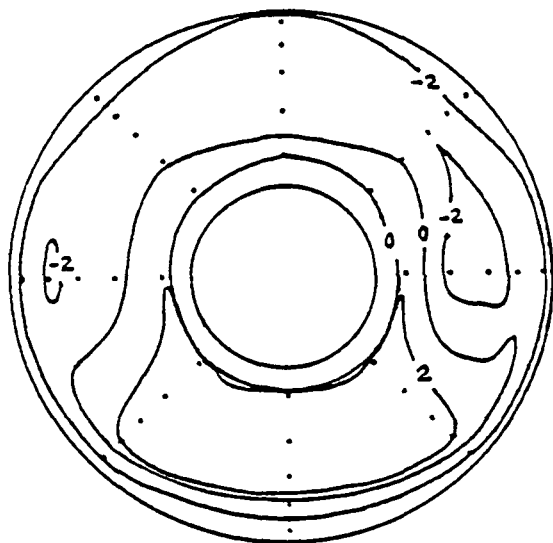
Sideslip Angle = -5 deg

(d)

Figure 19. Continued



Steady-state

Measured (DYNADEC)  
PeakPredicted (Melick)  
Peak

Data Point: 1948

Mach no. = 0.9

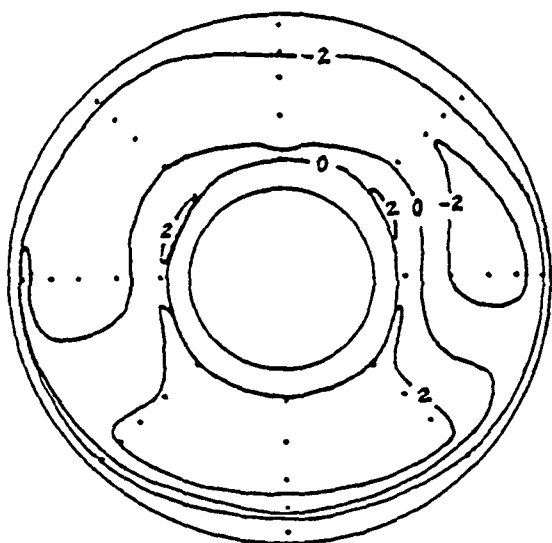
Angle of Attack = 7 deg

Sideslip Angle = 0 deg

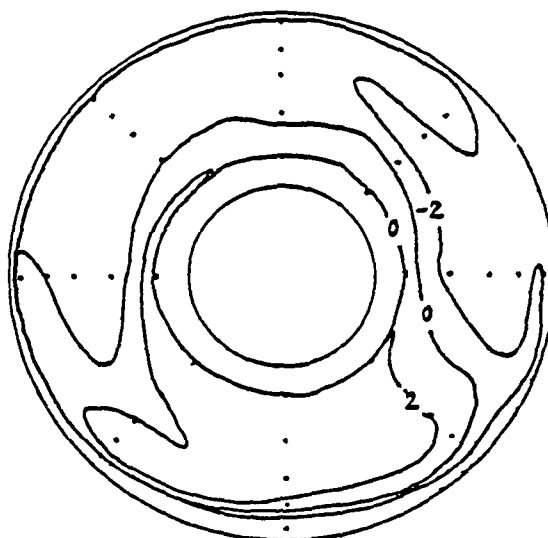
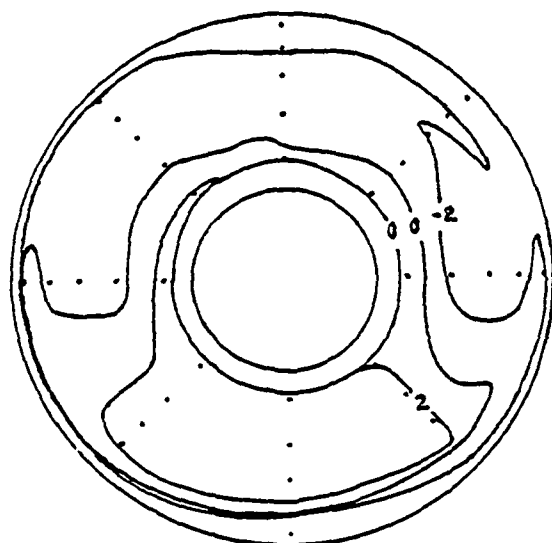
(e)

Figure 19. Continued





Steady-state

Measured (DYNADEC)  
Peak  
cPredicted (Melick)  
Peak

Data Point: 1964

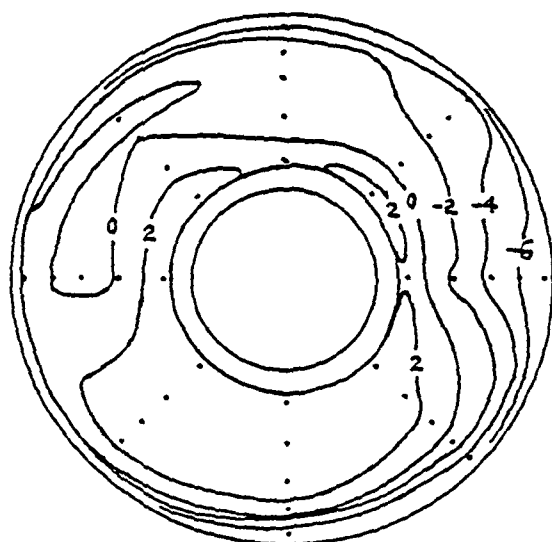
Mach no. = 0.9

Angle of attack = 7 deg

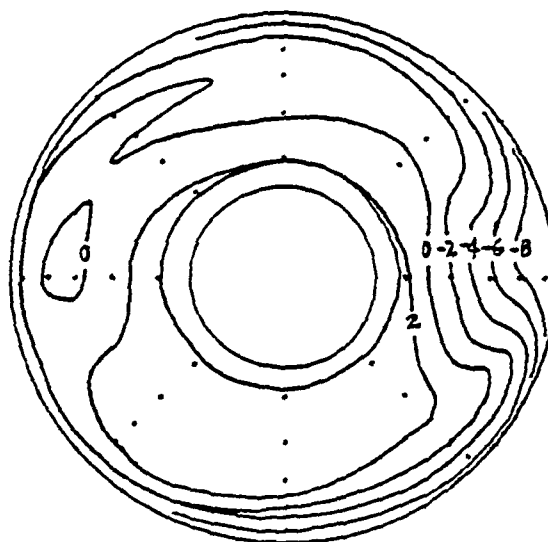
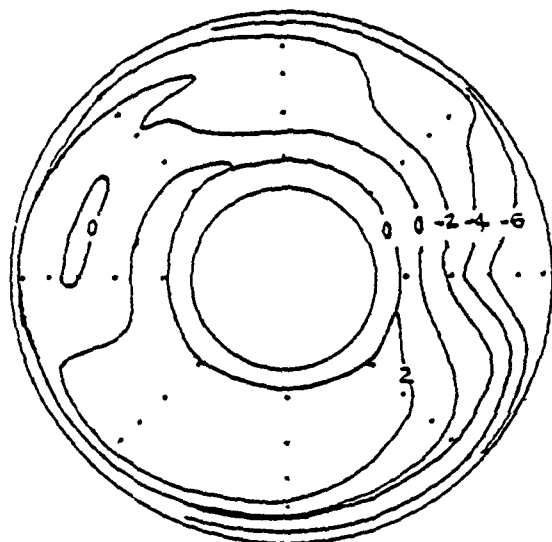
Sideslip Angle = -5 deg

(f)

Figure 19. Continued



Steady-state

Measured(DYNADEC)  
PeakPredicted(Melick)  
Peak

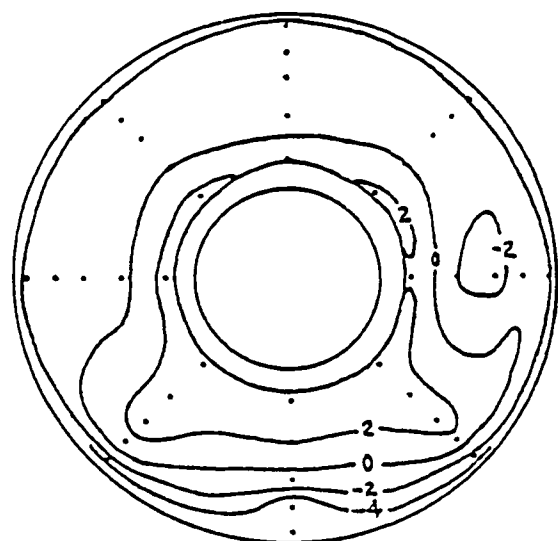
Data Point: 1972

Mach no. = 0.9

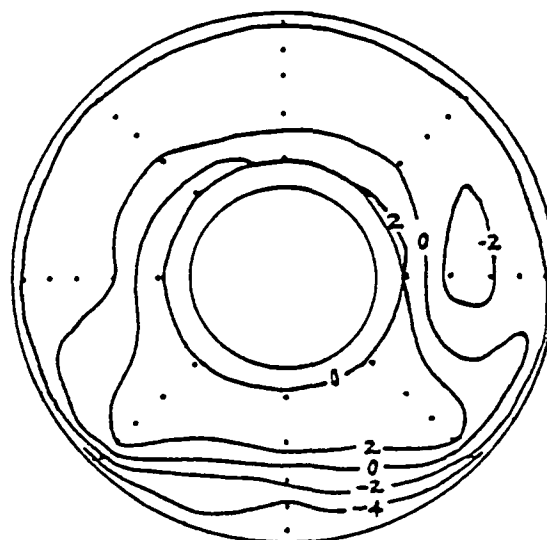
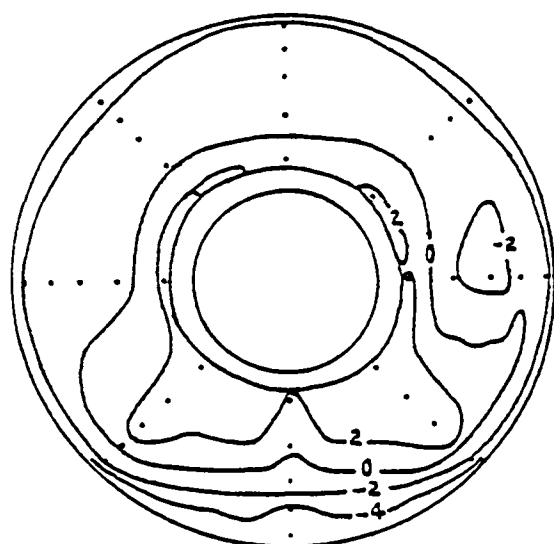
Angle of Attack = 10 deg

Sideslip Angle = -10 deg

(g)



Steady-state

Measured (DYNADEC)  
PeakPredicted (Melick)  
Peak

Data Point: 1956

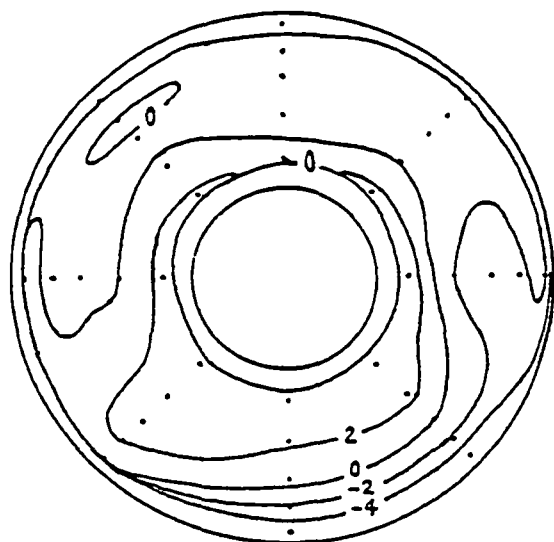
Mach no. = 0.9

Angle of Attack = 20 deg

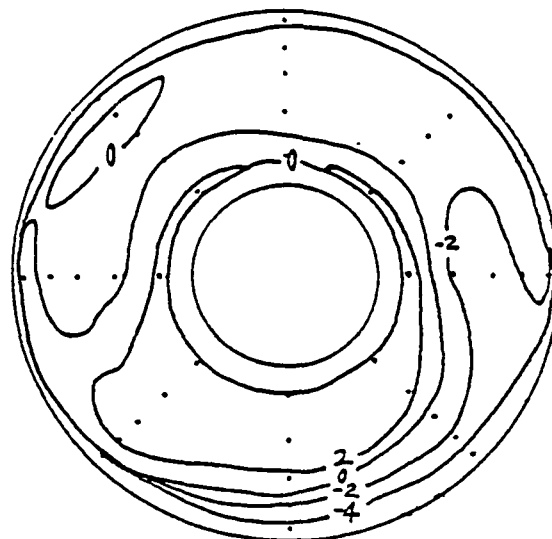
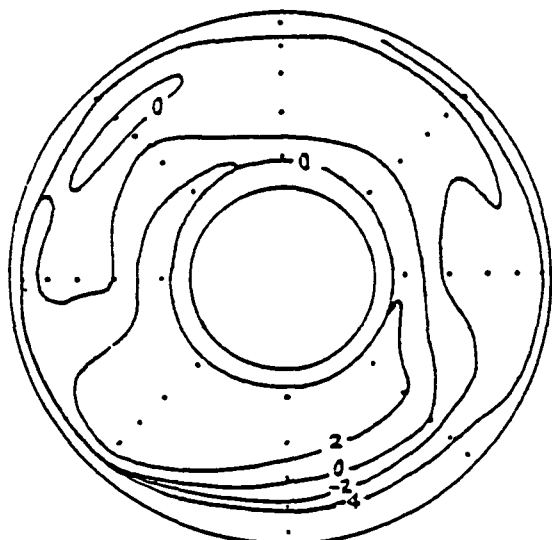
Sideslip Angle = 0 deg

(h)

Figure 19. Continued



Steady-state

Measured (DYNADec)  
PeakPredicted (Melick)  
Peak

Data Point: 1960

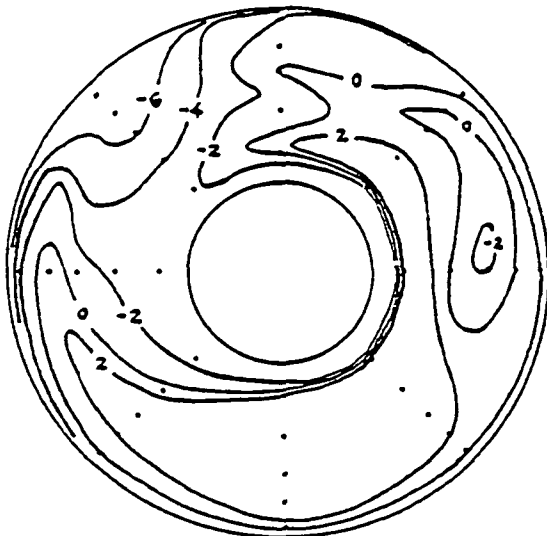
Mach no. = 0.9

Angle of Attack = 20 deg

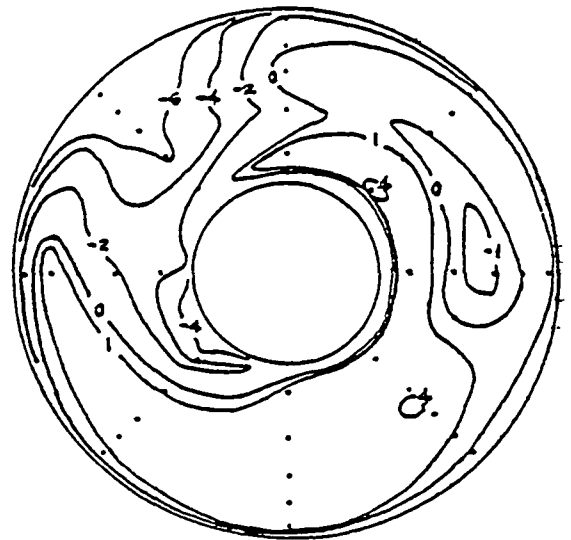
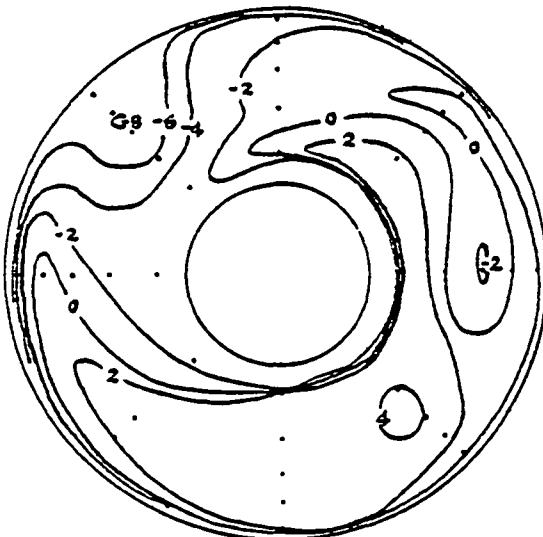
Sideslip Angle = -5 deg

(i)

Figure 19. Continued



Steady-state

Measured (DYNADEC)  
PeakPredicted (Melick)  
Peak

Data Point: 2361

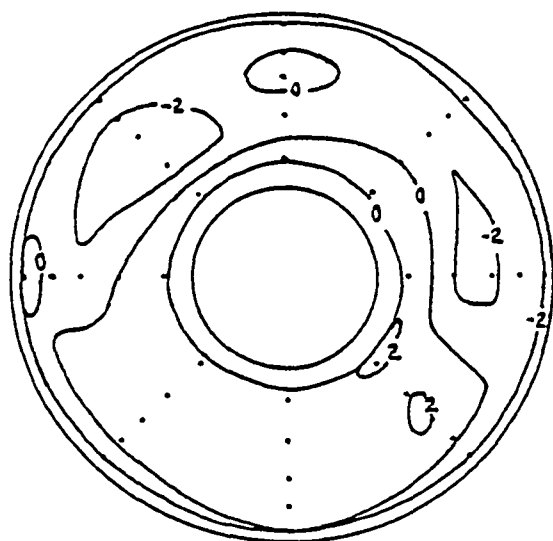
Mach no. = 1.36

Angle of Attack = -4 deg

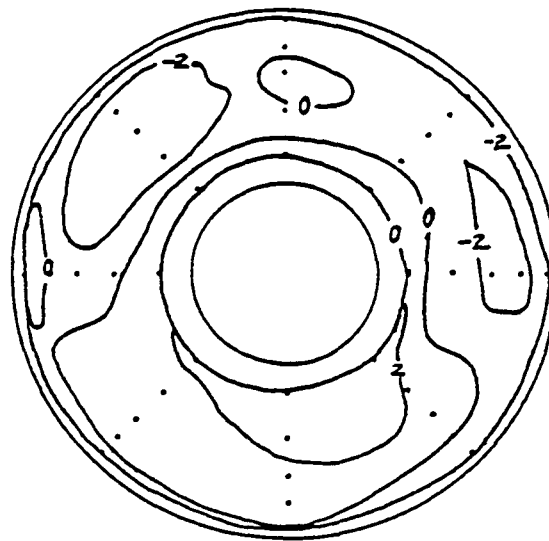
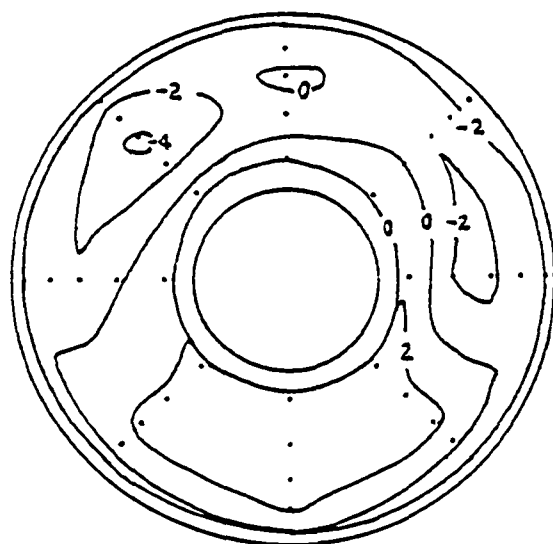
Sideslip Angle = -4 deg

(j)

Figure 19. Continued



Steady-state

Measured (DYNADEC)  
PeakPredicted (Melick)  
Peak

Data Point: 2363

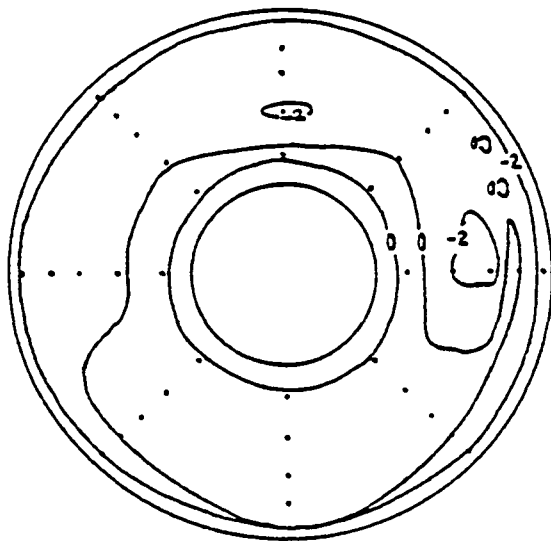
Mach no. = 1.36

Angle of Attack = 0 deg

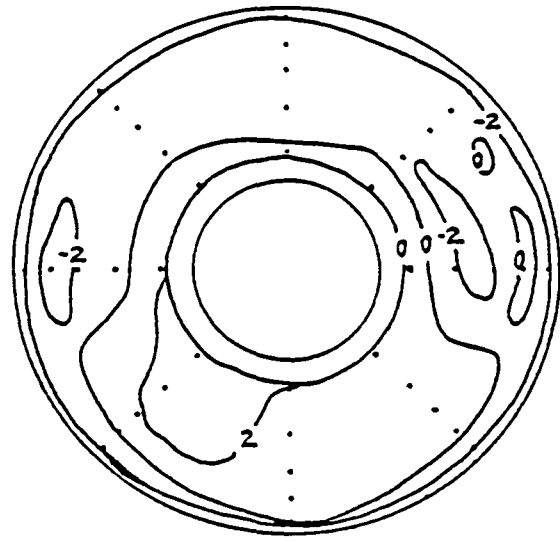
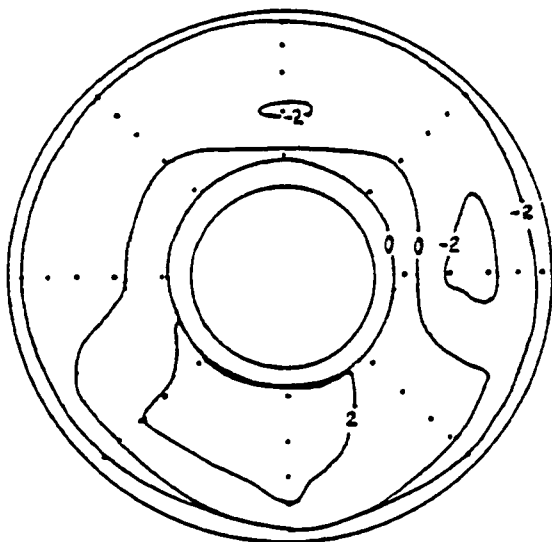
Sideslip Angle = -5 deg

(k)

Figure 19. Continued



Steady-state

Measured (DYNADEC)  
PeakPredicted (Melick)  
Peak

Data point: 2358

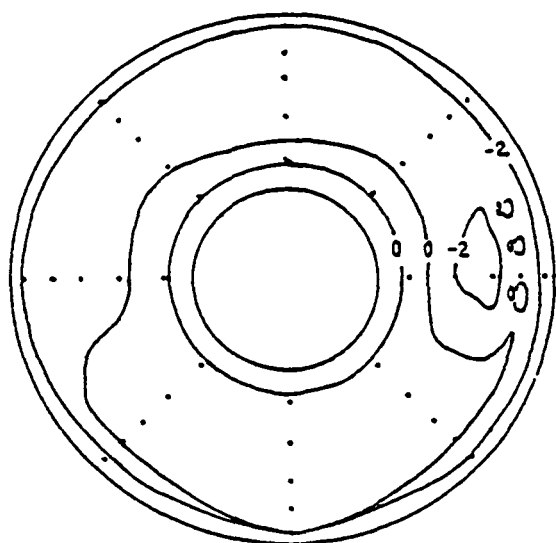
Mach no. = 1.36

Angle of Attack = 4 deg

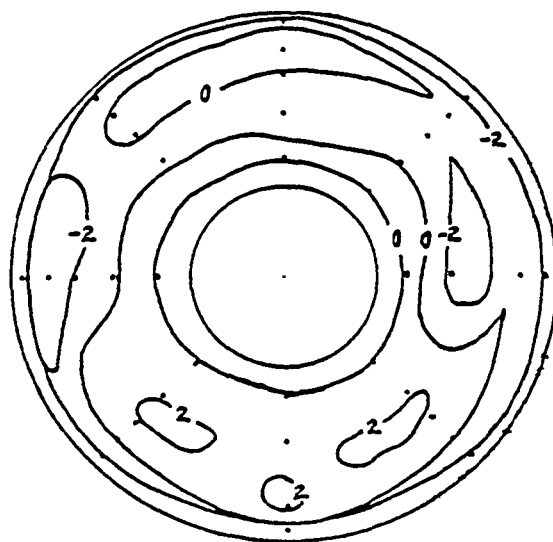
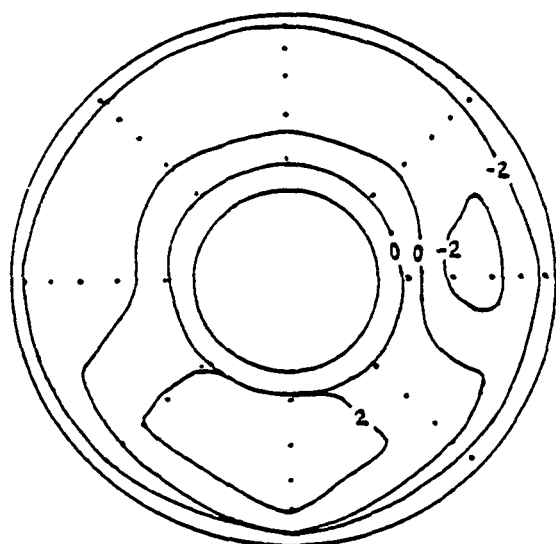
Sideslip Angle = 0 deg

(1)

Figure 19. Continued



Steady-state

Measured (DYNADEC)  
PeakPredicted (Melick)  
Peak

Data Point: 2360

Mach no. = 1.36

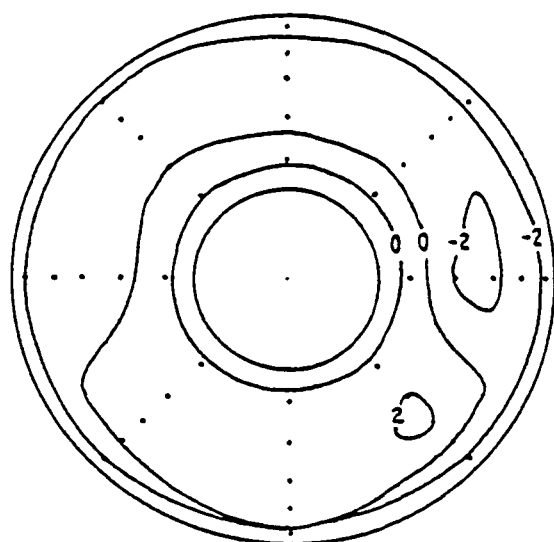
Angle of Attack = 15 deg

Sideslip Angle = 0 deg

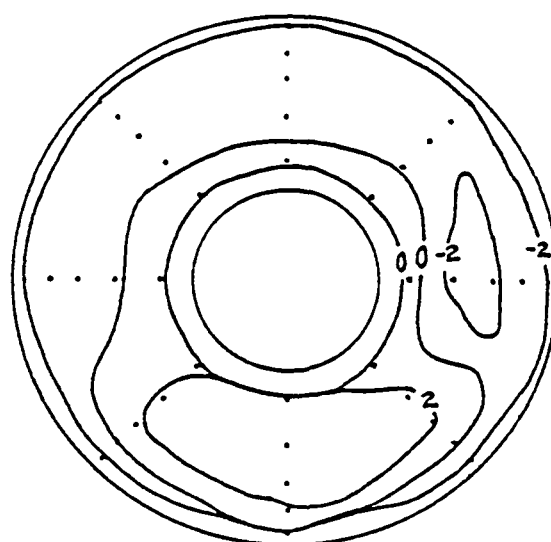
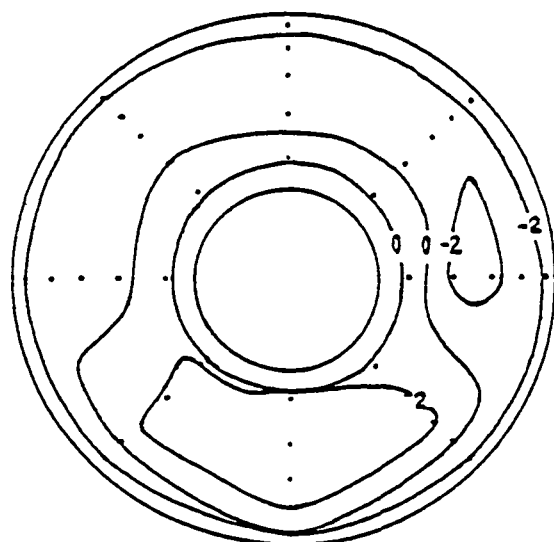
(m)

Figure 19. Continued





Steady-state

Measured (DYNADEC)  
PeakPredicted (Melick)  
Peak

Data Point: 2362

Mach no. = 1.36

Angle of Attack = 15 deg

Sideslip Angle = -4 deg

(n)

Figure 19. concluded

ORIGINAL PAGE IS  
OF POOR QUALITY

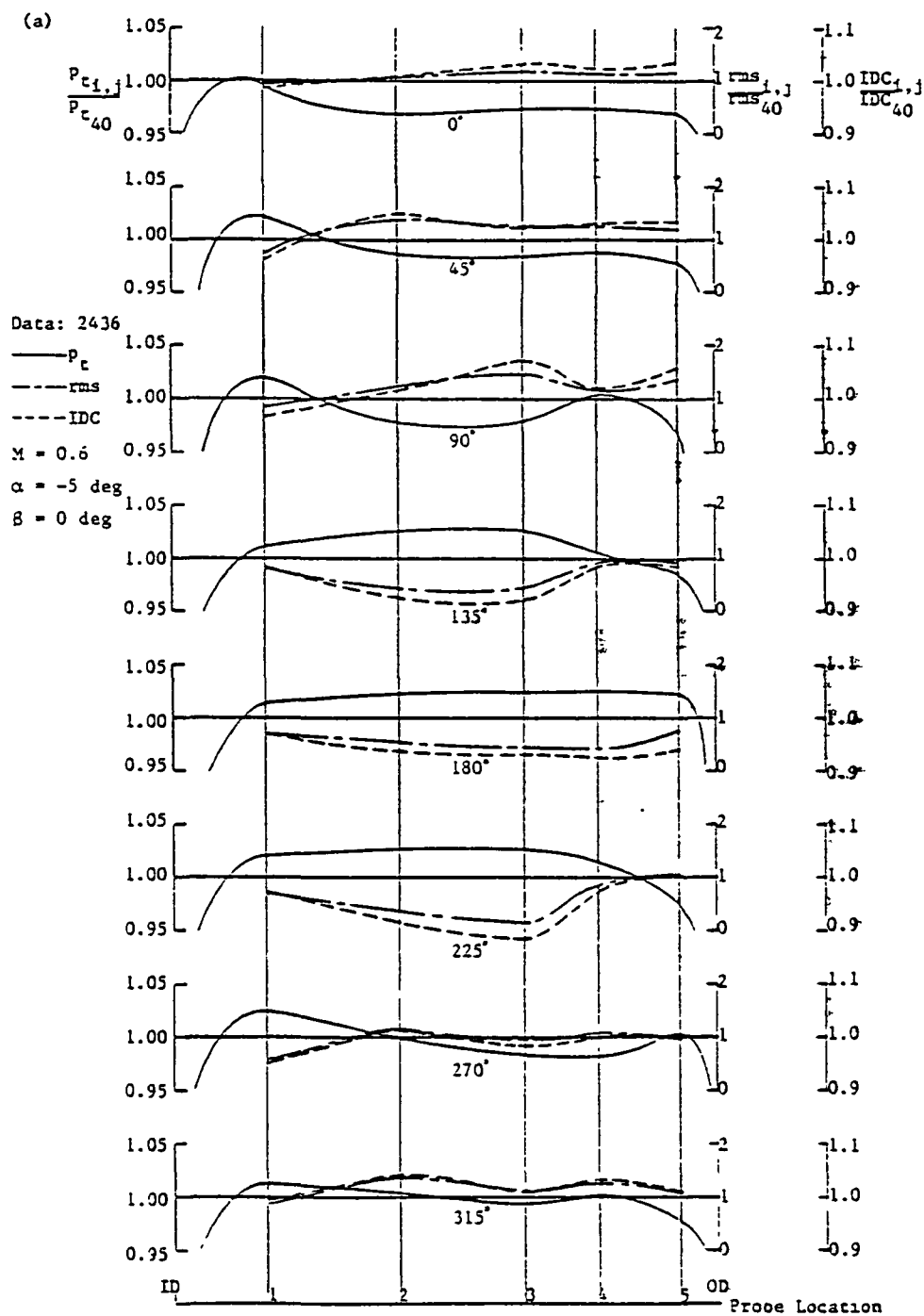


Figure 20. Comparisons of radial variations of steady-state total pressure, rms level and single-probe predicted peak distortion factor (IDC)

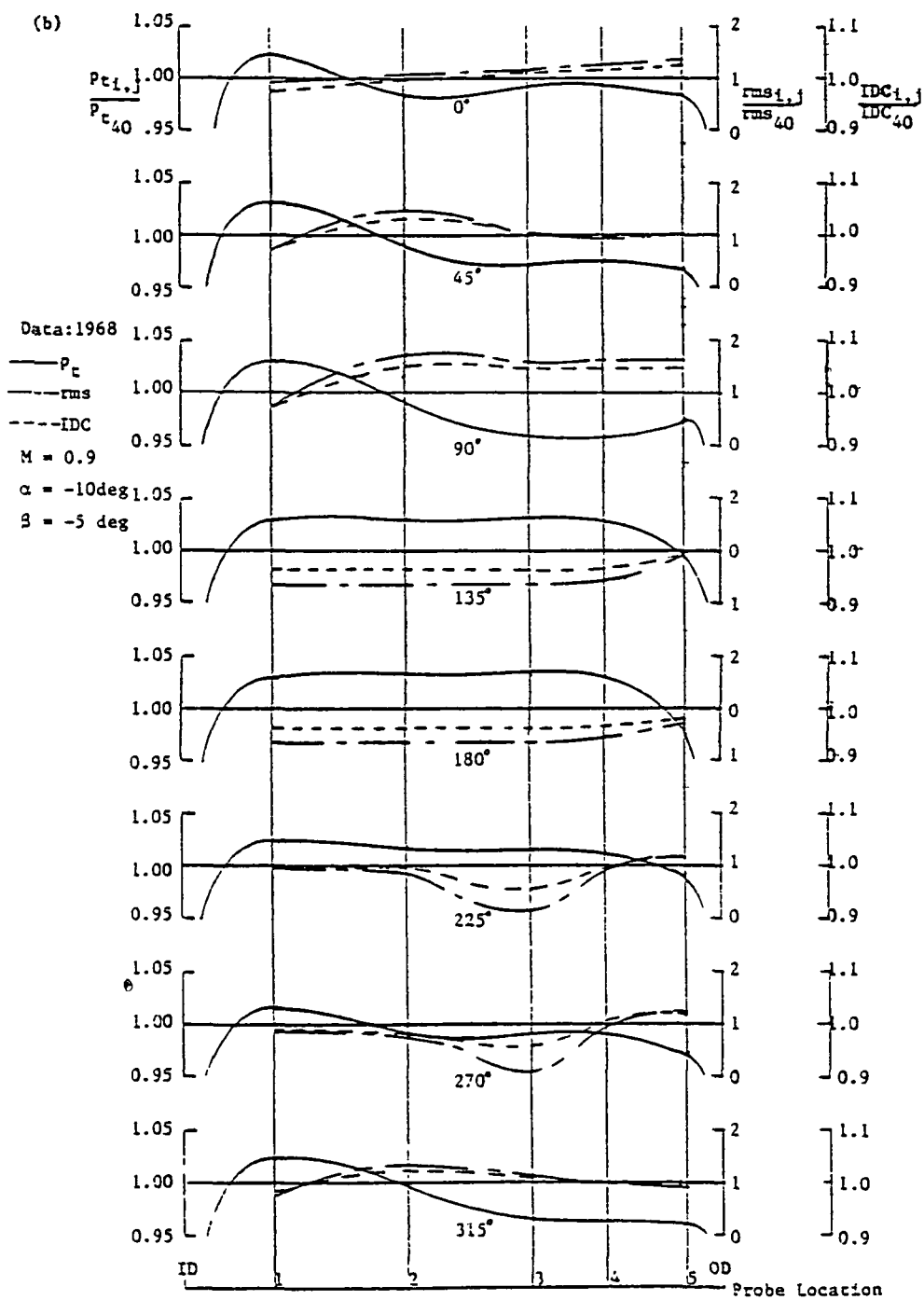


Figure 20. Continued

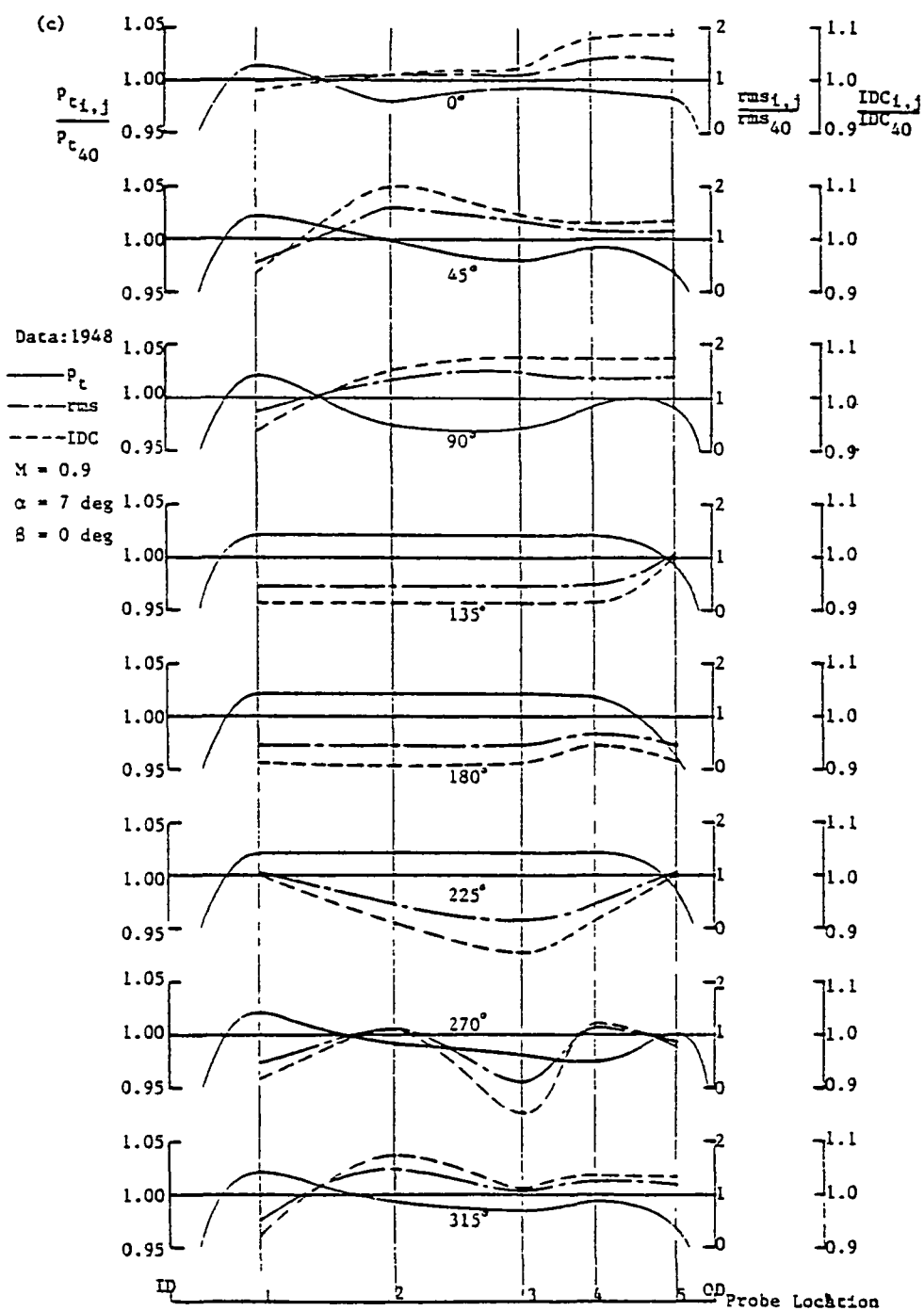


Figure 20. Continued

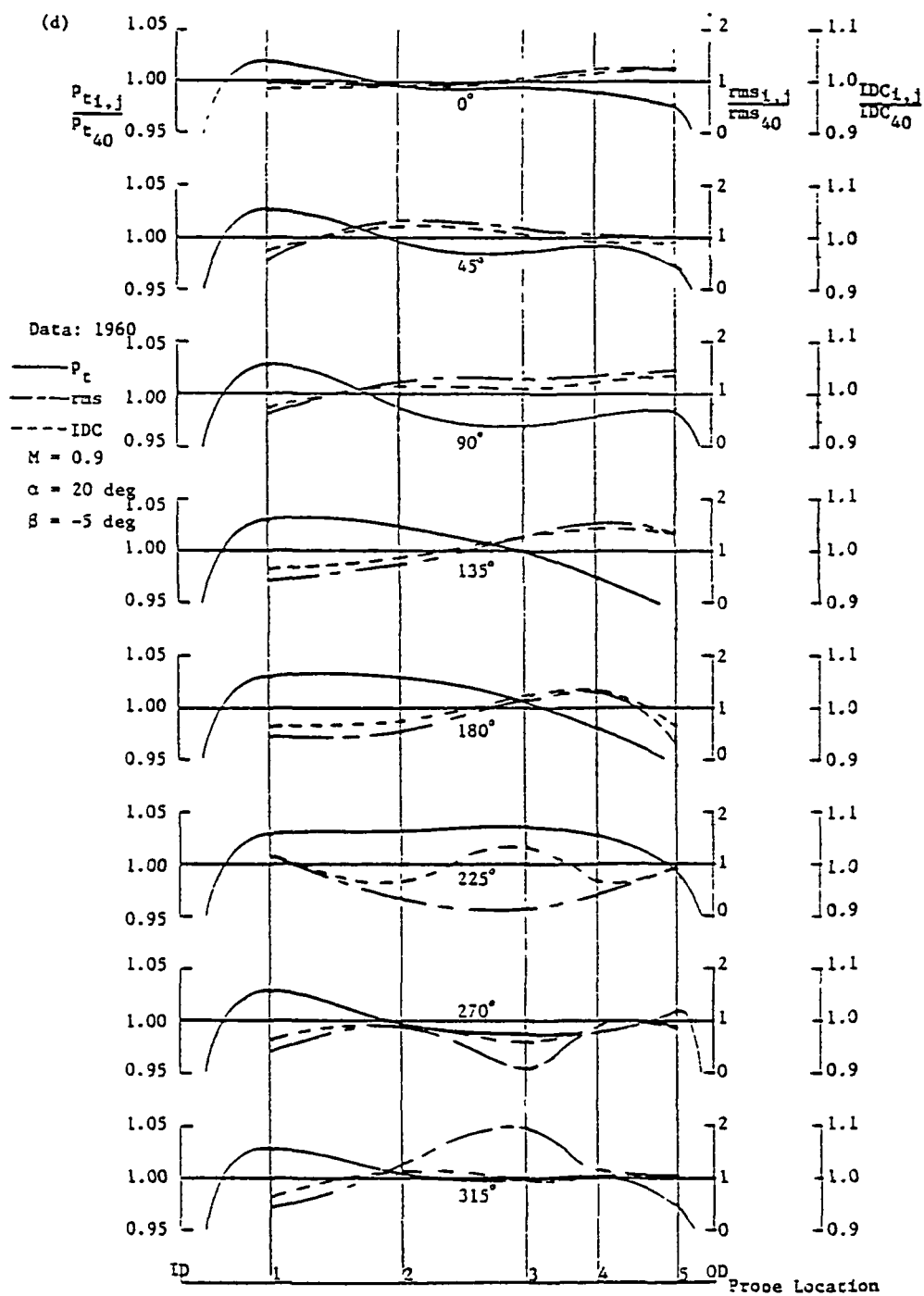


Figure 20. Continued

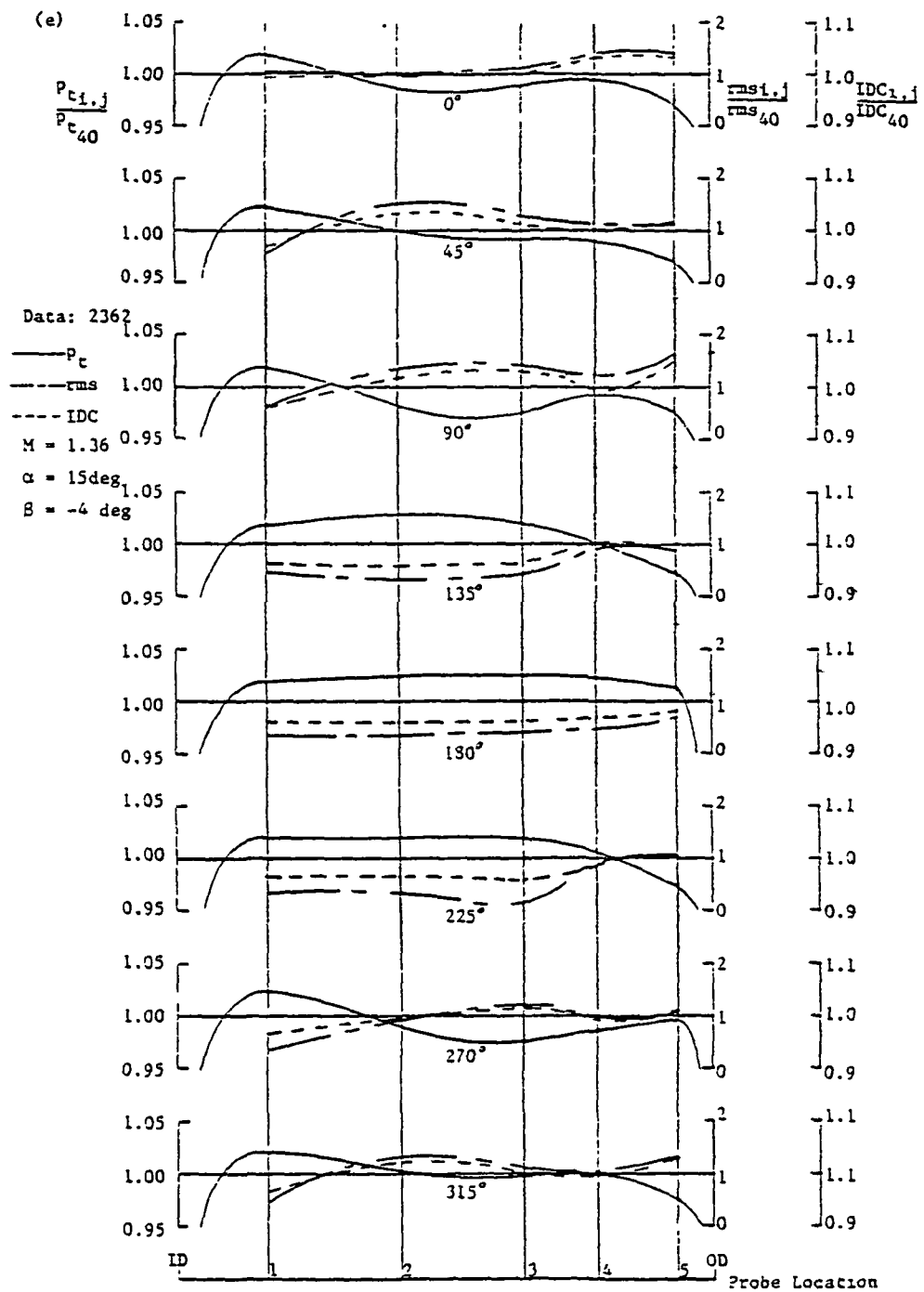


Figure 20. Continued

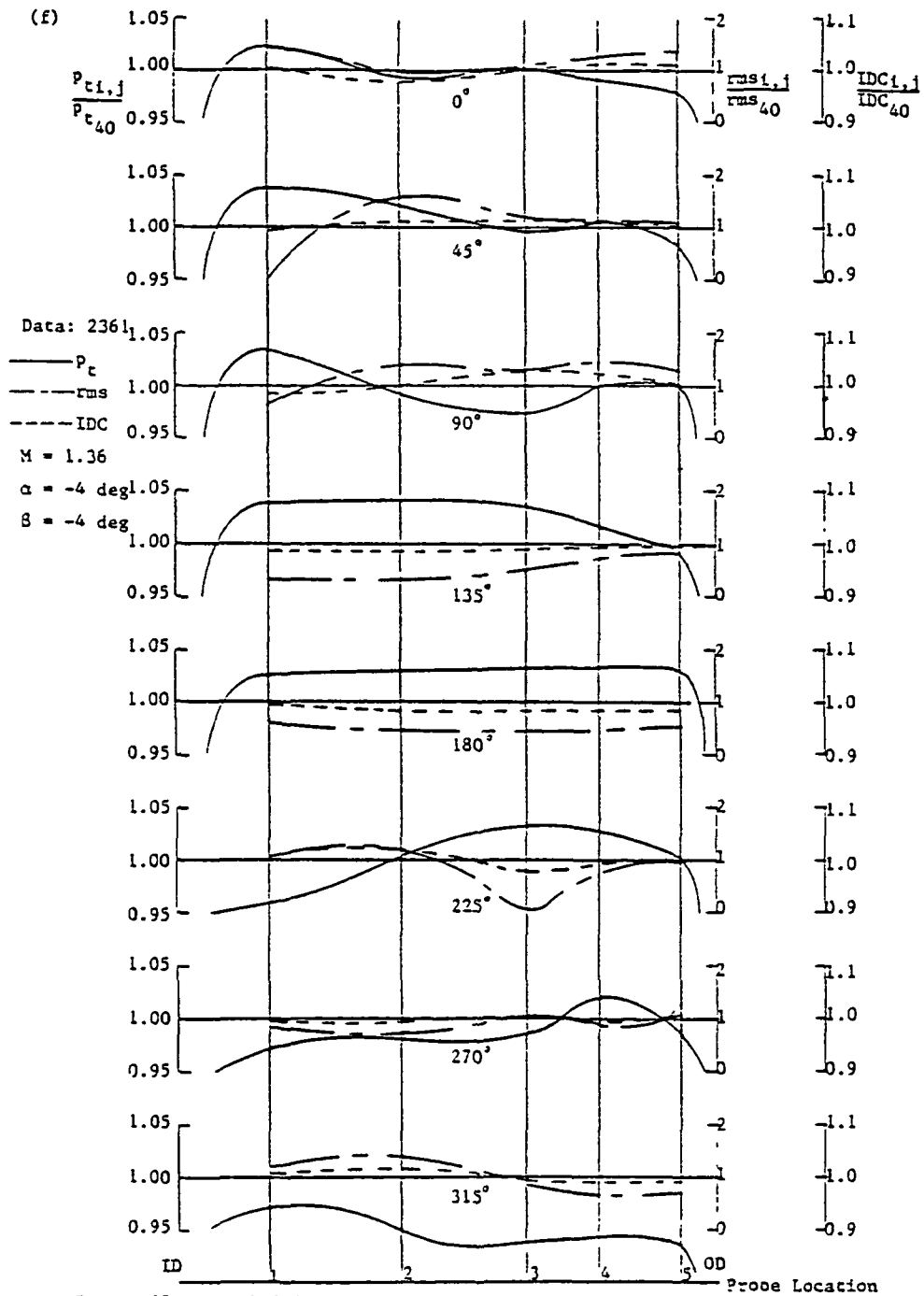


Figure 20. Concluded

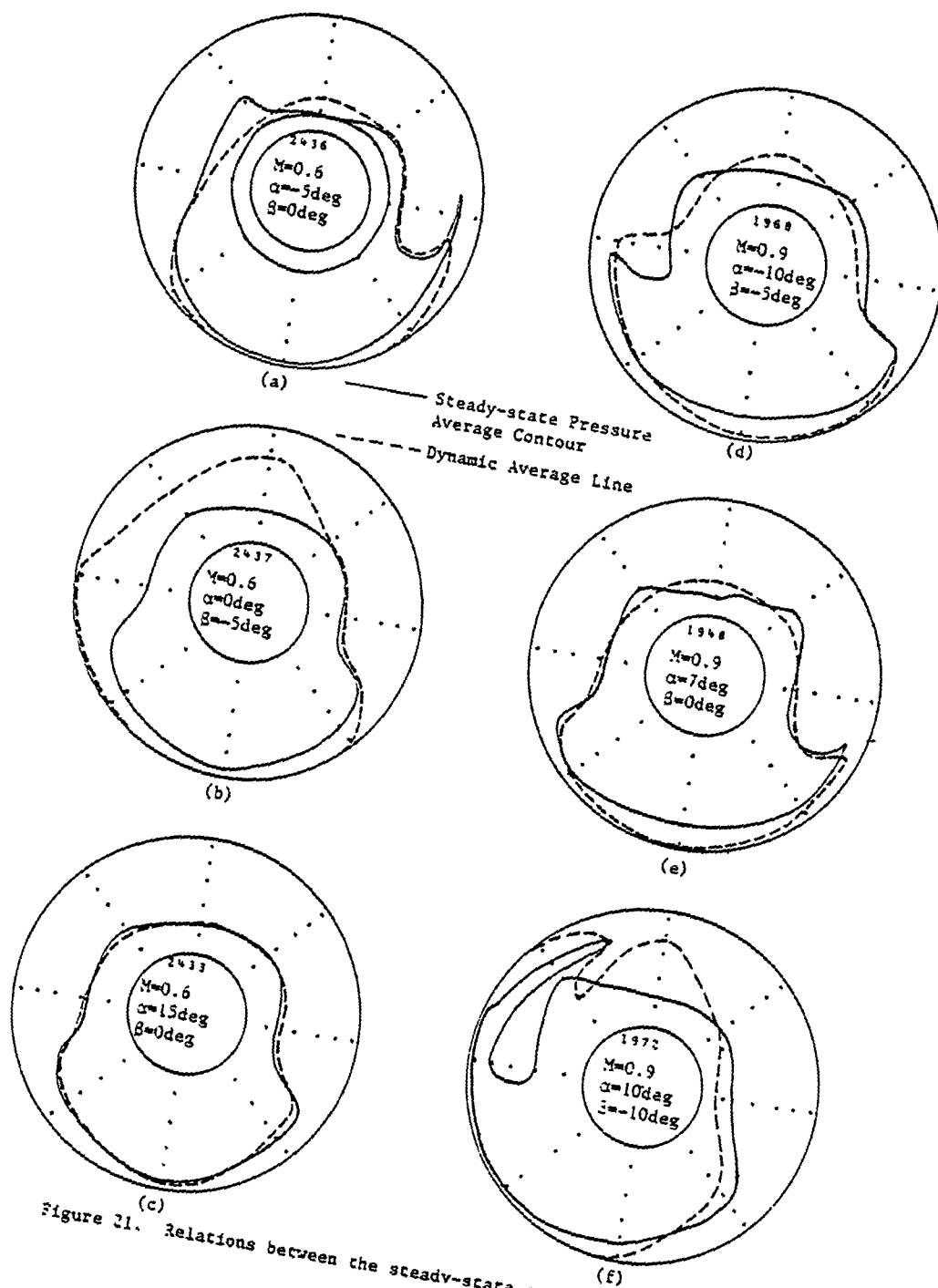


Figure 21. Relations between the steady-state and dynamic average contours



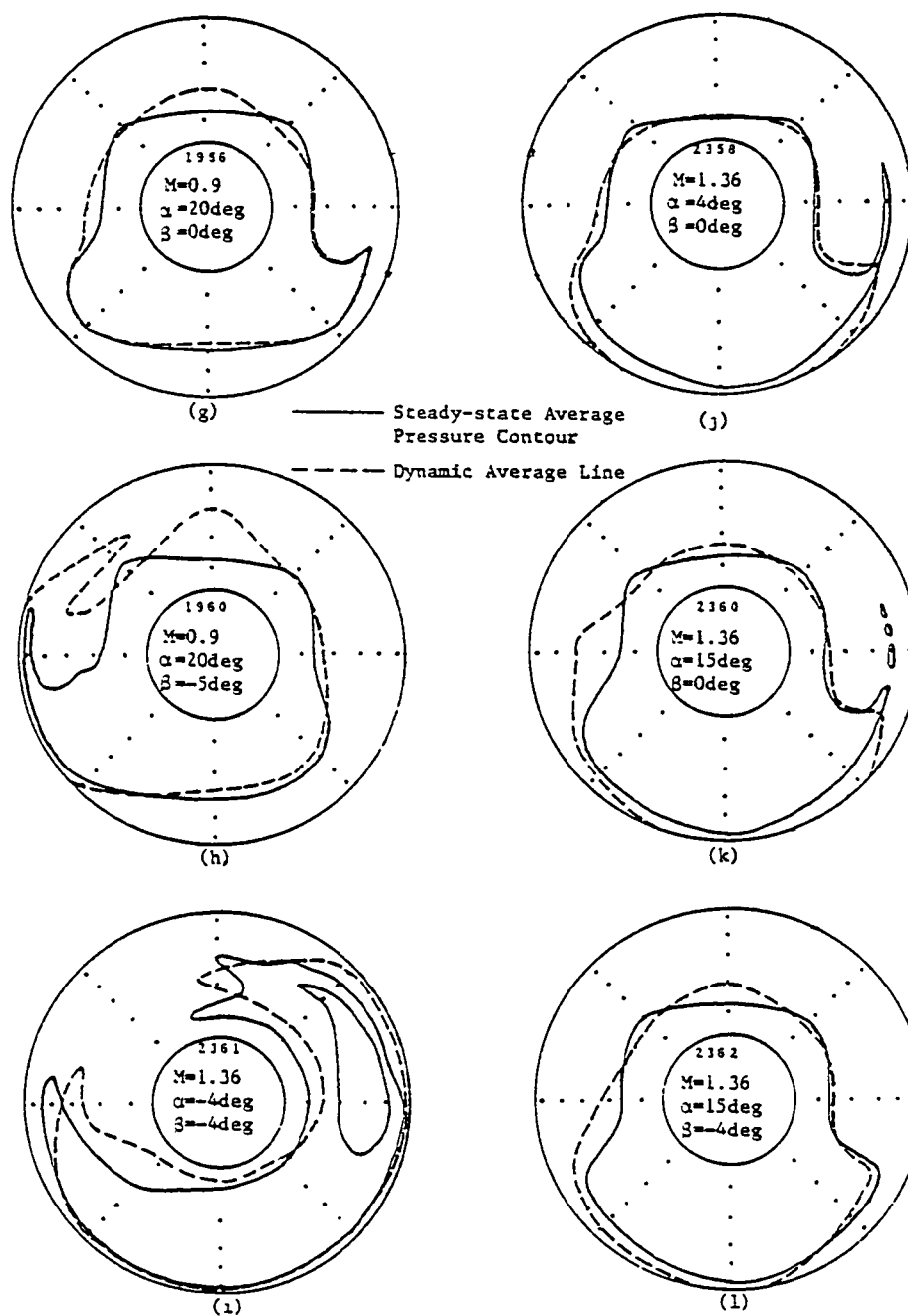


Figure 21. concluded

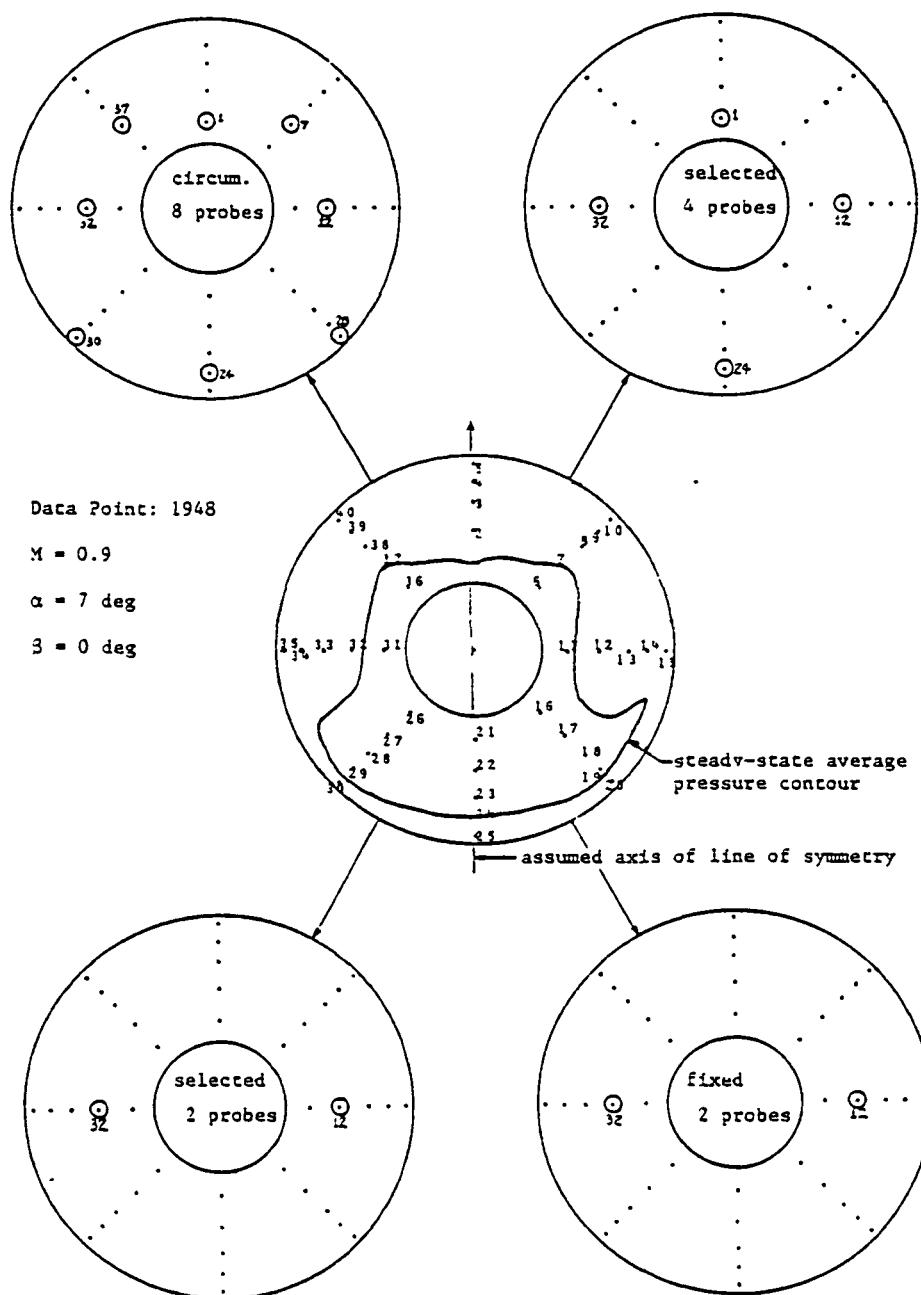


Figure 22. Example of dynamic probe selection using the general criteria

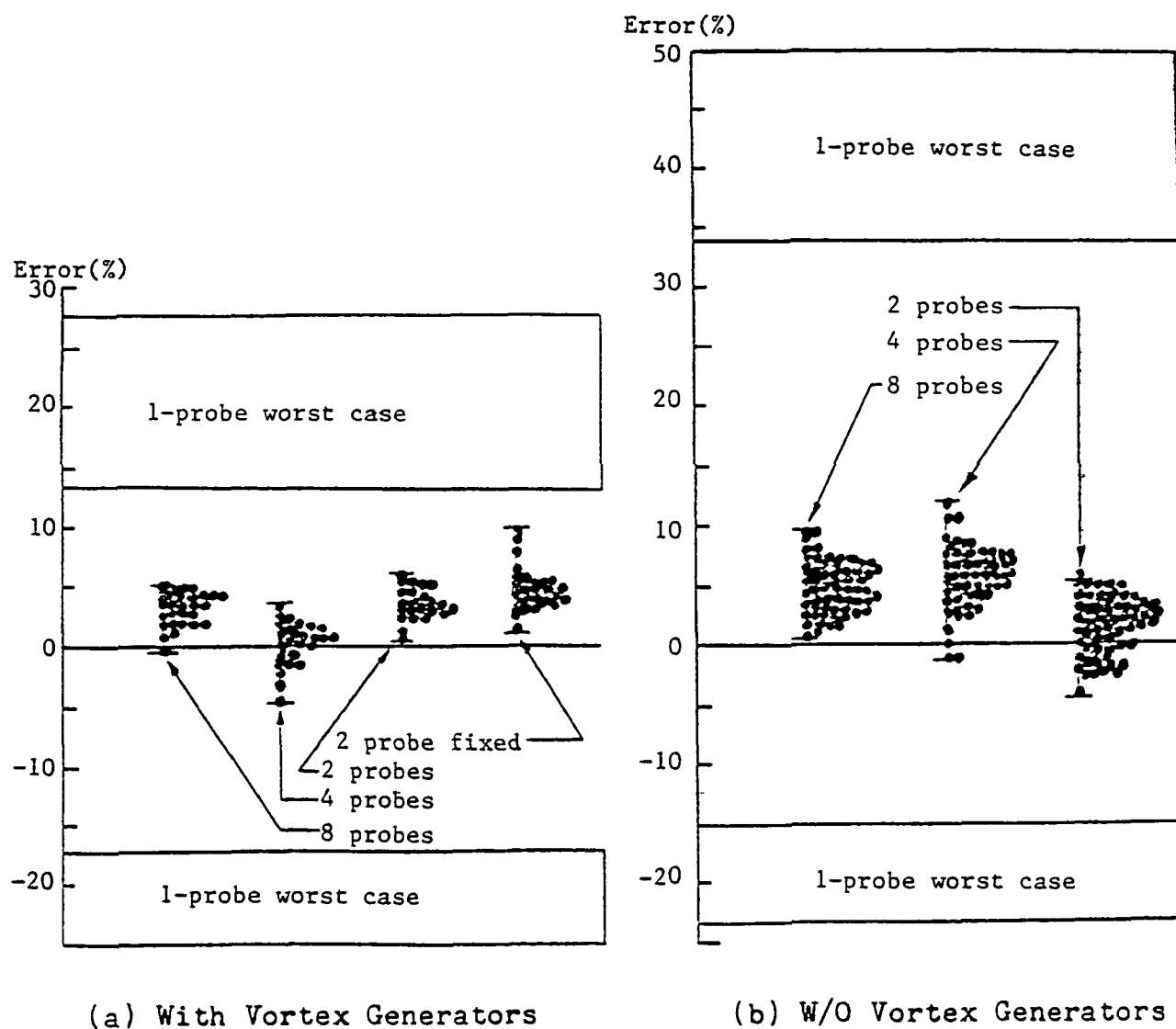


Figure 23. Accuracy of dynamic probes reduction (using the general criteria of dynamic probe selection) based on the 40-probe predicted peak distortion values

**PART II**

**INLET FLOW DYNAMIC DISTORTION  
PREDICTION -- WITHOUT RMS MEASUREMENTS**

## SUMMARY

A two-equation turbulence model, k- $\epsilon$  model, is used in the prediction of inlet flow dynamic distortion of jet aircraft based on steady state total pressure measurements only. This turbulence model is solved at the compressor face station by using a finite difference scheme. Total pressure rms level of the inlet flow is predicted by the turbulence model. The Melick statistical method is then employed to estimate the peak dynamic distortion based on the analytically predicted total pressure rms level.

A statistical method is developed for the estimation of boundary conditions for the turbulent equations.

In order to solve the set of nonlinear, coupled turbulent equations, an implicit formulation is utilized such that a set of discretized finite difference equations can be arranged into tridiagonal matrix equations for efficient numerical iterations.

Results of the prediction compare well with experimental measurements of subsonic, transonic and supersonic inlets under various flight conditions. The present method can be used in the preliminary inlet design phases to reduce the design costs.

## TABLE OF CONTENTS

	Page
1. LIST OF SYMBOLS .....	iii
2. INTRODUCTION .....	1
3. METHOD OF APPROACH .....	7
3.1 Mathematical Formulations .....	9
3.2 Boundary Conditions .....	11
3.3 Interfacing with the Melick Method for Predicting Peak Dynamic Distortions .....	17
4. NUMERICAL SCHEME .....	19
4.1 Grid System .....	19
4.2 Finite Difference Formulations .....	20
4.3 Numerical Convergence .....	24
5. SENSITIVITY STUDY .....	26
5.1 On the Velocity Distributions .....	26
5.2 On the Boundary Conditions .....	27
5.3 On the Parameters of the Turbulence Model .....	29
6. NUMERICAL RESULTS AND DISCUSSIONS .....	31
6.1 The HiMAT Inlet Data Set .....	31
6.2 The Melick Test Cases .....	34
6.3 Subsonic Inlet .....	35
6.4 Transonic Inlet .....	36
6.5 Supersonic Inlet .....	37
7. CONCLUSIONS .....	42
8. REFERENCES .....	45

APPENDIX A	Derivation of k- $\epsilon$ Turbulence Model .....	50
APPENDIX B	Measured Steady State Total Pressure and Velocity Distributions .....	54
APPENDIX C	Total Pressure RMS Level and Turbulent Kinetic Energy .....	58
APPENDIX D	Solution of Tridiagonal Matrix Equation ....	60

## 1. LIST OF SYMBOLS

<u>Symbols</u>	<u>Description</u>
A	Tridiagonal matrix
$C_p$	Specific heat at constant pressure
$C_k$	Correlation factor between boundary rms level and boundary total pressure loss
$C_{e1}$	Empirical constant of turbulence model
$C_{e2}$	Empirical constant of turbulence model
$C_\mu$	Empirical constant of turbulence model
$C'_\mu$	Empirical constant for Kolmogorov-Prandtl expression
$C_D$	Empirical constant for the expression of e
$E_r$	Relative percent error of each numerical iteration
F	Column matrix
$f_r$	Relaxation factor of the numerical scheme
G	Column matrix
$IDC_{max}$	Circumferential distortion factor, (see Table 1)
$K_{A2}$	Combined distortion factor, (see Table 1)
k	Turbulent kinetic energy (ft <sup>2</sup> /sec <sup>2</sup> )
L	Turbulence mixing length (ft)
$\log_{10}$	Logarithmic function with base 10
$M_o$	Free stream Mach number
ms	Mean square value of time variant total pressure (psi <sup>2</sup> )
$N_g$	Grid size parameter, (number of divisions between locations of total pressure probes)
$N_r$	Number of rings of total pressure probes



$N_p$	Number of rakes of total pressure probes
$\hat{P}$	Pressure, in pound per square inch (psi)
$P$	Nondimensional pressure
$R$	Gas constant, =1545.33 ft-lbf/lbmole-°R
$r$	Radial coordinate (ft) or recovery factor of total pressure probe
rms	Root mean square of time variant total pressure (psi)
$\overline{\text{rms}}$	Compressor-face-average rms level, $= \sqrt{\frac{1}{N_r \cdot N_p} \sum_1 \sum_j (\text{rms}_{i,j})^2}$
$T$	Air temperature (°R)
TN	Total number of non-boundary grid points
$U_2$	Compressor face average mean flow velocity (ft/sec)
$u$	Axial component of flow velocity (ft/sec)
$\overline{u'^2}$	Mean square value of axial velocity fluctuations (ft <sup>2</sup> /sec <sup>2</sup> )
$v$	Radial component of flow velocity (ft/sec)
$w$	Circumferential component of flow velocity (ft/sec)
$X$	Column matrix
$x$	Axial coordinate (ft)

#### Greek

$\alpha$	Angle of attack (degree)
$\beta$	Sideslip angle (degree)
$\gamma$	Specific heat ratio
$\epsilon$	Turbulent kinetic energy dissipation rate (ft <sup>2</sup> /sec <sup>3</sup> )

$\theta$	Circumferential coordinate (radian)
$\mu$	Absolute viscosity (slugs/ft-sec)
$\nu$	Kinematic viscosity, $= \mu/\rho$ (ft <sup>2</sup> /sec)
$\nu_t$	Turbulent viscosity, $= C_\mu k^2/\epsilon$ (ft <sup>2</sup> /sec)
$\rho$	Air density (slugs/ft <sup>3</sup> )
$\sigma$	Standard deviation
$\sigma_k$	Empirical constant of turbulence model
$\sigma_\epsilon$	Empirical constant of turbulence model
$\phi$	Arbitrary variable

#### subscripts

0	Free stream condition
1	Inlet throat flow condition
2	Compressor face flow condition
b	Boundary value, (i.e. near the wall)
i	Radial index or tensor index
j	Circumferential index or tensor index
m	Experimentally measured result
p	Analytically predicted result
s	Static condition
ss	Steady state value
t	Total or stagnant condition

### Superscripts

(n)	Indicate condition after the nth numerical iteration
*	Indicate solution of equations (22) & (23)
'	Time variant component
$\overline{\hspace{0.5em}}$ (over bar)	Time averaged value or compressor face average value

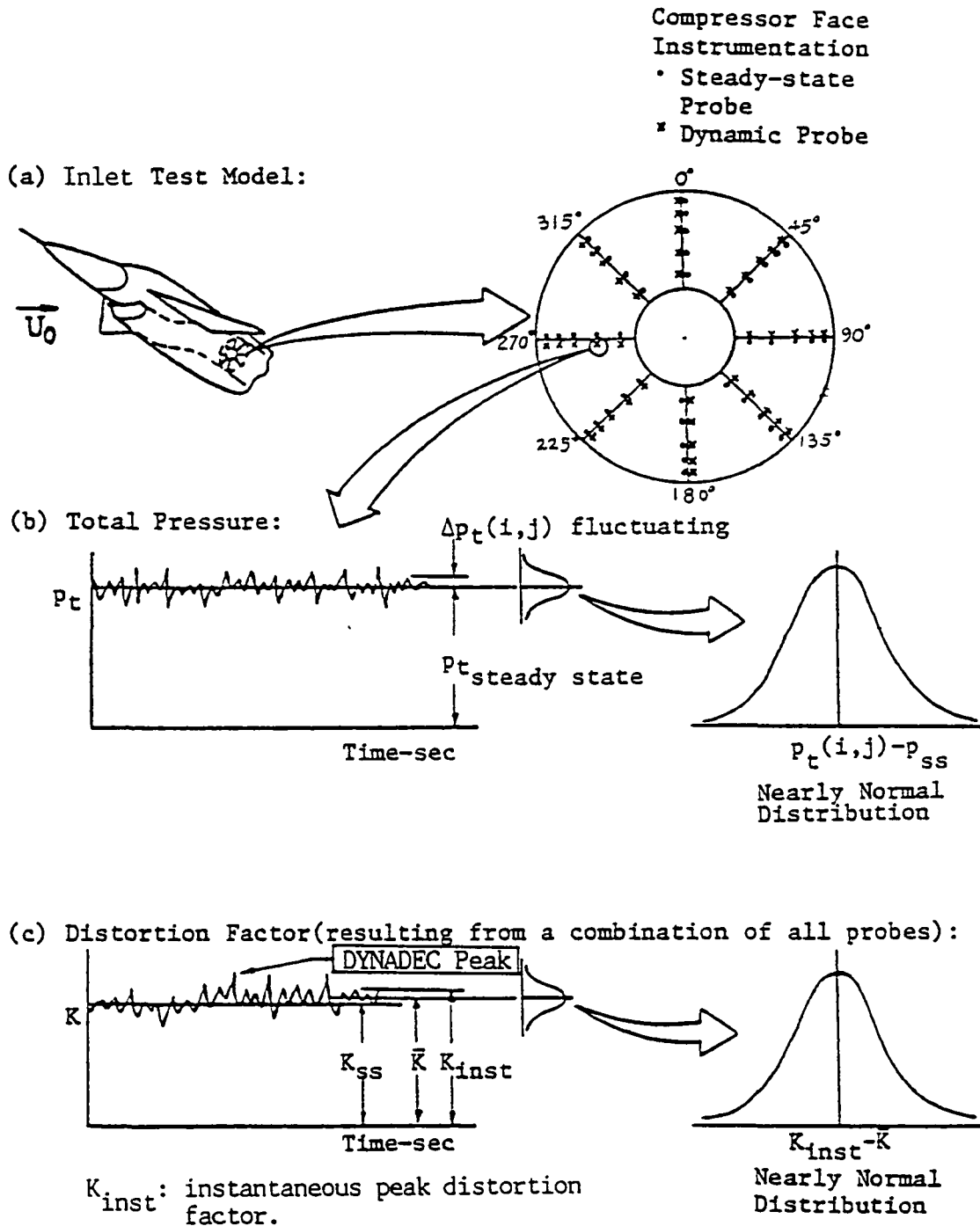
## 2. INTRODUCTION

Distortion of inlet flow plays an important role in determining the stable operating region of turbojet or turbofan engines, especially for highly maneuverable military aircraft. Time variant or dynamic distortion heightens this problem by creating peaks superimposed on top of the steady state distortion as illustrated in the adjacent figure. Thus, the occurrence of stall surge or other engine instabilities can not be readily predicted.

Traditionally, time variant total pressures of the inlet flow measured in the test are analyzed by several methods. These methods can be classified into two categories.

In the first category, time variant total pressures measured by high response total pressure probes over the compressor face are recorded in the test for a specified period of time. Then, these data are screened in the Dynamic Data Editing and Computing System (DYNADEC) deterministically based on a certain distortion factor (ref.1), (definitions of some distortion factors are given in Table 1). From the screening procedure, a maximum instantaneous peak distortion pattern corresponding to a maximum instantaneous peak distortion factor is determined (refs. 1,2). This is the most accurate method, but it is also the most costly and time consuming method. It will be the basis for data comparisons in this work.

ILLUSTRATION OF SOME FEATURES OF THE TIME VARIANT TOTAL PRESSURES AND DYNAMIC DISTORTION:



In the second category, the peak dynamic distortion is predicted using some form of statistical analysis (refs. 3, 4, 5, 6, 7, 8) which is more economic than the DYNADEC approach. There are three major statistical approaches. The first one, due to Jacocks, et al., uses Gumbel's extreme value theorem to extrapolate the peak dynamic distortion within a specified time period from the first short time segment of deterministic information (ref. 4). The second approach, due to Motycka, utilizes a random number generator to simulate the total pressure fluctuations at each probe based on the measured steady state total pressures and the measured total pressure rms levels. Time variant distortion factors are calculated using the generated instantaneous total pressures, from which the peak dynamic distortion is determined (ref. 5). The third approach, developed by Melick, et al., is a modeling approach that postulates that the dynamic effects in the inlet flow is totally attributed to the pressure disturbances caused by a sequence of convecting vortices in the inlet duct. The peak dynamic distortion is determined from this physical model and its statistical properties. Filtered and Unfiltered total pressure rms levels are used to identify main variables of the vortex flow model (ref. 3, 6). Among all the methods in this category, the Melick method is the most efficient in terms of numerical analysis whereas it is not as accurate as the Motycka method in predicting the peak dynamic distortion patterns (ref. 7).

Since the forementioned approaches require measurements in the time variant total pressures using high response total pressure probes, design of high performance inlet is costly in terms of instrumentation, analysis and testing time. Thus, it is highly desirable to develop analytical means for predicting peak dynamic distortions without dynamic measurements.

There are analytical methods of predicting steady state distortions but not the dynamic peak distortions. Also, these analytical methods are limited to qualitative predictions only, since the total pressure losses through the inlet duct can not be well predicted. A summarized review of the current analytical methods is included in reference 9. Reference 10 provides an application of the time marching finite volume method to the prediction of steady, quasi-inviscid inlet duct flows.

The present work makes the first attempt ever to predict the peak dynamic distortion based on the steady state total pressure measurements at the compressor face station. Once the approach of the present work is successful, it would be highly encouraging to extend the present analysis to a pure dynamic distortion predicting technique in the future research, without any experimental measurement, by incorporating the present analysis in an existing steady state distortion prediction code. This would allow early identification of possible dynamic distortion problems before the first wind tunnel model is

built.

In the present work, an analytical method of predicting the dynamic peak distortion, based on the steady state total pressure measurements, is proposed and evaluated. First, axial velocity distributions of the inlet flow are calculated from the measured steady state total pressures. A two-equation turbulence model, k- $\epsilon$  model, is then employed to solve for turbulent kinetic energy distributions over the compressor face using the calculated velocity distributions and statistically estimated boundary conditions. The total pressure rms levels are computed from the predicted turbulent kinetic energy. Finally, the dynamic peak distortions are estimated by the Melick program using the predicted total pressure rms levels.

In solving the turbulent equations which are coupled and nonlinear, a finite difference scheme is used to discretize these equations such that tridiagonal matrix equations are obtained for successive line relaxation iterations. Effects of the relaxation factor on the convergence of the numerical scheme are examined from which an optimum computational scheme is determined.

Sensitivity study of the variables and parameters of the turbulent equations to the final results is also included to reveal how the solutions vary with the variables and parameters.

Results of the present method are compared with those of the DYNADEC for five inlet data sets. These data sets



cover a range of Mach numbers from 0.6 to 2.5, a range of angles of attack from -10 degree to 25 degree and a range of angles of sideslip from 8 degree to -10 degree. Inlet configurations involved in these investigations are illustrated in Figures 1 through 5.

Major objectives of the present study are: (1) to provide an efficient tool for the preliminary inlet design and development in which only the steady state total pressure measurements are required; (2) to demonstrate that the peak dynamic distortions can be predicted by using the k- $\epsilon$  turbulence model; and (3) to suggest possible future studies in improving the analysis of the inlet flow dynamic distortion.

### 3. METHOD OF APPROACH

In the present analysis, a semi-empirical approach in predicting dynamic peak distortion of the inlet flow, based on compressor face steady-state total pressure measurements, is developed under the following major assumptions: (1) turbulent characteristics of the inlet flow, at the compressor face station, can be represented by an incompressible, high Reynolds number, two-equation turbulence model -- k- $\epsilon$  model (ref. 11); (2) the inlet flow near the compressor face is dominated by the axial velocity component such that secondary flow (flow components that are not parallel to the inlet duct) effect can be neglected; (3) streamwise variation of the turbulent characteristics is small and can be ignored from the turbulence model; and (4) boundary (near-wall) total pressure rms level is proportional to the total pressure loss near the wall of the inlet duct so that a statistical correlation between the measured steady-state total pressures and the boundary total pressure rms level can be developed using the HiMAT data set.

Assumption (1) is justifiable based on the following reasons: (a) compressibility effect on the turbulent characteristics of the inlet flow can be neglected since the flow near the compressor face station is always at low-subsonic speed; (b) the k- $\epsilon$  turbulence model is well tested for many types of turbulent flow such as turbulent

boundary layer along a flat plate (refs. 11, 12, 13, 14, 15, 16), turbulent flow inside rectangular channel or circular pipe (refs. 17, 18, 19, 20), free-shear turbulent flows (refs. 21, 22, 23) and other applications (refs. 24, 25); (c) although the accuracy of the k- $\epsilon$  model is comparable to other two-equation turbulence model, such as the one developed by Rotta and Vollmers (refs. 26, 27), it is found that the k- $\epsilon$  model is more efficient numerically.

Despite the fact that assumptions (2) and (3) may not be realistic from a theoretical point of view, for some inlet configurations and flight conditions, these two assumptions are imposed because there is normally no flow direction or streamwise turbulence information available.

It will be shown later that assumption (4) makes a major contribution to the present analysis. Assumption (4) is made in order to develop a reliable method for estimating the boundary conditions for the turbulent model.

Note that the present analysis does not take into account the effect of boundary layer bleed immediately upstream of the compressor face since turbulent structure of the inlet flow would be quite different in that case. Therefore, it is expected that the present model may not be suitable for inlet flow with strong boundary layer bleed.

Based on these four assumptions, developments of the mathematical formulations and the method of estimating the boundary conditions are described in the following two sections.

### 3.1 Mathematical Formulations

Partial differential equations of the k-ε turbulent model suitable for incompressible high Reynolds number turbulent pipe flow (ref. 12) can be written as:

$$\begin{aligned} \bar{u} \frac{\partial k}{\partial x} + \bar{v} \frac{\partial k}{\partial r} + \frac{\bar{w}}{r} \frac{\partial k}{\partial \theta} = \frac{1}{r} \frac{\partial}{\partial r} \left( \frac{C_\mu k^2}{\sigma_k \epsilon} r \frac{\partial k}{\partial r} \right) + \frac{1}{r^2} \frac{\partial}{\partial \theta} \left( \frac{C_\mu k^2}{\sigma_k \epsilon} \frac{\partial k}{\partial \theta} \right) + \\ + C_\mu \frac{k^2}{\epsilon} \left[ \left( \frac{\partial \bar{u}}{\partial r} \right)^2 + \frac{1}{r^2} \left( \frac{\partial \bar{u}}{\partial \theta} \right)^2 \right] - \epsilon \end{aligned} \quad (1)$$

$$\begin{aligned} \bar{u} \frac{\partial \epsilon}{\partial x} + \bar{v} \frac{\partial \epsilon}{\partial r} + \frac{\bar{w}}{r} \frac{\partial \epsilon}{\partial \theta} = \frac{1}{r} \frac{\partial}{\partial r} \left( \frac{C_\mu k^2}{\sigma_\epsilon \epsilon} r \frac{\partial \epsilon}{\partial r} \right) + \frac{1}{r^2} \frac{\partial}{\partial \theta} \left( \frac{C_\mu k^2}{\sigma_\epsilon \epsilon} \frac{\partial \epsilon}{\partial \theta} \right) + \\ + C_{\epsilon 1} C_\mu k \left[ \left( \frac{\partial \bar{u}}{\partial r} \right)^2 + \frac{1}{r^2} \left( \frac{\partial \bar{u}}{\partial \theta} \right)^2 \right] - C_{\epsilon 2} \frac{\epsilon^2}{k} \end{aligned} \quad (2)$$

where  $\bar{u}$ ,  $\bar{v}$  and  $\bar{w}$  are time-averaged velocity components in axial, x, radial, r, and circumferential,  $\theta$ , directions respectively. k represents turbulent kinetic energy,  $\epsilon$  is turbulent kinetic energy dissipation rate,  $\frac{\partial \bar{u}}{\partial r}$  is radial velocity gradient,  $\frac{\partial \bar{u}}{\partial \theta}$  is circumferential velocity gradient and the five empirical constants are:

$$\sigma_k = 1.0$$

$$\sigma_\epsilon = 1.3$$

$$C_\mu = 0.09$$

$$C_{\epsilon 1} = 1.45$$

$$C_{\epsilon 2} = 2.0$$

Detailed derivations of equations (1) and (2) are included in Appendix A.

Using assumptions (2) and (3), the left hand side of equations (1) and (2) can be eliminated. This results in:

$$\frac{1}{r} \frac{\partial}{\partial r} \left( \frac{C_u k^2}{\sigma_k \epsilon} r \frac{\partial k}{\partial r} \right) + \frac{1}{r^2} \frac{\partial}{\partial \theta} \left( \frac{C_u k^2}{\sigma_k \epsilon} \frac{\partial k}{\partial \theta} \right) + C_u \frac{k^2}{\epsilon} \left[ \left( \frac{\partial \bar{u}}{\partial r} \right)^2 + \frac{1}{r^2} \left( \frac{\partial \bar{u}}{\partial \theta} \right)^2 \right] - \epsilon = 0 \quad (3)$$

$$\frac{1}{r} \frac{\partial}{\partial r} \left( \frac{C_u k^2}{\sigma_\epsilon \epsilon} r \frac{\partial \epsilon}{\partial r} \right) + \frac{1}{r^2} \frac{\partial}{\partial \theta} \left( \frac{C_u k^2}{\sigma_\epsilon \epsilon} \frac{\partial \epsilon}{\partial \theta} \right) + C_{\epsilon 1} C_u k \left[ \left( \frac{\partial \bar{u}}{\partial r} \right)^2 + \frac{1}{r^2} \left( \frac{\partial \bar{u}}{\partial \theta} \right)^2 \right] - C_{\epsilon 2} \frac{\epsilon^2}{k} = 0 \quad (4)$$

In equations (3) and (4), the radial and circumferential velocity gradients are required as inputs which can be obtained from the measured steady-state total pressures. First, the axial flow velocity at each pressure probe location is computed from the steady-state total pressure measurement by the following equation:

$$\frac{\bar{u}}{U_2} \approx \sqrt{\frac{1}{\gamma \rho_s U_2^2} \left( \frac{\gamma}{\gamma - 1} \right) \left( \frac{P_t}{\rho_t / \rho_s} - P_s \right)} \quad (5)$$

where  $U_2$  is face-average flow velocity,  $\rho_t$  and  $\rho_s$  are total and static density respectively,  $P_t$  and  $P_s$  are total and static pressure respectively and  $\gamma = 1.4$ . Derivation of equation (5) is described in more detail in Appendix B.

A cubic spline interpolation subroutine is then employed to calculate and interpolate the radial and circumferential velocity gradients at every computational nodal point on the compressor face. An artificial smoothing

routine is also used to account for large velocity variations near the wall.

After the solution of turbulent kinetic energy is obtained from equations (3) and (4), total pressure rms level is computed from the turbulent kinetic energy using equation (6).

$$rms \approx \frac{P_t (\gamma - 1)}{\hat{P}_{t2} \gamma} \sqrt{(2 \bar{u}^2 k / 3) + k^2} \quad (6)$$

Note that rms has been normalized by the face-average total pressure (in psi),  $\hat{P}_{t2}$ . Appendix C describes the detailed derivation of equation (6). This equation is only an approximation since the relation of isotropic turbulence has been assumed in the derivation.

### 3.2 Boundary Conditions

In this section, a statistical correlation between the boundary total pressure rms level and the steady-state total pressure is obtained by applying assumption (4) to the HiMAT data set. Assumption (4) can also be expressed in the following equation:

$$C_k = \frac{(\text{rms})_{\text{ring - 5 - average}}}{1 - (\hat{P}_{t2})_{\text{ring - 5 - average}}} = \frac{rms_b}{1 - (\hat{P}_{t2})_b} \quad (7)$$

where  $\text{rms}_b = (\text{rms})_{\text{ring-5-average}}$ ,

$$(P_{t2})_b = (P_{t2})_{\text{ring-5-average}}$$

$C_k$  stands for a correlation factor and  $(P_{t2})_b$  and  $\text{rms}_b$  have been normalized by  $\hat{P}_{t0}$  and  $\hat{P}_{t2}$  respectively.  $\hat{P}_{t0}$  and  $\hat{P}_{t2}$  are free stream and face-average total pressure respectively (in psi).

Obviously,  $C_k$  is not a constant due to the fact that different turbulent structures of the inlet flow are produced in different flight conditions. Thus, a different proportion of the turbulent kinetic energy in the total energy loss is expected for different turbulent structures. Nevertheless, by examining the HiMAT inlet data set, there is a fairly consistent relation between the turbulence level and the face-average total pressure loss,  $(1-P_{t2})$ . From this clue, a statistical analysis between  $C_k$  and the face-average total pressure loss is done from which a second correlation between  $C_k$  and  $(1-P_{t2})$  is extracted from the HiMAT data set.

Figure 6 shows a linear regression of  $\log_{10} C_k$  on  $\log_{10}(1-P_{t2})$  for the HiMAT inlet data at subsonic and transonic speed. Data at supersonic speed will be handled differently, as will be discussed later, for the effect of inlet shock system. From Figure 6, the equation of a regression line is obtained. This is expressed by equation (8).

~~PRECEDING PAGE BLANK NOT FILMED~~

$$\log_{10} C_k = -0.9393 + (-0.2587) \log_{10}(1 - P_{t2}) \quad (8)$$

or,

$$C_k = 0.115 (1 - P_{t2})^{-0.2587} \quad (9)$$

It is shown clearly from Figure 6 that the regression line has a negative slope. This reveals the fact that the higher the turbulent level of the inlet flow the higher the total energy that is dissipated through turbulent mixing and redistribution up stream of the compressor face.

Tests of this regression line on other inlet data is also illustrated in Figure 6. It can be seen that this regression line, equation (8), represents the inlet flow turbulent characteristics of other inlet configurations equally well.

The same analysis is applied to supersonic cases of the HiMAT data set without accounting for the effect of inlet shock system. This is shown in Figure 7, which reveals discrepancy between equation (8) and the test data. The reason for this discrepancy is that the total pressure loss through the inlet shock system is due to the shock compression process which is not responsible for the major part of the generation of turbulent kinetic energy.

In order to obtain a consistent correlation between  $C_k$



and the steady-state total pressure for supersonic cases, equation (7) is revised to be:

$$C_k = \frac{rms_b}{P_{t1} - (P_{t2})_b} \quad (10)$$

where  $P_{t1}$ , normalized by the free stream total pressure, stands for the total pressure recovery through the inlet shock system. If  $P_{t1}$  is not measured in the test, it can be estimated from a set of curves of maximum total pressure recovery for 2-dimensional oblique shock and conical shock systems as shown in Figure 8 (ref. 28).

Again, a correlation between  $C_k$  and the face-average total pressure loss after inlet shock system,  $(P_{t1} - P_{t2})$ , for HiMAT inlet data at supersonic speed, is shown in Figure 9. Corrections for the effect of inlet shock system are obtained from the curve of one 2-dimensional oblique shock in Figure 8. A revised version of equation (8) is also shown in Figure 9. Equation (11) is the revised version of equation (8).

$$\log_{10} C_k = -0.9393 + (-0.2587) \log_{10} (P_{t1} - P_{t2}) \quad (11)$$

or,

$$C_k = 0.115 (P_{t1} - P_{t2})^{-0.2587} \quad (12)$$

In Figure 9, equation (11) represents higher value in  $C_k$  than the data points. This is due to the fact that the shock correction curves given in Figure 8 is the least amount of correction that a inlet can possibly attain under any flight condition. In reality the total pressure recovery through an inlet shock system is lower than that obtained from Figure 8 such that the mean of the data points in Figure 9 would be very close to equation (11). However, it is feasible to use equation (11) and Figure 8 for the estimation of  $C_k$  since a slight over estimation of  $C_k$  can be attained. This means that the boundary rms level would be slightly over estimated which is desirable for a conservative design process.

The validity of equation (11) is tested using other inlet configuration of Melick's supersonic test cases as shown in Figure 9. The correction for the effect of the inlet shock system is also accounted for by using Figure 8. Good correlation between equation (11) and the test data is shown clearly in Figure 9.

Conclusion of the statistical study described in this section can be summarized by the following equations which are combinations of equations (7) and (9), and equations (10) and (12).

For subsonic and transonic cases:

$$rms_b = 0.115 (1 - P_{t2})^{-0.2587} \cdot [1 - (P_{t2})_b] \quad (13)$$

For supersonic cases:

$$rms_b = 0.115 (P_{t1} - P_{t2})^{-0.2587} \cdot [P_{t1} - (P_{t2})_b] \quad (14)$$

Also, equation (6) can be written as:

$$k \approx -\frac{\bar{u}^2}{3} + \sqrt{\frac{\bar{u}^2}{9} + \left[ \frac{rms_{t2} \gamma}{\rho_t (\gamma - 1)} \right]^2} \quad (15)$$

Using equations (13), (14) and (15), boundary conditions for the turbulent kinetic energy,  $k$ , of the  $k$ - $\epsilon$  model can be estimated.

Note that the estimated boundary rms level is an average value near the wall rather than a circumferential distribution as the actual measured rms level would be. It is not only that there is no consistent rule for estimating the circumferential rms level distribution but that the use of an average boundary rms level predicts almost the same face-average rms level as that predicted by using the exact boundary rms level distribution. This will be described

later in more detail in section 5.2.

Boundary condition for the turbulent kinetic energy dissipation rate,  $\epsilon$ , is also required in order to solve equations (3) and (4). This boundary condition can be obtained by applying a wall function approach (ref. 11, 12, 17, 18) to the k-equation, equation (3). The wall function approach states that the turbulent energy generation term, the third term of equation (3), and the turbulent energy dissipation term, the last term of equation (3), are almost equal near the wall. The following equation supplements this statement.

$$\epsilon \approx \sqrt{C_\mu} k \sqrt{\left(\frac{\partial \bar{u}}{\partial r}\right)^2 + \frac{1}{r^2} \left(\frac{\partial \bar{u}}{\partial \theta}\right)^2} \quad (16)$$

Using equation (16), the boundary condition for the turbulent kinetic energy dissipation rate can be estimated.

### 3.3 Interfacing with the Melick Method for Predicting Peak Dynamic Distortions

Besides the compressor face steady-state total pressures and the face-average total pressure rms level, a ratio of the filtered to unfiltered mean square (ms) levels and the corresponding cut-off frequency are required as inputs for the prediction of dynamic peak distortion factors by using the Melick method (refs. 3, 6). Unless this ms

ratio and the cut-off frequency are determined experimentally, an approximation is suggested here. It is learned by examining the available test data sets that the ratio of filtered to unfiltered ms levels is around 0.5 at a cut-off frequency ranging from 800 hz to 1000 hz. This corresponds to fairly constant frequency response of the turbulent characteristics of the inlet flow. Also, it is mentioned in reference 3 that the prediction of dynamic peak distortion is not very sensitive to the ms ratio and the cut-off frequency. In the present analysis, an ms ratio of 0.5 at a cut-off frequency of 1000 hz are used for every data set. It will be shown from the results that this approximation is reasonable.

#### 4. NUMERICAL SCHEME

Since equations (3) and (4) are coupled and nonlinear, a finite difference numerical scheme is used to discretize these two equations (refs. 29, 30, 31). A computational grid system and a set of finite difference equations are arranged in such a way that an implicit numerical scheme is obtained. A set of tridiagonal matrix equations are also attained for efficient successive iterations. A relaxation factor and grid size parameter are determined in the analysis of numerical convergence in section 4.3.

##### 4.1 Grid System

A grid system based on the locations of total pressure probes on the compressor face is illustrated in Figure 10(a). Figure 10(a) shows a 40-probe compressor face instrumentation configuration. For better finite difference approximation, finer grids are used by dividing the space between probes into  $N_g$  equal spaces.  $N_g$ , an integer, is designated as the grid size parameter. In this way, smaller grid size can be attained near the wall where larger variation in turbulent characteristics is expected (ref. 18). Total number of non-boundary grid points of the grid system can be calculated by the following relation.

$$TN = (N_g)^2 \cdot N_r \cdot N_p \quad (17)$$

where TN denotes the total number of non-boundary grid points,  $N_g$  is the grid size parameter,  $N_r$  and  $N_p$  represent the number of rings and the number of rakes of the total pressure probes respectively.

#### 4.2 Finite Difference Formulations

In this section, a set of discretized difference equations are derived by applying central difference scheme to equations (3) and (4). Referring to Figure 10(b), the central difference equations, in radial (r) and circumferential ( $\theta$ ) directions, for any variable  $\phi$  about point p can be written as (ref. 30):

$$\frac{\partial \phi}{\partial r} \approx \frac{\Delta r_i}{\Delta r_{i-1} + \Delta r_i} \left( \frac{\phi_{i,j} - \phi_{i-1,j}}{\Delta r_{i-1}} \right) + \frac{\Delta r_{i-1}}{\Delta r_{i-1} + \Delta r_i} \left( \frac{\phi_{i+1,j} - \phi_{i,j}}{\Delta r_i} \right) \quad (18)$$

$$\frac{\partial \phi}{\partial \theta} \approx \frac{\phi_{i,j+1} - \phi_{i,j-1}}{2 \Delta \theta} \quad (19)$$

Note that an irregular grid spacing has been assumed in the radial, r, direction.

Applying equations (18) and (19) to equations (3) and (4), by changing  $\phi$  to k and  $\epsilon$  respectively, the following finite difference equations can be obtained.

$$A_{i,1} k_{i-1,j} + A_{i,2} k_{i,j} + A_{i,3} k_{i+1,j} = C_i \quad (20)$$

$$B_{i,1} \epsilon_{i-1,j} + B_{i,2} \epsilon_{i,j} + B_{i,3} \epsilon_{i+1,j} = D_i \quad (21)$$

where

$$A_{i,1} = \frac{r_i \left(\frac{H}{\alpha_k}\right)_{i,j} + r_{i-1} \left(\frac{H}{\alpha_k}\right)_{i-1,j}}{r_i \Delta r_i (\Delta r_i + \Delta r_{i+1})}$$

$$A_{i,2} = - \left\{ \frac{\Delta r_i [r_{i+1} \left(\frac{H}{\alpha_k}\right)_{i+1,j} + r_i \left(\frac{H}{\alpha_k}\right)_{i,j}] + \Delta r_{i+1} [r_i \left(\frac{H}{\alpha_k}\right)_{i,j} + r_{i-1} \left(\frac{H}{\alpha_k}\right)_{i-1,j}]}{r_i \Delta r_i \Delta r_{i+1} (\Delta r_i + \Delta r_{i+1})} + \right. \\ \left. + \frac{\left(\frac{H}{\alpha_k}\right)_{i,j+1} + 2\left(\frac{H}{\alpha_k}\right)_{i,j} + \left(\frac{H}{\alpha_k}\right)_{i,j-1}}{2 r_i^2 \Delta \theta^2} + \frac{1}{2} (F)_{i,j} \right\}$$

$$A_{i,3} = \frac{r_{i+1} \left(\frac{H}{\alpha_k}\right)_{i+1,j} + r_i \left(\frac{H}{\alpha_k}\right)_{i,j}}{r_i \Delta r_{i+1} (\Delta r_i + \Delta r_{i+1})}$$

$$C_i = - \left\{ \frac{k_{i,j+1} [\left(\frac{H}{\alpha_k}\right)_{i,j+1} + \left(\frac{H}{\alpha_k}\right)_{i,j}] + k_{i,j-1} [\left(\frac{H}{\alpha_k}\right)_{i,j} + \left(\frac{H}{\alpha_k}\right)_{i,j-1}]}{2 r_i^2 \Delta \theta^2} \right\}$$

$$B_{i,1} = \frac{r_i \left(\frac{H}{\sigma_e}\right)_{i,j} + r_{i-1} \left(\frac{H}{\sigma_e}\right)_{i-1,j}}{r_i \Delta r_i (\Delta r_i + \Delta r_{i+1})}$$

$$B_{i,2} = - \left\{ \frac{\Delta r_i [r_{i+1} \left(\frac{H}{\sigma_e}\right)_{i+1,j} + r_i \left(\frac{H}{\sigma_e}\right)_{i,j}] + \Delta r_{i+1} [r_i \left(\frac{H}{\sigma_e}\right)_{i,j} + r_{i-1} \left(\frac{H}{\sigma_e}\right)_{i-1,j}]}{r_i \Delta r_i \Delta r_{i+1} (\Delta r_i + \Delta r_{i+1})} + \right. \\ \left. + \frac{\left(\frac{H}{\sigma_e}\right)_{i,j+1} + 2\left(\frac{H}{\sigma_e}\right)_{i,j} + \left(\frac{H}{\sigma_e}\right)_{i,j-1}}{2 r_i^2 \Delta \theta^2} + \frac{1}{2} (G)_{i,j} \right\}$$



$$B_{i,3} = \frac{r_{i+1} \left(\frac{H}{\sigma_e}\right)_{i+1,j} + r_i \left(\frac{H}{\sigma_e}\right)_{i,j}}{r_i \Delta r_{i+1} (\Delta r_i + \Delta r_{i+1})}$$

$$D_i = - \left\{ \frac{\epsilon_{i,j+1} \left[ \left(\frac{H}{\sigma_e}\right)_{i,j+1} + \left(\frac{H}{\sigma_e}\right)_{i,j} \right] + \epsilon_{i,j-1} \left[ \left(\frac{H}{\sigma_e}\right)_{i,j} + \left(\frac{H}{\sigma_e}\right)_{i,j-1} \right]}{2 r_i^2 \Delta \theta^2} \right\}$$

$$H = C_\mu \frac{k^2}{\epsilon}$$

$$F = \frac{1}{k} \left( \epsilon - H \left[ \left(\frac{\partial \bar{u}}{\partial r}\right)^2 + \frac{1}{r^2} \left(\frac{\partial \bar{u}}{\partial \theta}\right)^2 \right] \right)$$

$$G = \frac{1}{k} \left( C_{\epsilon 2} \epsilon - C_{\epsilon 1} H \left[ \left(\frac{\partial \bar{u}}{\partial r}\right)^2 + \frac{1}{r^2} \left(\frac{\partial \bar{u}}{\partial \theta}\right)^2 \right] \right)$$

Note that equations (3) and (4) can not be applied to the point at the center of the inlet duct where  $r=0$ . This problem can be handled by rewriting equations (3) and (4) in Cartesian coordinates. The central differencing technique is then applied to the new equations about point p and the surrounding points n, e, s and w shown in Figure 10(c).

Equations (20) and (21) are then written for all points on a radial line, as shown in Figure 10(a), from point 0 to point n+1. From this, two tridiagonal matrix equations are obtained for efficient line relaxation iterations. These two matrix equations are expressed as:

$$\begin{bmatrix}
A_{1,2} & A_{1,3} & & & \\
A_{2,1} & A_{2,2} & A_{2,3} & & 0 \\
& \ddots & \ddots & \ddots & \ddots \\
& & \ddots & \ddots & \ddots \\
0 & & & A_{n-1,1} & A_{n-1,2} & A_{n-1,3} \\
& & & & A_{n,1} & A_{n,2}
\end{bmatrix}
\begin{Bmatrix}
k_{1,j} \\
k_{2,j} \\
\vdots \\
k_{n-1,j} \\
k_{n,j}
\end{Bmatrix}^* = 
\begin{Bmatrix}
C_1 - A_{1,1} k_{0,j} \\
C_2 \\
\vdots \\
C_{n-1} \\
C_n - A_{n,3} k_{n+1,j}
\end{Bmatrix} \quad (22)$$

$$\begin{bmatrix}
B_{1,2} & B_{1,3} & & & \\
B_{2,1} & B_{2,2} & B_{2,3} & & 0 \\
& \ddots & \ddots & \ddots & \ddots \\
& & \ddots & \ddots & \ddots \\
0 & & & B_{n-1,1} & B_{n-1,2} & B_{n-1,3} \\
& & & & B_{n,1} & B_{n,2}
\end{bmatrix}
\begin{Bmatrix}
e_{1,j} \\
e_{2,j} \\
\vdots \\
e_{n-1,j} \\
e_{n,j}
\end{Bmatrix}^* = 
\begin{Bmatrix}
D_1 - B_{1,1} e_{0,j} \\
D_2 \\
\vdots \\
D_{n-1} \\
D_n - B_{n,3} e_{n+1,j}
\end{Bmatrix} \quad (23)$$

Equations (22) and (23) can be solved easily by the routine described in Appendix D.

In order to start the implicit iterative numerical scheme, initial guess of the values of  $k$  and  $e$  for every non-boundary grid point must be given. Initially, the boundary values of  $k$  and  $e$ , estimated from equations (13), (14), (15) and (16), are assigned to every grid point to start the iteration.

A relaxation factor,  $f_r$ , is then used to control the convergence of the numerical scheme (ref. 31). Effect of the relaxation factor on the rate of convergence will be

presented in the next section. Using the relaxation factor,  $f_r$ , the updated solutions of  $k$  and  $\epsilon$  are obtained from the following relations:

$$k^{(n+1)} = k^{(n)} + f_r [ k^* - k^{(n)} ] \quad (24)$$

$$\epsilon^{(n+1)} = \epsilon^{(n)} + f_r [ \epsilon^* - \epsilon^{(n)} ] \quad (25)$$

where  $k^*$  and  $\epsilon^*$  are solutions of equations (22) and (23), and superscripts  $(n)$  and  $(n+1)$  stand for the old and new values respectively.

#### 4.3 Numerical Convergence

Numerical convergence of the finite difference scheme described in the previous section depends on two factors: the relaxation factor,  $f_r$ , and the grid size parameter,  $N_g$ . To study the effect of  $f_r$  and  $N_g$  on the rate of convergence of the numerical scheme such that an optimum numerical scheme can be determined, a relative percent error of each iteration is defined as:

$$E_r = \frac{1}{TN} \sum [ \frac{|k^* - k^{(n)}|}{k^{(n)}} + \frac{|\epsilon^* - \epsilon^{(n)}|}{\epsilon^{(n)}} ] \cdot 100\% \quad (26)$$

where  $TN$  is the total number of non-boundary grid points and

the sign,  $\sum$ , stands for the summation over all non-boundary grid points.

Steady-state total pressure data used in this study is obtained from the HiMAT data set.

To determine the value of  $f_r$ , the relative percent error,  $E_r$ , at the end of the 30th iteration for several values of  $f_r$  and boundary rms levels,  $rms_b$ , is computed and presented in Figure 11. It is seen clearly from Figure 11 that  $E_r$  is decreasing with the increase in  $f_r$ , until  $f_r$  exceeds a boundary beyond which the numerical scheme becomes divergent. The boundary for divergent and the rate of convergence depend also on the boundary rms level,  $rms_b$ . From this a value of  $f_r=1.0$  is selected for relatively good characteristics of convergence and allowing a margin to the divergent boundary for safety operation of the numerical scheme.

To determine the grid size parameter,  $N_g$ , the relative percent error in 30 iterations,  $E_r$ , for several values of  $N_g$  is computed and illustrated in Figure 12.  $f_r$  and  $rms_b$  are fixed at values of 1.0 and 0.011 respectively. It is shown in Figure 12 that  $E_r$  stays at almost a minimum value beyond  $N_g=4$ . For efficient numerical scheme in terms of computing time and good characteristics of convergence,  $N_g=4$  is chosen for successive computations.

## 5. SENSITIVITY STUDY

Prediction of the face-average total pressure rms level and the dynamic peak distortion by using the present analysis depends on the following factors: (1) the measured steady-state total pressure profiles; (2) the estimated boundary rms level; and (3) the empirical parameters of the k-e turbulence model. In the following sections, effects of these factors on the prediction will be examined from which the sensitivity of these factors on the present approach can be identified.

### 5.1 On the Velocity Distributions

Study included in this section will concentrate only on the effects of radial variations of the flow velocity.

In Figure 13(a), five radial steady-state total pressure profiles, which are equivalent to the velocity profiles, are assumed. These total pressure profiles cover a range of boundary layer characteristics from a favorable boundary layer, profile ①, to a separated boundary layer, profile ⑤. Note that profile ④ stands for the boundary between separated and non-separated boundary layer profiles. To predict the dynamic distortion, in this study, a constant boundary rms level,  $rms_b=0.02$ , is used for each pressure profile.

Results of the prediction using the present analysis, based on the assumed five steady-state total pressure

profiles are illustrated in Figure 13(b). In Figure 13(b), only profile ① produces lower rms level near the center of the inlet duct. The rms level is heightened near the duct center as the total pressure profile is close to the separated flow.

Figure 13(c) shows the predicted face-average rms level,  $\overline{rms}_p$ , and the dynamic contribution to a distortion factor,  $K_{A2}$ , for the five total pressure profiles. It is shown clearly that the profile with a favorable boundary layer, profile ①, produces the lowest  $\overline{rms}_p$  and dynamic contribution to  $K_{A2}$  while the separated flow, profile ⑤, predicts the highest  $\overline{rms}_p$  and dynamic contribution to  $K_{A2}$ .

This study shows that: (1) the present method is sensitive to the measured steady-state total pressure profiles; and (2) the dynamic contribution to the peak distortion can be minimized by designing the inlet contour or using boundary layer treatment devices, (e.g. vortex generators,) so that a favorable boundary layer profile can be attained.

## 5.2 On the Boundary Conditions

In this section, effects of the distribution and magnitude of the boundary rms level,  $rms_b$ , on the prediction are presented. Steady-state total pressure data used in this investigation is obtained from an inlet test case, with the test condition shown on the top of Figure 14 (data point 1948,) of the HiMAT data set with vortex generators.

First, the effect of the boundary rms distribution on the predicted rms distributions on the compressor face is illustrated in Figure 14. In Figure 14, the circular symbol stands for the measured rms levels, the solid line is the result of the prediction using a constant boundary rms level estimated by equation (13) and the dashed line represents the result of the prediction based on the actual measured boundary rms level, which is not a constant circumferentially. The indicated number of degrees on the upper left corner of each of the eight figures in Figure 14 denotes the angular position of the pressure rakes on the compressor face. The measured and predicted face-average rms levels,  $\overline{rms}$ , are also shown in the upper portion of Figure 14.

It is shown clearly in Figure 14 that the use of the actual  $rms_b$  distribution improves the prediction, especially for the pressure rake at 180 degree. However, a discrepancy in the prediction of face-average rms level,  $\overline{rms}$ , is not very significant.

In Figure 14, discrepancies between the measured and predicted rms distributions can be seen clearly. This is due mainly to the inevitable assumptions of the theoretical model, assumptions (2) and (3), in which the effects of the secondary flow and the axial variations of  $k$  and  $\epsilon$  are omitted.

Note that the computed value of rms using the constant  $rms_b$  is slightly over-predicted over the measured rms and

the one computed using the actual  $\text{rms}_b$  distribution is under-predicted. The same result is obtained for several test cases of the HiMAT data set. From this, the use of the estimated constant  $\text{rms}_b$  in the present analysis is feasible in the inlet design process.

Next, effects of the magnitude of  $\text{rms}_b$  on the predicted value of face-average rms level,  $\overline{\text{rms}}_p$ , and the dynamic peak distortion factor,  $K_{A2,\text{peak}}$ , are presented in Figure 15(a) and Figure 15(b) respectively. It is shown in Figure 15 that  $\overline{\text{rms}}_p$  and  $K_{A2,\text{peak}}$  are very sensitive to the variation of  $\text{rms}_b$ . This means that good predictions of the face-average rms level and the dynamic peak distortion depend on a good estimation of the boundary rms level. Validity of the present analysis may largely be attributed to the statistical estimation of the boundary rms level,  $\text{rms}_b$ .

### 5.3 On the Parameters of the Turbulence Model

Effects of the values of the five empirical constants,  $\sigma_k$ ,  $\sigma_\epsilon$ ,  $C_\mu$ ,  $C_{\epsilon 1}$  and  $C_{\epsilon 2}$ , on the predictions of face-average rms level,  $\overline{\text{rms}}_p$ , and dynamic peak distortion factor,  $K_{A2,\text{peak}}$ , are investigated in this section. This is done by varying one of the parameters while keeping the other parameters at constant values. Results of this study is illustrated in Figure 15.

It can be seen clearly from Figure 15 that the predicted face-average rms level and the dynamic peak



distortion factor are not sensitive to the changes in the five parameters of the turbulence model. Therefore, an accurate estimation of the boundary rms level is far more crucial than any adjustment in the empirical constants of the turbulence model.

## 6. NUMERICAL RESULTS AND DISCUSSIONS

In the following sections, numerical predictions by the present analysis and data comparisons with five inlet data sets are included. The five inlet data sets consist of experimental results of subsonic, transonic and supersonic inlet configurations under various flight conditions. Inlet configurations and some measured results of these data sets are illustrated in Figure 1 through Figure 5. Three aspects of data comparisons will be included. They are: face-average total pressure rms level comparison; peak dynamic distortion factors comparison; and detailed rms level distributions on the compressor face comparison.

### 6.1 The HiMAT Inlet Data Set

Reference 34 describes an experimental investigation of a subscale HiMAT model with forebody, canard, inlet duct and optional boundary layer control devices, vortex generators. The HiMAT inlet tests were conducted by NASA in the NASA Lewis 8'x6' supersonic wind tunnel facility. The HiMAT model has an under-fuselage inlet with a high-divergence S-shape subsonic diffuser. At the compressor face station, there were 40 steady-state total pressure probes and 40 dynamic high response total pressure probes installed in an 8-rake, 5-ring configuration as illustrated in Figure 1.

Using the present analysis, face-average total pressure rms levels and peak dynamic distortions are predicted based

on the steady-state total pressure measurements of the HiMAT data set. Comparisons of the analytically predicted and experimentally measured rms levels and peak dynamic distortions, for the HiMAT inlet model without vortex generators, are shown in Figure 16. Reasonably good accuracy of the present method in predicting the face-average rms levels is revealed from Figure 16. However, Figure 16 also shows that the present analysis underpredicts the peak dynamic distortion factors for most cases of the HiMAT data set without vortex generators. Since these test cases contain incipient or intermittent separated flow, under-prediction of the Melick statistical method can be expected (refs. 3, 34). Note, in Figure 16, the measured peak dynamic distortion factors,  $\Delta PRS_m$  (defined in Table 1,) are the DYNADEC results (ref. 1).

Figure 17 illustrates comparisons of the peak dynamic distortions, in terms of  $IDC_{max}$ , predicted by the present analysis and the Melick method based on measured rms levels for the HiMAT data set without vortex generators. It is shown in Figure 17 that predictions of the present analysis compare well with the Melick predictions. Note that the peak dynamic distortion factors of Melick's prediction,  $IDC_{max, Melick's-prediction}$ , are obtained from the Melick statistical predictions using 40 total pressure rms measurements.

Figure 18, (a) through (c), presents comparisons of the predicted and measured rms level distributions at the

compressor face for three test cases selected from the HiMAT data set (without vortex generators.) Discrepancies between the predicted and measured rms level distributions can be observed in Figure 18. Since the HiMAT inlet model has a short S-shape inlet duct with large streamwise curvature, substantial secondary flow components can be expected (ref. 17). The presence of the secondary flow violates assumption (2) of the theoretical model. Therefore, some discrepancies in the prediction of the rms level distributions should be expected. However, the face-average rms level is predicted well which is responsible for the good prediction of peak dynamic distortion using the Melick statistical method.

In Figure 19, comparisons of the predicted and measured face-average rms levels and peak dynamic distortion factor are presented for test cases of the HiMAT data set with vortex generators. The predictions shown in Figure 19 are more accurate than those cases without vortex generators, Figure 16. For these cases with vortex generators, boundary layer of the inlet flow is controlled by the vortex generators successfully (ref. 34), which results in better predictions of the Melick statistical method.

Figure 20 illustrates comparisons of the peak dynamic distortions, in terms of  $IDC_{max}$ , predicted by the present analysis and the Melick method based on measured rms levels for the HiMAT data set with vortex generators. It is shown in Figure 20 that predictions of the present analysis

compare well with the Melick predictions. Note that the peak dynamic distortion factors of Melick's prediction,  $IDC_{\max, \text{Melick's-prediction}}$ , are obtained from the Melick statistical predictions using 40 total pressure rms measurements.

Data comparisons of the rms level distributions are illustrated in Figure 21, (a) through (c). These cases are selected from the HiMAT data set with vortex generators. As for the previous cases, discrepancies in these comparisons can be observed. Further study is needed to improve the prediction of rms level distributions on the compressor face.

## 6.2 The Melick Test Cases

Configuration of a supersonic mixed compression axisymmetric inlet model, used to supply the test cases for Melick's computer program, is illustrated in Figure 2 (ref. 35). This inlet model consists of a center body with fixed cone angles. Free stream Mach numbers of the test are 1.6 and 2.5 with total pressure recovery through the inlet shock system assumed to be 0.995 and 0.9 respectively for this type of inlet. Three test cases are available for data comparisons.

In Figure 22, comparisons of the analytically predicted and experimentally measured face-average rms levels and peak dynamic distortion factor are illustrated for the three test cases. Good predictions by the present method are shown

clearly in Figure 22. Note the measured face-average rms level,  $\overline{rms}_m$ , is an average of 14 total pressure rms measurements and the peak dynamic distortion factor of Melick's prediction,  $K_{A2, \text{Melick's-prediction}}$ , is obtained from the Melick statistical prediction using the 14 total pressure rms measurements. For these test cases, there are no DYNADEC results available for data comparisons.

The compressor face rms level distributions are predicted and compared with the measured results. This is shown in Figure 23, (a) through (c). Again, discrepancies in these comparisons can be seen in Figure 23. Although this inlet model is axisymmetric, substantial secondary flow components can still be expected with an inlet angle of attack or sideslip angle.

### 6.3 Subsonic Inlet

Configuration of a subsonic full scale short S-shape inlet model, which is very much like the HiMAT inlet model, is shown in Figure 3. Center line of the engine is tilted as shown in Figure 3. Free stream Mach number of the test is subsonic. There are six test cases available for data comparisons. These data were provided by the Air Force (AFFDL), Wright-Patterson Air Force Base, Ohio.

Comparisons of the predicted and measured results are illustrated in Figure 24, Figure 25 and Figure 26, (a) through (f). Reasonably good accuracy of the present analysis in predicting the face-average total pressure rms

levels and the peak dynamic distortion factors is shown in Figure 24. Note the measured peak dynamic distortion factor,  $IDC_{\max_m}$ , is obtained from the DYNADEC system (ref. 1).

It is seen from Figure 24 that the present method slightly underpredicts the peak dynamic distortion factor for some cases. This is due to the limitation of the Melick statistical method that it can not properly predict the peak dynamic distortion for inlet flow with separated boundary layer (ref. 3). Unfortunately, every case of this subsonic inlet test data set contains separated boundary layer at the compressor face station. Further study is required to improve the Melick statistical method to handle the separated flow conditions.

Good comparisons of the predictions of the present analysis and the Melick method based on rms measurements are illustrated in Figure 25.

Similar comparisons of the rms level distributions of the six test cases are shown in Figure 26, (a) through (f).

#### 6.4 Transonic Inlet

Configuration of a transonic subscale long S-shape inlet model is illustrated in Figure 4. Six test cases of this inlet model are available for data comparisons. These data were also provided by the Air Force (AFFDL).

Comparisons of the predicted and measured results are shown in Figure 27, Figure 28 and Figure 29, (a) through

(f). Good accuracy of the present method in predicting the face-average total pressure rms levels and the peak dynamic distortions is shown clearly in Figure 27. In contrast to the results described in the previous section, or Figure 24, the present analysis overpredicts the peak dynamic distortions slightly, which is illustrated in Figure 27. Since every case of this data set retains attached boundary layer at the compressor face station, better prediction of the peak dynamic distortions, by the Melick statistical method, can be expected. This results in Figure 27. Note the measured peak dynamic distortion factor,  $K_{A2_m}$ , is obtained from the DYNADEC system.

Figure 28 illustrates good comparisons of the predictions of the present analysis and the results of the Melick predictions based on total pressure rms measurements.

Also, slightly improved predictions of the rms level distributions are obtained since a long S-shape inlet duct produces less streamwise curvature effect which incurs smaller amount of secondary flow components which is closer to the theoretical assumptions of the present analysis. Results of the predictions of rms level distributions for the six transonic cases are illustrated in Figure 29, (a) through (f).

## 6.5 Supersonic Inlet

Configurations of four supersonic inlet testing models are illustrated in Figure 5. These inlet models are



designated as A-1, A-2, B-3 and B-4. There are thirteen test cases of the supersonic inlet models available for data comparisons. These data were also provided by the Air Force (AFFDL) (ref.36). Data included in this data set are the steady-state total pressures and the peak dynamic distortions which were screened based on  $K_{A2}$ . There is no information about the measured rms level available for data comparisons. Inlet configurations of the four models are described in more detail in the following paragraphs.

The inlet model, A-1, is a two-dimensional fuselage side-mounted external compression inlet. The compression surface consists of three variable ramps including an articulated first ramp to allow a variable capture area. There is also a variable fourth ramp. A large slot at the throat between the trailing edge of the third ramp and leading edge of the fourth ramp provides for bypass flow and choking control.

The A-2 inlet design is a 180 degree axisymmetric, fuselage side-mounted, external compression inlet. The center body consists of a first cone fixed at 18 degree with a variable radius second cone that has a range from 12 degree to 30 degree.

The B-3 inlet is identical with A-2 except that it is located beneath the wing of a flat-bottomed blended body fuselage. The subsonic diffuser length is constrained by the location of the inlet and engine beneath the wing with the resultant decrease in diffuser length and increase in

diffuser divergence angle.

The B-4 inlet is identical with A-1 except that it is also located beneath the wing in much the same position as B-3 inlet. The diffuser length is constrained by the inlet and engine locations as well.

Results of the prediction of the peak dynamic distortion are computed by the present method and compared with the measured results. This is shown in Figure 30 for  $IDC_{max}$  and  $K_{A2}$ . Since the measured peak dynamic distortions of these test cases were screened based on  $K_{A2}$ , better comparisons are shown in Figure 30 for peak  $K_{A2}$ . Note that most of the test cases are underpredicted slightly. This is because most of these test cases have separated boundary layers at the compressor face station. This causes the Melick statistical method to underpredict the peak dynamic distortions.

Finally, accuracy of the present analysis in predicting the face-average rms level and peak dynamic distortion factor is summarized in Figure 31. Figure 31 is presented in terms of percent error of the prediction compared to the measured data of all available test cases of the five forementioned inlet test data sets.

In Figure 31, three histograms of the percent error in predicting the face-average rms level and peak dynamic distortion factor are presented. If the normal probability distribution is assumed for these three histograms then the mean and standard deviation for the histogram of rms level

are 15.5% and 15.2% respectively. The mean and standard deviation for the histogram of peak dynamic distortion factor, for test cases without separated flow, are 19.51% and 15.57% respectively. The mean and standard deviation for the histogram of peak dynamic distortion factor, for test cases with separated flow, are -3.31% and 17.86% respectively. The distribution of the rms histogram represents the statistical characteristics of the boundary condition estimation technique of the present analysis, equations (13) and (14). The distributions of the peak distortion factor histograms represent the combined statistical characteristics of the rms level prediction technique and the Melick statistical method. In Figure 31, the peak distortion factor histograms show that the present analysis has nearly 93% of chance to overpredict the peak distortion factor, by about 19.51%, for inlet flow without boundary layer separation which is the feature of the conventional type of inlet. This is a good design characteristics. Nevertheless, for inlet flow with separated boundary layer, the present analysis has more than 55% of chance to underpredict the peak dynamic distortion factor, by about -3.31%, which is not a feasible design characteristics. Further study is required to improve the Melick statistical method to handle the separated flow condition.

This result can be used as an inlet design reference in using the present method. In other words, this information

can be used in inlet design process in using the present analysis to see how accurate the present analysis can be in predicting the face-average rms level and peak dynamic distortion factors.

One final comment about the prediction of peak dynamic distortion of the inlet flow using the present analysis is that the present method, owing to the characteristics of the Melick statistical method, will underpredict the peak dynamic distortion for separated flow. If it is found from the steady state total pressure measurements that the flow is separated then the peak distortion factor histogram for separated flow, in Figure 31, can be used as design reference for the predictions of the peak dynamic distortion factors.

## 7. CONCLUSIONS

An analytical method in predicting total pressure rms level and peak dynamic distortion, based on steady-state total pressure measurements, has been developed. The total pressure rms level is predicted by a two-equation turbulence model -- k- $\epsilon$  model. The Melick statistical method is then used to estimate the peak dynamic distortion based on the predicted total pressure rms level and the steady-state total pressure measurements.

A finite difference scheme has been used to solve the two-equation turbulence model. A statistical correlation between the measured steady-state total pressures and total pressure rms level near the wall has been developed using the HiMAT inlet data set. Thus, boundary conditions of the turbulence model can be estimated from the steady-state total pressure measurements.

A central differencing scheme has been applied to the turbulence model to discretize the equations of the turbulence model. Thus, an implicit line relaxation formulation is obtained. The finite difference equations have been arranged into a set of tridiagonal matrix equations for efficient numerical iterations.

Numerical convergence of the finite difference scheme has been investigated in order to determine a relaxation factor and grid size for the numerical scheme. Sensitivity study has also been included to see how sensitive the

present analysis is to the input data and empirical parameters of the turbulence model.

Accuracy of the present analysis has been demonstrated through data comparisons for subsonic, transonic and supersonic inlet models at various angles of attack and sideslip. Five sets of inlet test data have been used for this purpose. Results of the data comparisons have shown that the present method predicts good results of the face-average rms level and peak dynamic distortion factor. Around 20% of accuracy in predicting peak distortion factors is attained for subsonic, transonic and supersonic inlet test cases without separated flow. Further research is required to improve the present analysis to handle the separated flow conditions.

As far as the prediction of peak dynamic distortion factor is concerned, the present analysis can be used as an efficient preliminary inlet design tool without total pressure rms measurements. Only the steady-state total pressure measurements are required to predict the peak dynamic distortion factor.

A logical extension of the current work would be to predict the dynamic distortion of the inlet flow directly from an analytical point of view so that no experimental information would be required in the prediction. This would require a flow field calculation external to the inlet duct and a compressible turbulent flow computation along the subsonic inlet duct. This approach would require a large

computational effort with long computing time, but it would be an inlet design tool that would provide early estimates of peak dynamic distortion prior to the time when inlet models and test data are available.

## 8. REFERENCES

1. Marous, J. J. & Sedlock, D., "Dynamic Data Editing and Computing System (DYNADEC)," Proceedings of Air Force System Command Science and Engineering Symposium, AFSC-TR-003, Vol. 1, October 1973.
2. Marous, J. J. & Sedlock, D., "An Analog Editing System for Inlet Dynamic Flow Distortion, DYNADEC--Past, Present and Future," AIAA Paper 80-1108, July 1980, 10 pp.
3. Chen, Y. S., "Statistical Prediction of Dynamic Distortion of Inlet Flow Using Minimum Dynamic Measurements--An Application to the Melick Statistical Method," M. S. Thesis, 1983.
4. Jacocks, J. L., et al., "Statistical Prediction of Maximum Time Variant Inlet Distortion Levels," Arnold Engineering Development Center, AD/A-004-104, January 1975.
5. Motycka, D. L., "Determination of Maximum Expected Instantaneous Distortion Patterns From Statistical Properties of Inlet Pressure Data," AIAA Paper 76-705, July 1976.
6. Melick, H. C., Jr., Ybarra, A. H. & Beneze, D. P., "Estimating Maximum Instantaneous Distortion from Inlet Total Pressure rms Measurements," AIAA Paper 78-970, July 1978.
7. Sanders, M. E., "An Evaluation of Statistical Methods for the Prediction of Maximum Time-Variant Inlet Total Pressure Distortion," AIAA Paper 80-1110, July 1980.



8. Borg, R., "A Synthesis Method for Estimating Maximum Instantaneous Inlet Distortion Based on Measured Inlet Steady State & RMS Pressures," In AGARD Aerodynamics of Power Plant Installation, Sep. 1981, N82-13083.
9. Paynter, Gerald C., "Current Status of Inlet Flow Prediction Methods," Boeing Military Airplane Development, Seattle, AD-A111784, N82-26311, May 14, 1981.
10. Colbourne, D. E. & Flitcroft, J. E., "Prediction and Measurement of Time-Variant Three-Dimensional Flows in Military Aircraft Intakes," N82-13069, In AGARD Aerodynamics of Power Plant Installation, Sep. 1981.
11. Launder, B. E. & Spalding, D. B., "The Numerical Computation of Turbulent Flows," Computer Methods in Applied Mechanics and Engineering, Vol. 3, 1974, p. 269.
12. Taylor, C., Morgan, K. & Brebbia, C. A., Numerical Methods in Laminar and Turbulent Flow, Proceedings of the First International Conference held at University College Swansea, U. K., July 1978, AHalsted Press Book, John Wiley & Sons, N. Y.
13. Bradshow, P., Cebeci, T. & Whitelaw, J. H., Engineering Calculation Methods for Turbulent Flow, Academic Press, London, 1981.
14. Frost, W. & Moulden, T. H., Handbook of Turbulence, Vol. 1, Plenum Press, N. Y., 1977.

15. Launder, B. E. & Spalding, D. B., Mathematical Models of Turbulence, Academic Press, N. Y., 1972.
16. Rodi, W., "Examples of Turbulence Models for Incompressible Flows," AIAA Journal, Vol. 20, No. 7, p. 87, July 1982.
17. Patankar, S. V., Prataap, V. S. & Spalding, D. B., "Prediction of Turbulent Flow in Curved Pipes," Journal of Fluid Mechanics, 1975, Vol. 67, Part 3, pp. 583-595.
18. Chieng, C. C. & Launder, B. E., "On the Calculation of Turbulent Heat Transfer Downstream From an Abrupt Expansion," Numerical Heat Transfer, Vol. 3, pp. 189-200, 1980.
19. Pourahmadi, F. and Humphrey, A. C., "Prediction of Curved Channel Flow With An Extended k-e Model of Turbulence," AIAA Journal, Vol. 21, No. 10, October 1983.
20. Chien, Kuei-Yuan, "Predictions of Channel and Boundary-Layer Flows with a Low-Reynolds-Number Turbulence Model," AIAA Journal, Vol. 20, No. 1, p. 33, January 1982.
21. Launder, B. E., Morse, A. P., Rodi, W. and Spalding, D. B., "The Prediction of Free-Shear Flows--A Comparison of the Performance of six Turbulence Models," Proceedings of the NASA Langley Free Turbulent Shear Flows Conference, Vol. 1, NASA-SP 320, 1973.
22. Hah, C. & Lakshminarayana, B., "Prediction of Two- and Three-Dimensional Asymmetrical Turbulent Wakes, Including Curvature and Rotation Effects," AIAA Journal, Vol. 18, No. 10, p.1197, October 1980.

23. Demuren, A. O., "Numerical Calculations of Steady Three-Dimensional Turbulent Jets in Cross Flow," Computer Methods in Applied Mechanics and Engineering 37, pp. 309-328, North-Holland Publishing Company, 1983.
24. Marvin, Joseph G., "Turbulence Modeling for Computational Aerodynamics," AIAA Journal, Vol. 21, No. 7, July 1983.
25. Wilcox, D. C. and Rubesin, M. W., "Progress in Turbulence Modeling for Complex Flow Fields Including the Effects of Compressibility," NASA TP-1517, 1980.
26. Vollmers, H. & Rotta, J. C., "Similar Solutions of the Mean Velocity, Turbulent Energy and Length Scale Equations," AIAA Journal, Vol. 15, No.5, p. 714, May 1977.
27. Rotta, J. C. & Vollmers, H., "Similar Solutions of the Differential Equations for Mean Velocity, Turbulence Energy and Turbulence Length," Translation of DLR-FB 76-24, ESA TT-354, Nov. 1976.
28. Nicolai, Leland M., Fundamentals of Aircraft Design, Aero. Engineering, University of Dayton, Dayton, Ohio, 1975.
29. Patankar, S. V. & Spalding, D. B., Heat and Mass Transfer in Boundary Layers, 2nd ed., Intertext, London, 1970.
30. Patankar, S. V., Numerical Heat Transfer and Fluid Flow, Series in Computational Methods in Mechanics and Thermal Sciences, McGraw-Hill Book Company, 1980.
31. Chow, Chuen-Yen, An Introduction to Computational Fluid Mechanics, John Wiley & Sons, 1979.

32. Discus, J. H., "Fortran Program to Generate Engine Inlet Flow Contour Maps and Distortion Parameters," NASA TM X-2967, 1974.
33. Melick, H. C., Jr., "Analysis of Inlet Flow Distortion and Turbulence Effects on Compressor Stability," NASA CR-114577, 1973.
34. Neumann, H. E., Povinelli, L. A. and Coltrin, R. E., "An Analytical and Experimental Study of a Short S-Shaped Subsonic Diffuser of a Supersonic Inlet," AIAA Paper 80-386, January 1980.
35. Burstadt, P. L. and Calogeras, J. E., "Instantaneous Distortion in a Mach 2.5 40-Percent-Internal-Contraction Inlet and Its Effects on Turbojet Stall Margin," NASA TM X-3002, 1974.
36. Sedlock, D., "Analog Screening of Tailor-Mate I .25 Scale Inlet Data, Basic Configuration," AFFDL-TM-75-165-FXM, Dec. 1975.

## APPENDIX A

### Derivation of k-ε turbulence Model

The continuity and momentum equations for incompressible flow can be written in tensor notation as following:

$$\frac{\partial u_j}{\partial x_j} = 0 \quad (A1)$$

$$\rho \left( \frac{\partial u_i}{\partial t} + u_j \frac{\partial u_i}{\partial x_j} \right) = - \frac{\partial P}{\partial x_i} + \mu \frac{\partial^2 u_i}{\partial x_j^2} \quad (A2)$$

where  $u_i$  and  $P$  represent velocity components and pressure of the flow respectively.  $\rho$  and  $\mu$  denote flow density and flow viscosity respectively.

For turbulent flow, the velocity components and the pressure can be decomposed into a time-averaged component and a time dependent component. This is given in the following relations.

$$u_i = \bar{u}_i + u'_i, \quad P = \bar{P} + P'$$

Substituting these relations into equations (A1) and (A2) and taking time averaging of the resultant expressions, the following time-averaged equations of equations (A1) and (A2) can be obtained.

$$\frac{\partial \bar{u}_j}{\partial x_j} = 0 \quad (A3)$$

$$\rho \left[ \frac{\partial \bar{u}_i}{\partial t} + \frac{\partial}{\partial x_j} (\bar{u}_i \bar{u}_j + \overline{u'_i u'_j}) \right] = - \frac{\partial \bar{p}}{\partial x_i} + \mu \frac{\partial^2 \bar{u}_i}{\partial x_j^2} \quad (A4)$$

Subtracting equation (A3) from equation (A1) and subtracting equation (A4) from equation (A2), the following time dependent equations are obtained.

$$\frac{\partial u'_i}{\partial x_j} = 0 \quad (A5)$$

$$\rho \left[ \frac{\partial u'_i}{\partial t} + \bar{u}_j \frac{\partial u'_i}{\partial x_j} + u'_j \frac{\partial \bar{u}_i}{\partial x_j} + u'_j \frac{\partial u'_i}{\partial x_j} - \frac{\partial}{\partial x_j} (\overline{u'_i u'_j}) \right] = - \frac{\partial p'}{\partial x_i} + \mu \frac{\partial^2 u'_i}{\partial x_j^2} \quad (A6)$$

Multiplying equation (A6) by  $u'_i$  and then taking time averaging, equation (A7) is obtained.

$$\begin{aligned} \rho \left[ \frac{\partial}{\partial t} \left( \frac{\overline{u'^2_i}}{2} \right) + \bar{u}_j \frac{\partial}{\partial x_j} \left( \frac{\overline{u'^2_i}}{2} \right) + \overline{u'_i u'_j} \frac{\partial \bar{u}_i}{\partial x_j} + \overline{u'_j \frac{\partial u'_i}{\partial x_j}} \right] = \\ = - \frac{\partial (\overline{u'_i p'})}{\partial x_i} + \mu \overline{u'_i \frac{\partial^2 u'_i}{\partial x_j^2}} \end{aligned} \quad (A7)$$

Taking summation of equation (A7) for all  $i=1, 2, 3$  and using equation (A5) and the definition of turbulent kinetic energy,  $k=(1/2)\sum \overline{u'^2_i}$ , equation (A8) is obtained.

$$\frac{\partial k}{\partial t} + \bar{u}_j \frac{\partial k}{\partial x_j} = \underbrace{\frac{\partial}{\partial x_j} \left( \nu \frac{\partial k}{\partial x_j} - \overline{u'_j \left( \frac{p'}{\rho} + k' \right)} \right)}_{\text{(I) Diffusion}} + \underbrace{\left( - \overline{u'_i u'_j} \right) \frac{\partial \bar{u}_i}{\partial x_j}}_{\text{(II) Production}} - \underbrace{\nu \overline{\left( \frac{\partial u'_i}{\partial x_j} \right)^2}}_{\text{(III) Dissipation rate}} \quad (A8)$$

where  $\nu = \frac{\mu}{\rho}$

$$\text{and } \overline{u'_i \frac{\partial u'_i}{\partial x'_j}} = \overline{\frac{\partial}{\partial x'_j} \left( \frac{u'^2_i}{2} \right)} - \overline{\left( \frac{\partial u'_i}{\partial x'_j} \right)^2} \quad \text{have been used.}$$

The following empirical approximations were suggested by Launder (ref. 16).

$$(I) \approx \frac{\partial}{\partial x_j} \left( \frac{\nu_t}{\sigma_k} \frac{\partial k}{\partial x_j} \right) \quad \text{with } \sigma_k = 1.0$$

$$(-u'_i u'_j) \approx \nu_t \frac{\partial \bar{u}_i}{\partial x_j}$$

$$(III) \equiv \epsilon$$

where  $\nu_t = C'_\mu \sqrt{k} L$  is the well known Kolmogorov-Prandtl expression for turbulent viscosity. Also, from dimensional analysis,  $\epsilon$  can be written as:

$$\epsilon = C_D \frac{k^{3/2}}{L}$$

Thus, the following relation is obtained.

$$\nu_t = C'_\mu C_D \frac{k^2}{\epsilon} = C_\mu \frac{k^2}{\epsilon}$$

where  $C_\mu = 0.09$  and  $C_D = 0.08$  are empirical constants.

Using these approximations, equation (A8) is written as:

$$\frac{Dk}{Dt} = \frac{\partial}{\partial x_j} \left( \frac{C_\mu}{\sigma_k} \frac{k^2}{\epsilon} \frac{\partial k}{\partial x_j} \right) + k \left[ C_\mu \frac{k}{\epsilon} \left( \frac{\partial \bar{u}_i}{\partial x_j} \right)^2 - \frac{\epsilon}{k} \right] \quad (A9)$$

It is sheerly empirical that an equation for  $\epsilon$  was

suggested by Launder. It is assumed that the  $\epsilon$ -equation have the same form as the  $k$ -equation with different empirical constants. This results in the following relation.

$$\frac{D\epsilon}{Dt} = \frac{\partial}{\partial x_j} \left( \frac{C_\mu}{\sigma_\epsilon} \frac{k^2}{\epsilon} \frac{\partial \epsilon}{\partial x_j} \right) + \epsilon [C_{\epsilon 1} C_\mu \frac{k}{\epsilon} \left( \frac{\partial \bar{u}_i}{\partial x_j} \right)^2 - C_{\epsilon 2} \frac{\epsilon}{k}] \quad (A10)$$

where  $\sigma_\epsilon = 1.3$ ,  $C_{\epsilon 1} = 1.45$  and  $C_{\epsilon 2} = 2.0$  are additional empirical constants.

Finally, equations (A9) and (A10) can be rewritten in cylindrical coordinates for steady pipe flow:

$$\begin{aligned} \bar{u} \frac{\partial k}{\partial x} + \bar{v} \frac{\partial k}{\partial r} + \frac{\bar{w}}{r} \frac{\partial k}{\partial \theta} = \frac{1}{r} \frac{\partial}{\partial r} \left( \frac{C_\mu}{\sigma_k} \frac{k^2}{\epsilon} r \frac{\partial k}{\partial r} \right) + \frac{1}{r^2} \frac{\partial}{\partial \theta} \left( \frac{C_\mu}{\sigma_k} \frac{k^2}{\epsilon} \frac{\partial k}{\partial \theta} \right) + \\ + C_\mu \frac{k^2}{\epsilon} \left[ \left( \frac{\partial \bar{u}}{\partial r} \right)^2 + \frac{1}{r^2} \left( \frac{\partial \bar{u}}{\partial \theta} \right)^2 \right] - \epsilon \end{aligned} \quad (A11)$$

$$\begin{aligned} \bar{u} \frac{\partial \epsilon}{\partial x} + \bar{v} \frac{\partial \epsilon}{\partial r} + \frac{\bar{w}}{r} \frac{\partial \epsilon}{\partial \theta} = \frac{1}{r} \frac{\partial}{\partial r} \left( \frac{C_\mu}{\sigma_\epsilon} \frac{k^2}{\epsilon} r \frac{\partial \epsilon}{\partial r} \right) + \frac{1}{r^2} \frac{\partial}{\partial \theta} \left( \frac{C_\mu}{\sigma_\epsilon} \frac{k^2}{\epsilon} \frac{\partial \epsilon}{\partial \theta} \right) + \\ + C_{\epsilon 1} C_\mu k \left[ \left( \frac{\partial \bar{u}}{\partial r} \right)^2 + \frac{1}{r^2} \left( \frac{\partial \bar{u}}{\partial \theta} \right)^2 \right] - C_{\epsilon 2} \frac{\epsilon^2}{k} \end{aligned} \quad (A12)$$



APPENDIX B  
Measured Steady State Total Pressure  
and Velocity Distributions

Relationship between the measured steady state total pressure and the axial mean flow velocity is derived under the following assumptions:

1. The flow is ideal gas.
2. The flow is adiabatic.
3. The flow is steady.
4. There is no static pressure variation in the direction normal to the wall.
5. Loss in the total pressure measurement is accounted for by a recovery factor,  $r$ .

Under these assumptions, total energy of the flow without turbulence at the instrumentation station is picked up by the total pressure probe. Effect of turbulence will be considered later. The following equation describes this relation.

$$E_t = E_1 \tag{B1}$$

where  $E_t$  stands for the total energy of the flow after the flow stagnates and  $E_1$  denotes the total energy of the flow just before entering the total pressure probe. For adiabatic flow,

$$E_t = C_p T_t, \quad E_1 = C_p T_s + V^2/2 + g(\text{curl } V)$$

where  $C_p$  is the specific heat of the flow at constant pressure,  $T_t$  and  $T_s$  are total and static temperatures respectively and  $g$  function stands for rotational energy of the flow inside the boundary layer. Assume that  $g$  is very small and can be neglected since the measurement is not made very close to the wall. Also,  $V$  denotes the absolute velocity of the flow at the total pressure probe location. The equations of state of the ideal gas are:

$$T_t = \frac{P_t}{\rho_t R}, \quad T_s = \frac{P_s}{\rho_s R} \quad \text{and} \quad \frac{C_p}{R} = \frac{\gamma}{\gamma-1}$$

where  $\gamma=1.4$ . After substituting these relations into equation (B1), the following equation is obtained.

$$\frac{\gamma}{\gamma-1} \frac{P_t}{\rho_t} \approx \frac{\gamma}{\gamma-1} \frac{P_s}{\rho_s} + \frac{1}{2} V^2, \quad \text{where } V^2 = u^2 + v^2 + w^2 \quad (\text{B2})$$

Considering loss in the total pressure measurement, a recovery factor,  $r$ , is introduced for the total pressure probe. That is,

$$r = \frac{P_{ti}}{P_t}, \quad \text{where } P_{ti} \text{ is the indicated total pressure.}$$

Equation (B2) becomes:

$$\frac{\gamma}{\gamma-1} \frac{P_{ti}}{\rho_t} \approx \frac{\gamma}{\gamma-1} \frac{P_s}{\rho_s} + \frac{1}{2} (u^2 + v^2 + w^2) \quad (B3)$$

The effect of turbulence is accounted for by the following relations:

$$P_t = \bar{P}_t + P'_t, \quad P_s = \bar{P}_s + P'_s, \quad \rho_t = \bar{\rho}_t + \rho'_t, \quad \rho_s = \bar{\rho}_s + \rho'_s$$

$$u = \bar{u} + u', \quad v = \bar{v} + v', \quad w = \bar{w} + w'$$

where the pressure, velocity and density terms are replaced by their time-averaged terms plus time-variant fluctuation terms. Substituting these relations into equation (B2), a time-averaged equation and a time-variant equation can be obtained. They are:

$$\frac{\gamma}{\gamma-1} \frac{\bar{P}_t}{\bar{\rho}_t} \approx \frac{\gamma}{\gamma-1} \frac{\bar{P}_s}{\bar{\rho}_s} + \frac{1}{2} (\bar{u}^2 + \bar{v}^2 + \bar{w}^2) + \frac{1}{2} (\overline{u'^2} + \overline{v'^2} + \overline{w'^2}) \quad (B4)$$

$$\frac{\gamma}{\gamma-1} \frac{P'_t}{\rho_t} \approx \frac{\gamma}{\gamma-1} \frac{P'_s}{\rho_s} + (\bar{u}u' + \bar{v}v' + \bar{w}w') + \frac{1}{2} (u'^2 + v'^2 + w'^2) \quad (B5)$$

Notice that it has been assumed that  $\rho'_t$  and  $\rho'_s$  are small and can be neglected in obtaining equation (B5). Introducing the definition of turbulent kinetic energy,  $k = (\overline{u'^2} + \overline{v'^2} + \overline{w'^2})/2$ , and considering the loss in the total pressure measurement, equation (B4) results in:

Since  $\bar{u} \gg \bar{v}$  and  $\bar{u} \gg \bar{w}$ , the above equation can be further simplified by neglecting  $\bar{v}$  and  $\bar{w}$ .

$$\frac{\gamma}{\gamma-1} \frac{P_{ti}}{r p_t} \approx \frac{\gamma}{\gamma-1} \frac{P_s}{\rho_s} + \frac{1}{2} \bar{u}^2 + k$$

or,

$$\frac{\bar{u}}{U_2} \approx \sqrt{\left[ \frac{1}{\frac{1}{2} \rho_s U_2^2} \left( \frac{\gamma}{\gamma-1} \right) \left( \frac{\bar{P}_{ti}}{r p_t / \rho_s} - \bar{P}_s \right) - 2 \frac{k}{U_2^2} \right]} \quad (B6)$$

where  $U_2$  is the compressor face average flow velocity.

Since  $k/U_2^2$  is very small, equation (B6) can be approximated by:

$$\frac{\bar{u}}{U_2} \approx \sqrt{\frac{1}{\frac{1}{2} \rho_s U_2^2} \left( \frac{\gamma}{\gamma-1} \right) \left( \frac{P_t}{p_t / \rho_s} - P_s \right)} \quad (B7)$$

where  $r=1.0$  for most of the total pressure probe used in experiment.

## APPENDIX C

### Total Pressure rms Level and Turbulent Kinetic Energy

Relationship between total pressure rms level and turbulent kinetic energy is derived in this section by the use of equation (B5) derived in APPENDIX B. Assumptions stated in APPENDIX B are also employed here. Equation (B5) is:

$$\frac{\gamma}{\gamma-1} \frac{P'_t}{\rho_t} \approx \frac{\gamma}{\gamma-1} \frac{P'_s}{\rho_s} + (\bar{u}u' + \bar{v}v' + \bar{w}w') + \frac{1}{2} (u'^2 + v'^2 + w'^2)$$

It is further assumed that the fluctuations of the static pressure makes only a small contribution in the above equation and can be neglected. Taking root mean square (rms) on both sides of the above equation, the total pressure rms level can be written as:

$$rms = \sqrt{\overline{P_t'^2}} \approx \frac{\rho_t(\gamma-1)}{\gamma} \sqrt{[(\bar{u}u' + \bar{v}v' + \bar{w}w') + \frac{1}{2} (u'^2 + v'^2 + w'^2)]^2}$$

Since  $\bar{u} \gg \bar{v}$  and  $\bar{u} \gg \bar{w}$  and neglecting the higher order terms, the above expression can be simplified as:

$$rms \approx \frac{\rho_t(\gamma-1)}{\gamma} \sqrt{\bar{u}^2 \overline{u'^2} + k^2} \quad (C1)$$

For isotropic turbulence (i.e. for flow away from the wall),

$\overline{u'^2}$  can be written in terms of  $k$  (ref. 12). That is:

$$\overline{u'^2} = (2/3) k$$

Substituting this relation into equation (C1), an expression in relating total pressure rms level, rms, and turbulent kinetic energy,  $k$ , can be written as:

$$rms \approx \frac{\rho_t(\gamma-1)}{\gamma} \sqrt{(2/3)\overline{u'^2}k + k^2} \quad (C2)$$

Equation (C2) is an approximation for flow which is not very close to the wall.

## APPENDIX D

### Solution of Tridiagonal Matrix Equation

A typical tridiagonal matrix equation can be written as:

$$AX = F \quad (D1)$$

where

$$A = \begin{bmatrix} a_1 & c_1 & & & 0 \\ b_2 & a_2 & c_2 & & \\ \cdot & \cdot & \cdot & \cdot & \\ \cdot & \cdot & \cdot & \cdot & \\ 0 & & b_{n-1} & a_{n-1} & c_{n-1} \\ & & & b_n & a_n \end{bmatrix}$$

$$X = \begin{bmatrix} x_1 \\ x_2 \\ \cdot \\ \cdot \\ \cdot \\ \cdot \\ x_n \end{bmatrix} \quad F = \begin{bmatrix} f_1 \\ f_2 \\ \cdot \\ \cdot \\ \cdot \\ \cdot \\ f_n \end{bmatrix}$$

The tridiagonal matrix, A, can be decomposed into two matrices, U and V. That is:

$$A = UV \quad (D2)$$

or,

$$\begin{bmatrix} a_1 & c_1 & & & 0 \\ b_2 & a_2 & c_2 & & \\ & b_3 & a_3 & c_3 & \\ & & \ddots & \ddots & \ddots \\ 0 & & & b_n & a_n \end{bmatrix} = \begin{bmatrix} p_1 & & & & 0 \\ b_2 & p_2 & & & \\ & b_3 & p_3 & & \\ & & \ddots & \ddots & \ddots \\ 0 & & & b_n & p_n \end{bmatrix} \begin{bmatrix} 1 & r_1 & & & 0 \\ & 1 & r_2 & & \\ & & 1 & r_3 & \\ & & & \ddots & \ddots \\ & 0 & & 1 & r_{n-1} \\ & & & & 1 \end{bmatrix}$$

where  $p_1 = a_1$ ,  $r_1 = c_1/p_1$

$p_i = a_i - b_i r_{i-1}$ ,  $i = 2, 3, 4, \dots, n$

$r_i = c_i/p_i$ ,  $i = 2, 3, 4, \dots, n$

Using relation (D2), equation (D1) can be written as:

$$UVX = F$$

Letting  $VX = G$ , the above relation becomes:

$$UG = F \quad (D3)$$

Thus, solution for  $G$  can be obtained from the following recursion formula:

$$g_1 = f_1/p_1$$

$$g_i = (f_i - b_i g_{i-1})/p_i, \quad i = 2, 3, 4, \dots, n$$



Finally,  $X$  can be solved from  $VX = G$ . Solution for  $X$  is obtained from the following formula:

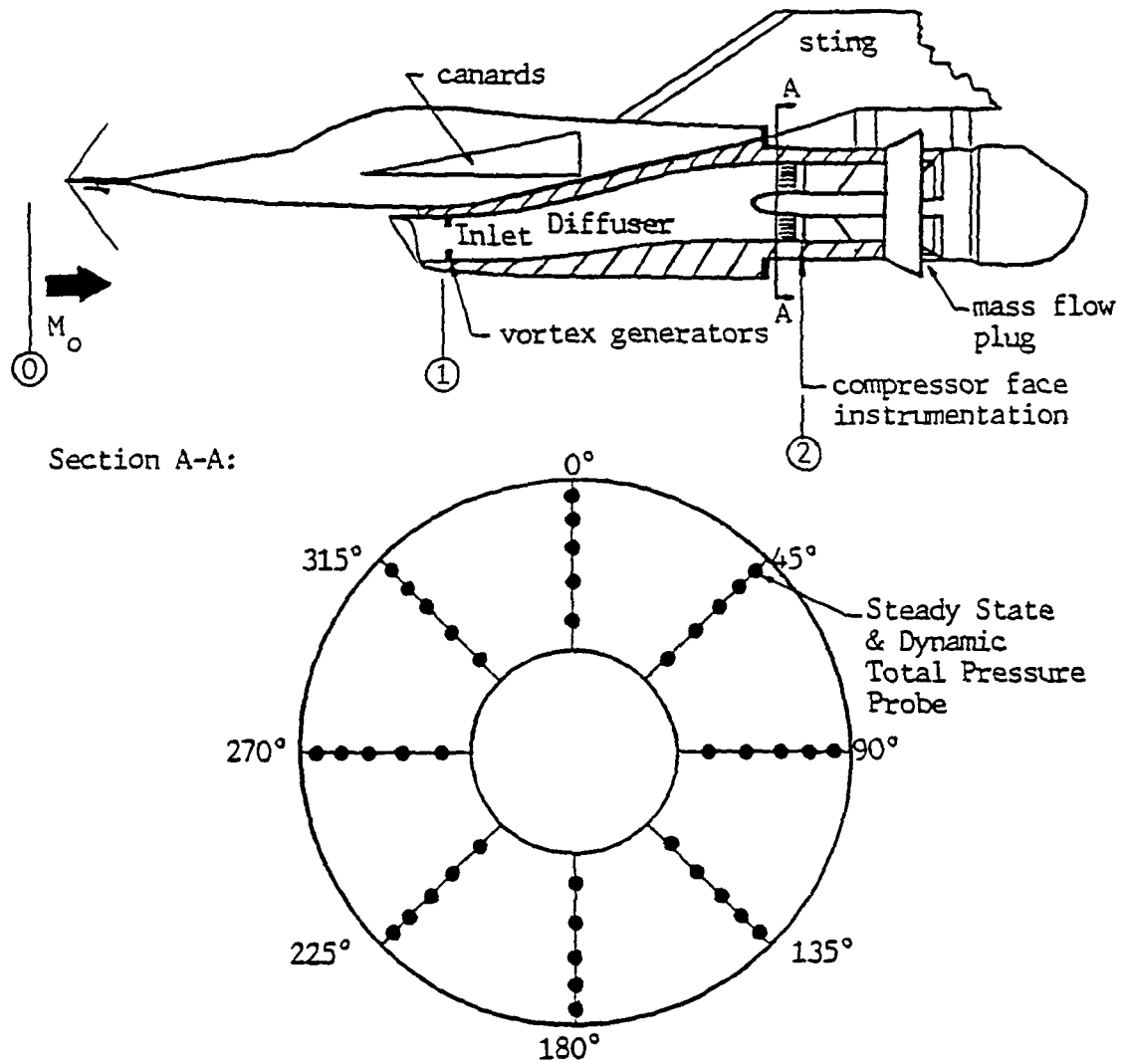
$$x_n = g_n$$

$$x_i = g_i - r_i x_{i+1}, \quad i = n-1, n-2, \dots, 1$$

Factor	Equation	Supplemental equations	Definitions	Ref.
$IDC_{max}$	$IDC_{max} = \max \{ \frac{1}{2}(IDC_1 + IDC_2), \frac{1}{2}(IDC_4 + IDC_5) \}$	$IDC_j = \frac{(\bar{p}_t)_j - (p_{t,min})_j}{\bar{p}_t}$	$(\bar{p}_t)_j$ = average total pressure for ring j $(p_{t,min})_j$ = minimum total pressure reading in ring j	32
$IDR_{max}$	$IDR_{max} = \max(IDR_1, IDR_5)$	$IDR_j = \frac{\bar{p}_t - (p_{t,min})_j}{\bar{p}_t}$	$\bar{p}_t$ = average total pressure at engine face	
$K_{D2}$	$K_{D2} = \frac{\sum_{j=1}^{NR} \bar{\theta}_j (\Delta p_t / p_t) (OD/D_j)}{\sum_{j=1}^{NR} (OD/D_j)}$	$\frac{\Delta p_t}{p_t} = \frac{(\bar{p}_t)_j - (p_{t,min})_j}{(\bar{p}_t)_j} * 100$	$(\bar{p}_t)_j, (p_{t,min})_j$ = see above $\bar{\theta}_j$ = circumferential extent of largest continuous total pressure depression below $(\bar{p}_t)_j$ , degrees $D_j$ = diameter of ring j; NR = number of ring OD = outer duct diameter	1
$K_{\theta}$	$K_{\theta} = \frac{\sum_{j=1}^{NR} (A_1)_j (1/D_j)}{(q/\bar{p}_t) \sum_{j=1}^{NR} (1/D_j)}$	$(A_1)_j = (a_1^2 + b_1^2)_j$ $(a_1)_j = \frac{1}{M} \left( \sum_{i=1}^M \frac{p_{t1}}{\bar{p}_t} \cos(\theta_1) \right)_j$ $(b_1)_j = \frac{1}{M} \left( \sum_{i=1}^M \frac{p_{t1}}{\bar{p}_t} \sin(\theta_1) \right)_j$	$\bar{p}_t, (\bar{p}_t)_j, D_j$ = see above $\bar{q}$ = average dynamic pressure at engine face M = number of rakes $(p_{t1})_j$ = individual total pressure; rake i 0 = angular position of $p_{t1}$ $(p_{t,base})_j = \frac{(p_{t,base})_j}{\bar{p}_t}$ = base radial profile for ring j; set = 1 for all j b = radial distortion weighting factor=1.0	1
$K_{RAD}$	$K_{RAD} = \sum_{j=1}^{NR} \left  \frac{\Delta p_{t1}}{\bar{p}_t} \right  \frac{\bar{p}_t}{q} \frac{1}{D_j}$	$\frac{\Delta p_{t1}}{\bar{p}_t} = \frac{(p_{t,base})_j}{\bar{p}_t} - \frac{(p_{t,base})_j}{\bar{p}_t}$		
$K_{A2}$	$K_{A2} = K_0 + bK_{RAD}$			
$\frac{\Delta SPR}{Dist}$	$\frac{\Delta SPR}{Dist} = \frac{\Delta SPR}{((\bar{p}_t - p_{t,min})/\bar{p}_t)} = f(k)$		$\bar{p}_t$ = see above $p_{t,min}$ = minimum total pressure at engine face	33
$\Delta PRS$	$\Delta PRS = k_c (IDC)_b + k_r (IDR)$		$k$ = compressor reduced frequency $k_c$ = circumferential distortion sensitivity factor $k_r$ = radial distortion sensitivity factor $b_r$ = circumferential distortion weighting factor	34

Table 1. Definition of distortion factors

(a) HiMAT Inlet Test Model:

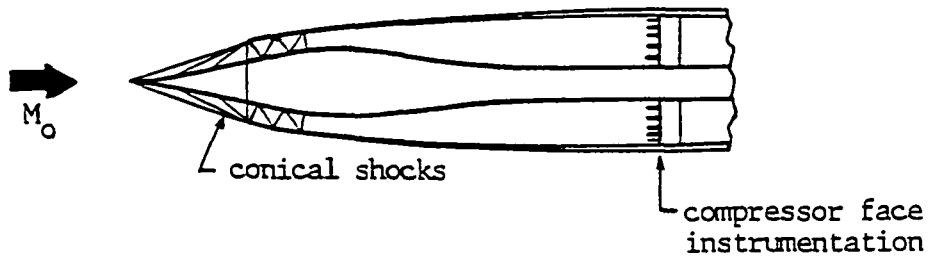


(b) Range of Test Conditions:

Mach No. = 0.4 ~ 1.36  
 Angles of Attack =  $-10^\circ$  ~  $+25^\circ$   
 Angles of Sideslip =  $0^\circ$  ~  $-10^\circ$   
 With and Without Vortex Generators

Figure 1. Illustration of HiMAT Inlet Test Model and Test Conditions (ref. 34)

(a) Supersonic Mixed Compression Axisymmetric Inlet Model:

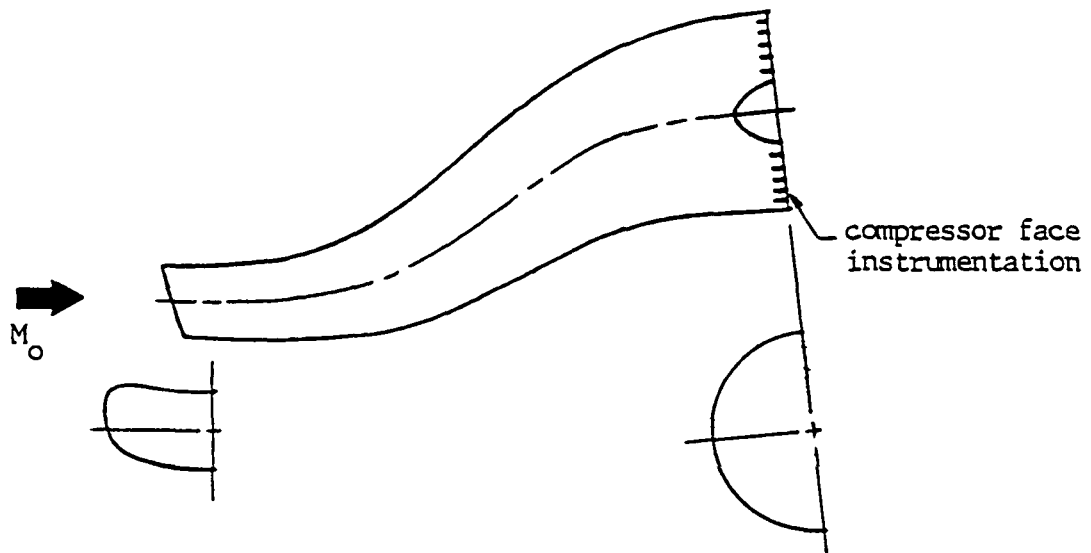


(b) Test Conditions and Measured  $\overline{rms}$  of 3 Melick's Test Cases:

Case No.	Mach No.	$\alpha$	$\beta$	$\overline{rms}$ (14-probe average)
1	2.5	5	0	.0126
2	1.6	5	1	.0194
3	2.5	5	0	.0173

Figure 2. Illustration of the Inlet Test Model of Melick's Test Cases and some Test Results (ref. 35)

(a) Subsonic Full Scale Inlet Model:

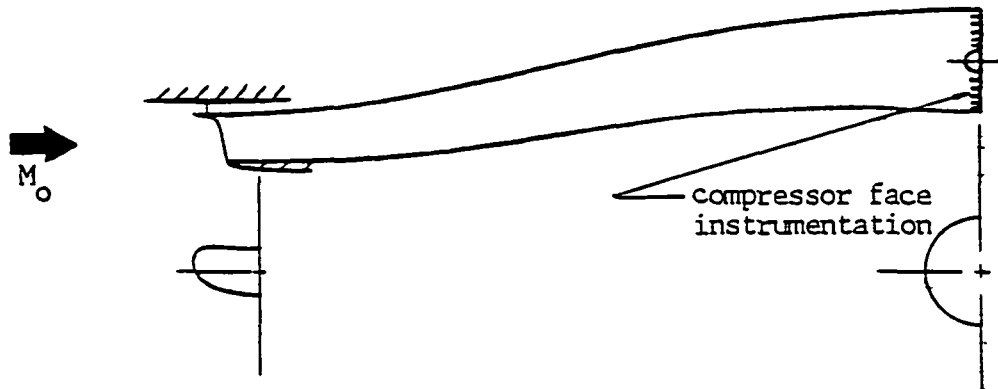


(b) Test Conditions and Some Measured Results:

Data pt.	Mach No.	$P_{t2}$	$\overline{rms}_m$	IDC <sub>max, peak</sub>
20.40	subsonic	.887	.0336	.225
54.30	subsonic	.853	.0478	.326
81.40	subsonic	.925	.0337	.127
111.30	subsonic	.868	.0537	.319
112.30	subsonic	.873	.0475	.329
137.50	subsonic	.926	.0360	.144

Figure 3. Illustration of a Subsonic Inlet Test Model and some Test Results (unpublished data from Air Force Flight Dynamics Laboratory, Wright-Patterson Air Force Base, Dayton, Ohio)

(a) Transonic .15 scale Inlet Model:

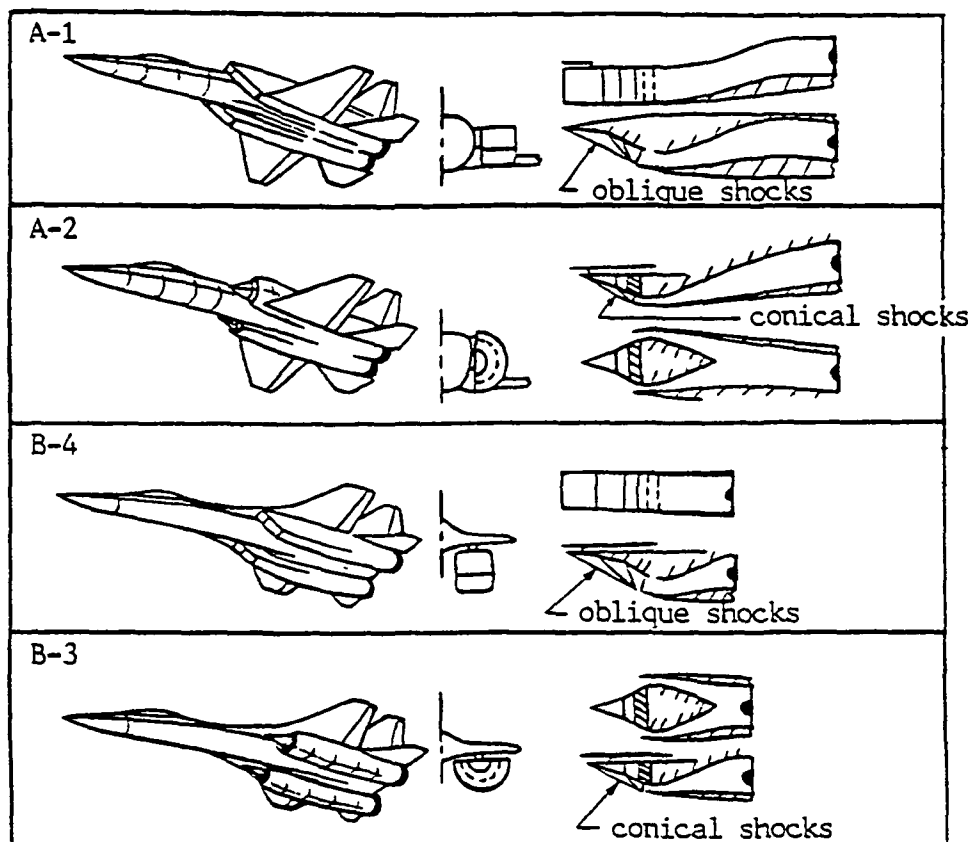


(b) Test Conditions and Some Measured Results:

Data pt.	Mach No.	$P_{t2}$	$\overline{rms}_m$	$K_{A2, peak}$
464.12	transonic	.860	.0422	.303
465.11	transonic	.912	.0281	.522
473.12	transonic	.928	.0217	.565
485.10	transonic	.891	.0414	.819
487.80	transonic	.857	.0493	1.025
498.12	transonic	.913	.0299	.777

Figure 4. Illustration of a Transonic Inlet Test Model and some Test Results (unpublished data from Air Force Flight Dynamics Laboratory, Wright-Patterson Air Force Base, Dayton, Ohio)

(a) Configurations of four .25 scale Tailor-Mate Model:



(b) Test Conditions and Some Measured Results:

Inlet	Data pt.	Mach No.	$\alpha$	$\beta$	$P_{t2}$	$IDC_{max}$	$K_{A2, peak}$
A-1	182/1	2.2	5	4	.833	.150	1.384
	189/3	2.2	15	0	.829	.076	1.020
	216/3	1.6	10	4	.894	.086	.900
A-2	243/3	2.2	5	4	.768	.078	1.123
	246/3	2.2	15	0	.666	.111	1.446
	247/2	2.2	15	4	.579	.163	1.572
B-4	433/3	2.2	0	0	.814	.090	1.254
	437/3	2.2	5	0	.872	.125	1.511
	1554/4	0.9	20	8	.918	.074	.597
B-3	640/2	2.2	5	-4	.945	.092	.887
	643/3	2.2	15	0	.935	.078	.738
	695/1	1.65	0	-8	.845	.136	1.271
	1334/2	0.9	25	4	.933	.121	.649

Figure 5. Illustration of four Supersonic Inlet Test Model and some Test Results (ref. 36)

HiMAT Data Set:		Other Available Inlet Data:	
Symbol	Mach no.	Symbol	Mach no.
$\Delta$	0.6	$\Delta$	subsonic
$\odot$	0.9	$\odot$	transonic

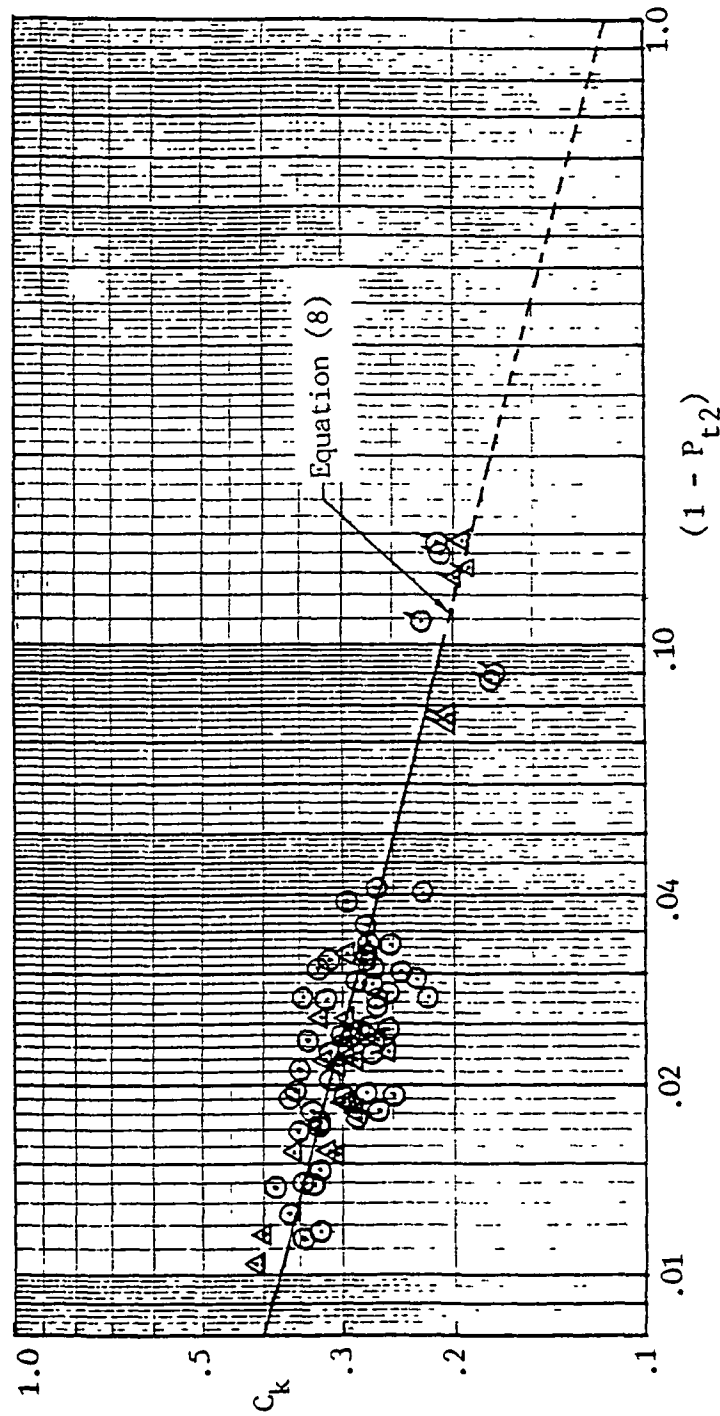


Figure 6. Linear Regression of  $\log_{10} C_k$  on  $\log_{10} (1 - P_{t2})$  for HiMAT Inlet Data at Subsonic and Transonic Speeds



ORIGINAL PAGE IS  
OF POOR QUALITY

HiMAT Data Set:

Symbol	Mach no.
□	1.2
▽	1.36

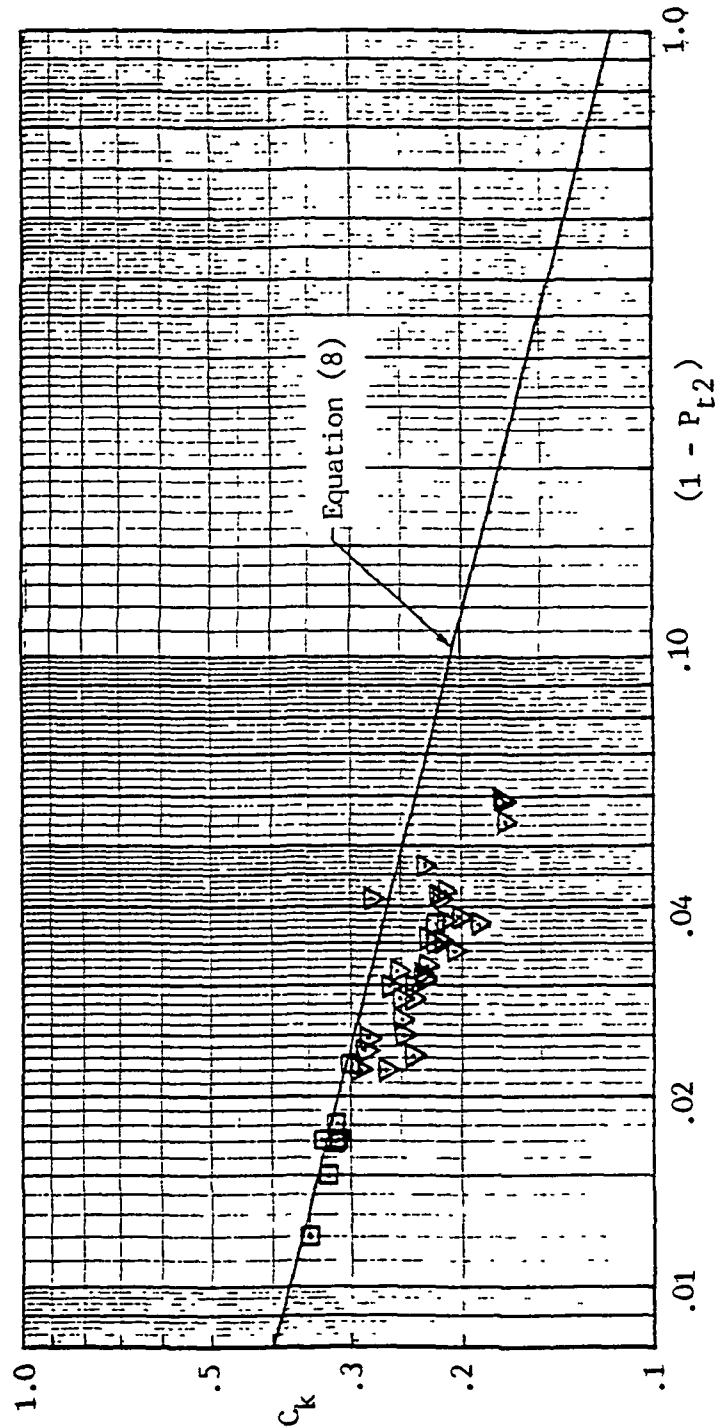


Figure 7. Test of the Regression Equation on HiMAT Inlet Test Data at Supersonic Speed

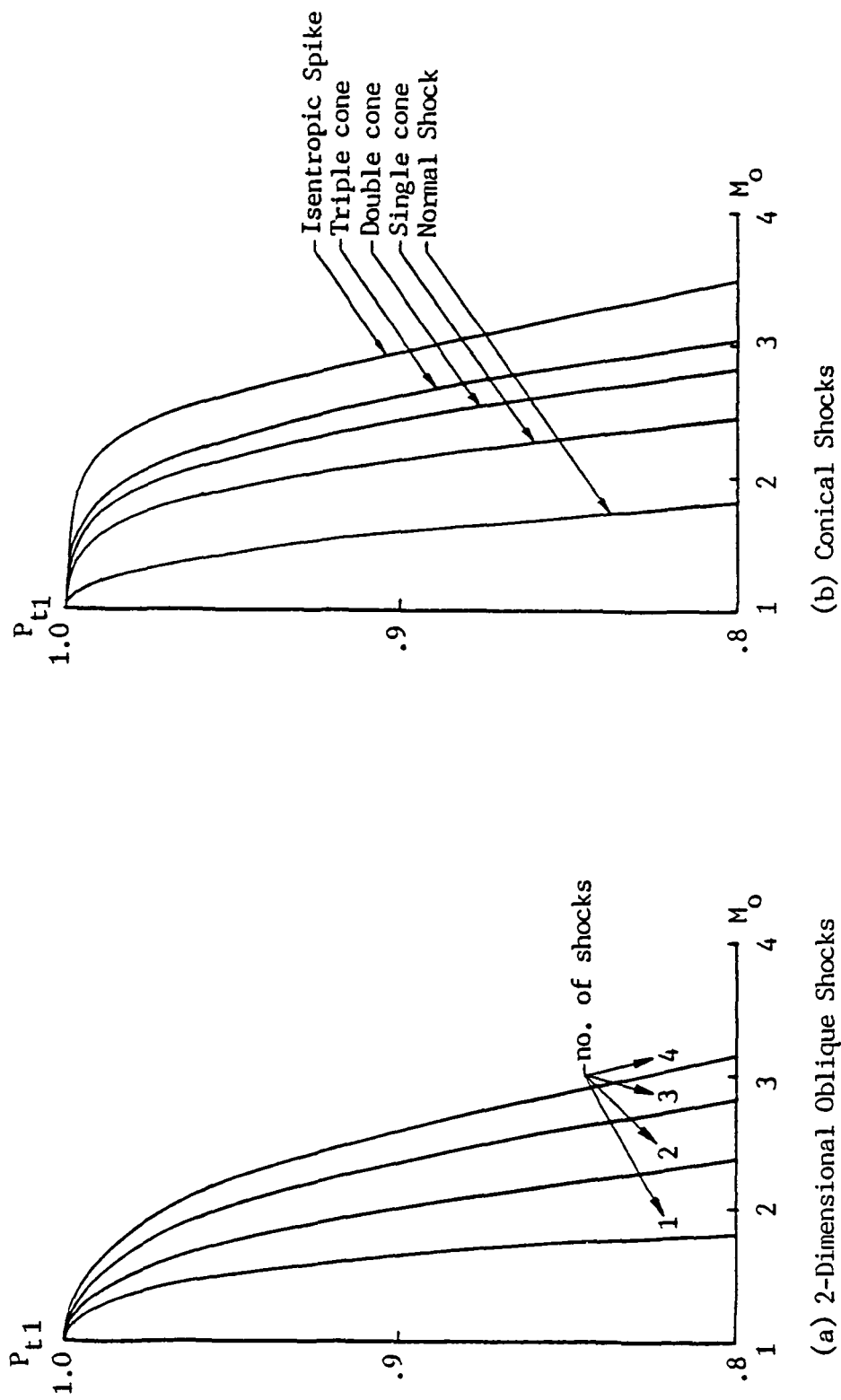


Figure 8. Maximum Total Pressure Recovery of Oblique and Conical Inlet Shock Systems (Ref. 28)

HiMAT Data Set:			Melick's Test Cases:		
Symbol	Mach no.	$P_{t1}$	Symbol	Mach no.	$P_{t1}$
□	1.2	0.995	⊖	1.6	0.995
▽	1.36	0.990	⊗	2.5	0.900

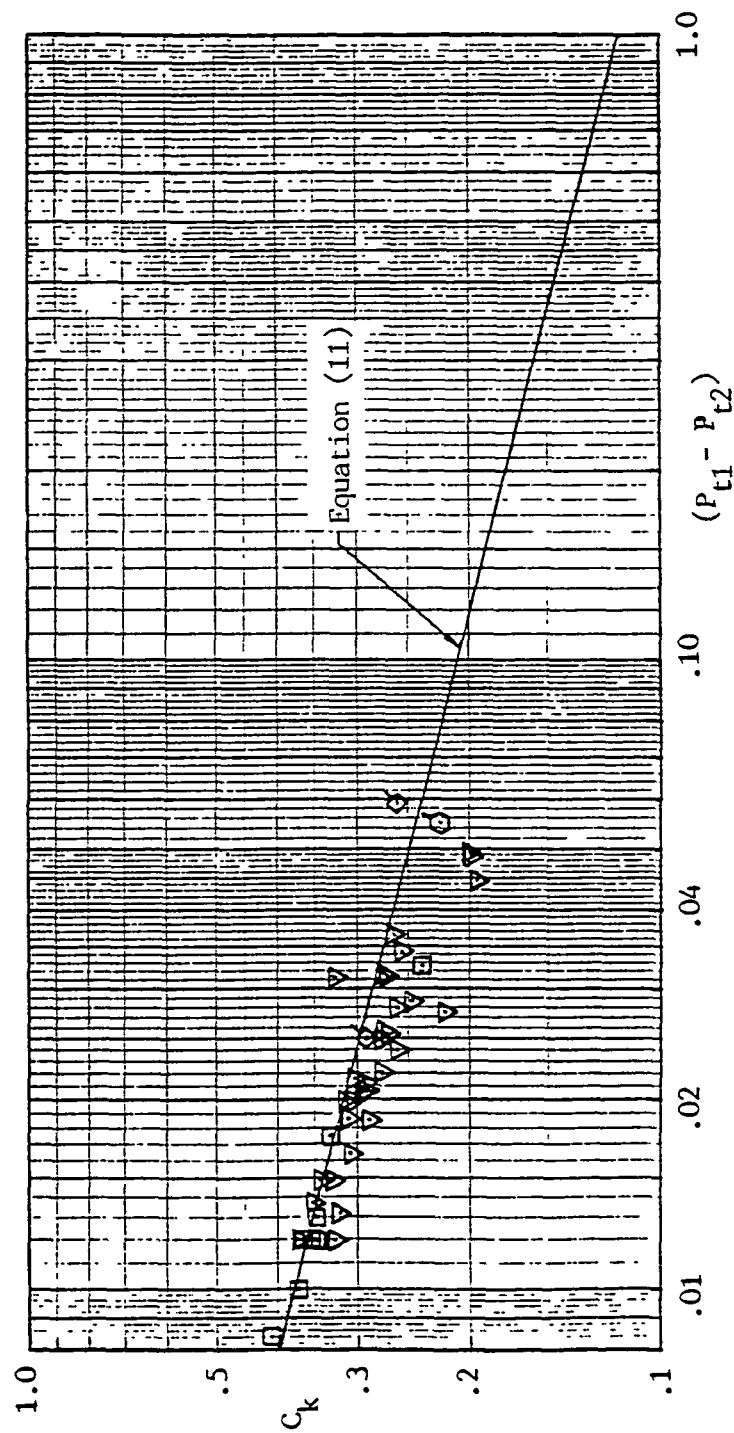


Figure 9. Linear Regression of  $\log_{10} C_k$  on  $\log_{10} (P_{t1} - P_{t2})$  for Inlet Test Data at Supersonic Speed

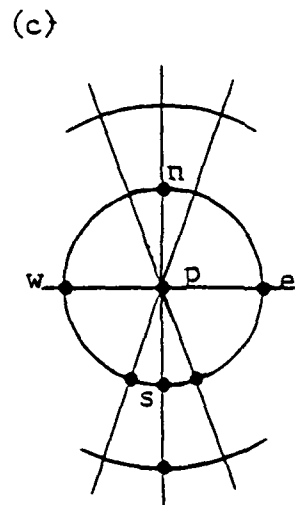
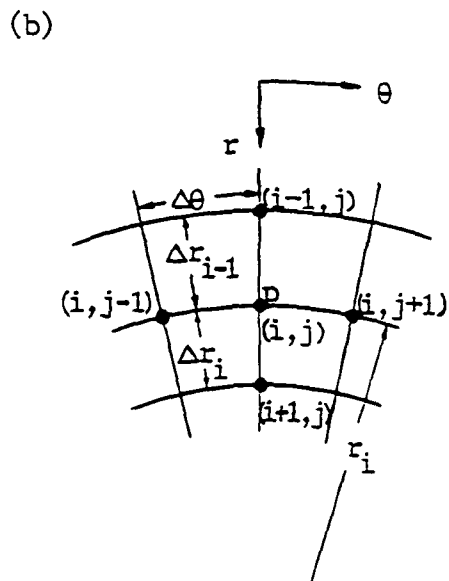
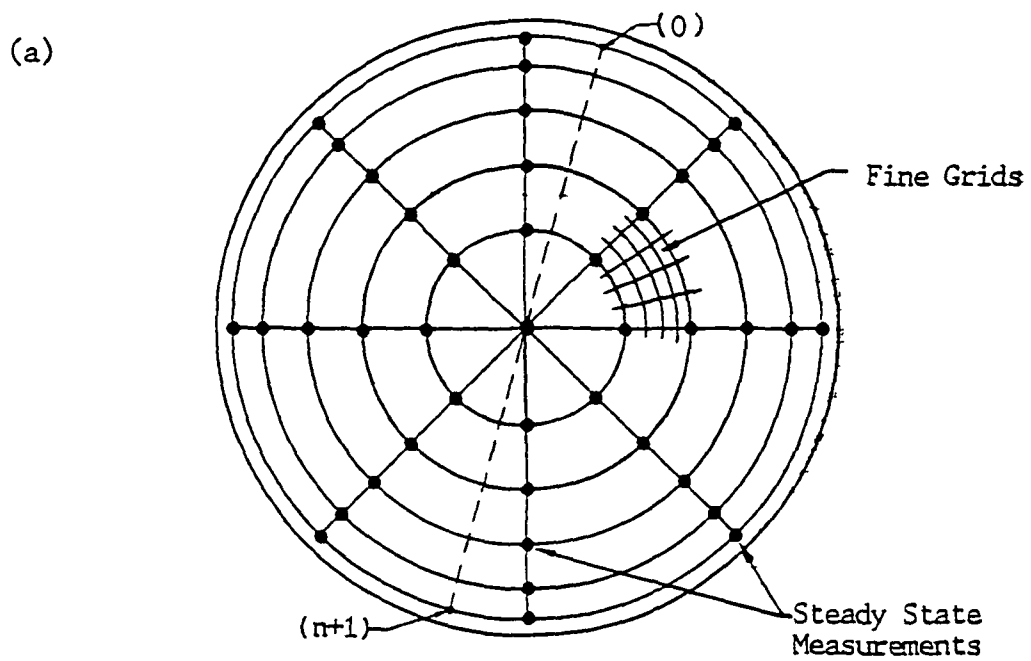


Figure 10. Schematic Illustration of Computational Grid System for Finite Difference Scheme

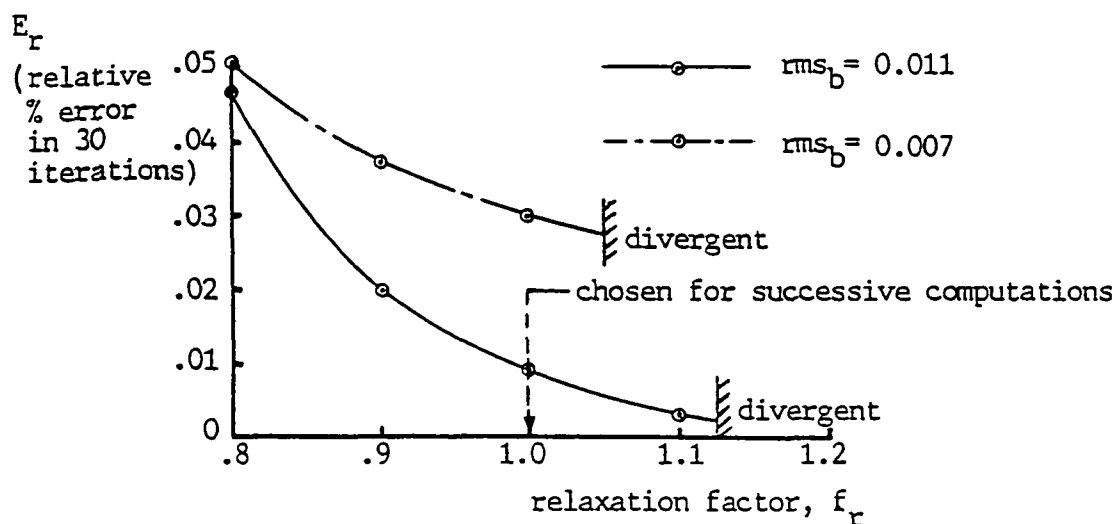


Figure 11. Study of Numerical Convergence

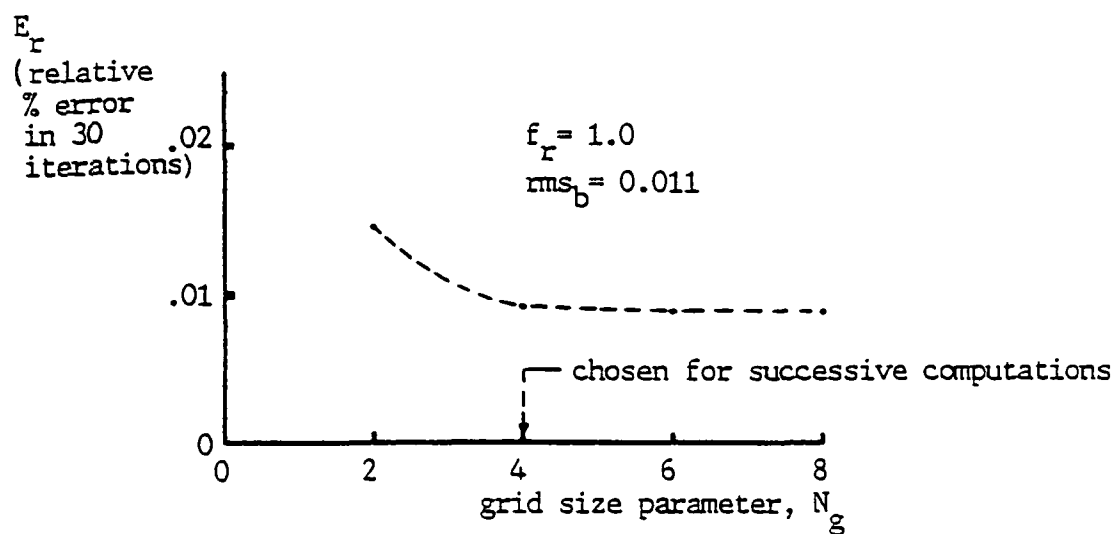
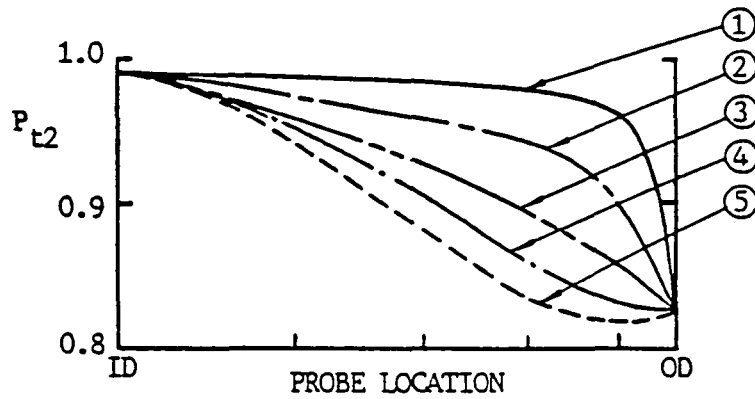
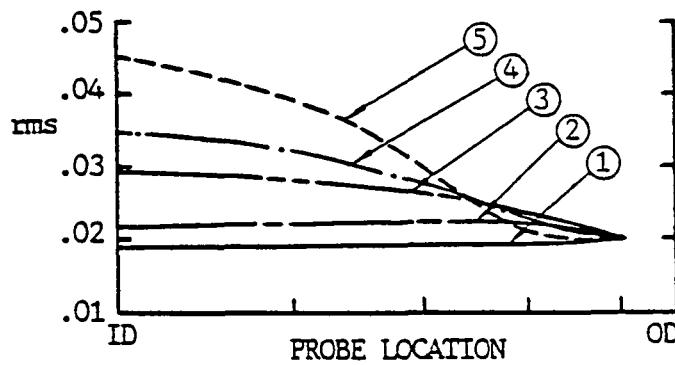


Figure 12. Effect of Grid Size on the Accuracy of Computation

(a) Assumed four total pressure profiles:



(b) Resultant rms distributions:



(c) Comparisons of Dynamic Contributions:

Profile	$\overline{rms}_p$	Dynamic Contribution ( $K_{A2,peak} - K_{A2,ss}$ )
————— ①	.0195	.1720
- - - - - ②	.0217	.2382
- . - . - ③	.0257	.3407
- . . . - ④	.0283	.4880
- - - - - ⑤	.0326	.6688

Figure 13. Effect of Radial Total Pressure Distributions (equivalent to velocity distributions) on the Predicted rms Distributions and Dynamic Peak Distortions

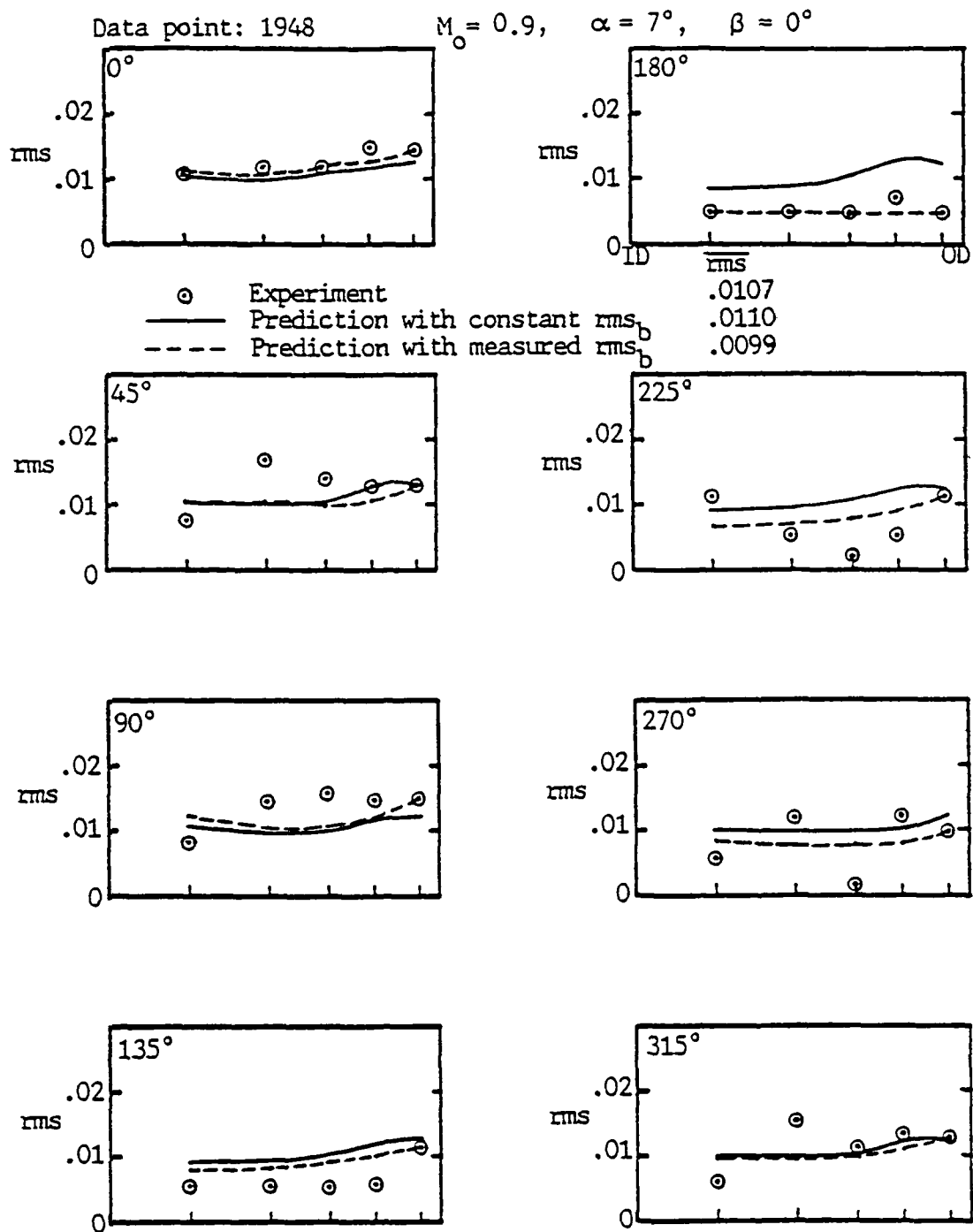


Figure 14. Effect of Boundary rms Distributions on the Prediction

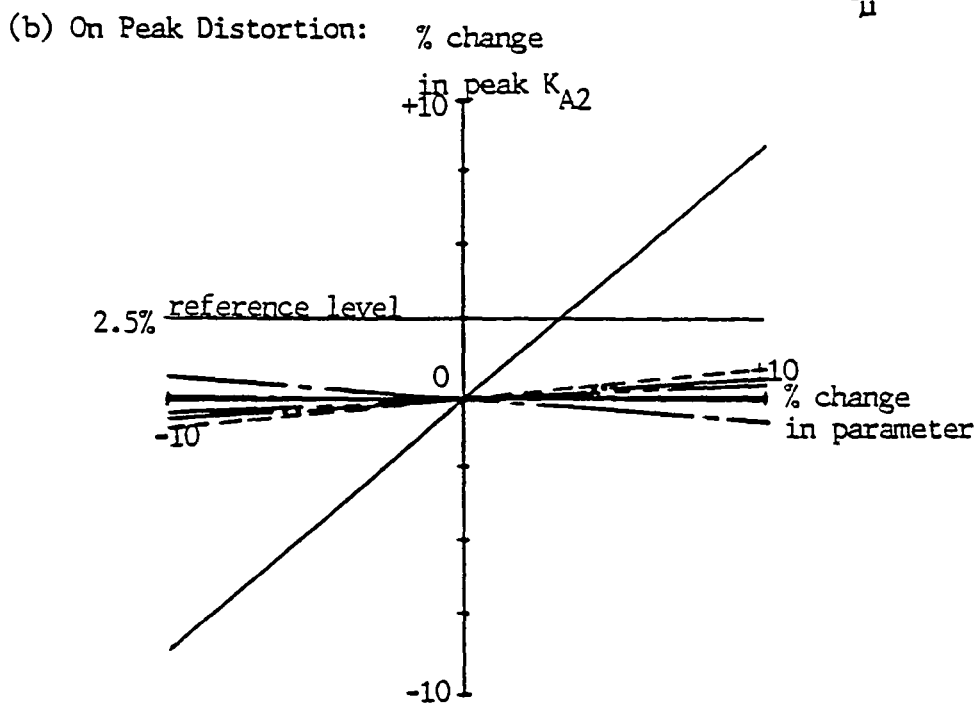
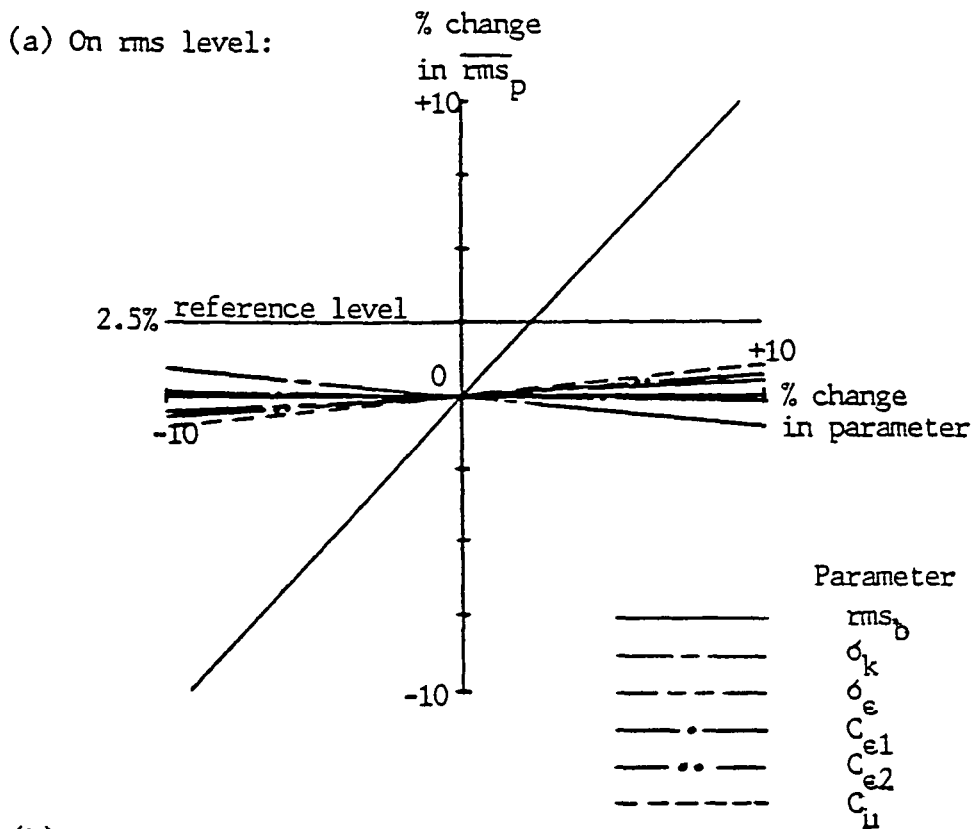


Figure 15. Sensitivities of the predicted rms level and peak distortion to several parameters of the computational scheme



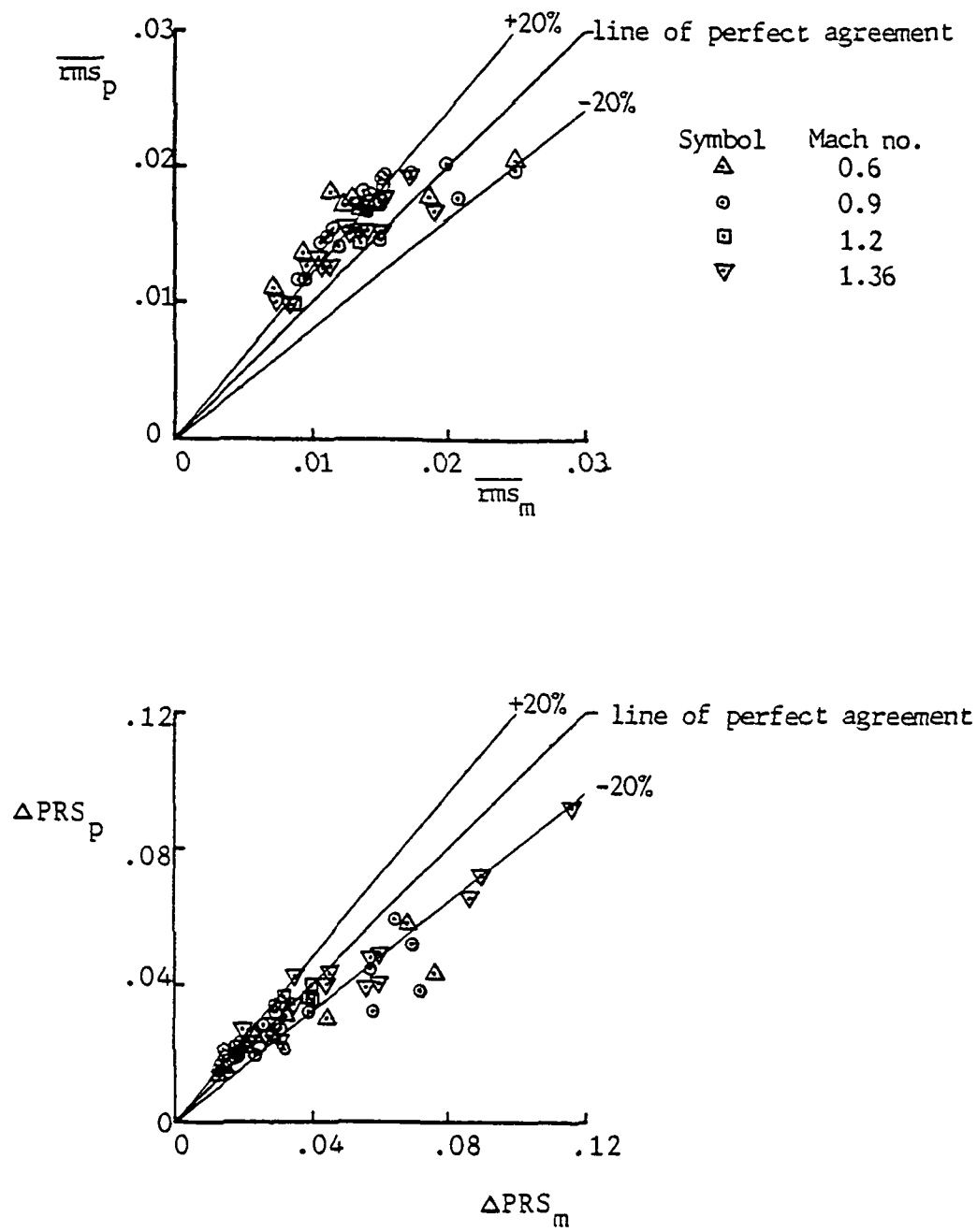


Figure 16. Comparisons of the Predicted and Measured rms Levels and Peak Distortion Factor for HiMAT Inlet Model without Vortex Generators (ref. 34, see Figure 1)

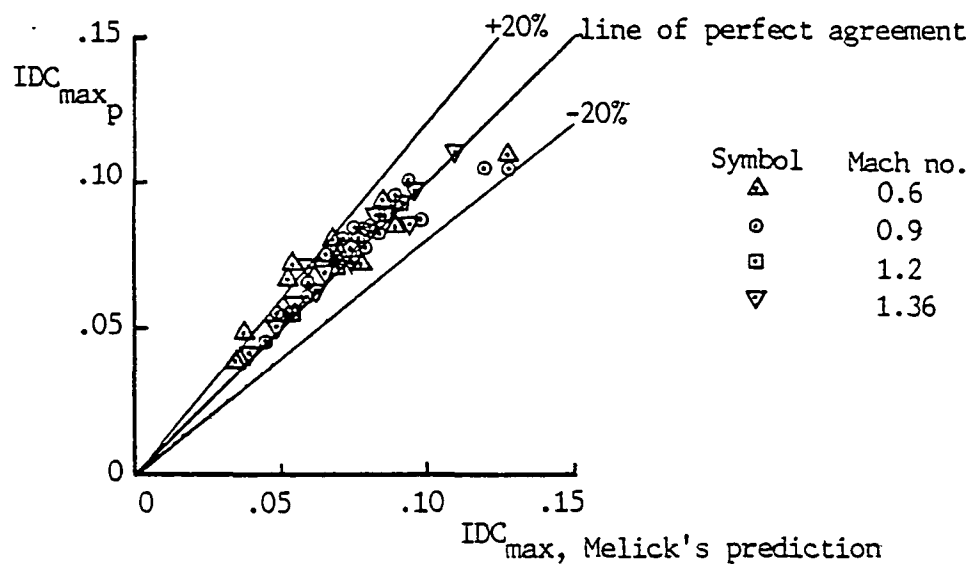


Figure 17. Comparisons of peak distortion factors predicted by the present analysis and Melick's statistical method based on the total pressure rms measurements for HiMAT inlet data set without vortex generators (ref. 34, see Figure 1)

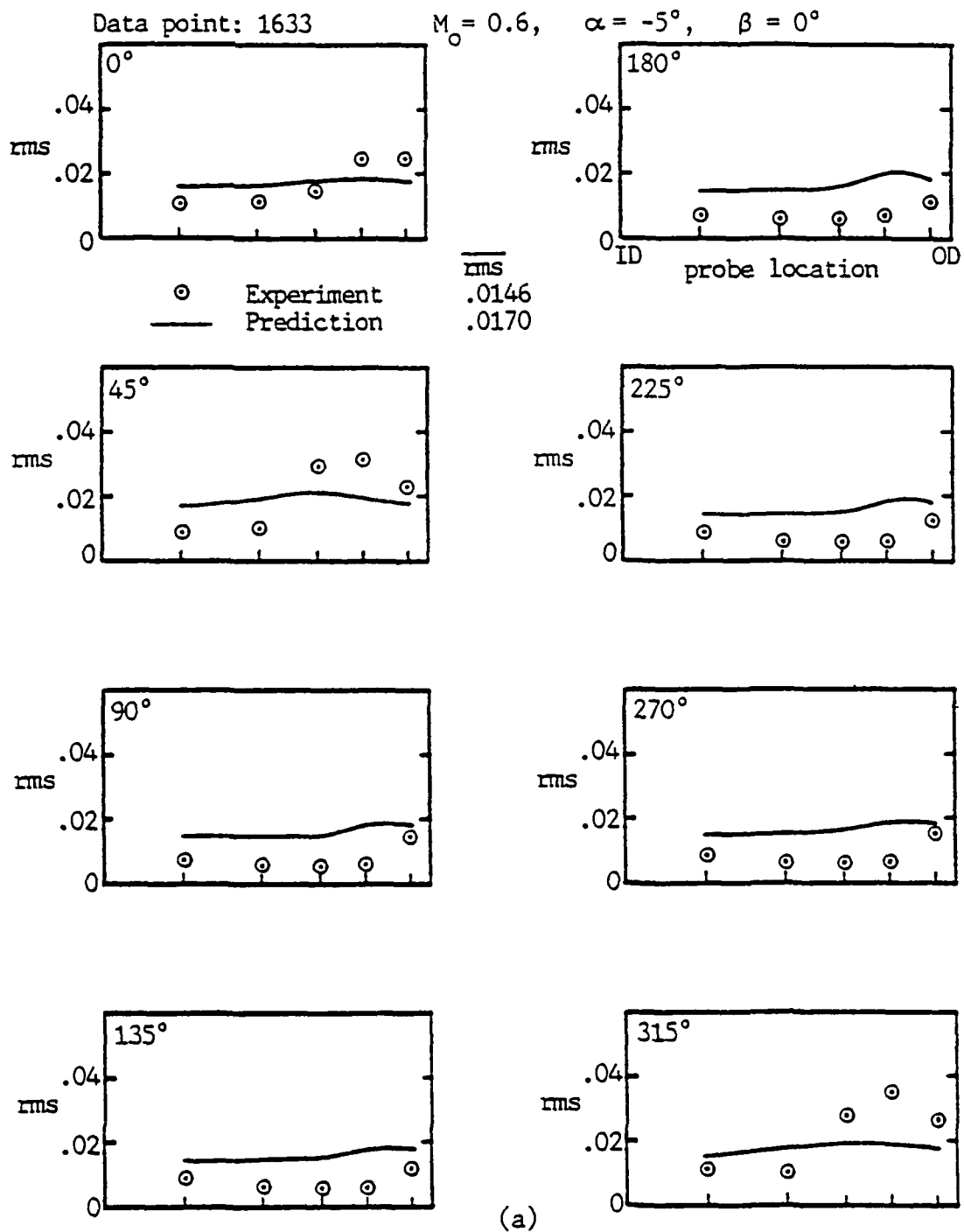


Figure 18. Comparisons of the Predicted and Measured rms Distributions for HiMAT Inlet Model without Vortex Generators (ref. 34, see Figure 1)

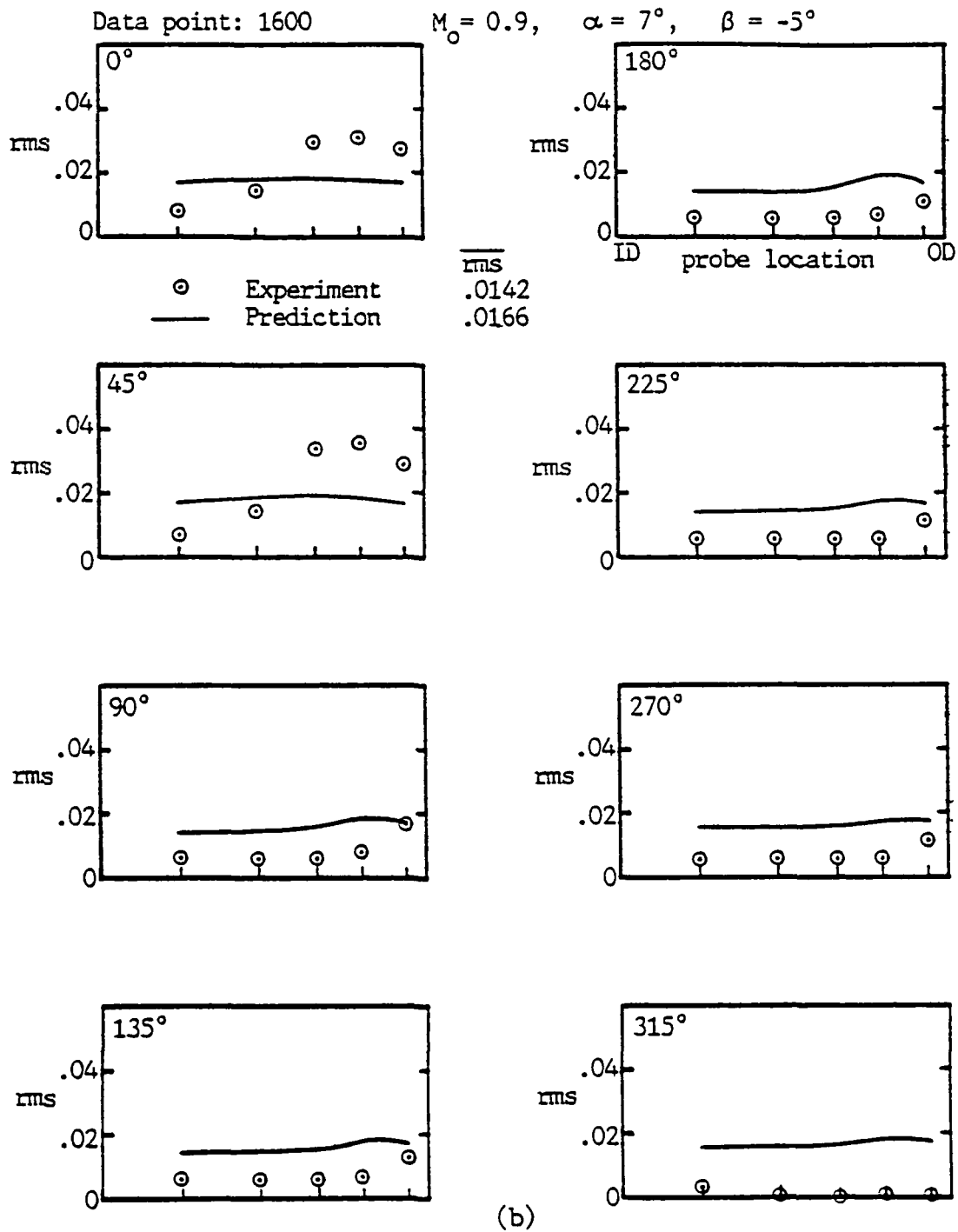


Figure 18. Continued

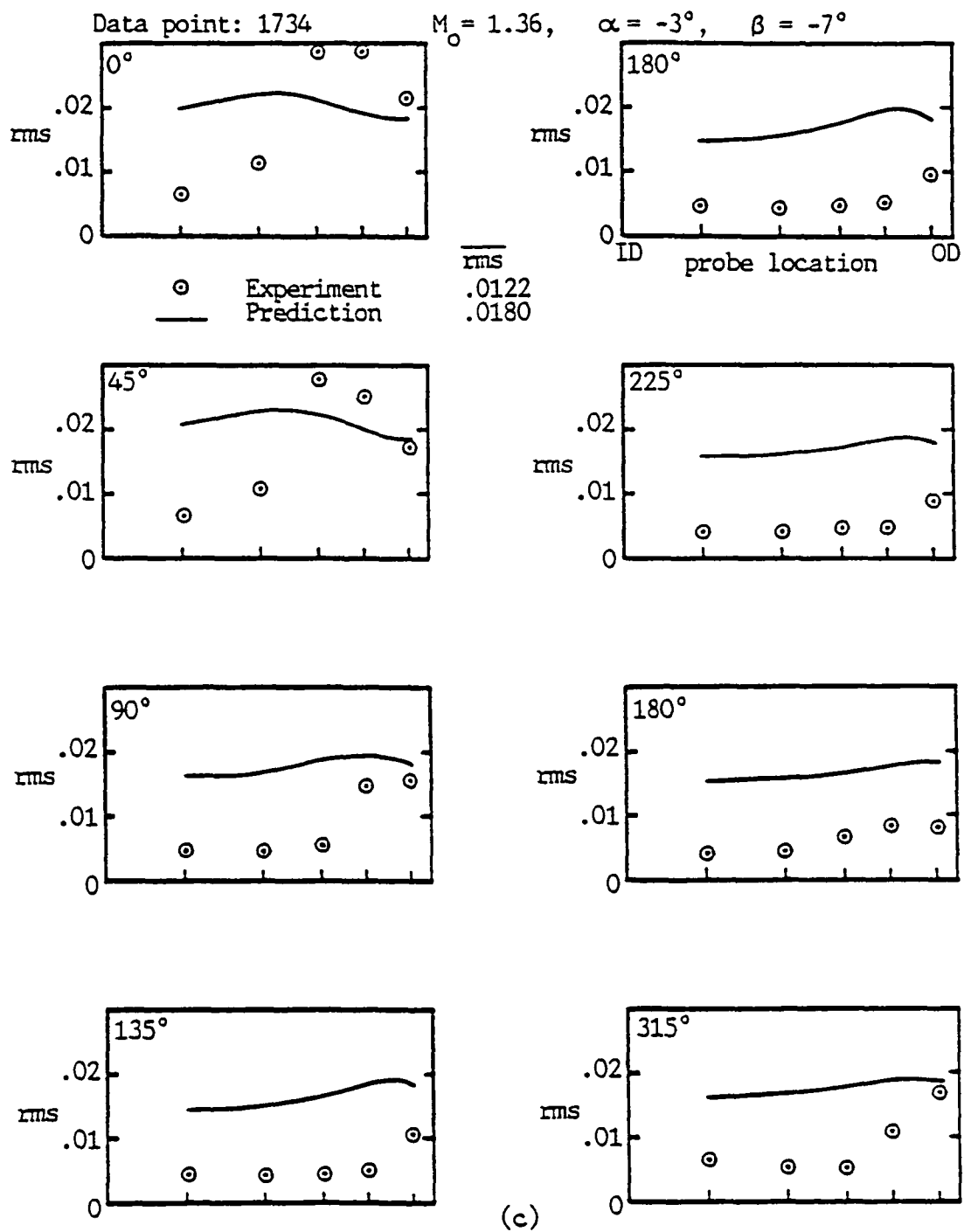


Figure 18. Concluded.

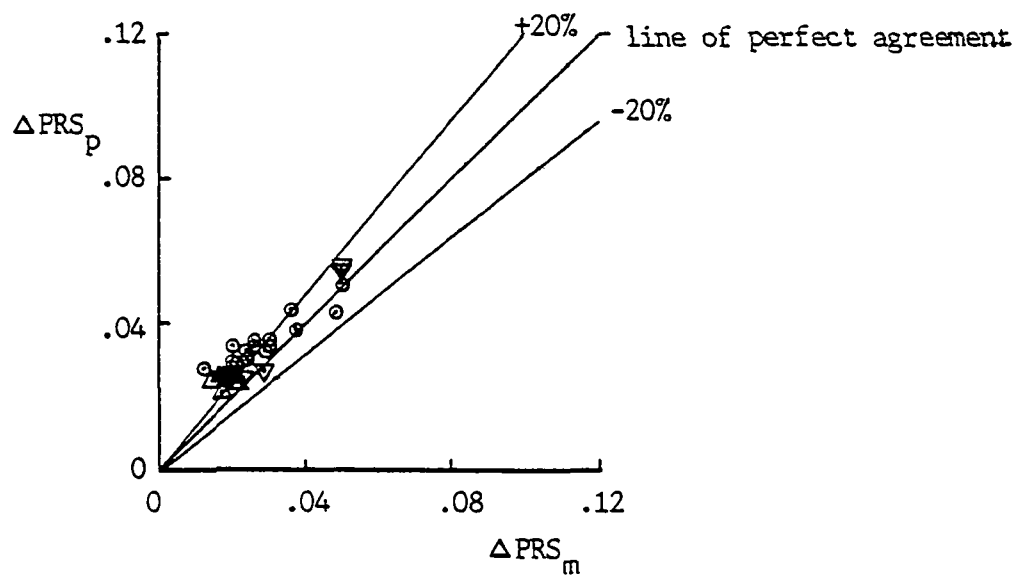
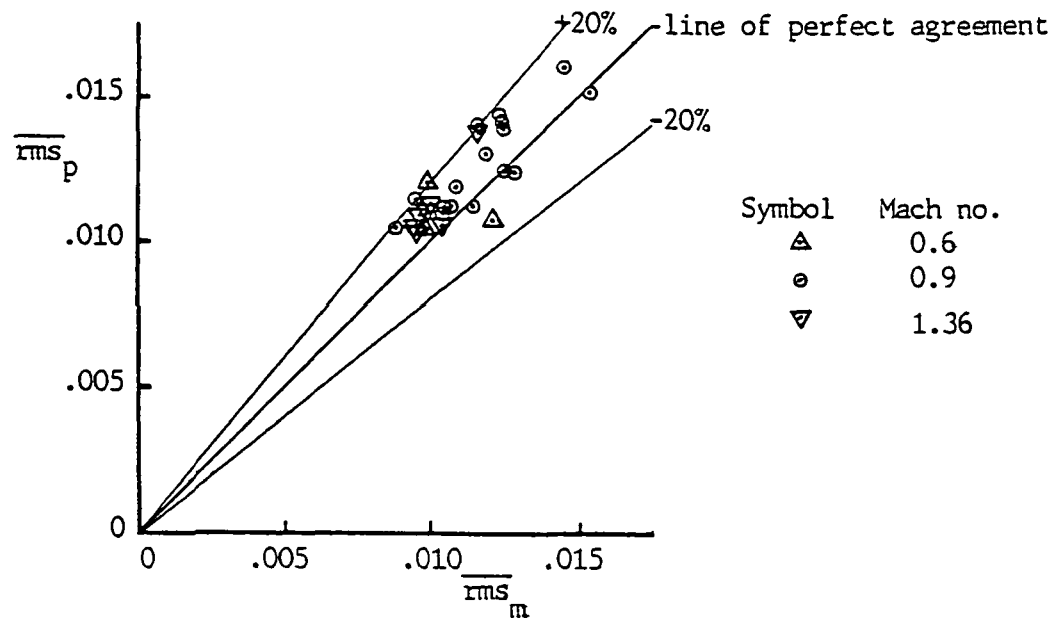


Figure 19. Comparisons of the Predicted and Measured rms Levels and Peak Distortion Factors for HiMAT Inlet Model with Vortex Generators (ref. 34, see Figure 1)

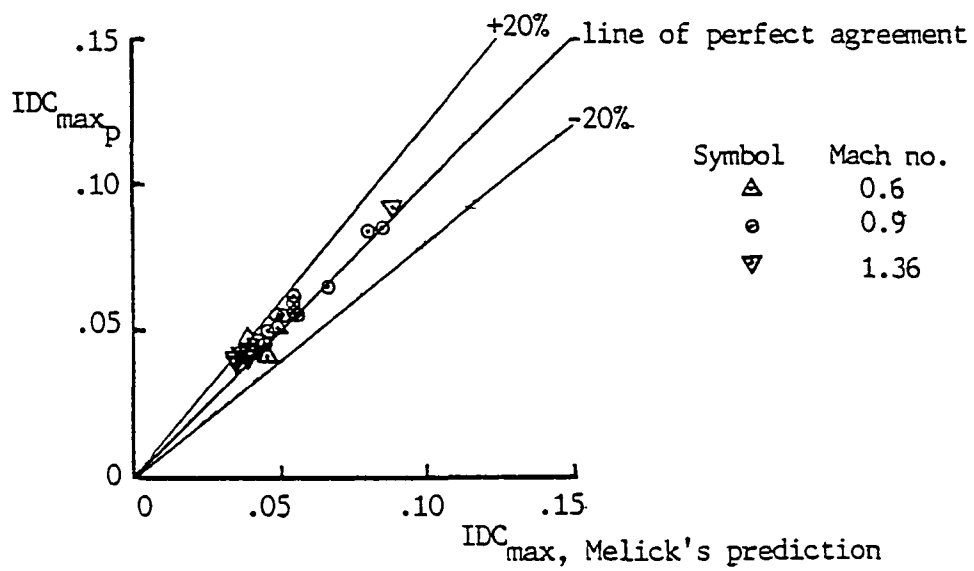


Figure 20. Comparisons of peak distortion factors predicted by the present analysis and the Melick method based on the total pressure rms measurements for the HiMAT data set with vortex generators (ref. 34, see Figure 1)

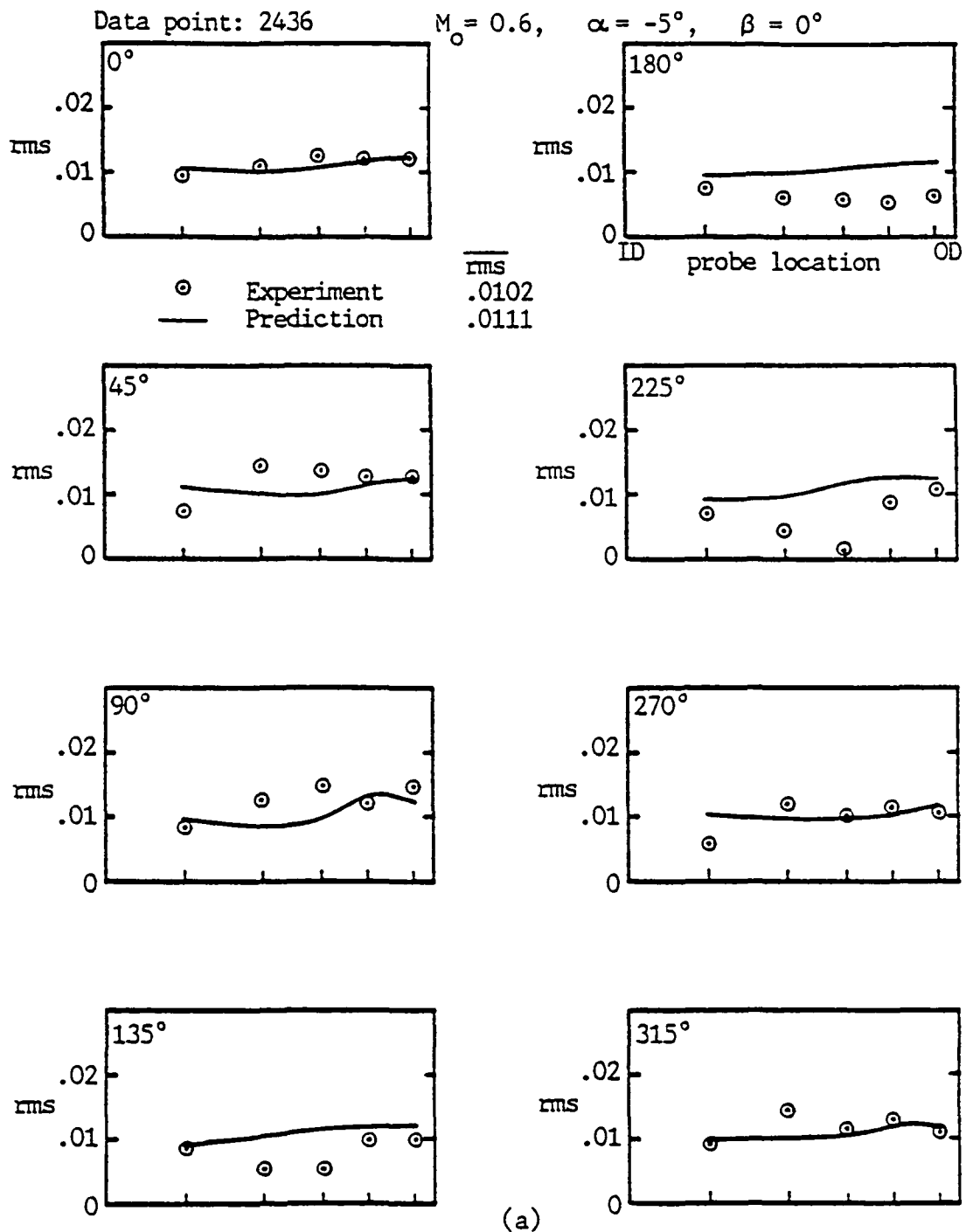


Figure 21. Comparisons of the Predicted and Measured rms Distributions for HiMAT Inlet Model with Vortex Generators (ref. 34, see Figure 1)



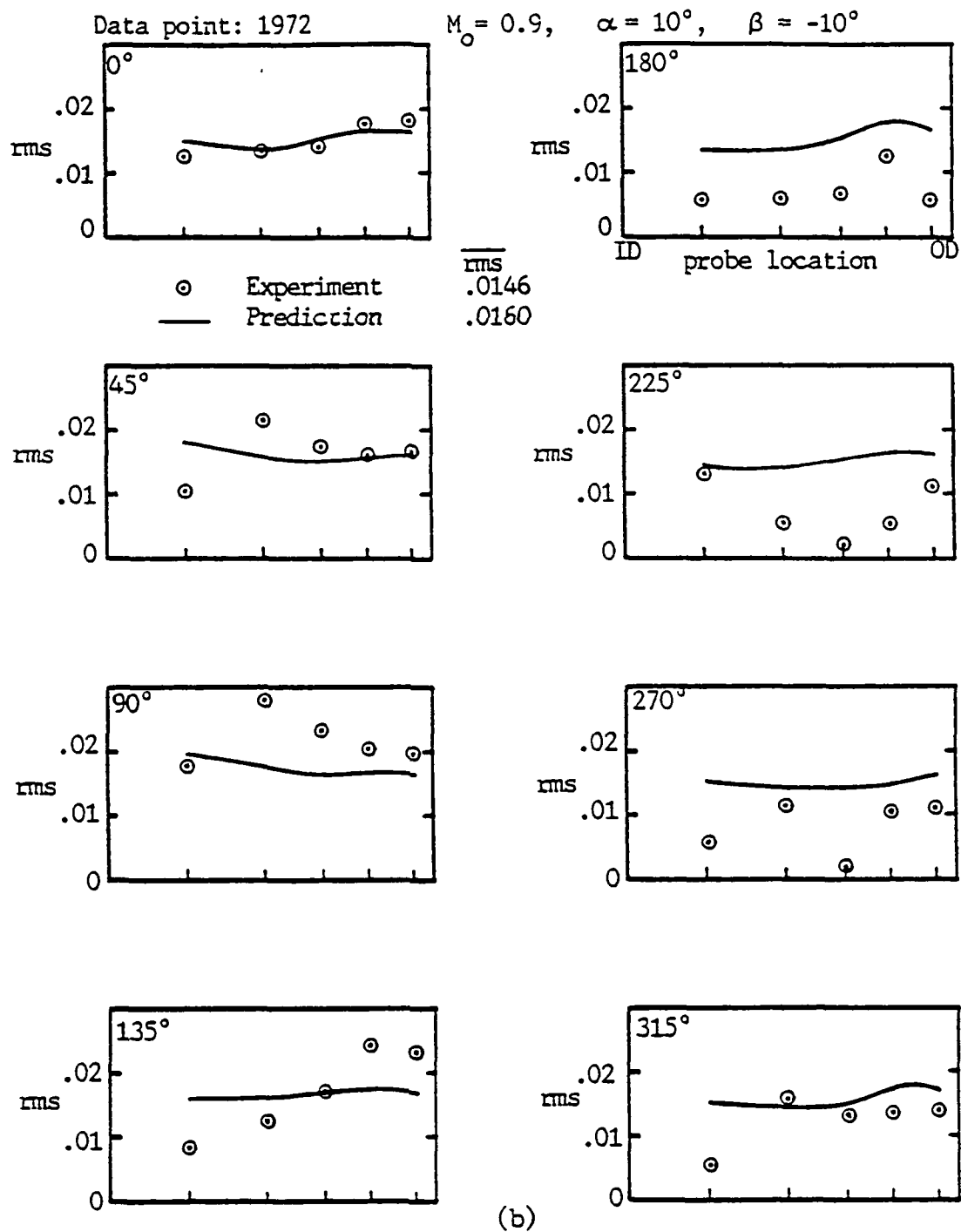


Figure 21. Continued

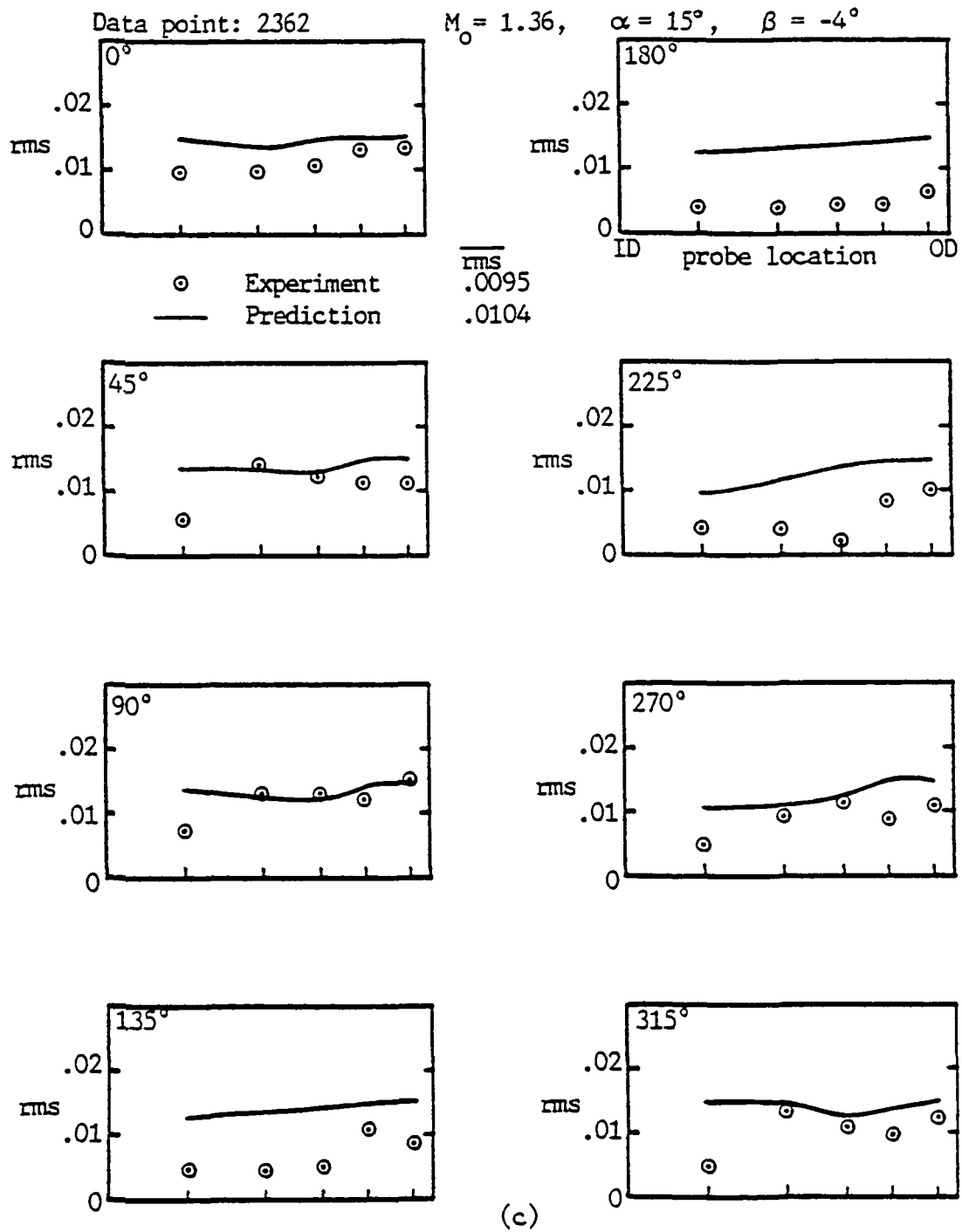


Figure 21. Concluded.

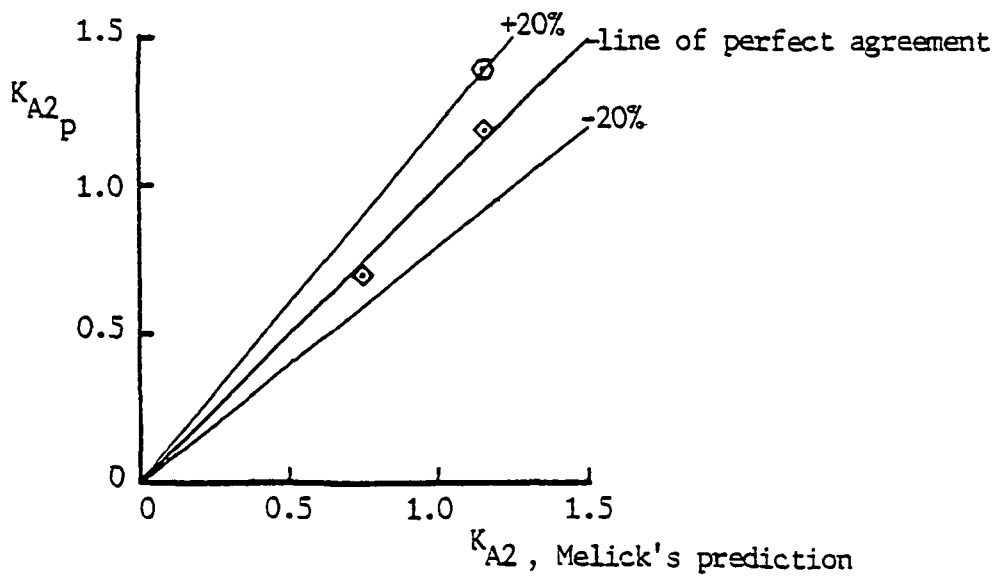
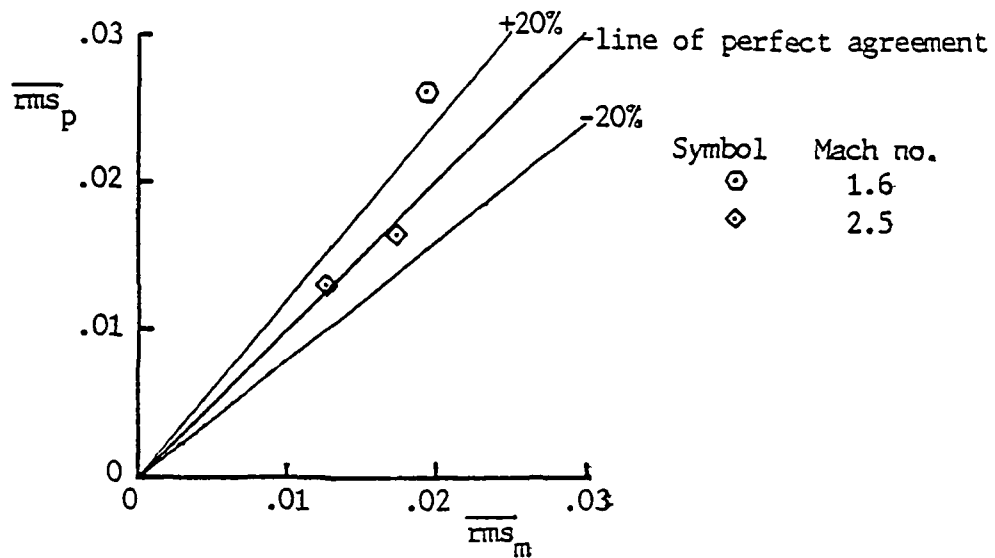


Figure 22. Comparisons of the Predicted and Measured rms Levels and Peak Distortion Factor for Melick's Test Cases (ref. 35, see Figure 2)

C-3

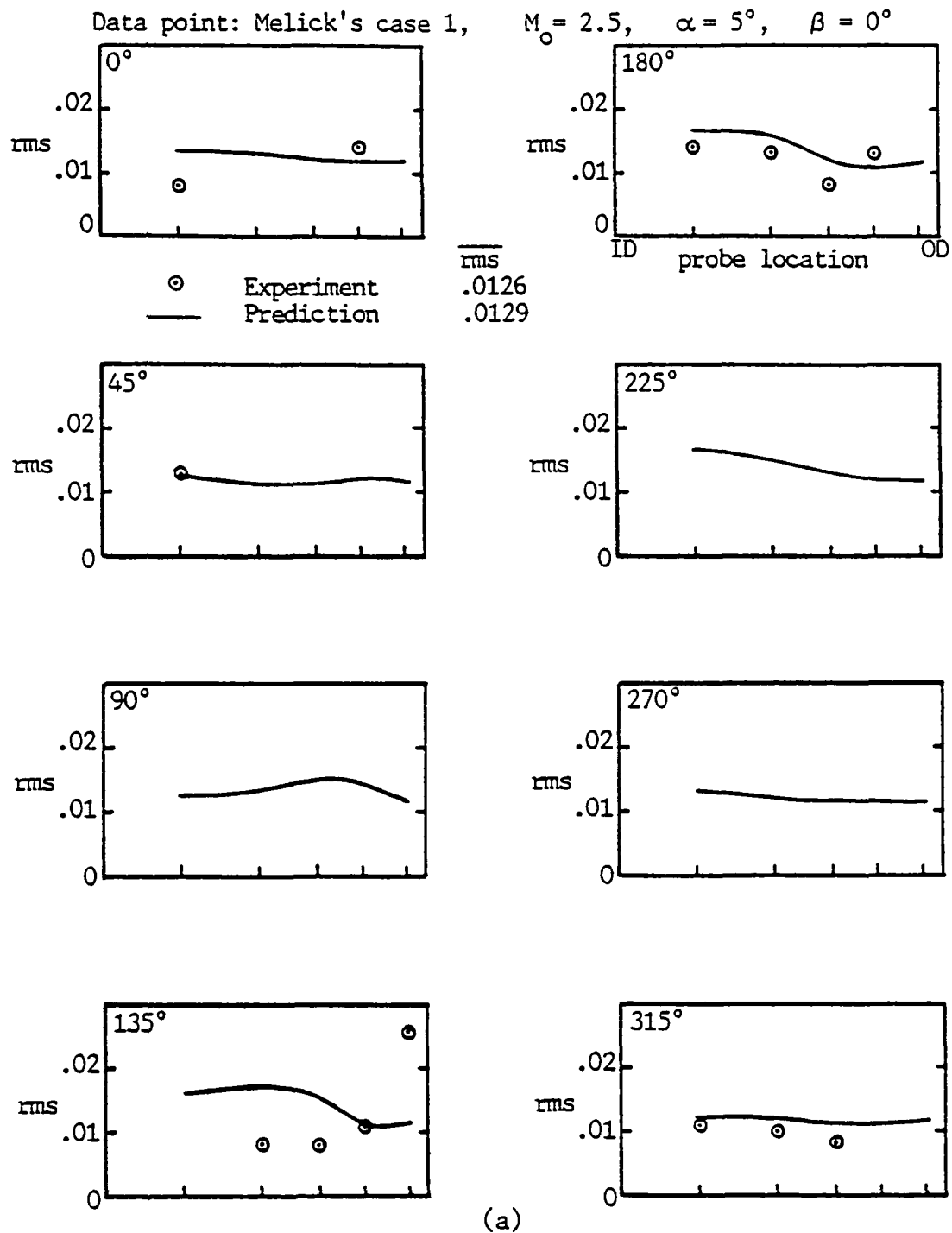


Figure 23. Comparisons of the Predicted and Measured rms Distributions for Melick's Test Cases (ref. 35, see Figure 2)

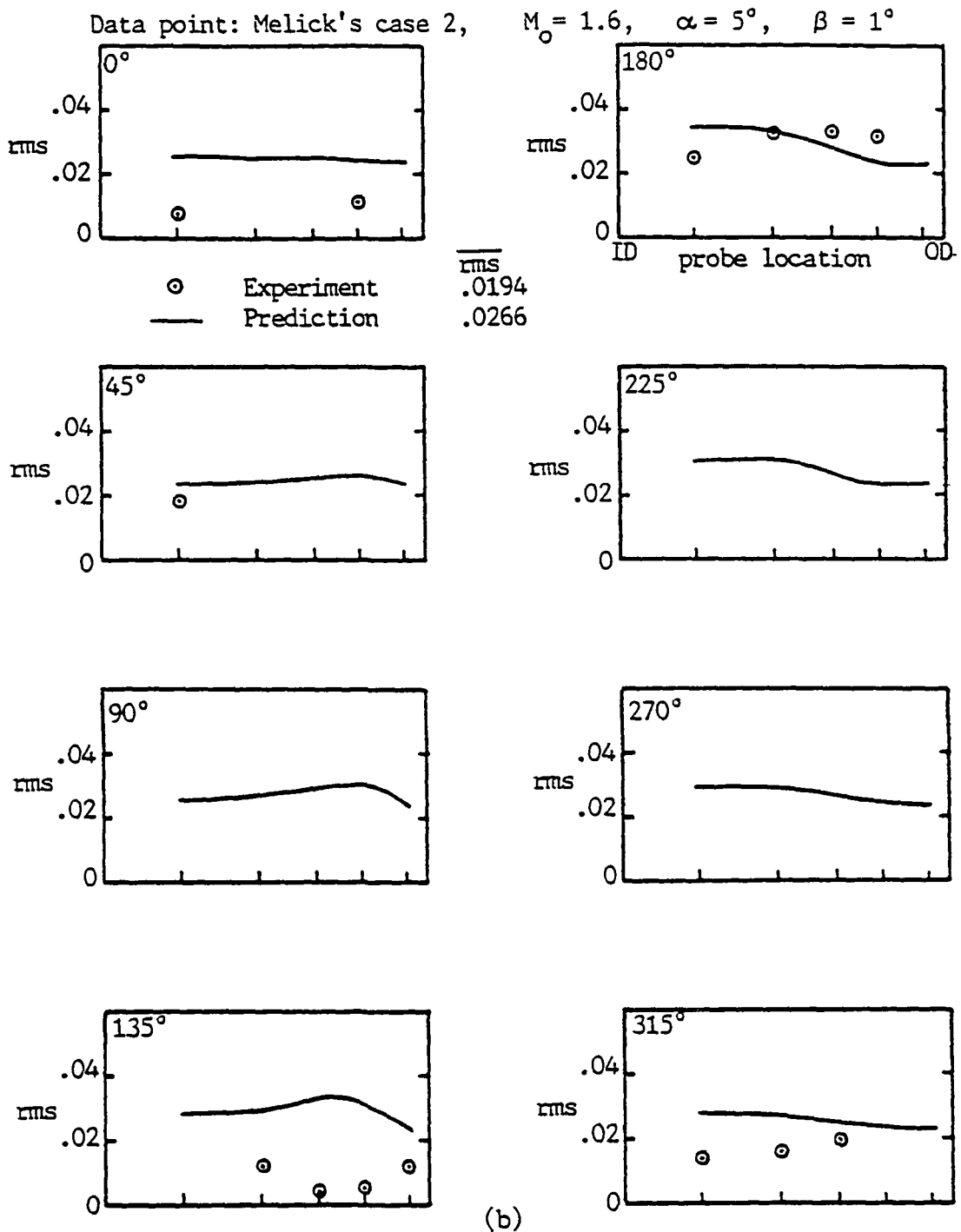


Figure 23. Continued

*[Handwritten signature]*

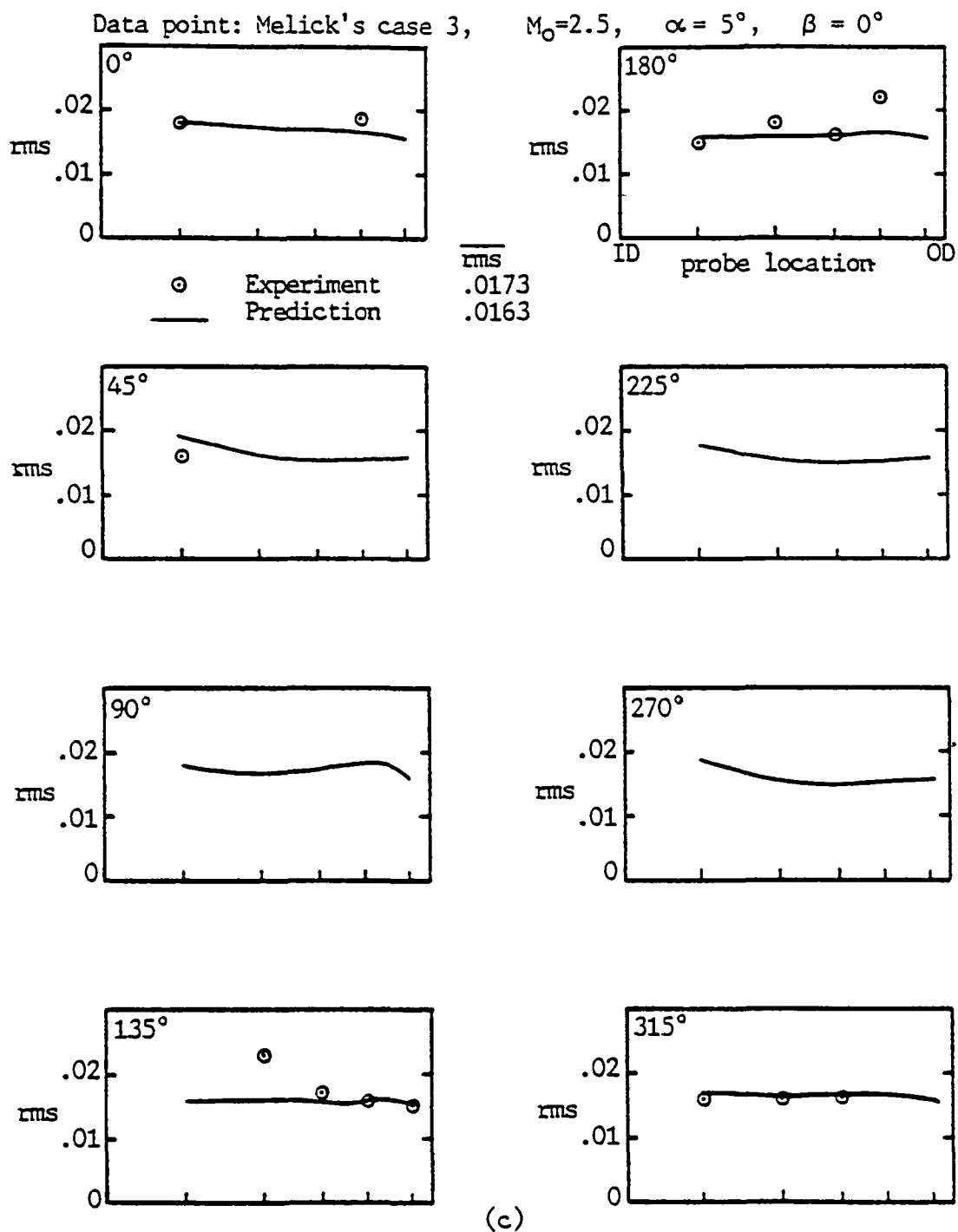


Figure 23. Concluded.

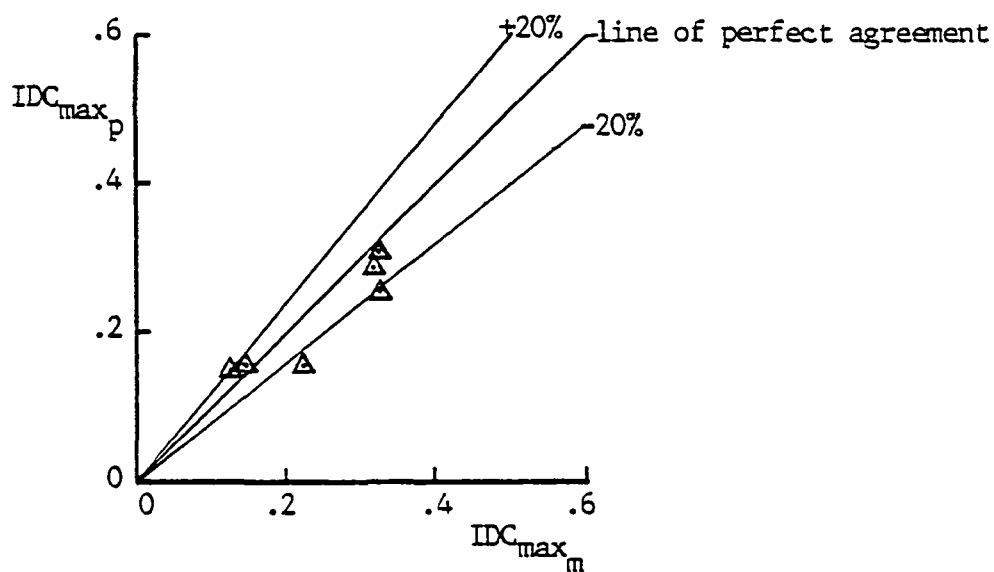
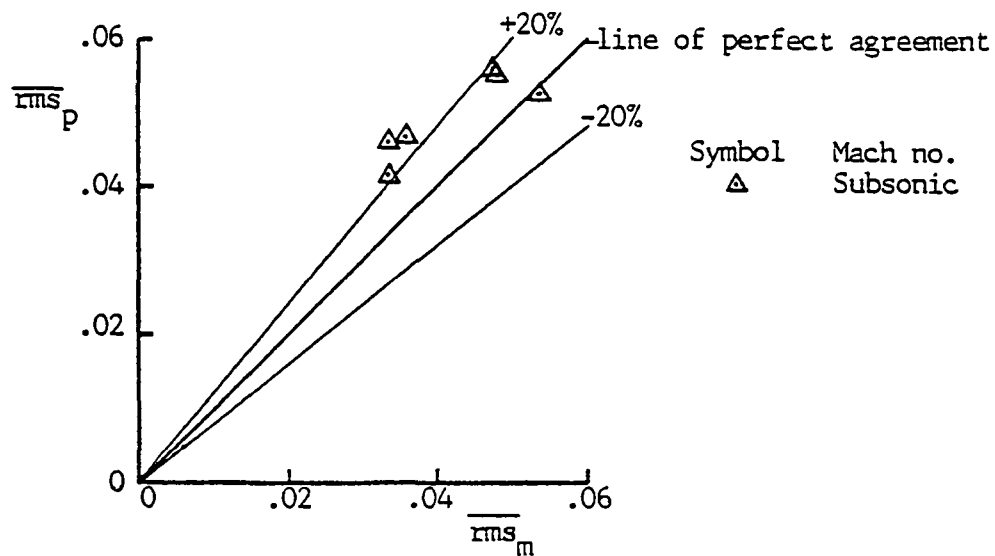


Figure 24. Comparisons of the Predicted and Measured rms Level and Peak Distortion Factor for the Subsonic Inlet Model shown in Figure 3. (unpublished data)

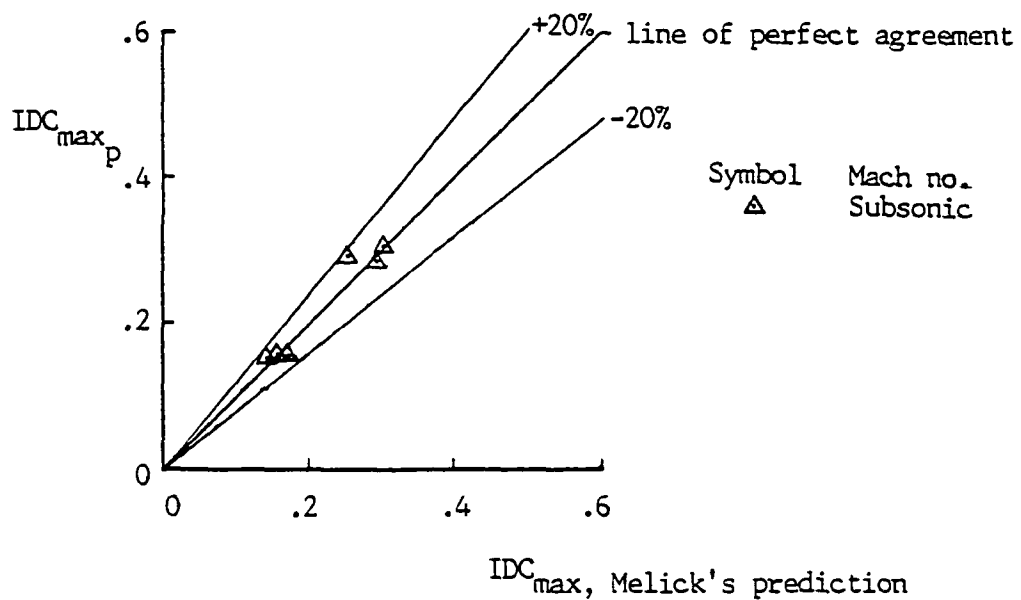


Figure 25. Comparisons of peak distortion factors predicted by the present analysis and the Melick method based on the total pressure rms measurements for the subsonic inlet data set (unpublished data)



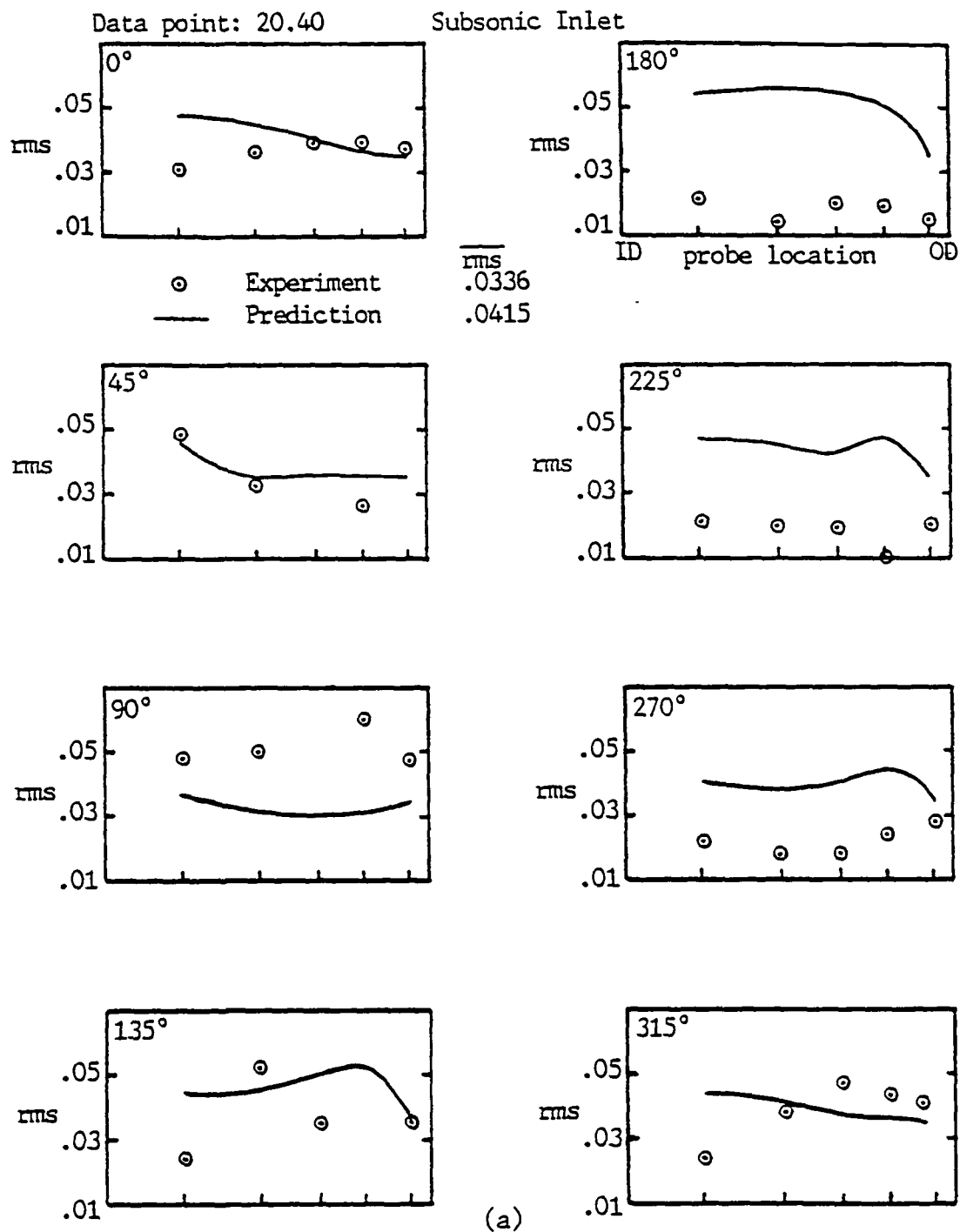


Figure 26. Comparisons of the Predicted and Measured rms Distributions for the Subsonic Inlet Model shown in Figure 3. (unpublished data)

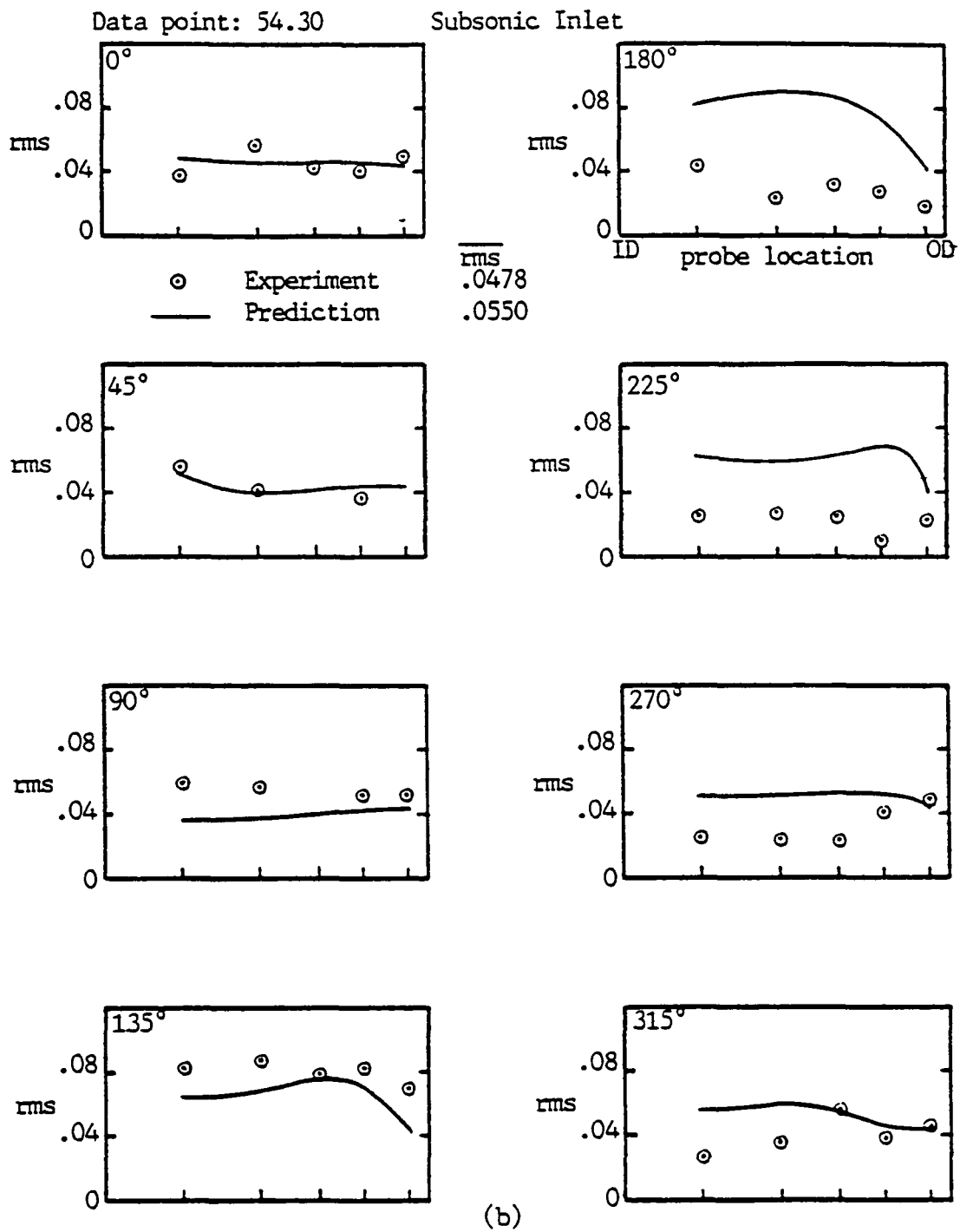


Figure 26. Continued

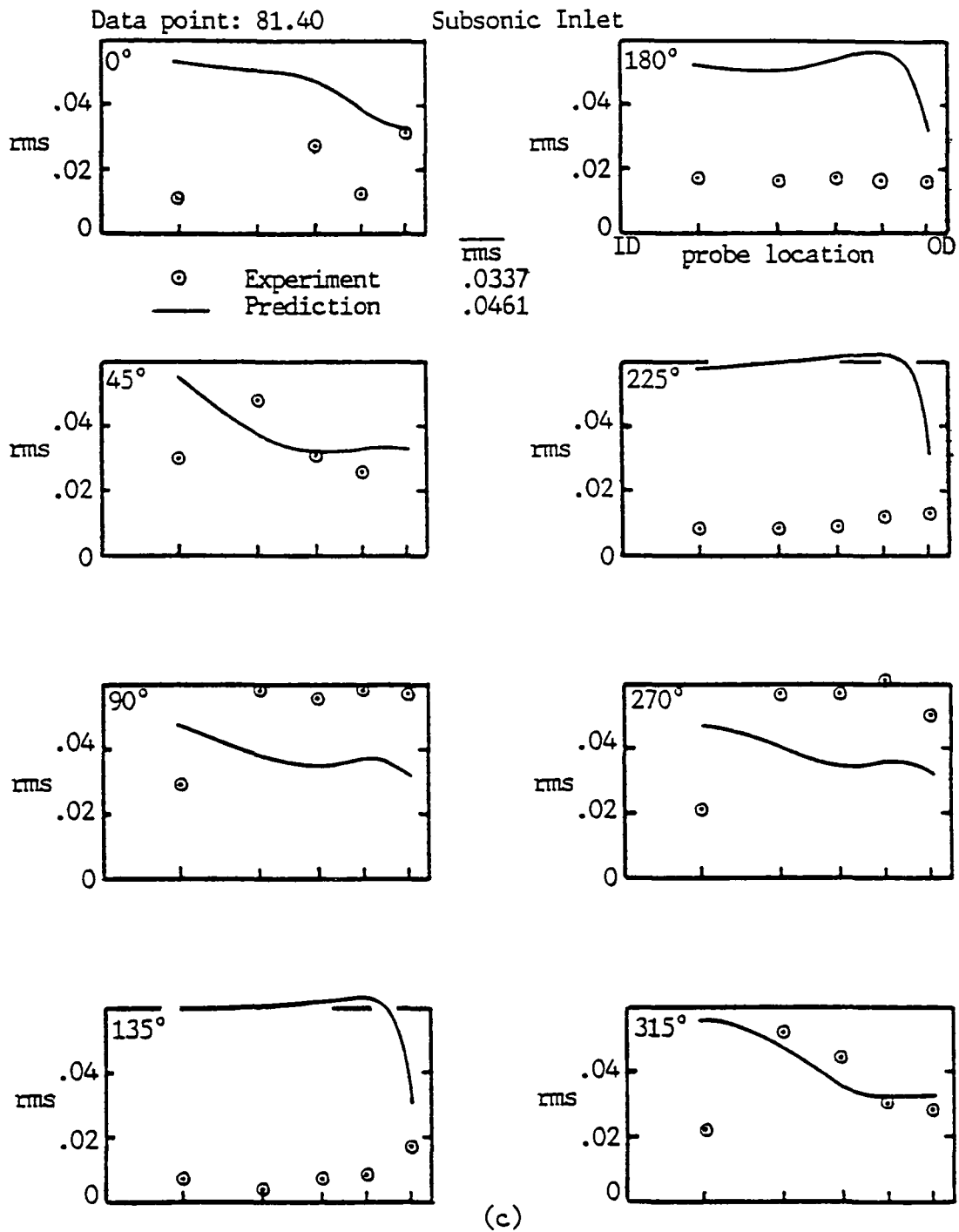


Figure 26. Continued

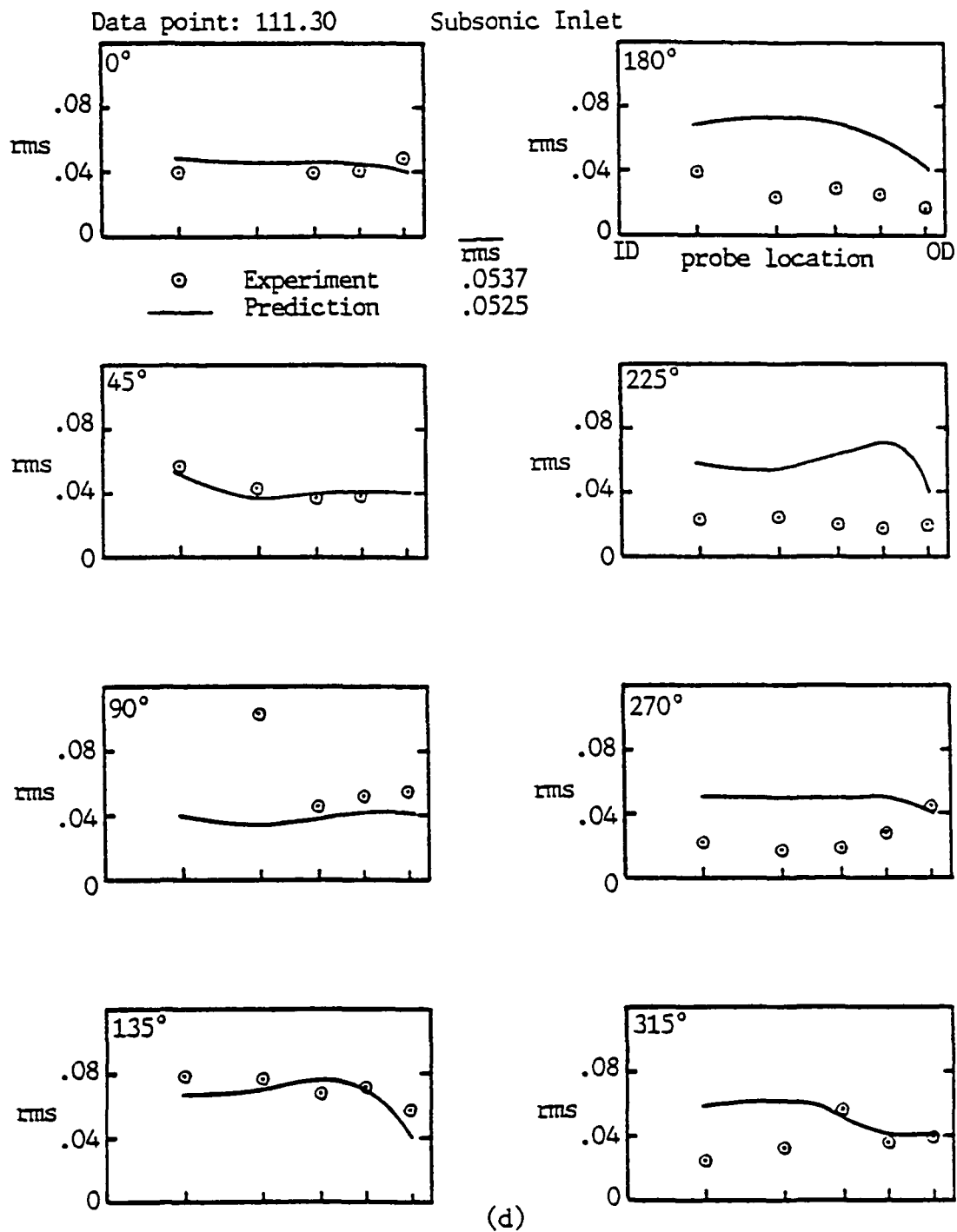


Figure 26. Continued

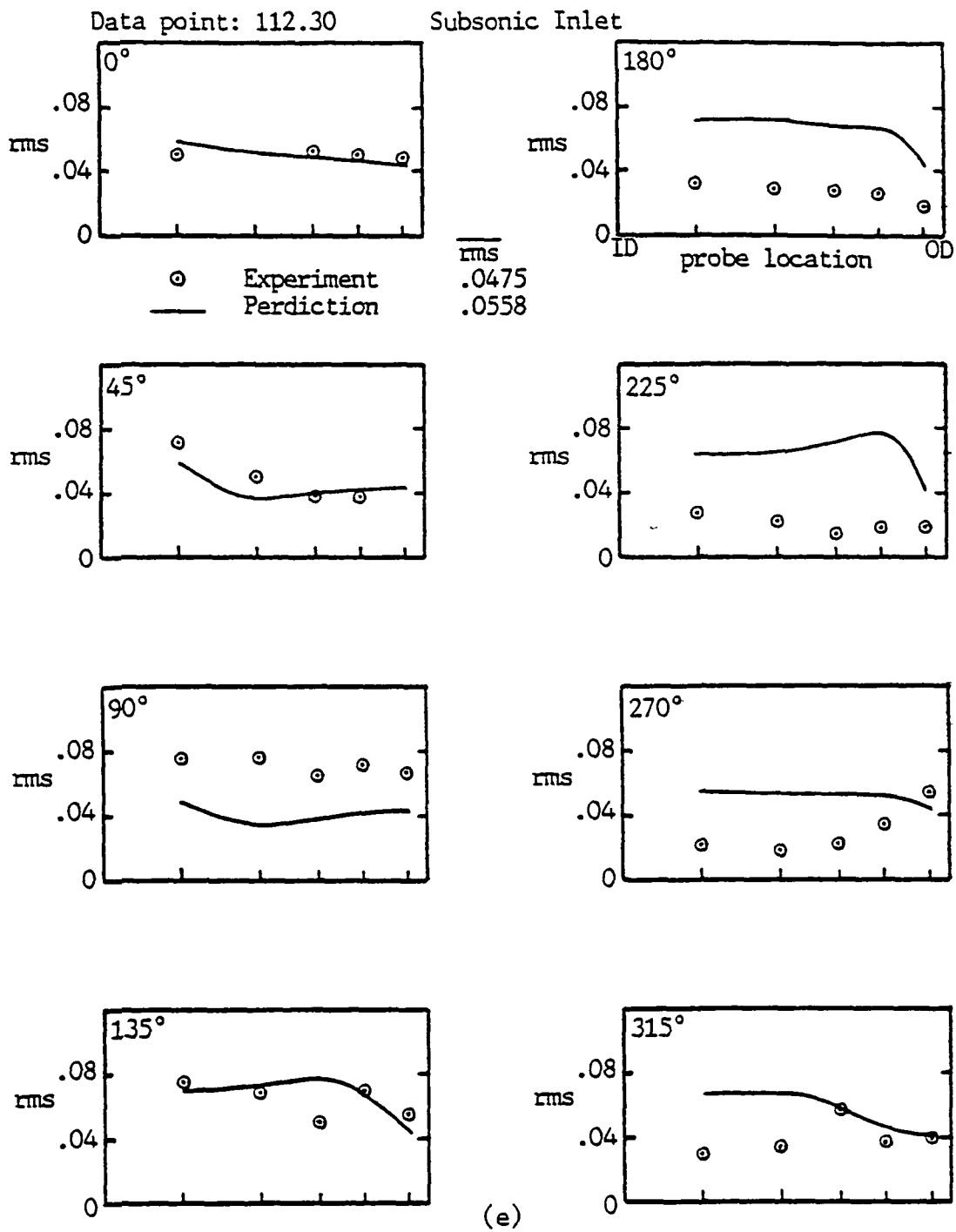


Figure 26. Continued

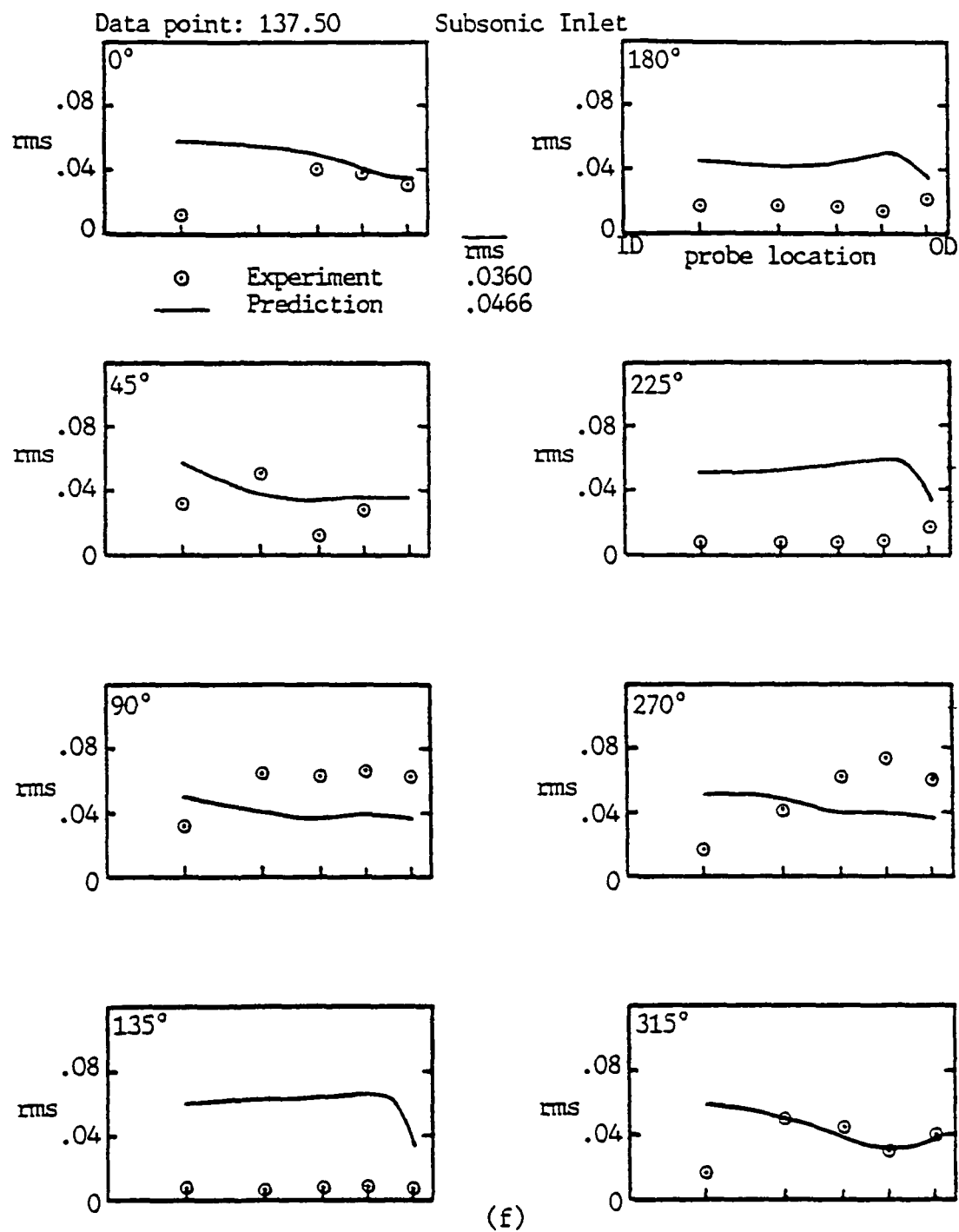


Figure 26. Concluded.

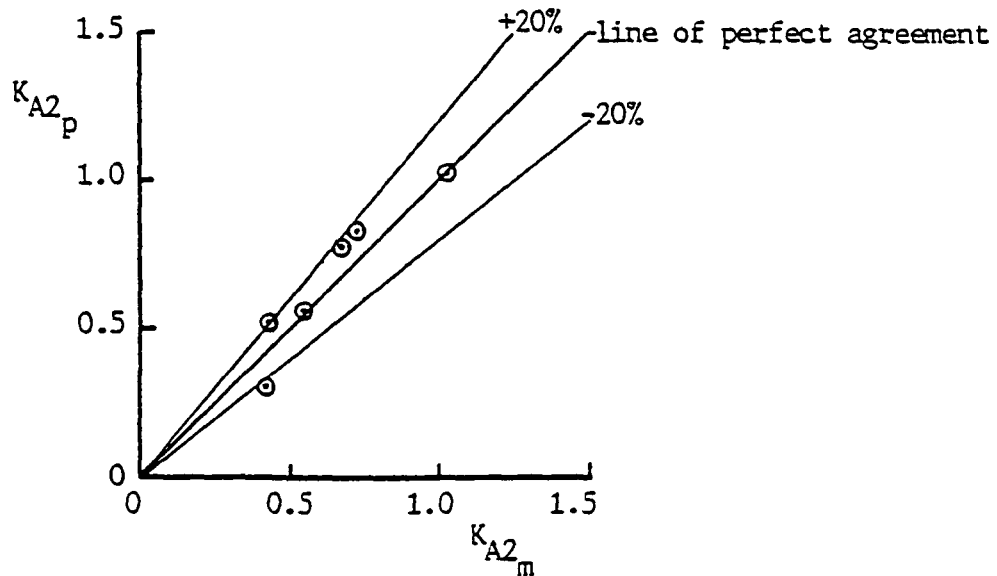
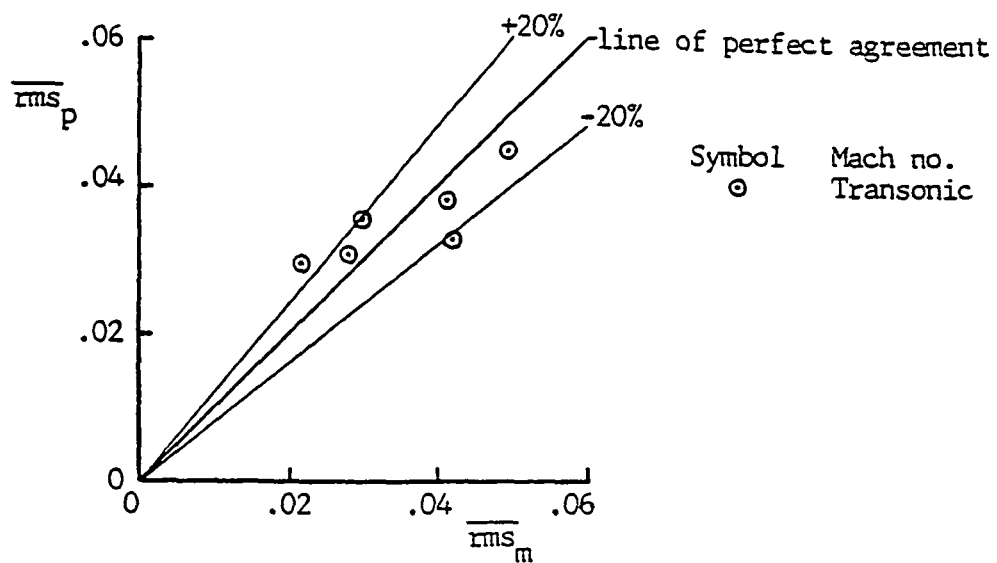


Figure 27. Comparisons of the Predicted and Measured rms Level and Peak Distortion Factor for the Transonic Inlet Model shown in Figure 4. (unpublished data)

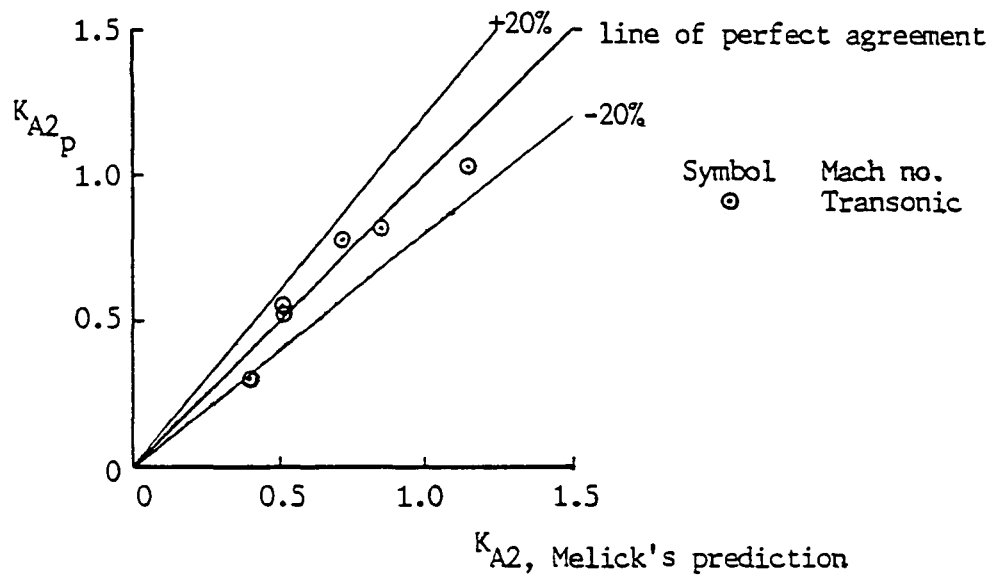


Figure 28. Comparisons of peak distortion factors predicted by the present analysis and the Melick method based on the total pressure rms measurements for the transonic inlet data set (unpublished data)



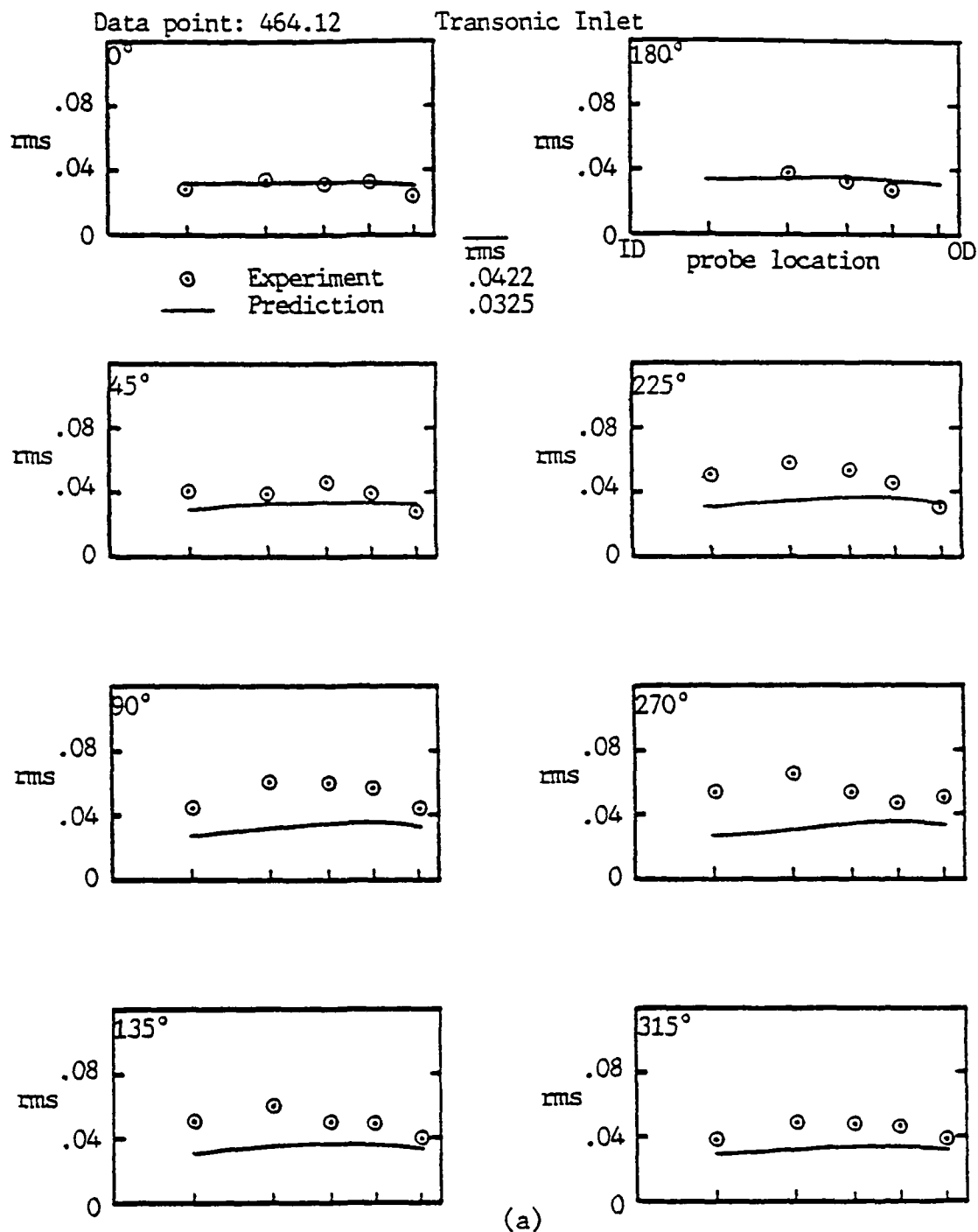


Figure 29. Comparisons of the Predicted and Measured rms Distributions for the Transonic Inlet Model shown in Figure 4. (unpublished data)

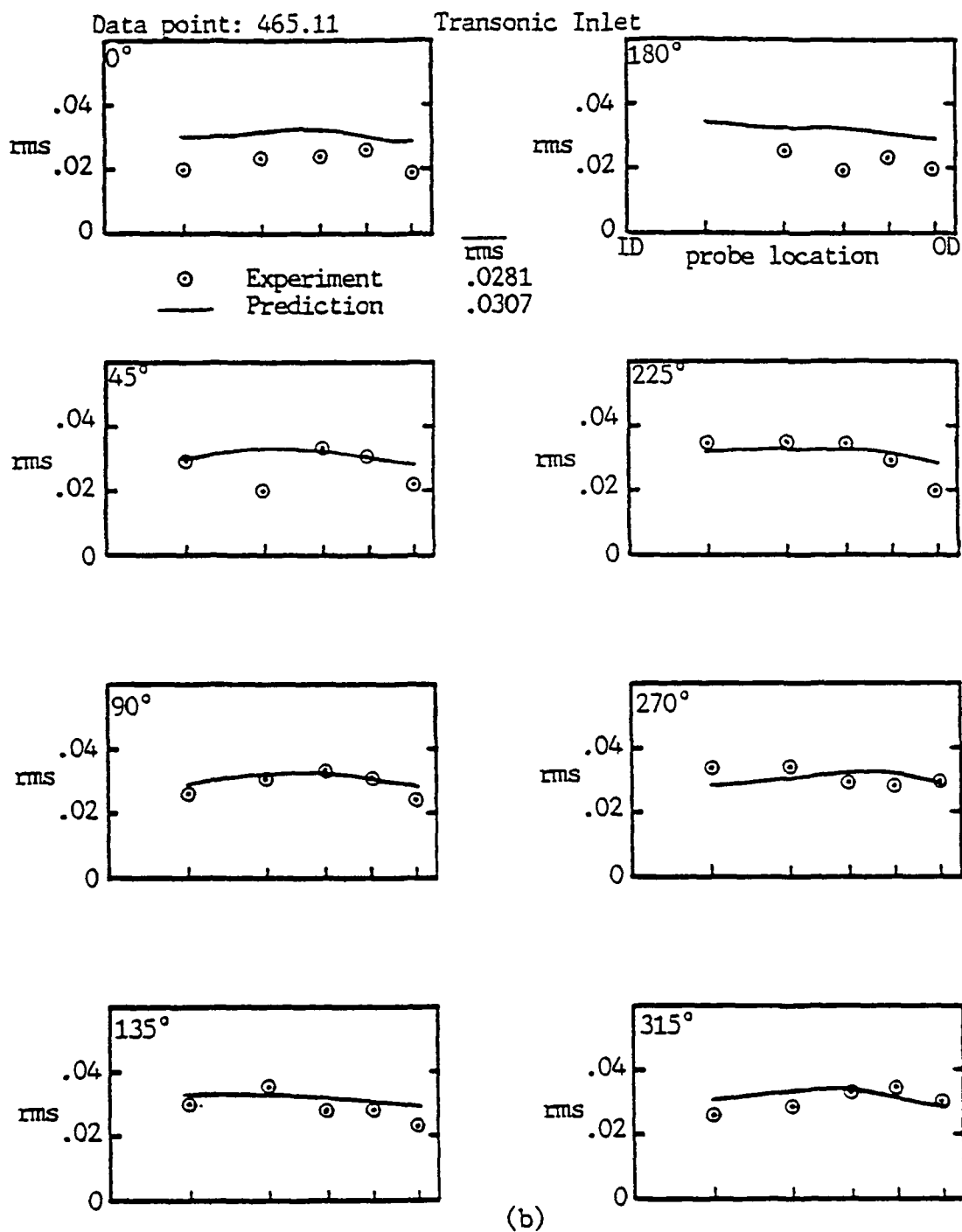


Figure 29. Continued

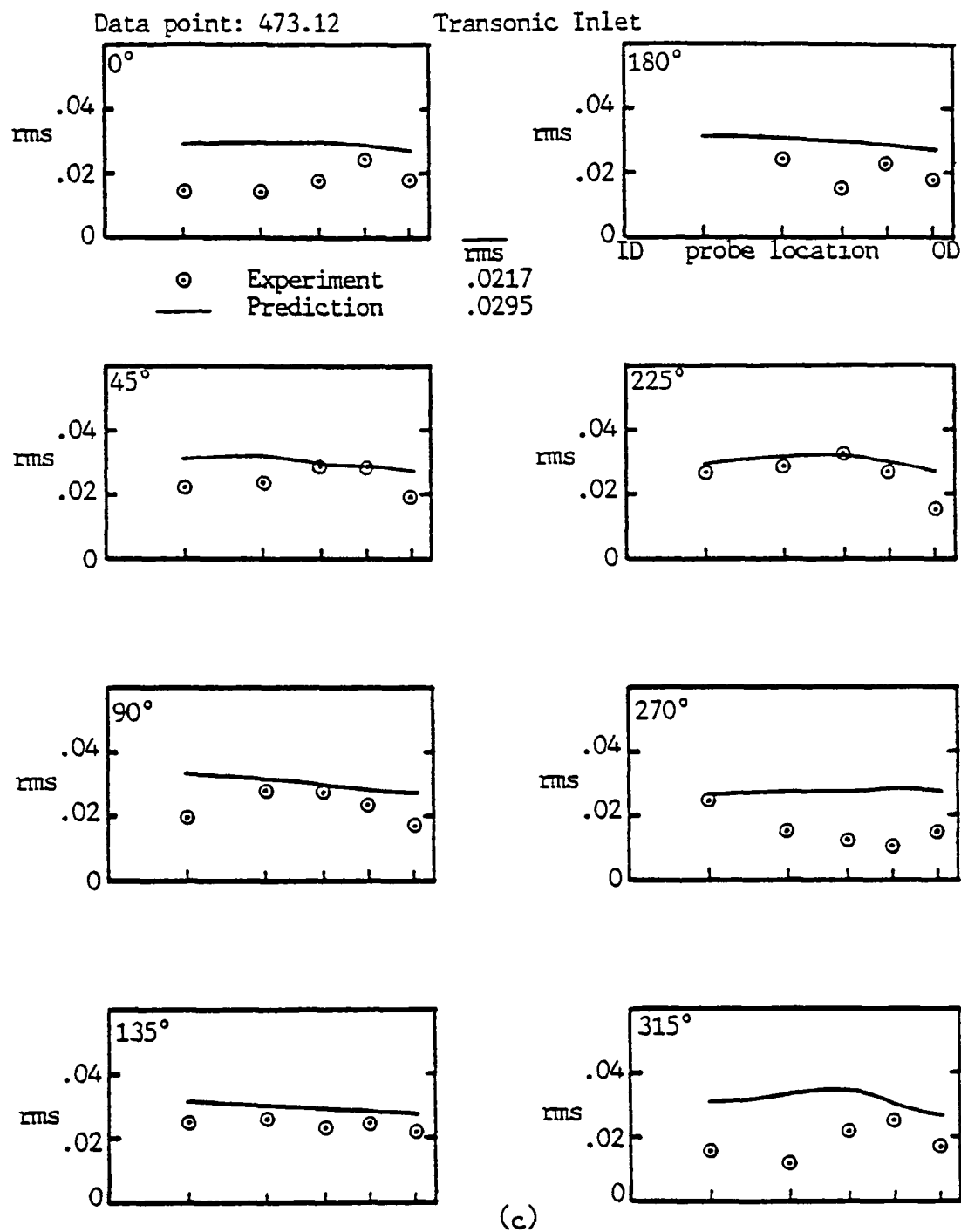


Figure 29. Continued

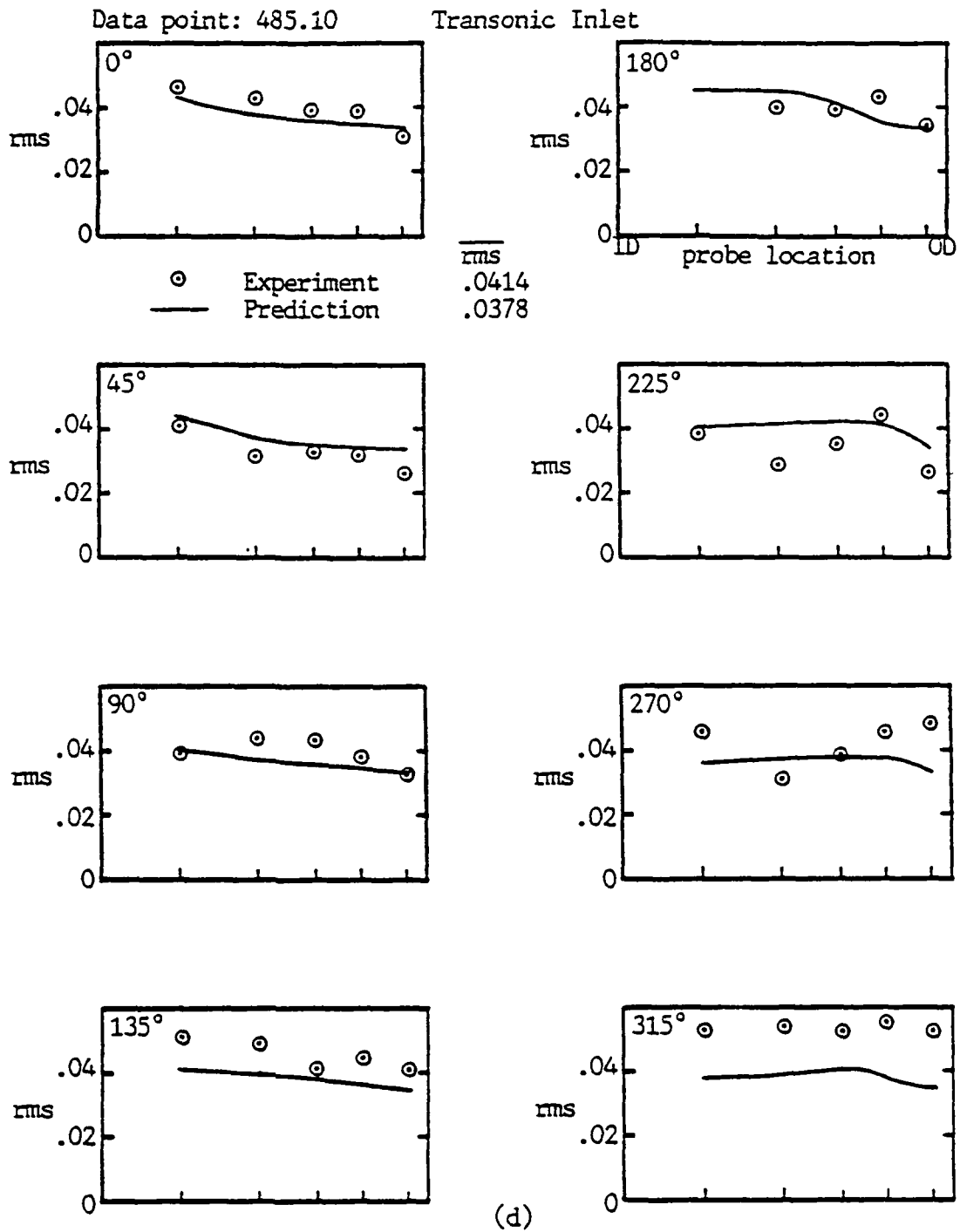


Figure 29. Continued

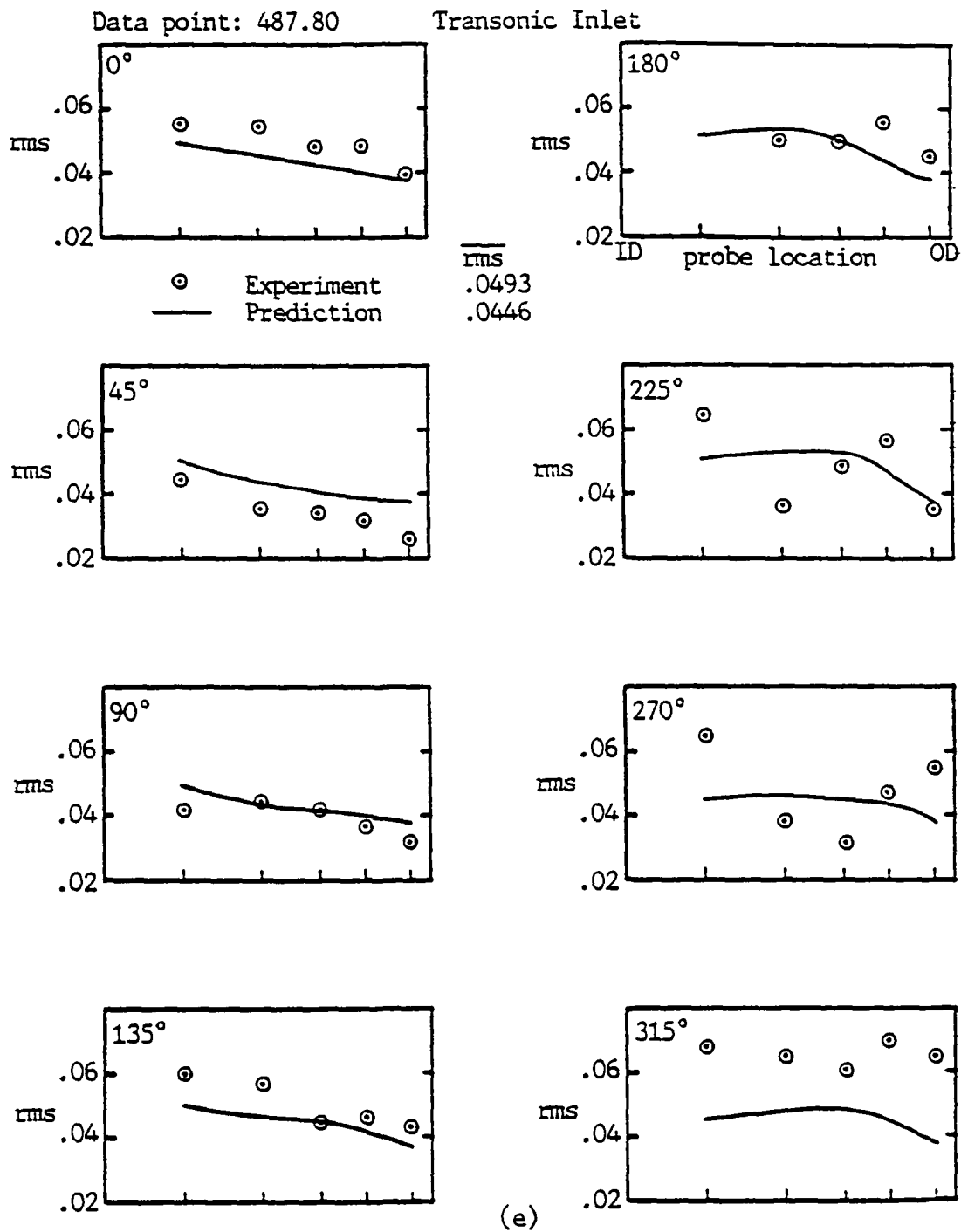


Figure 29. Continued

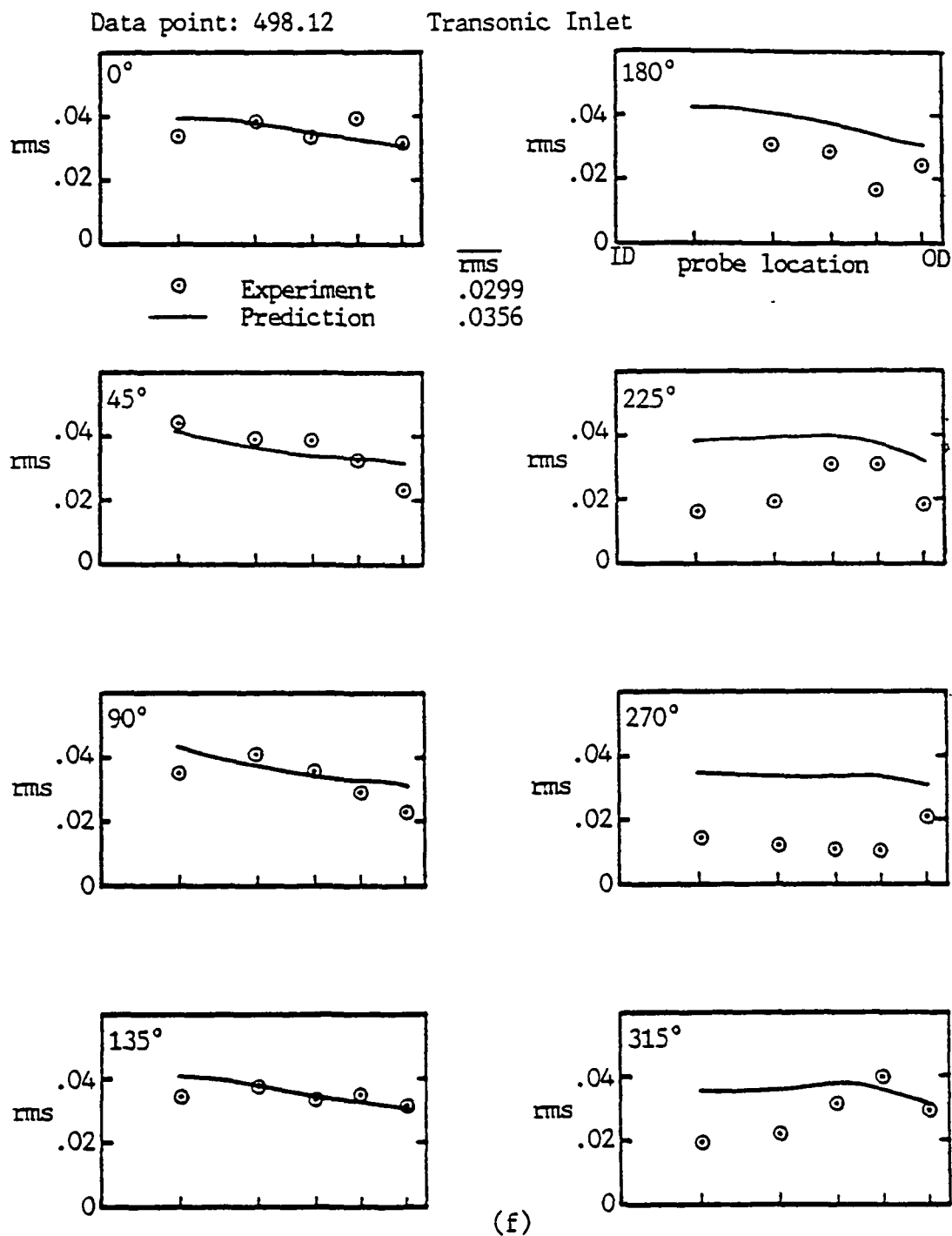
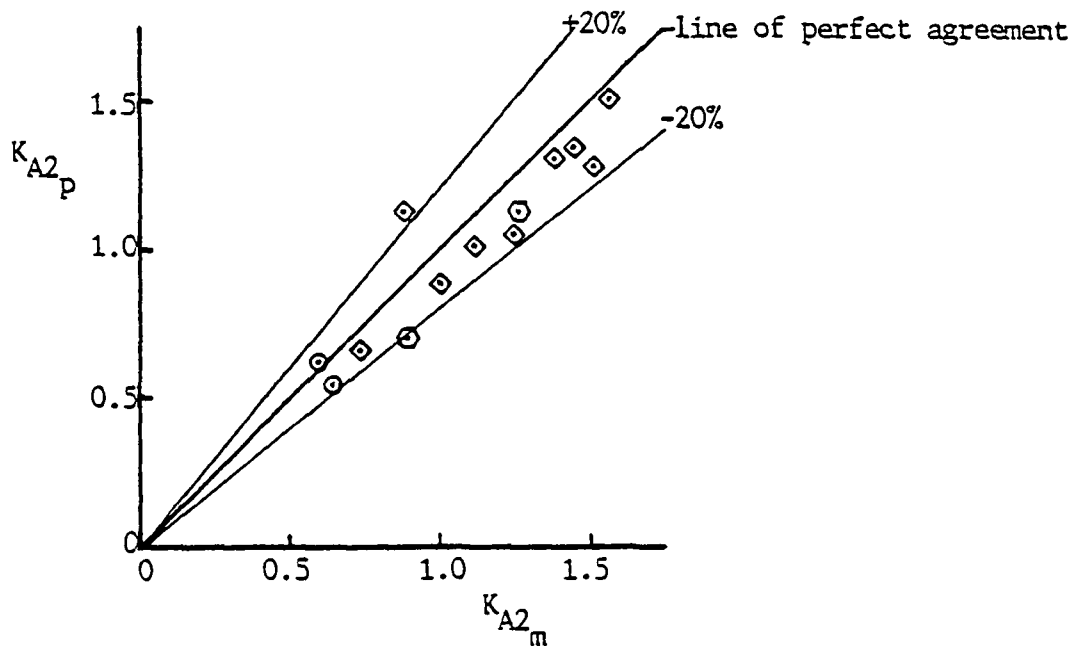
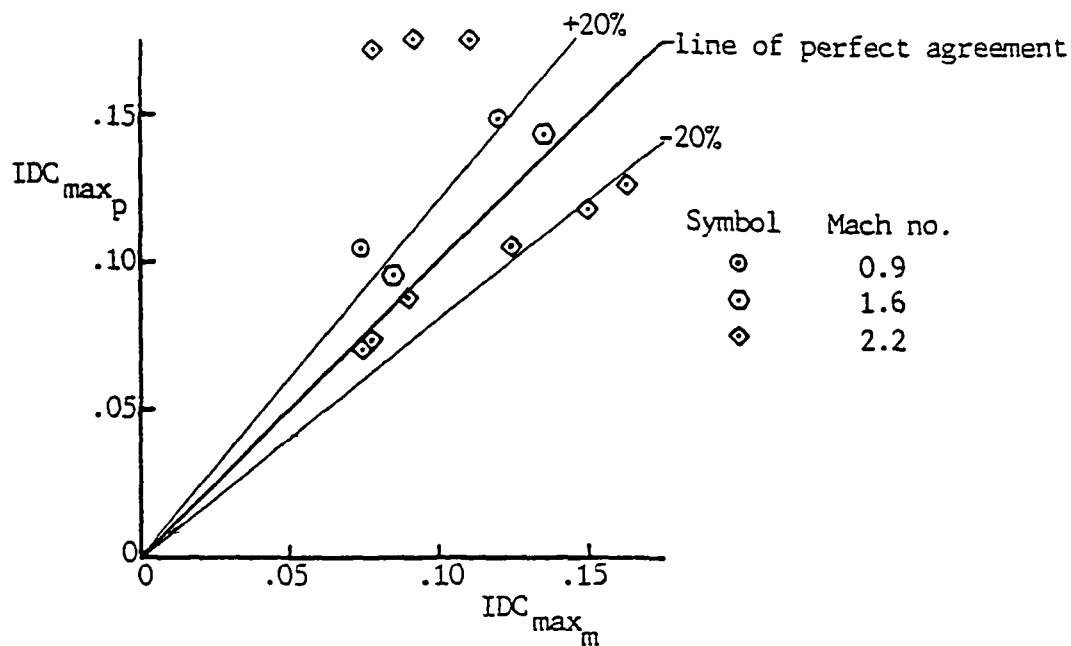


Figure 29. Concluded.



Note: The measured data was screened on  $K_{A2}$  for peak distortion

Figure 30. Comparisons of the Predicted and Measured Peak Distortion Factors for four Tailor-Mate Supersonic Inlet Models (ref. 36, see Figure 5)

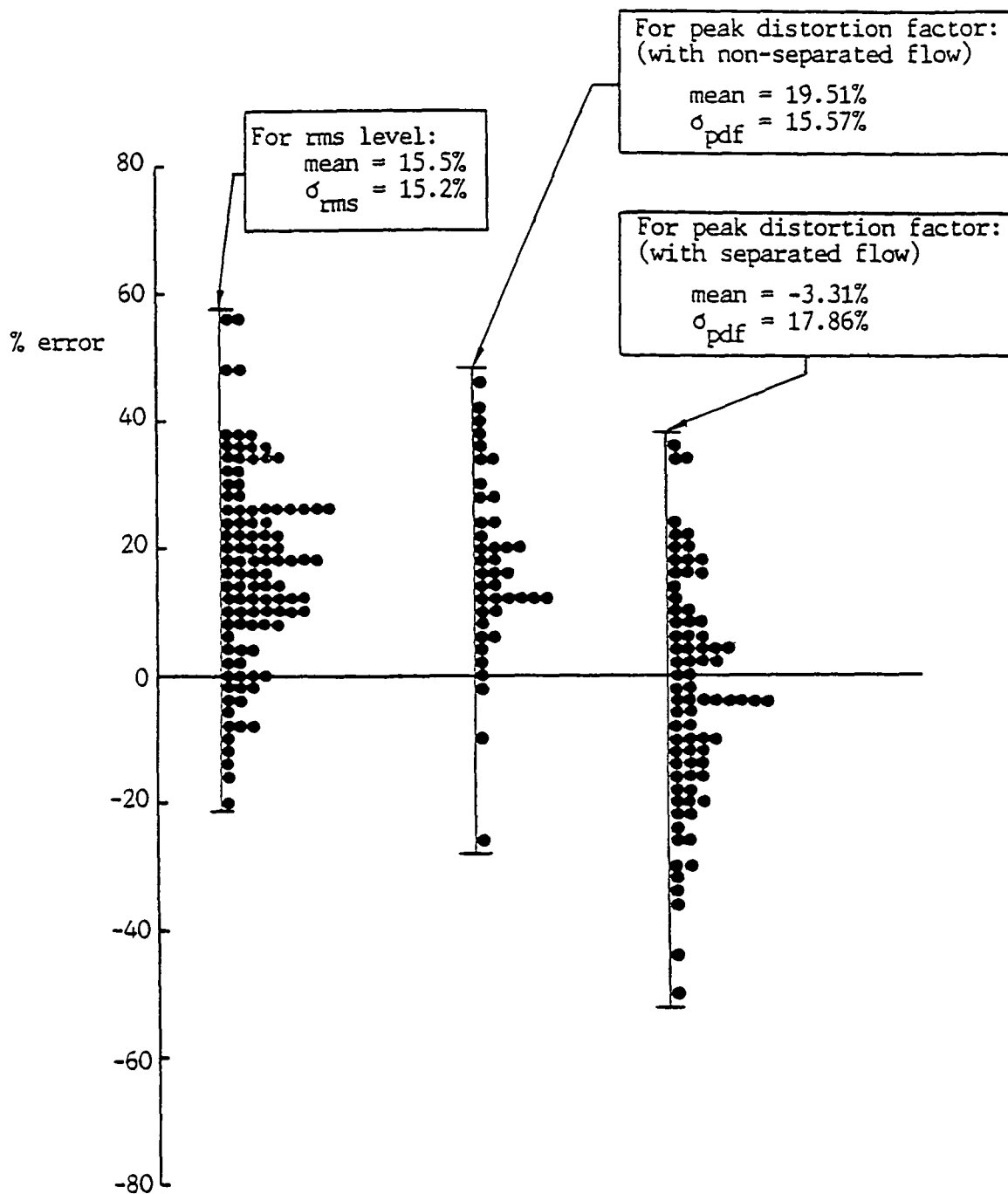


Figure 31. Accuracy of the Present Method in Predicting rms Levels and Dynamic Peak Distortion Factors